NEW PLATFORMS FOR CREATING MULTI-MODAL PROBES

SYNTHESIS AND EVALUATION OF MULTIMODAL NEAR-INFRARED/TECHNETIUM-99M PROBES FOR IMAGING CANCER AND BONE INJURY

By SAMANTHA R. SLIKBOER, B.Sc.

A Thesis Submitted to the School of Graduate Studies in Partial Fulfilment of the Requirements for the Degree Doctor of Philosophy

McMaster University DOCTOR OF PHILOSOPHY (2019) Hamilton, Ontario (Chemical Biology)

TITLE: Synthesis and Evaluation of Multimodal Near-Infrared/Technetium-99m Probes for Imaging Cancer and Bone Injury

AUTHOR: Samantha R. Slikboer, B.Sc. (Sir Wilfrid Laurier University)

SUPERVISOR: Professor John Fitzmaurice Valliant

Number of Pages: xix, 201

Lay Abstract

New and general-purpose methods for creating molecular imaging probes for cancer and bone injury were developed and studied. The approach combines medical isotopes, which can be used to image the whole body of patients, and photoacoustic or luminescent molecules which allow for high resolution imaging of sites of disease identified by the former. More specifically, two novel near-infrared dyes were created which utilize a reaction that allows them to be linked to targeting molecules specific to bone injury. The ability of these new molecules to bind albumin and to localize in tumours through the enhanced permeability and retention effect was demonstrated. One key platform that was developed proved to be particularly effective over several disease models and has significant potential for creating new molecular imaging probes to improve patient care.

Abstract

To address the need for better technologies for imaging disease, new strategies for the synthesis of nuclear, optical and photoacoustic (PA) multi-modal probes were developed. Initially, a library of phenyl-1H-imidazo-[4,5]-f-1,10-phenanthroline (PIP) ligands were synthesized to create isostructural optical and nuclear probes. The ^{99m}Tc complexes of the ligands were prepared in high yield and showed excellent stability *in vitro*. Biodistribution studies were completed where the lipophilic Tc(I) complexes had significant retention in the liver, lung, and spleen.

To overcome this, a second-generation was created. Specifically, a polar cyanine dye, IR783, was linked to a PIP ligand (IR783-PIP) to reduce non-specific binding and enhance blood half-life via albumin binding. An added benefit of using IR783 is that it enabled photoacoustic (PA) imaging to be used in place of optical imaging. *In vitro* testing showed that it was possible to separate the PA signal of IR783-PIP from oxy- and deoxyhemoglobin. Radiolabelling of the IR783-PIP ligand with ^{99m}Tc was also achieved in 41 % yield.

Because it proved difficult to target IR783-PIP, a tetrazine derived cyanine dye was prepared creating the opportunity to link the PA agent to *trans*-cyclooctene (TCO) modified targeting molecules. IR783-HYNIC-Tz was prepared in 2 steps in high yield through a hydrazine-based coupling strategy. The bifunctional dye bound albumin and its PA signal was separable from the signals arising in blood. *In vivo* studies in osteosarcoma and glioblastoma multiforme tumour models were performed where images showed clear tumour uptake. For targeting, IR783-HYNIC-Tz was used in combination with a TCO-derived bisphosphonate for imaging calcium accretion in knee and shoulder joints. The conjugate was also labelled with ^{99m}Tc which verified uptake in the joints (3-5% injected dose per gram) out to 24 hours. Lastly, the IR783-HYNIC-Tz dye was employed to tag TCO-derived gas vesicles to create a new generation of PA/ultrasound imaging agents.

Overall, the strategies reported are platforms for the creation of targeted multimodal probes. They are designed to exploit biorthogonal reactions and can therefore be utilized with a wide range of targeting molecules.

Acknowledgements

I would like to thank my supervisor, Dr. John Valliant, for giving me the opportunity to conduct my graduate research in his lab. I am so grateful for all the advice and time you have invested in me and my project. It has been amazing getting the chance to work in a state-of-the-art facility and conduct innovative research. I have gained immeasurable experience that I will carry with me for the rest of my life.

I would like to express my great appreciation to my committee members, Dr. Ryan Wylie and Dr. Gillian Goward for their patient guidance and constructive feedback. Thank you for the time you put into my thesis and helping me become a more well-rounded scientist.

I would like to acknowledge the support from the past and present Valliant research group members for their support during my time at McMaster. Special to thanks to Dr. Aimen Zlitni, Holly Bilton, Zainab Ahmad, Stephanie Rathmann, Rowan Swann, Zoya Naperstkow, Natalie Mercanti, Kevin Wyszatko, and George Baidoo who have all contributed to my valuable experience. I also could not have done anything without help from Dr. Afaf Genady, Nancy Janzen and Amber Faraday. Thank you for all you have taught me. I extremely grateful to all the amazing friends I have made through my university experience. Mike Wolfe, Kelsey Henry, Chelsea Morash, Alex Nielsen, and Anna D'Angela thank you for always being there in my time of need.

Finally, I would like to thank my family for their unwavering support and love during my university career. Your constant encouragement taught me I can do anything I set my mind to. Thank you for the visits, pep talks, and puppy sitting. I would also like to thank my sister Niki for the long phone calls and adventures. I am lucky to always have your love and support. Lastly, I am also so glad to have had my dog Zoey for the unconditional love and always brightening my day.

Thank you all.

Table of Contents

List of Figures

List of Tables

List of Schemes

List of Abbreviations and Symbols

Ana	Anabanea flos-aquae
Aq	Aqueous
BBB	Blood-brain-barrier
BSA	Bovine serum albumin
BTB	Blood-tumour-barrier
δ	Chemical shift in ppm
CEUS	Contrast enhanced ultrasound
CNS	Central nervous system
DMSO	
E_{max}	Maximum energy
EPR effect	Enhanced permeability and retention
ESI	Electrospray ionization
FDG	Fluorodeoxyglucose
FRET	Fluorescence resonance energy transfer
GBM	Glioblastoma multiforme
GVs	Gas vesicles
h	Hour
Halo	Halobacterrium NRC-1
H&E	Hematoxylin and eosin
HPLC	High performance liquid chromatography
HSA	Human serum albumin
HRMS	High resolution mass spectrometry
HYNIC	Hydrazinonicotinic acid
ICG	Indocyanine Green
ID/g	Injected dose per gram
ID/O	Injected dose per organ
IEDDA	Inverse electron demand Diels-Alder
ImTz	Imidazole linked tetrazine
IR:	Infrared
LFB	Luxol fast blue
mAb	Monoclonal antibody
MI	Molecular imaging
MDP	Methylene diphosphonate
MS	Mass spectrometry
MSA	Mouse serum albumin
NIR	Near Infrared
NMR	Nuclear magnetic resonance
NMI	N-methylimidazole
NHS	N-Hydroxysuccinimide
$^1O_2$	Singlet oxygen
OI	Optical imaging
PAI	Photoacoustic Imaging
PBS	Phosphate buffered saline
PET	Positron emission tomography
PeT	Photon-induced electron transfer
PIP	Phenyl-imidazole-fuzed phenanthroline
PyBOP	Benzotriazole-1-yl-oxytripyrrolidinophosphonium hexafluorophosphate
QY	Quantum yield
RadioTLC	Radioactive thin layer chromatography
RCY	Radiochemical yield
RES	Reticuloendothelial system
R_t	Retention time
SAAC	Single amino acid chelate
SAACQ	Single amino acid chelate quinolone
SPACC	Strain-promoted azide-alkyne cycloaddition
SPECT	Single photon emission computed tomography
$t_{1/2}$	Half life
TLC	Thin layer chromatography
TCO	*Trans*-cyclooctene
TCO-BP	*Trans*-cyclooctene linked bisphosphonate
TCO-GVs	*Trans*-cyclooctene linked gas vesicles

TCO-NHS	*Trans*-4-cycloocten-1-yl 2,5-dioxo-1-pyrrolidinyl ester carbonic acid	μ	Micro
		US	Ultrasound
TCO-OH	(*E*)-cyclooct-4-enol	UV	Ultraviolet
Tz	Tetrazine		

Declaration of Academic Achievement

All chemistry in this thesis was performed by S.R. Slikboer unless noted otherwise. The compounds in Chapter 2 were prepared collaboratively by S.R. Slikboer and T.S. Pitchumony, a former post-doctoral trainee in the Valliant research groups. The gas vesicle construct prepared in Chapter 5 was completed collaboratively by S.R. Slikboer and fellow Ph.D. candidate H.A. Bilton.

All assays and biological studies were performed by S.R. Slikboer with assistance from N. Janzen and A. Faraday, biologists in the Valliant research group. The glioblastoma multiforme model was provided by Dr. Sheila Singh. Histiology was done at the McMaster Immunology Research Centre. Pathology was performed by Dr. Jacek M. Kwiecien.

Publications

Textbook Chapter

Rathmann S.M., Ahmad Z., **Slikboer S**., Bilton H.A., Snider D.P., Valliant J.F. (2019) The Radiopharmaceutical Chemistry of Technetium-99m. In: Lewis J., Windhorst A., Zeglis B. (eds) Radiopharmaceutical Chemistry. Springer, Cham.

Published meeting abstracts:

- Imidazole fused phenanthroline (PIP) ligand for the preparation of multimodal Re(I) and Tc-99m (I) probes. Tamil Selvi Pitchumony, Samantha R. Slikboer, John Valliant. J Label Compd Radiopharm. 2015; 58(S1):S136.
- Imidazole-fused phenanthroline-dyes for the preparation of multimodal nuclear and optical imaging probes. S. Slikboer, J.F. Valliant. J Labelled Compd Radiopharm. 2017; 60(S1):S605

Manuscripts under preparation for submission:

- Synthesis and evaluation of imidazole fused phenanthroline (PIP) ligands as a platform for the preparation of Re(I) and ^{99m}Tc(I) multimodal probes. Samantha R. Slikboer, Tamil Selvi Pitchumony, Laura Banevicius, Patricia E. Edem, John F. Valliant.
- An albumin-binding tetrazine-derived near-infrared dye as a facile reagent for developing targeted photoacoustic imaging agents Samantha R. Slikboer, Zoya Naperstkow, Nancy Janzen, Amber Faraday, Yohannes Soenjaya, Stuart Foster, John F. Valliant.

Patents

WO patent application submitted May 22, 2019. John F. Valliant, **Samantha Slikboer**, Zoya Naperstkow.

Chapter 1: Introduction

1.1 Molecular Imaging

Molecular imaging (MI) describes methods used to noninvasively observe biochemical markers and processes and are therefore used to detect unique biomarkers associated with diseases such as cancer. MI can be used for diagnosis, monitoring the efficacy of treatment, and as a way to identify the presence or absence of a drug target. The latter is gaining importance because of the rapidly increasing number of targeted therapeutic options available.[1] There are several different MI modalities including positron emission tomography (PET), single-photon emission computed tomography (SPECT), optical imaging (OI), ultrasound (US) imaging, and photoacoustic (PA) imaging; each having unique strengths and limitations (Table 1.1).

Table 5.1 Summary of the strengths and limitations of various MI techniques.[1–3]

Imaging Modality	Strengths	Limitations
PET	- Unlimited depth penetration - Whole body imaging - Quantitative molecular imaging possible - High sensitivity	- Radiation exposure - Expensive - Low spatial resolution - Long acquisition time
SPECT	- Unlimited depth penetration - Whole body imaging - High sensitivity - Quantitative - Theranostic option	- Radiation exposure - Low spatial resolution - Long acquisition time
Optical imaging	- No ionizing irradiation - Real-time imaging/short acquisition time - Relatively high spatial resolution - Inexpensive - High sensitivity	- Limited depth penetration - Whole body imaging not currently accessible
Ultrasound	- High spatial resolution - No ionizing irradiation - Real-time imaging - Inexpensive	- Limited depth of penetration - Whole body imaging not possible
Photoacoustic imaging	- High spatial resolution - No ionizing irradiation - Inexpensive - Quantitation possible - High sensitivity - Greater depth of penetration vs optical imaging	- Limited depth of penetration versus nuclear methods - Whole body imaging not possible

1.1.1 PET

PET is a nuclear imaging technique that produces a 3-D image of the distribution of a radioactive tracer. A PET scanner records the two coincident gamma rays associated with positron annihilation, which strike the detector at the same time. PET has superior resolution compared to SPECT and the most commonly employed PET imaging agent is ^{18}F-FDG (fluorodeoxyglucose) which is used to assess glucose metabolism in tumours and other diseases.

1.1.2 SPECT

SPECT, like PET, is a sensitive and widely used MI method.[4] SPECT images are generated by detecting gamma rays emitted from radiolabelled compounds following their administration to patients. The energy emitted from medical isotopes passes through a collimator and contacts a detector that typically consists of a thallium-doped sodium iodide crystal. Upon contact with a gamma ray, these detectors emit a flash of light which is amplified using photomultipliers and counted as electrical pulses. A 3D image is obtained by mounting the scintillation camera on a rotating gantry, recording multiple images at different angles and reconstructing the activity distribution.

Examples of gamma emitting medical isotopes used for SPECT include ^{99m}Tc, ^{123}I, and ^{111}In (Table 1.2). ^{99m}Tc is the most widely utilized radionuclide in diagnostic medicine, accounting for 80% of all imaging procedures.[5] It is a metastable nuclear isomer of ^{99}Tc, which is obtained from a ^{99}Mo generator in which the parent isotope (^{99}Mo) bound to alumina as MoO_4^{2-} decays to the daughter (^{99m}Tc) in the form of $^{99m}TcO_4^-$.[6] $^{99m}TcO_4^-$ can be eluted on a daily basis using saline thus ^{99}Mo/^{99m}Tc generators are a convenient source of ^{99m}Tc that can be housed in radiopharmacies.

Table 1.6 Commonly used medical isotopes for SPECT and key nuclear properties [4]

	$t_{1/2}$	E_{max}
^{99m}Tc	6.02 h	141 keV
^{123}I	13.0 h	529 keV
^{111}In	67.2 h	245 keV

^{99m}Tc is a nearly ideal isotope for SPECT as it produces a photon having an optimal energy for detection (140 keV) while delivering a low dose burden to patients. The latter is a result of the modest amount of photoelectric effect and Compton scattering that occurs at this energy. ^{99m}Tc has a half-life (6.01 h), which affords sufficient time for synthesis of Tc-radiopharmaceuticals and transportation from the radiopharmacy to the imaging clinic. The isotope also has a fairly low cost since ^{99}Mo is the byproduct of uranium fission and neutron bombardment of ^{98}Mo.

1.1.3 Optical Imaging

Although PET and SPECT are used routinely for whole body imaging, administrating radioactivity is not always ideal or warranted. As an alternative, optical imaging (OI) uses non-radioactive molecular probes to visualize biological processes at both the cellular and molecular level. OI is cost effective, widely available, and sensitivities at probe concentrations comparable to PET and SPECT (10^{-9} to 10^{-12} M) are possible.[7,8] OI also has good spatial resolution (2-10 mm) and can utilize a wide array of different fluorophores.[7] OI avoids exposing subjects to ionizing radiation and imaging can be performed in real time, and is therefore particularly useful for surgical guidance and when repeat imaging studies within a short period of time are needed. Furthermore, OI can be used to assess specific biochemical changes due to the sensitivity of certain fluorophores to changes in various ion concentrations, hydrophobicity, and pH.[9]

Targeted OI probes are typically comprised of a targeting molecule tagged with one or more fluorophores. It is imperative to tune *in vivo* imaging parameters such as the absorbance and emission

spectra of the fluorophore with desired application since scattering and autofluorescence are prominent issues.[10] Imaging parameters are typically designed to avoid any potential interference from background fluorescence making the near infrared (NIR) spectral region (650-900 nm) ideal. NIR fluorescence imaging represents a vast improvement over imaging in the visible region due to reduced autofluorescence and lower tissue scattering and emission. Longer wavelengths in the NIR region also enhances the signal-to-noise ratio since there is limited autofluorescence and allows for deeper tissue penetration.

There are generally two classes of OI probes: targeted optical probes and activated optical probes.[11] Targeted optical probes accumulate at the site of interest, resulting in an increase in signal over time. Due to their constant fluorescent state, these probes are considered "turned-on" and sufficient time should be allowed for them accumulate at the site of interest and clear non-targeted tissue before imaging. Various fluorescent dyes have been used in the development of targeted optical probes. The most well-known example is indocyanine green (ICG) which is a cyanine dye approved for use in humans.[12] There are a wide range of next generation targeted fluorescent OI probes being developed to increase targeting specificity while decreasing the amount of fluorophore required to achieve high quality images. Unfortunately, since these probes are always "on", it is a challenge to achieve optimal signal-to-noise ratios.[7,10,13]

The second type of OI probes are activated probes, which can be turned "on" or "off" typically through exploiting a specific quenching mechanism.[11] The interaction of these probe with a specific target would either elicit a conformational or chemical change causing the probe to emit light or stop emission of energy.[10,13] There are several mechanisms that can impact the emission of a fluorophore, which include photon-induced electron transfer (PeT), fluorescence resonance energy transfer (FRET), and self-quenching.[8] The PeT mechanism works via an electron transfer from the donor to acceptor fluorophore (when they are in the same molecule) (Figure 1.1A).[14] This transfer

quenches any light that would otherwise be emitted. FRET results in the non-radiative transfer of energy between a donor and acceptor (or quencher) causing a fluorescent output (Figure 1.1B).[15] The important factor for FRET is the distance between the donor and acceptor (maximum distance of 9 nm).[16] Lastly, self-quenching occurs when fluorophores are conjugated to the same target in close proximity or when they aggregate (Figure 1.2C).[8] These activated probes have high signal-to-noise ratios, with intensities increasing more than 200× upon "turning on" and binding to their target of interest.

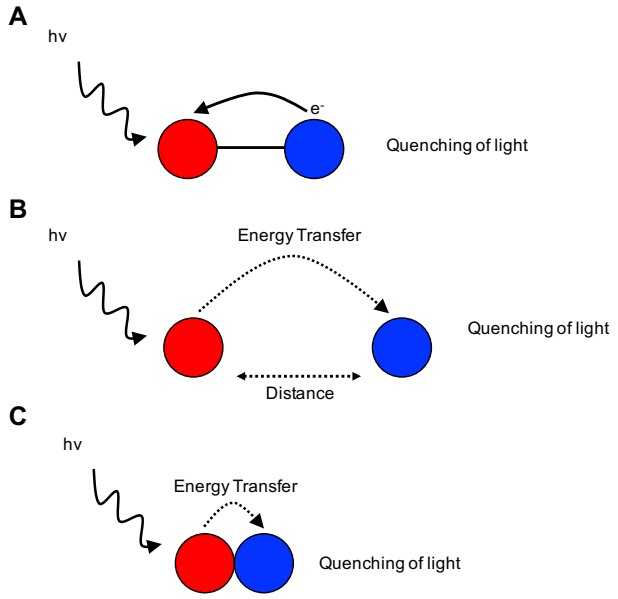

Figure 1.1 Schematic representations of fluorescence quenching mechanisms. (A) = PeT; (B) = FRET; (C) = Self-Quenching

The major limitation of optical imaging is the lack of depth of penetration, which is restricted to 1-2 centimeters.[17] The limited depth of penetration is related to the absorption and scattering of light, which is primarily a function of the wavelength of excitation.[18] Incident light is absorbed by endogenous chromophores found in living tissues such as hemoglobin, melanin, and lipids. Light absorption and scattering decreases with increasing wavelengths where below 700 nm (visible region) there is shallow penetration, however above 900 nm water absorption interferes with signal generation.

The most prevalent use of fluorescence imaging has been as a guide for surgeons to identify diseased tissue during surgical resections. Surgeons rely on their senses when excising a tumour; looking at the colour of the tissue, probing the tissue temperature and stiffness meaning that surgical outcomes can vary from surgeon to surgeon. Fluorescent agents can be used to visualize tumours to be removed or critical structures to be avoided (bile ducts, ureters, nerves, and vessels). Ongoing and completed clinical trials suggest fluorescence guidance can have a positive impact on cancer surgery (lymph node mapping, liver and ovarian cancer imaging) and general surgery (ureters, bile ducts, and vessel imaging). There are at present several imaging systems used in human surgery using contrast agents like indocyanine green and methylene blue.[19,20]

1.1.4 Ultrasound Imaging

Ultrasound (US) imaging is the second most widely used imaging modality, next to conventional x-ray. US gives real time images, is low cost, widely available, and portable. It works by sending pulses of high frequency US waves from a transducer through different structures in the body where the waves get reflected or scattered (Figure 1.2). The US transducer then detects a portion of the scattered sound waves and converts them into electrical pulses and 2D images generated. It is typically used for preliminary screening and follow up and also to get anatomical information, most commonly during pregnancies.

US waves can be disrupted by air or gas and they have difficulty penetrating dense structures such as bone. Soft and hollow areas do not reflect sound waves and appear dark on images whereas the denser a structure is, a bright white colour will show up on the US image. Ultrasound scattering is low compared to scattering seen in optical imaging therefore it has superior depth of penetration. There is tunability with the US frequencies used depending on the area of interest for imaging. High frequency waves offer better resolution at the cost of penetration depth while low frequency US gives

deeper penetration with lower resolution. This allows the ideal frequency to be selected depending on the information needed from an US scan.

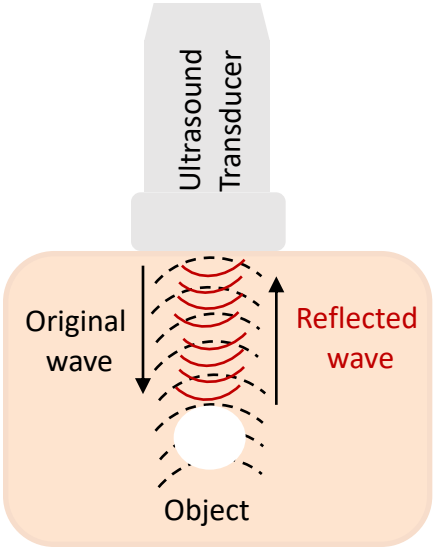

Figure 1.2 Generalized schematic showing how ultrasound images are generated.

1.1.5 Photoacoustic Imaging

The photoacoustic effect is the process by which light energy is converted into vibrational energy or sound. It occurs via the absorption of a photon from a light pulse by a molecule. Heat is produced as a result of the absorption of energy, which in turn will translate into thermoelastic expansion of the chromophore. The expansion is followed by a rapid contraction when the light pulse ends which produces a pressure/sound wave (Figure 1.3). A light pulse duration shorter than 1 microsecond produces pressure in frequencies up to several MHz notably in the ultrasound region. The sound waves produced depends on the length of laser pulse, where nanosecond pulses produce ultrasound waves that can be measured using ultrasound probes. PA imaging has advantages over OI because it has higher depth of penetration (7 cm) and higher spatial resolution (100 μm) (Figure 1.4).

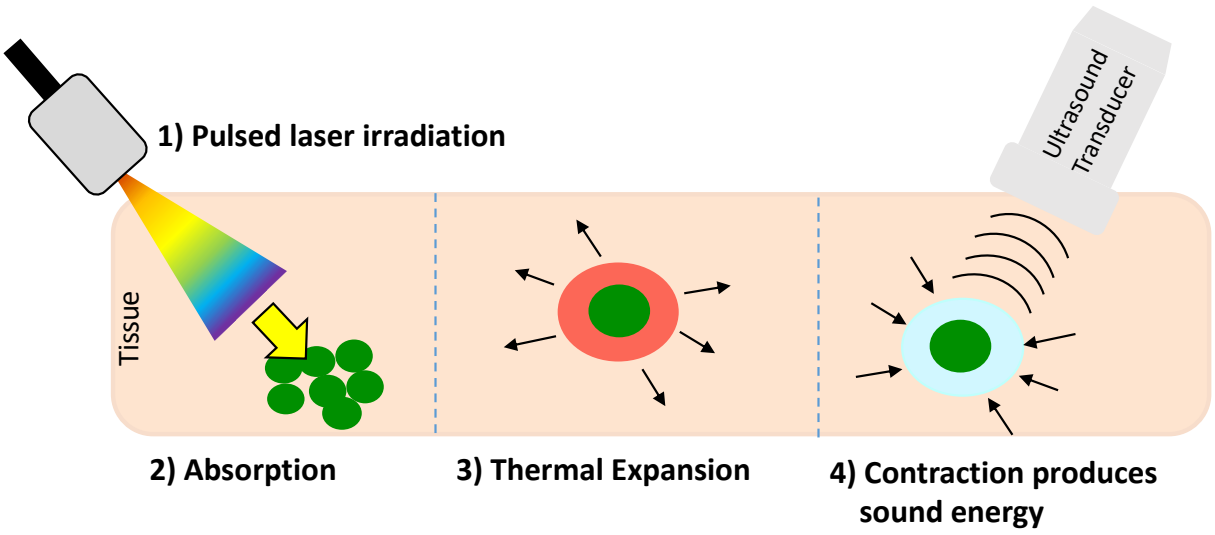

Figure 1.3 Schematic showing the basic components of photoacoustic imaging.

Figure 1.4 Images showing the differences in spatial resolution of optical versus photoacoustic imaging. The same sample of a dye printed on paper was visualized using optical imaging (left seen in red and orange) and photoacoustic imaging (seen on the right in green). Images were collected by S.R. Slikboer using the dye **28** reported in Chapter 4.

Small molecule dyes, such as cyanine dyes, are highly conjugated where the delocalized electrons require modest energy for excitation. The relaxation of the excited electrons can occur in radiative (fluorescence) or nonradiative processes, depending on the lifetime and electronic configuration of the excited states. For PA imaging, large nonradiative relaxation such as that found in certain cyanine dyes, is required and is often associated with dyes having low quantum yields.

1.2 Near Infrared Dyes

There are a wide range of commercially available fluorescent dyes available, but only a limited number emit in the NIR region and of those only a handful are suitable for *in vivo* applications.[21–25] When designing a fluorescent dye for *in vivo* applications, it must be water soluble, have high quantum yields, possess structural and chemical stability, and optimally would have a site for conjugation to biomolecules.[11] There are two main families of dyes which meet these criteria: cyanines and rhodamines (Figure 1.5).

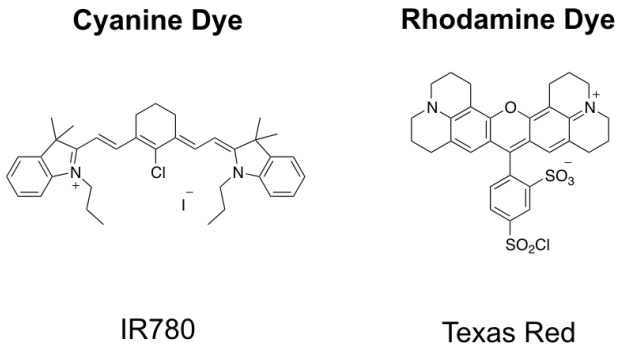

Figure 1.5 Representative structures of cyanine and rhodamine dyes.

1.2.1 Rhodamine Dyes

Rhodamine dyes contain a honeycomb-like structure. They differ from cyanine dyes in that they have high absorption coefficients, larger quantum yields, and a broader fluorescence spectrum in both visible and NIR regions.[11] Some examples include Texas Red, Rhodamine B, 5-carboxytetramethylrhodamine (TAMRA), and Alexa Fluor 610 (Figure 1.6).

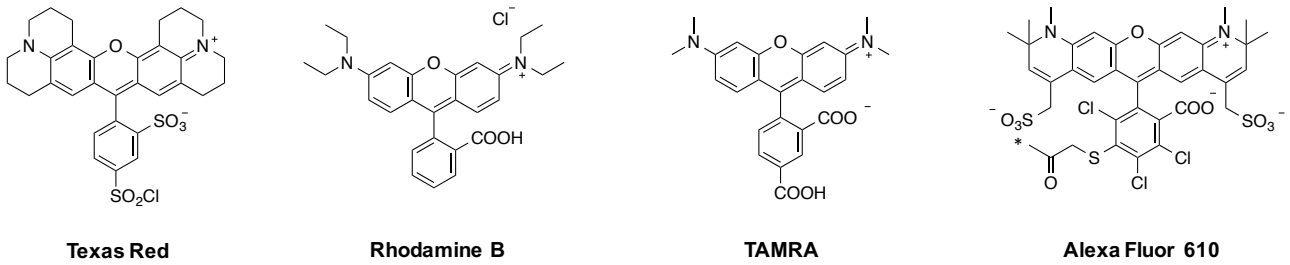

Figure 1.6 Rhodamine dyes.

1.2.2 Cyanine Dyes

Cyanine dyes are a general class of dyes that are characterized by linear methine chains. They have versatile chemistry which allows modifications at multiple positions along the carbon backbone.[11] This enables tuning the absorbance wavelength, improving the solubility and chemical stability, and biomolecule conjugation. These dyes are generally not pH sensitive making them attractive for *in vivo* applications as their spectra will not be altered by changes in the tumour environment.[11] The near-infrared absorbance and emission are also ideal features *in vivo* imaging as it will not overlap or interfere with most endogenous ligands. Examples of cyanine dyes include IR780, IR820, indocyanine green, and Cy3 (Figure 1.7). By adding a sulfonate group, the water solubility of cyanine dyes can be increased, while dye aggregation and nonspecific binding to cellular constituents are reduced.

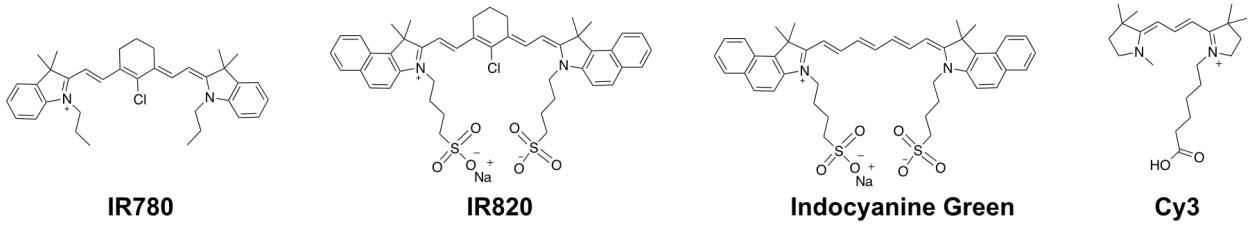

Figure 1.7 Example of cyanine dyes.

ICG is a tricarbocyanine dye approved for blood volume determination, cardiac output, liver function, visualization of retinal and choroidal vasculature, photodynamic therapy and imaging lymph drainage.[26] It is a contrast agent that doesn't have functional groups that easily allow for simple conjugation to biological carriers to enhance its target selectivity *in vivo*. It also has limited solubility in aqueous solutions and its short plasma residence time of 3.5 min restricts the optimal imaging window.

Heptamethine cyanine dyes containing a rigid chlorocyclohexene ring in the backbone of the molecule demonstrate increased photostability and quantum yield compared to cyanine dyes lacking this structural motif. Delocalization of the positive charge generates strong intermolecular van der Waals interactions that promote aggregation in aqueous solution. These aggregates exhibit different absorbance bands than the monomeric dye. Red (bathochromic) shift aggregate bands are called J-aggregates and blue (hypsochromic) shifted aggregates are called H-aggregates. H-aggregates stack parallel (plane to plane) and the dipoles are completely coupled and promoted to higher energy excited states (shorter wavelengths) and do not fluoresce (low molecular extinction and quantum yield). J-aggregates stack head-to-tail (end-to-end) and are only partially coupled, therefore are only excited to the lowest energy excited state (longer wavelengths). Thus J-aggregates will produce a fluorescence signal since electrons in their lowest excited state can fluoresce (large quantum yield (QY)).

1.2.3 Targeted cyanine dyes for OI

To use cyanine dyes for the detection of specific disease markers, synthetic modifications are needed to ligate to targeting vectors. There are several example of this in the literature such as Cy7 which has been modified to include deoxymannose which have been shown to promote uptake in tumour-associated macrophages.[27] Cy7 has also been modified to tag antibodies as well as provide a site for ^{18}F labelling to create a multimodal PET/OI imaging agent which targets prostate cancer.[28] Several cyanine dyes were attached to amino acid conjugates which are not fluorescent in water, but

give off a strong signal when bound to DNA or RNA.[29,30] IRDye800CW is a cyanine dye linked to estradiol which has been developed to target and image breast cancer.[31] Some cyanine dyes have been modified to include peptides such as CyA-cRGD which targets $\alpha_v\beta_3$ integrin expressing tumours.[32] Although these probes have all shown promise, they were engineered to study a single biological target. A new probe needs to be synthesized and extensively tested for each novel target, which is costly, time consuming and requires extensive synthetic expertise. Creating a single cyanine dye that can be easily linked to a wide array of targeting vector would be enabling and fill a major void in the MI field.

1.3 Dual-Modality Imaging Agents

Rather than using a single technique to visualize disease, multimodal imaging systems and the associated probes can combine the strengths and mitigate limitations of single modality instruments. For instance, there is substantial interest in developing molecular imaging probes that can be used for both optical[33–36] and SPECT imaging.[37–40] The advantage of combining these two modalities is that SPECT imaging provides the ability to detect, characterize, and monitor disease via whole-body imaging non-invasively. Optical imaging in turn can aid in surgical and biopsy guidance, while minimizing exposure of the patient and surgeon to radioactive material. Unfortunately, there are a limited number of truly multimodal optical and nuclear probes. One of the approaches taken in this thesis is to create complementary pairs of luminescent Re complexes and their isostructural ^{99m}Tc analogues. This approach creates the opportunity to correlate optical and nuclear imaging data using a single structural motif (Figure 1.8).

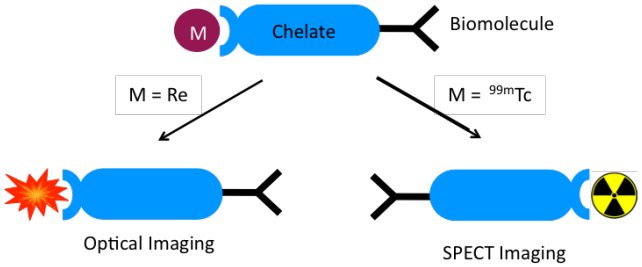

Figure 1.8 Representation of a strategy for creating isostructural SPECT/luminescent probes derived from Re and ^{99m}Tc.

1.3.1 SPECT/OI Agents

One example of a SPECT/OI multimodal probes in the literature is a cyanine dye-Re/^{99m}Tc chelate complex (Pam-Tc/Re-800, Figure 1.9).[41] This compound utilizes bisphosphonate as a targeting vector to bind hydroxyapatite to image microcalcifications associated with breast cancer metastasis.[41] The structure also contains IRDye800CW for optical imaging along with a metal binding portion to coordinate with ^{99m}Tc(V) for SPECT imaging. Frangioni *et al.* evaluated this construct for its fluorescent properties, stability and target binding *in vivo*.[41] The radiolabelled version was produced in high radiochemical purity (~98%) when complexed with ^{99m}Tc(V). The fluorescent properties of the corresponding Re(V) complex showed an absorption (781 nm) and emission (800 nm) in the NIR region. Furthermore, the probe had a high quantum yield of 8.9% in PBS. *In vivo* whole-body distribution studies using the ^{99m}Tc(V) complex showed localization at sites of microcalcification and clearance of the construct through the renal system. Additionally, the accumulation of the labelled construct in the bone was higher than that of ^{99m}Tc-methylene diphosphonate (MDP) (structure shown in Figure 1.10) which is the gold standard for bone imaging.[41] With the presence of the cyanine dye it was also possible to generate high resolution optical images of microcalcifications.

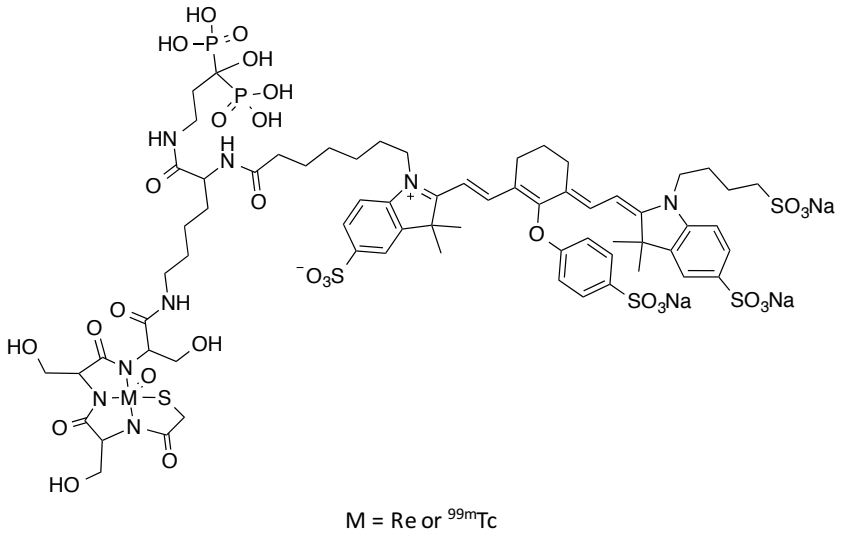

Figure 1.9 PAM-Tc/Re-800. [41]

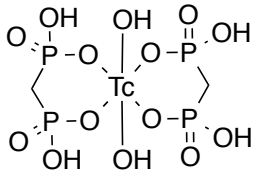

Figure 1.10 Postulated structure of ^{99m}Tc-MDP.[42]

1.4 The Chemistry of Re/Tc

As there are no stable isotopes of technetium, its congener Re is often used to prepare reference standards for new ^{99m}Tc complexes. When ^{99m}Tc complexes are prepared they are typically generated in nanomolar quantities making direct analysis challenging. Re complexes have similar structure to the Tc analogue because of the lanthanide contraction.[43] Their chemistry is also similar particularly in low oxidation states where it is possible to prepare isostructural Tc(I) and Re(I) complexes in aqueous media from $[(M(CO)_3(OH_2)_3]^+$. This reagent can conveniently be synthesized in a single step from MO_4^- (M = Re, Tc).[44–46] However, it should be noted that Tc and Re complexes often have different redox potentials where reactions with Re compounds can require higher temperatures, lower pH, and higher concentrations of reducing agents.[47]

1.4.1 Organometallic Complexes of Re and Tc

With the appropriate ligand, metal complexes of Re(I) have been shown to be luminescent creating the opportunity to prepare multi-modal and isostructural OI/SPECT probes.[48–51] Example of such agents include Re(l) complexes of polypyridine ligands which have been used for *in vitro* and *in vivo* OI applications.[52–55] The luminescent Re complexes are attractive because of their broad absorbance (extending into the visible spectrum) and emission spectra (extending into the near-infrared spectrum), their long-lifetime, polarized emission and large Stoke's shift.[53,56–59] Most Re(I) complexes in this class contain either a bidentate ligand such as 1,10-phenanthroline,[60,61] or 2,2′-

bipyridine[56,57], or a tridentate ligand such as the single amino acid chelate quinoline (SAACQ) ligand (Figure 1.11).[62]

The tridentate chelate SAACQ was developed to improve the optical properties of first-generation single amino acid chelate (SAAC) ligands. SAAC ligands form complexes with the $M(CO)_3^+$ core (M= Re(I), Tc(I)) and can be incorporated into peptides as if they were an amino acid.[62] Unfortunately, the corresponding Re(I) complexes were not luminescent, so a quinoline group was added to improve the luminescence while retaining the ability to bind with ^{99m}Tc(I). Although this modification was an improvement, the excitation spectrum was in the UV-visible region (301 and 366 nm), which is not ideal for OI due to the possibility of damaging tissue and competition from autofluorescence.[63–65] The Re(I) SAACQ complex had an emission spectra with two main transitions (425 and 580 nm) and a sufficient lifetime (4.31-9.76 μs) to perform imaging studies. The low quantum yield ranged from 0.3% to 1.5% in various solvents as well as in the presence of air which is comparable to other reported rhenium-based optical imaging probes.[66,67] A further issue with SAACQ was that it was not particularly reactive with ^{99m}Tc(I) and required heating and longer reaction times compared with SAAC ligands. Finally, the hydrophobicity of SAACQ (which promotes non-specific binding) limits its utility *in vivo*.

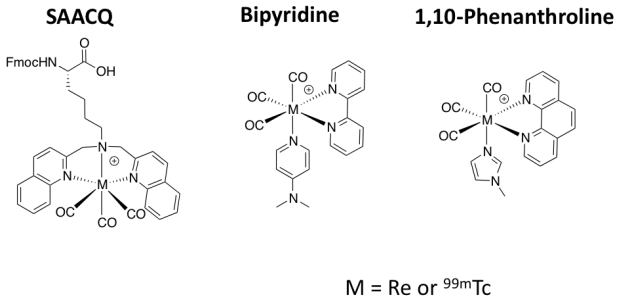

Figure 1.11 Three examples of ^{99m}Tc(I)/Re(I) metal complexes used for multimodal imaging.

As an alternative to tridentate complexes, is a [2+1] ligand complex that has been used to create a second generation of isostructural SPECT/OI probes (Figure 1.12). The "2" refers to the

bidentate ligand and the "1" the monodentate ligand. The most widely studied system was derived from bipyridine where Re(I) complexes were shown to have attractive photophysical properties that were used to create an array of cellular dyes.[56,57] The [2+1] systems provide a great deal of synthetic flexibility in that by simply changing the monodentate ligand, the solubility and absorbance and emission spectra of complexes can be altered without the need to synthesize an entirely new metal complex.

While a large number of Re(I) complexes using bipyridine have been investigated, there has been limited work on the corresponding ^{99m}Tc(I) complexes.[51,56,57,67] The main reason for the limited number of studies is the potential for loss of the monodentate ligand *in vivo* which can lead to non-specific binding as well as added complexities with radiochemical synthesis. It was recently shown that when the appropriate combination of bidentate and monodentate ligands are used, the ^{99m}Tc(I) complexes can be prepared with adequate stability to be suitable for *in vivo* imaging applications.[57]

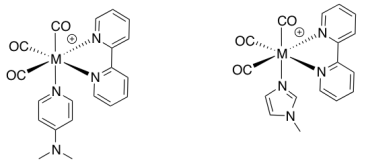

Figure 1.12 Two examples of bipyridine based [2+1] metal complexes.

A second generation of [2+1] system for SPECT/OI was created using the bidentate ligand 1,10-phenanthroline. Specifically 1,10-phenanthroline based ligands are of great interest due to its ability to form metal complexes having attractive luminescent properties for cellular imaging.[59] The bidentate ligand can be easily modified to introduce different substituents (R and R^1 in Figure 1.13) to fine tune the optical properties and enhance the aqueous solubility of the ligand and associated metal complexes. The optical properties of Re(I) 1,10-phenanthroline complexes have been studied extensively, but again the properties of the corresponding ^{99m}Tc(I) complexes remained

unexplored.[55,59,67–71] The Valliant research group showed that a related [2+1] system derived from phenyl-1H-imidazo[4,5-f][1,10]phenanthroline (PIP) had good optical properties for cellular imaging applications and it could be labelled with ^{99m}Tc(I). One major drawback of the first-generation agents was their poor water solubility making them unsuitable for *in vivo* studies.

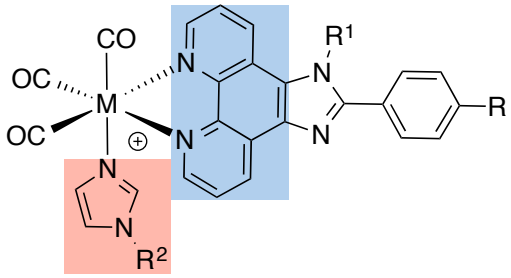

Figure 1.13 Example of a [2+1] complex (the bidentate imidazole fused phenanthroline ligand is highlighted in blue and the monodentate imidazole ligand in red. (M = Re(I)/^{99m}Tc(I)).

1.5 Thesis Overview

There is a need for platform technologies that can be used to create multimodal optical, PA and nuclear probes. The effectiveness of new probes require enhanced physicochemical properties over existing strategies and simpler strategies for linking them to targeting molecules. To this end, the first objective was to develop a platform for preparing and evaluating multimodal Re(I)/Tc(I) complexes from bifunctional PIP ligands (Chapter 2). This effort aimed to produce a combined SPECT/OI probe for whole body imaging using the ^{99m}Tc derivative, and an OI analogue derived from the Re(I) analogue. While several new ligands and metal complexes were produced, better optical properties and improved pharmacokinetics were needed. To this end a subsequent goal was to link the PIP ligands to a cyanine dye to leverage the well-established and superior photophysical and albumin binding properties of the dye (Chapter 3). Through a new synthetic strategy, a second cyanine dye ligand functionalized with a tetrazine, IR-HYNIC-Tz, was developed (Chapter 4). This new dye was shown to have attractive PA imaging properties and selective uptake in tumours. The presence of

the tetrazine also made it possible to target using *trans*-cyclooctene (TCO)-derivatives and to produce radiolabelled derivatives. The utility of this new PA agent was demonstrated *in vivo* where the IR-HYNIC-Tz was directed to bind regions of high calcium metabolism in healthy mice. The accumulation was verified through PA imaging and biodistribution studies using a ^{99m}Tc labelled derivative.

The broader utility of the IR-HYNIC-Tz was demonstrated by linking it to TCO-gas vesicles creating the first example of a PA/US probe (Chapter 5). An additional application using IR-HYNIC-Tz was explored in a glioblastoma model where the ability of the cyanine dye to localize in orthotopic models was demonstrated. PA imaging when combined with IR-HYNIC-Tz was shown to be useful for monitoring cell implantation studies in mice (Chapter 6). Chapter 7 describes potential future directions and preliminary work towards preparing dye-antibody conjugates for molecularly targeted PA imaging.

1.7 References

[1] J. C. Paeng, D. S. Lee, *Open Nucl. Med. J.* **2010**, *2*, 145–152.

[2] N. Deshpande, A. Needles, J. K. Willmann, *Clin. Radiol.* **2010**, *65*, 567–581.

[3] M. Wu, J. Shu, *Contrast Media Mol. Imaging* **2018**, *2018*, DOI 10.1155/2018/1382183.

[4] D. Utsunomiya, S. Tomiguchi, *Cancer Imaging*, **2008**.

[5] C. A. Kluba, T. L. Mindt, *Molecules* **2013**, *18*, 3206–26.

[6] K. Schwochau, *Angew. Chem. Int. Ed. Engl.* **1994**, *33*, 2258–2267.

[7] M. Lecchi, L. Ottobrini, C. Martelli, A. Del Sole, G. Lucignani, *Q J Nucl Med Mol Imag* **2007**, *51*, 111–126.

[8] R. Alford, M. Ogawa, P. L. Choyke, H. Kobayashi, *Mol. Biosyst.* **2009**, *5*, 1279–1291.

[9] Molecular Probes, *The Molecular Probes ® Handbook - Introduction to Fluorescence Techniques*, **2010**.

[10] S. A. Hilderbrand, R. Weissleder, *Curr. Opin. Chem. Biol.* **2010**, *14*, 71–79.

[11] D. D. D. Nolting, J. C. J. C. Gore, W. Pham, *Curr Org Synth* **2011**, *8*, 521–534.

[12] J. C. Rasmussen, I. C. Tan, M. V. Marshall, C. E. Fife, E. M. Sevick-Muraca, *Curr. Opin. Biotechnol.* **2009**, *20*, 74–82.

[13] C. Bremer, V. Ntziachristos, R. Weissleder, *Eur. Radiol.* **2003**, *13*, 231–243.

[14] Y. Urano, M. Kamiya, K. Kanda, T. Ueno, K. Hirose, T. Nagano, *J. Am. Chem. Soc.* **2005**, *127*, 4888–4894.

[15] S. Lee, K. Park, K. Kim, K. Choi, I. C. Kwon, *Chem. Commun. (Camb).* **2008**, 4250–4260.

[16] J. R. Lakowicz, *Principles of Fluorescence Spectroscopy*, **2006**.

[17] J. V Frangioni, **2008**, *26*, DOI 10.1200/JCO.2007.14.3065.

[18] A. Dvornikov, R. Edwards, W. W. Mantulin, E. Gratton, *J. Biomed. Opt.* **2012**, *17*, 1160231–1160237.

[19] L. Van Manen, M. Diana, J. Dijkstra, T. Ishizawa, A. L. Vahrmeijer, J. Sven, D. Mieog, *J Surg Oncol* **2018**, *118*, 283–300.

[20] S. Keereweer, T. J. A. Snoeks, J. D. F. Kerrebijn, A. L. Vahrmeijer, *Clin. cancer Res.* **2013**, *19*, DOI 10.1158/1078-0432.CCR-12-3598.

[21] F. P. R. Verbeek, Q. R. J. G. Tummers, D. D. D. Rietbergen, A. A. W. Peters, B. E. Schaafsma, C. J. H. van de Velde, J. V Frangioni, F. W. B. van Leeuwen, K. N. Gaarenstroom, A. L. Vahrmeijer, *Int. J. Gynecol. Cancer* **2015**, *25*, 1086–1093.

[22] C. Chi, Y. Du, J. Ye, D. Kou, J. Qiu, J. Wang, J. Tian, X. Chen, *Theranostics* **2014**, *4*, 1072–1084.

[23] Q. R. J. G. Tummers, A. Schepers, J. F. Hamming, J. Kievit, J. V Frangioni, C. J. H. van de Velde, A. L. Vahrmeijer,

Surgery **2015**, *158*, 1323–30.

[24] S. Onoe, T. Temma, Y. Shimizu, M. Ono, H. Saji, *Cancer Med.* **2014**, *3*, 775–786.

[25] A. D. Watson, Binding Studies of Near Infrared Cyanine Dyes with Human Serum Albumin and Poly-L-Lysine Using Optical Spectroscopy Methods By, **2008**.

[26] J. T. Alander, I. Kaartinen, A. Laakso, T. Pätilä, T. Spillmann, V. V. Tuchin, M. Venermo, P. Välisuo, *Int. J. Biomed. Imaging* **2012**, *2012*, 1–26.

[27] C. Jiang, H. Cai, X. Peng, P. Zhang, *Mol. Imaging* **2017**, *16*, 1–10.

[28] E. A. Rodriguez, Y. Wang, J. L. Crisp, D. R. Vera, R. Y. Tsien, *Bioconj Chem* **2016**, *27*, 1390–1399.

[29] T. Šmidlehner, A. Kurutos, J. Slade, R. Belužić, D. L. Ang, A. Rodger, I. Piantanida, *Eur JOC* **2018**, 1682–1692.

[30] A. Kurutos, I. Orehovec, D. Safti, L. Horvat, I. Crnolatac, I. Piantanida, T. Deligeorgiev, *Dye. Pigment.* **2018**, *158*, 517–525.

[31] C. Tang, Y. Du, Q. Liang, Z. Cheng, J. Tian, *Mol. Pharm.* **2018**, *15*, 4702–4709.

[32] Z. Yuan, L. Gui, J. Zheng, Y. Chen, S. Qu, Y. Shen, F. Wang, M. Er, Y. Gu, H. Chen, *ACS Appl. Mater. Interfaces* **2018**, *10*, 30994–31007.

[33] Q. T. Nguyen, R. Y. Tsien, *Nat. Rev. Cancer* **2013**, *13*, 653–662.

[34] S. Dufort, L. Sancey, C. Wenk, V. Josserand, J. L. Coll, *Biochim. Biophys. Acta* **2010**, *1798*, 2266–2273.

[35] J. Xu, Q. Li, Y. Yue, Y. Guo, S. Shao, *Biosens. Bioelectron.* **2014**, *56*, 58–63.

[36] I. Yapici, K. S. S. Lee, T. Berbasova, M. Nosrati, X. Jia, C. Vasileiou, W. Wang, E. M. Santos, J. H. Geiger, B. Borhan, *J. Am. Chem. Soc.* **2015**, *137*, 1073–1080.

[37] A. M. Marcinow, N. Hall, E. Byrum, T. N. Teknos, M. O. Old, A. Agrawal, *JAMA Otolaryngol. Neck Surg.* **2013**, *139*, 895.

[38] L. Qiu, J. Lin, W. Cheng, Y. Wang, S. Luo, *Med. Chem. Res.* **2013**, *22*, 6154–6162.

[39] S. Vallabhajosula, A. Nikolopoulou, J. W. Babich, J. R. Osborne, S. T. Tagawa, I. Lipai, L. Solnes, K. P. Maresca, T. Armor, J. L. Joyal, et al., *J. Nucl. Med.* **2014**, *55*, 1791–8.

[40] S. M. Hillier, K. P. Maresca, G. L. Lu, R. D. Merkin, J. C. Marquis, C. N. Zimmerman, W. C. Eckelman, J. L. Joyal, J. W. Babich, *J. Nucl. Med.* **2013**, *54*, 1369–1376.

[41] K. R. Bhushan, P. Misra, F. Liu, S. Mathur, R. E. Lenkinski, J. V Frangioni, *J. Am. Chem. Soc.* **2008**, *130*, 17648–17649.

[42] D. G. Correia, M. P. C. Campello, I. Santos, E. Palma, *Mol. BioSyst* **2011**, *7*, 2950–2966.

[43] B. Krebs, K. D. Hasse, *Acta Crystallogr. Sect. B Struct. Crystallogr. Cryst. Chem.* **1976**, *32*, 1334–1337.

[44] R. Alberto, R. Schibli, A. Egli, P. August Schubiger, W. a. Herrmann, G. Artus, U. Abram, T. a. Kaden, *J. Organomet. Chem.* **1995**, *493*, 119–127.

[45] R. Alberto, R. Schibli, A. P. Schubiger, V. Di, U. Abram, D.- Dresden, T. A. Kaden, **1998**, *3*, 7987–7988.

[46] a Egli, R. Alberto, L. Tannahill, R. Schibli, U. Abram, a Schaffland, R. Waibel, D. Tourwé, L. Jeannin, K. Iterbeke, et al., *J. Nucl. Med.* **1999**, *40*, 1913–1917.

[47] V. Carroll, D. Demoin, T. Hoffman, S. Jurisson, *Radiochim Acta* **2012**, *100*, 653–667.

[48] D. Sun, W. Zhang, M. Lv, E. Yang, Q. Zhao, W. Wang, *Bioorganic Med. Chem. Lett.* **2015**, *25*, 2068–2073.

[49] B. Sun, J. X. Guan, L. Xu, B. Le Yu, L. Jiang, J. F. Kou, L. Wang, X. D. Ding, H. Chao, L. N. Ji, *Inorg. Chem.* **2009**, *48*, 4637–4639.

[50] D. Sun, Y. Liu, Q. Yu, Y. Zhou, R. Zhang, X. Chen, A. Hong, J. Liu, *Biomaterials* **2013**, *34*, 171–180.

[51] F. Zhao, J. X. Wang, Y. B. Wang, *Comput. Theor. Chem.* **2011**, *973*, 40–46.

[52] N. Agorastos, L. Borsig, A. Renard, P. Antoni, G. Viola, B. Spingler, P. Kurz, R. Alberto, *Chem. - A Eur. J.* **2007**, *13*, 3842–3852.

[53] X. Li, D. Zhang, G. Lu, G. Xiao, H. Chi, Y. Dong, Z. Zhang, Z. Hu, *J. Photochem. Photobiol. A Chem.* **2012**, *241*, 1–7.

[54] C. B. Liu, J. Li, B. Li, Z. R. Hong, F. F. Zhao, S. Y. Liu, W. L. Li, *Chem. Phys. Lett.* **2007**, *435*, 54–58.

[55] F. Zhao, J. X. Wang, Y. B. Wang, *Inorganica Chim. Acta* **2012**, *387*, 100–105.

[56] T. S. Pitchumony, L. Banevicius, N. Janzen, J. Zubieta, J. F. Valliant, *Inorg. Chem.* **2013**, *52*, 13521–13528.

[57] A. Yazdani, N. Janzen, L. Banevicius, S. Czorny, J. F. Valliant, *Inorg. Chem.* **2015**, *54*, 1728–36.

[58] K. K.-W. Lo, A. W.-T. Choi, W. H.-T. Law, *Dalt. Trans.* **2012**, *41*, 6021.

[59] X. Li, D. Zhang, W. Li, B. Chu, L. Han, J. Zhu, Z. Su, D. Bi, D. Wang, D. Yang, et al., *Appl. Phys. Lett.* **2008**, *92*, 083302.

[60] N. J. Lundin, A. G. Blackman, K. C. Gordon, D. L. Officer, *Angew. Chemie* **2006**, *118*, 2644–2646.

[61] F. Li, M. Zhang, G. Cheng, J. Feng, Y. Zhao, Y. Ma, S. Liu, J. Shen, *Appl. Phys. Lett.* **2004**, *84*, 148.

[62] K. a. Stephenson, S. R. Banerjee, T. Besanger, O. O. Sogbein, M. K. Levadala, N. Mcfarlane, J. a. Lemon, D. R. Boreham, K. P. Maresca, J. D. Brennan, et al., *J. Am. Chem. Soc.* **2004**, *126*, 8598–8599.

[63] R. Lavker, K. Kaidbey, *J. Invest. Dermatol.* **1997**, *108*, 17–21.

[64] J. Moan, *Radiat. home, outdoors Work.* **2001**, 69–85.

[65] P. Board, **1981**, *81*.

[66] K. K. W. Lo, W. K. Hui, D. C. M. Ng, K. K. Cheung, *Inorg. Chem.* **2002**, *41*, 40–46.

[67] X. Guo, F. N. Castellano, L. Li, J. R. Lakowicz, **1998**, *70*, 3372–3377.

[68] X. Guo, F. N. Castellano, L. Li, H. Szmacinski, J. R. Lakowicz, J. Sipior, **1997**, *186*, 179–186.

[69] S. Mandal, D. K. Poria, R. Ghosh, P. S. Ray, P. Gupta, *Dalton Trans.* **2014**, *43*, 17463–74.

[70] T. Cardinaels, J. Ramaekers, P. Nockemann, K. Driesen, K. Van Hecke, L. Van Meervelt, S. Lei, S. De Feyter, D. Guillon, B. Donnio, et al., *Chem. Mater.* **2008**, *20*, 1278–1291.

[71] X. Yi, J. Zhao, W. Wu, D. Huang, S. Ji, J. Sun, *Dalt. Trans.* **2012**, *41*, 8931.

Chapter 2: Synthesis and Evaluation of Imidazole Fused Phenanthroline (PIP) Ligands as a Platform for the Preparation for Re(I) and ^{99m}Tc(I) Multimodal Probes

Samantha R. Slikboer, Tamil Selvi Pitchumony, Laura Banevicius, Patricia E. Edem, John F. Valliant

2.1 Description of Contributions

The following chapter is formatted in a manuscript that is ready for submission. S.R. Slikboer in collaboration with T.S. Pithumony were responsible for the synthesis and evaluation of the compounds described. S.R. Slikboer was also responsible for drafting the manuscript and experimental section. L. Banevicius and P.E. Edem performed the preliminary excitation and emission spectra. Dr. Valliant is the principle investigator.

2.2 Abstract

A small library of [2+1] ^{99m}Tc(I) complexes based on phenyl-imidazole-fused phenanthroline (PIP) ligands were synthesized and evaluated as multimodal molecular imaging probes. Using either a two-step or a one-pot synthesis method, ^{99m}Tc-PIP complexes containing N-methylimidazole as the monodentate ligand were prepared and isolated in good (54 to 89 %) radiochemical yield, with the exception of one derivative bearing a strongly electron-withdrawing substituent. The stability of the [2+1] complexes were assessed in saline and in cysteine and histidine challenge studies, and showed 6 hour stability, making them suitable for *in vivo* studies. In parallel, the Re(I) analogues were prepared as reference standards to verify the structure of the ^{99m}Tc complexes. The optical properties were consistent with other previously reported [2+1] type Re(I) complexes that have been used as cellular dyes and sensors. To facilitate the development of targeted derivatives, a tetrazine-PIP ligand was also synthesized. The ^{99m}Tc complex of the tetrazine PIP ligand effectively coupled to compounds containing a *trans*-cyclooctene (TCO) group including a TCO-albumin derivative, which was prepared

as a model targeting molecule. An added benefit of the Re-PIP-Tz construct is that the emission from the metal complex was quenched by the presence of the tetrazine. Following the addition of TCO, there was a 70-fold increase in fluorescence emission, which can in future be leveraged during *in vitro* studies to reduce background signal.

2.3 Introduction

Multifunctional molecular imaging (MI) probes offer the means to noninvasively monitor biochemical targets and processes *in vitro* and *in vivo* through the application of more than one imaging modality.[1–5] For example, molecules containing both a radiolabelled prosthetic group and a near infrared (IR) fluorophore make it possible to employ nuclear imaging methods to assess whole-body biodistribution of a specific target while fluorescence microscopy can be used to visualize the expression of the target and distribution of the probe within different cell lines and tissues.[6–11] As well, single photon emission computed tomography (SPECT) or positron emission tomography (PET) is being used to identify the presence of tumours by targeting specific biomarkers, while intraoperative fluorescence imaging using the optical properties of the probe is used to assist with margin determination during surgical resection.[6,12–16]

The typical approach used to prepare multimodal optical-nuclear MI probes is to derivatize a targeting molecule with a fluorescent molecule and a radionuclide. The limitation here is that the addition of two prosthetic groups can have a detrimental influence on pharmacokinetics and the ability of the targeting molecule to retain affinity for the target. This is particularly true for small molecules. An alternative strategy is to use radiolabelled dyes[5,6,17–26] or transition metal complexes[9,11,27] that are luminescent and that have radioactive isotopes or radioactive congeners suitable for nuclear imaging. One archetypal example of the latter involves ^{99m}Tc, which is the most widely used radionuclide in diagnostic medicine, where select complexes of technetium's congener rhenium are luminescent, providing a means of preparing isostructural multifunctional optical-nuclear probes.[28–32]

There are a significant number of Re(I) complexes that have been used as luminescent probes. In particular, mixed ligand complexes of the $[Re(CO)_3]^+$ core derived from bidentate polypyridine ligands and an aromatic monodentate ligand, commonly referred to as [2+1] complexes, have been particularly effective as probes for imaging subcellular structures. These complexes have attractive optical properties including broad absorbance (extending into the visible spectrum) and emission spectra (extending into the near-infrared spectrum), a large Stokes shift, and long fluorescent lifetimes.[9,11,33] For many luminescent [2+1] complexes of this type, the Re chemistry is well developed, whereas methods for preparing the corresponding ^{99m}Tc(I) complexes and studying the chemical and biological properties of the resulting products are notably lacking.

Phenyl imidazole-fused phenanthroline ligands (PIP) have been widely used to create a range of different luminescent probes and sensors. These include metal,[34–37] ion,[38,39] and singlet oxygen ($^1O_2$) sensing constructs.[40,41] Xi *et al.* reported Re tricarbonyl polypyridine complexes, using imidazole-fused phenanthroline ligands, which were shown to have strong absorption bands in the visible region as well as a long-lived triplet excited state.[42] This showed the first use for Re(I) complexes as triplet photosensitizers for triplet-triplet annihilation. To assess the utility of PIP ligands as the basis for creating isostructural optical-nuclear probes, a method to prepare ^{99m}Tc complexes of PIP ligands was developed and the properties of the radiometal complexes studied. This included creating and evaluating bifunctional derivatives that can be linked to targeting molecules using bioorthogonal chemistry.

2.4 Results and Discussion

2.4.1 Ligand Synthesis

To assess the impact of substituents on radiochemical yield and stability of the target ^{99m}Tc complexes, a small library of PIP ligands containing a series of electron donating and withdrawing groups were prepared. The approach used to synthesize the ligands **3a-f** (Scheme 2.1) was adapted

from a literature procedure[42] where 1,10-phenanthroline-5,6-dione, benzaldehydes **2a-f** and ammonium acetate were added to degassed glacial acetic acid. After purging with argon, the mixture was heated to reflux for 3 hours and the desired products collected in 72 to 93% yield by filtration following the addition of water. In addition to known PIP derivatives (**3a, c-e**),[43] new ligands containing a carboxylic acid (**3b**) and boronic acid (**3f**) were also prepared to provide a means of further derivatization including the addition of a tetrazine to facilitate bioconjugation (*vide infra*). Characterization data for **3a-3f** can be found in the SI (Figure S2.1-S2.24, in the Supporting Information).

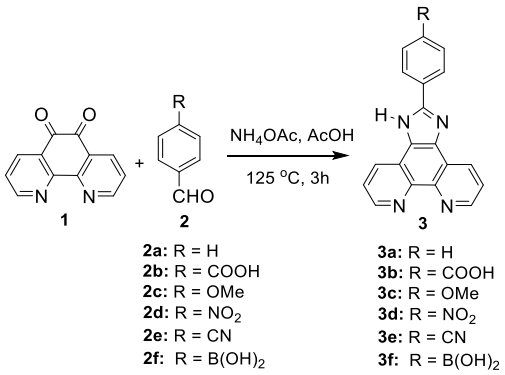

Scheme 2.7 Synthesis of Imidazo[4,5-f]-1,10-phenanthroline ligands **3a-f**.

2.4.2 Preparation and Characterization of Re Complexes

Prior to radiolabelling studies with ^{99m}Tc, the Re(I) complexes of the PIP ligands were prepared as reference standards. This is a necessary step because ^{99m}Tc-labelling reactions are typically performed using picomoles of the metal; amounts that are below the sensitivity of standard characterization methods (NMR, MS, etc.). To address this, the Re complexes are prepared and characterized and used as HPLC reference standards, where the ^{99m}Tc and Re complexes are co-injected and their retention time (detected by gamma and UV detectors respectively) compared.

Re complexes were synthesized following a literature procedure.[42] PIP ligands (**3a-e**) were combined with pentacarbonylchlororhenium(I) in toluene and the mixture heated to reflux for 2 hours (Scheme 2.2). The products (**4a-e**), were isolated by HPLC in good yield (average = 78%), where characterization data (Figures S2.25-S2.39, in the Supporting Information) were consistent with previously reported values for comparable Re(I) complexes.[42]

Compounds **4a-f** are unsuitable as molecular imaging probes because the chloride ligand can be easily substituted by proteins in the blood, such as albumin. For [2+1] complexes this has been shown to result in unwanted delivery of the radiometal complex to the liver, hindering target uptake.[11] We previously demonstrated that the extent of non-specific binding with analogous bipyridine complexes *in vivo* can be reduced by replacing the chloride ligand with an N-substituted imidazole.[11] With this in mind, compounds **4a-e** were treated with N-methylimidazole (NMI) with stirring at room temperature overnight to form the hitherto unknown PIP complexes **5a-c**,**e** (Scheme 2.2). The products were isolated by HPLC in 51-80% yield and characterized by NMR and HRMS (Figures S2.40-S2.51, in the Supporting Information). The only exception was compound **5d**, which did not form, likely due to the strong electron withdrawing effect of the nitro group. Similarly, only small amounts of compound **5e** could be isolated, which is also likely due to the electron withdrawing effect of the cyano group.

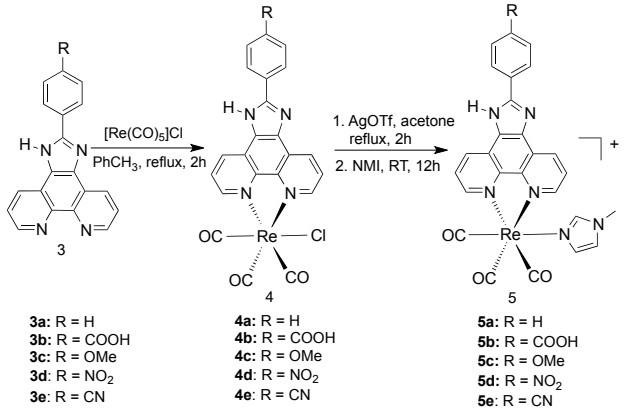

Scheme 2.8 Synthesis of Re-PIP complexes **4a-e** and **5a-c,e**. NMI = N-methylimidazole.

Unfortunately, derivative **5f** could not be prepared using conventional heating due to the poor solubility of the starting material (**3f**) in organic solvents. Nevertheless, **5f** was desirable because the boronic acid group provides a convenient site to use Suzuki-Miyaura coupling chemistry for further ligand modification or to promote targeting through conjugation to carbohydrates.[44,45] An alternative method using microwave heating was employed to prepare **5f**. In place of $[Re(CO)_5]Cl$, $[Re(CO)_3(OH_2)_3]Br$ was prepared following the method of Lazarova *et al.*[46] and added to the PIP ligand and the solution heated in a microwave at 110 °C for 5 min. The NMI ligand was added and the mixture was heated again at 110 °C for 5 minutes (Scheme 2.3). The product was then isolated by HPLC to afford **5f** in 19% yield (Figures S2.52-S2.55, in the Supporting Information). In an attempt to improve the yield, the order of addition was changed where NMI was combined with $[Re(CO)_3(OH_2)_3]Br$ and the mixture heated followed by the addition of PIP ligand. However, there was no further increase in the yield of **5f**. Nonetheless, the amount of product obtained with the former procedure was sufficient for use as reference standard for the corresponding ^{99m}Tc complex.

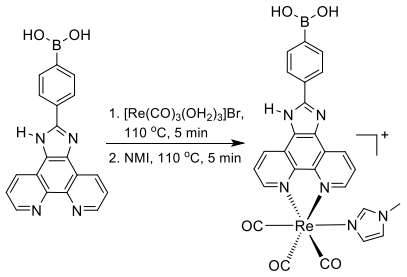

Scheme 2.9 Microwave-mediated synthesis of **5f.**

2.4.3 Optical Properties

The optical properties of the Re complexes were evaluated to determine the effect that substituents on the PIP ligand have on absorption and emission spectra.[47] The absorption spectra for compounds **4a-e** showed a broad peak between 351-412 nm, while for **5a-c**,**e**,**f**, the comparable

absorption band appeared between 399-414 nm (Table 2.1). The corresponding emission spectra appeared between 596-649 nm for **4a-e** and 574-632 nm for **5a-c**,**e**,**f** respectively (Figures S2.63-S2.82, in the Supporting Information). The addition of the NMI group generally caused a blue shift in the absorbance/emission spectra compared to the precursor compounds containing a chloride ligand in place of the heterocycle. Electron withdrawing substituents (**4d**, **4e**, and **4b**) generally were blue shifted relative to those with electron donating groups on the PIP ligand with the unsubstituted ring (**4a**) falling between the two groups as expected. In general, the values are comparable to literature data on PIP complexes of Re(I).[41]

Table 2.1 Absorbance and emission maxima of compounds **4a-e** and **5a-f**.

	4a-f		**5a-f**	
Compound	Absorbance (nm)	Emission (nm)	Absorbance (nm)	Emission (nm)
a: R = H	406	612	400	594
b: R = COOH	404	596	407	595
c: R = OMe	412	616	414	574
d: R = NO_2	351	649	[b]	[b]
e: R = CN	399	611	399	611
f: R = $B(OH)_2$	-	-	406	586

[a] Absorbance and emission data were collected at 50 μM in methanol. Spectra for all compounds are reported in the ESI.

[b] The Re complex **5d** was not sufficiently stable to allow for measurement.

2.4.4 Radiochemistry

The ^{99m}Tc complexes were prepared using $[^{99m}Tc][Tc(CO)_3(H_2O)_3]^+$, which was generated from $[^{99m}TcO_4]^-$ following literature methods.[48–50] The ligands **3a-e** (1 mg) were added to a vial containing $[^{99m}Tc][Tc(CO)_3(H_2O)_3]^+$ under argon, and the mixture heated at either 40 or 65 °C for 1 hour (Scheme 2.4). Radio-HPLC of the reaction mixtures showed a single peak and no evidence of residual technetium starting material. Next, the NMI complexes were prepared by adding the monodentate ligand to compounds **6a-d** and heating the mixture for 1 hour at 40 °C. Radio-HPLC again showed

the formation of a single peak at a retention time that matched that for the corresponding Re analogues. Compounds **7a-d** were isolated free from excess NMI using HPLC in 57-82% radiochemical yield (Figures S2.86-S2.98, in the Supporting Information). Compounds containing ligands with electron withdrawing groups (**3d** and **3e**) showed poor labelling yield compared to the other derivatives.

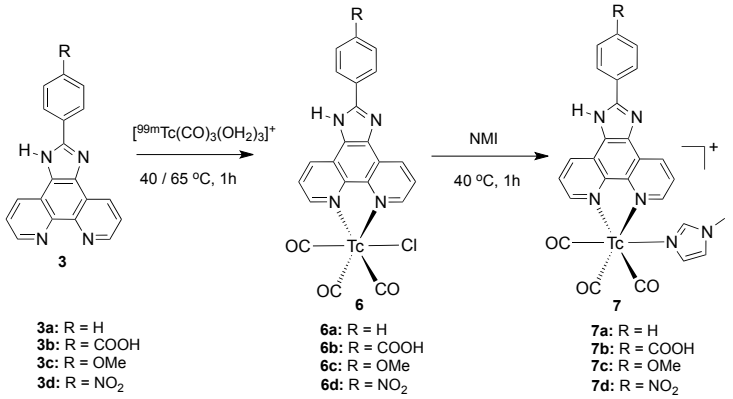

Scheme 2.10 Synthesis of ^{99m}Tc-labelled PIP complexes **6a-d** and **7a-d**.

In order to improve the overall efficiency of the synthesis, attempts were made to develop a one-pot labelling method following an approach we reported previously for bipyridine type ligands.[9,11] As a model ligand, **3e** was added to a microwave vial along with $[^{99m}Tc(CO)_3(H_2O)_3]^+$ and an excess of NMI. The vial was sealed under argon and heated at 40 °C for 1 hour. Radio-HPLC confirmed that a single product formed that had the same HPLC retention time as the product produced in the two-step labelling, where **7e** was obtained in a 55% radiochemical yield (Scheme 2.5). The same one-pot method was used to generate **7f**. Interestingly, when one-pot reactions were attempted with rhenium using $[Re(CO)_3(H_2O)_3]^+$, yields were low (<20 %) and required higher temperatures (110 °C). Nevertheless, the ability to produce the [2+1] ^{99m}Tc complex using a one-pot labelling method at modest temperatures and times creates the opportunity to develop instant kits, which simplifies getting approval to use these types of ^{99m}Tc complexes in clinical studies.

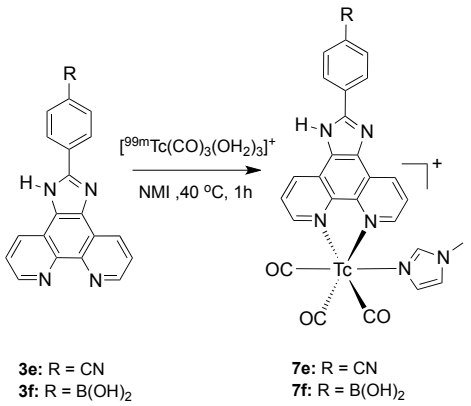

Scheme 2.11 One-pot synthesis of **7e** and **7f**.

2.4.5 Stability Studies

The stability of the ^{99m}Tc-complexes (**7a-f**) in saline were monitored by HPLC at 6 to 24 hours. After no evidence of degradation was noted, the metal complexes were treated with an excess (2 mM) of cysteine or histidine at 37 °C. Radio-HPLC of the ^{99m}Tc-complexes again showed no signs of degradation over 6 hours, which is equivalent to one half-life of ^{99m}Tc (Figures S2.85-S2.101, in the Supporting Information). These results are consistent with other [2+1] ^{99m}Tc(I) complexes containing NMI as the monodentate ligand.[11,27]

2.4.6 Tetrazine Derivatives

The [2+1] PIP complexes can be used to create targeted MI probes through a number of strategies. This includes the addition of targeting vectors through the monodentate imidazole ligand, which we have described previously for bipyridine complexes,[11,27] or by coupling to a functional group on the bidentate ligand. In the case of the PIP ligands reported here, the carboxylic acid in compounds **3b** can be readily conjugated to amino groups using simple active ester chemistry. This approach can be used to create "actively" targeted MI probes (*i.e.* bioconjugation prior to administration), or it can

be employed with pretargeting strategies where coupling between a conjugated tetrazine and strained alkenes can take place *in vivo*.[51] The use of tetrazines has the added benefit that the heterocycle can quench the luminescence of the Re complex creating turn-on type probes.[52,53]

To this end the PIP ligand **3b** was derivatized with the commercially available tetrazine 4-(1,2,4,5-tetrazin-3-yl)phenyl)methanamine hydrochloride (**8**), which has been used successfully to create radiolabelled tetrazines.[27,51,54–57] Coupling was achieved (Scheme 2.6) using benzotriazol-1-yl-oxytripyrrolidinophosphonium hexafluorophosphate (PyBOP), where the desired product (**9**) was isolated in 68% yield (Figures S2.56-S2.58, in the Supporting Information). The thermal sensitivity of tetrazines precluded preparation of the Re reference standard from **9**. As a result, **4b** (Re complex of **3b**) was coupled to **8** and the desired product **10** obtained in 37% yield (Figures S2.59-S2.61, in the Supporting Information). The ligand exchange of the water ligand with NMI was unsuccessful with the Re complex possibly due to the limited temperature and pH options available that can be used with the highly reactive tetrazine. The fluorescence spectra of **10** was however collected and showed an absorbance peak of 425 nm and an emission peak of 593 nm, where there was a 70-fold increase in emission intensity (λ_{ex} = 395 nm) upon the addition of an excess of *(E)*-cyclooct-4-enol (TCO-OH) (Figure 2.1).

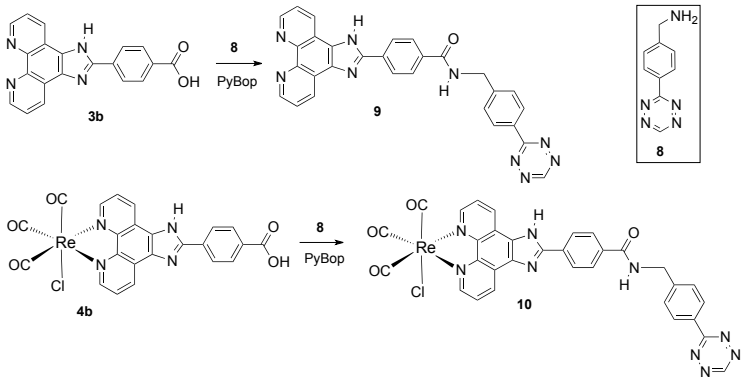

Scheme 2.6 Synthesis of tetrazine functionalized PIP ligand **9** and its Re complex **10**. Reactants and conditions: DIPEA, RT, 12 h in DMF.

The PIP-tetrazine ligand was subsequently labelled with ^{99m}Tc in a two-step reaction (Scheme 2.7). The reaction showed the formation of a new peak at 12.5 min where the product was isolated in 40% yield by HPLC which was verified by coinjection with the Re congener. Addition of NMI resulted in a shift in retention time consistent with compounds **6a-e** to **7a-e**. To verify that the product contained the desired tetrazine, TCO-OH was added, resulting in a small shift in retention time and change in the number of peaks that is consistent with the cycloaddition reaction.[58] In addition to coupling to a small molecule TCO derivative, a TCO-derivative of albumin was prepared as a model protein-based targeting molecule. The TCO-derivative of albumin was prepared by adding *trans*-4-cycloocten-1-yl 2,5-dioxo-1-pyrrolidinyl ester carbonic acid (TCO-NHS) with bovine serum albumin (BSA) at 4 °C for 12 hours. Following dialysis, the product **14** contained 2.7 TCO groups per albumin molecule (Figure S2.62, in the Supporting Information). When **14** was added to ^{99m}Tc-labelled tetrazine **13** (Scheme 2.8), complete and nearly instantaneous consumption of the labelled tetrazine was evident by radio-HPLC.

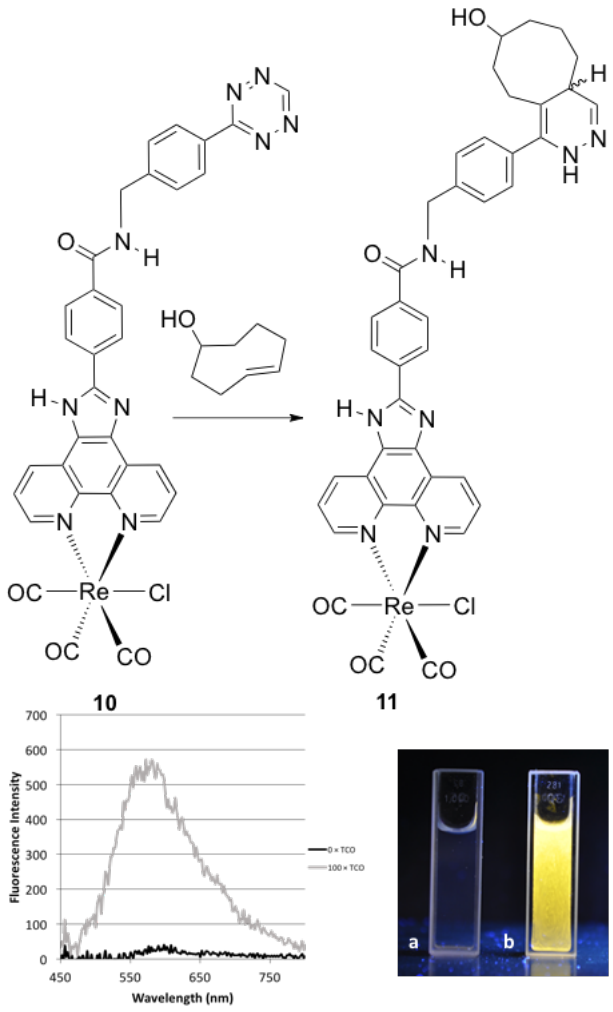

Figure 2.1 Top: A scheme illustrating the reaction of Re-tetrazine **10** with *(E)*-cyclooct-4-enol (TCO-OH) to produce **11**. Bottom left: The emission spectra (λ_{ex} = 395 nm) for **10** before (black line) and after (grey line) the addition of an excess of TCO-OH (50 μM in PBS). Bottom right: Photograph of **10** under UV light prior to (a) and after (b) treatment with TCO-OH (sample dissolved in DMSO and diluted to 50 μM with PBS).

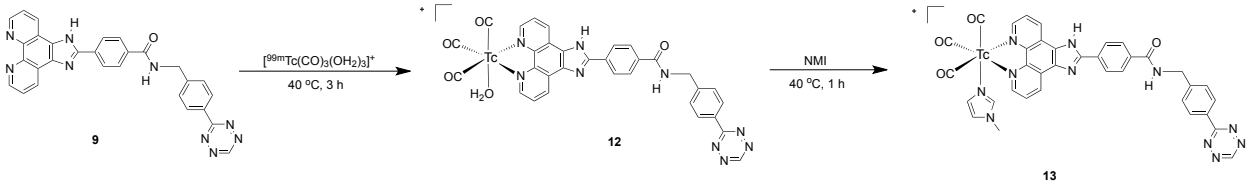

Scheme 2.7 Two-step radiolabelling of **9.**

The TCO-albumin derivative is a convenient tool to test the reactivity of tetrazines. It may also offer a way to use the protein to improve solubility and pharmacokinetics of tetrazine derived metal complexes. In addition, there is growing interest in radiolabelled albumins for imaging tumours, lymph nodes, and infection and as a tool for blood volume estimation.[59,60]

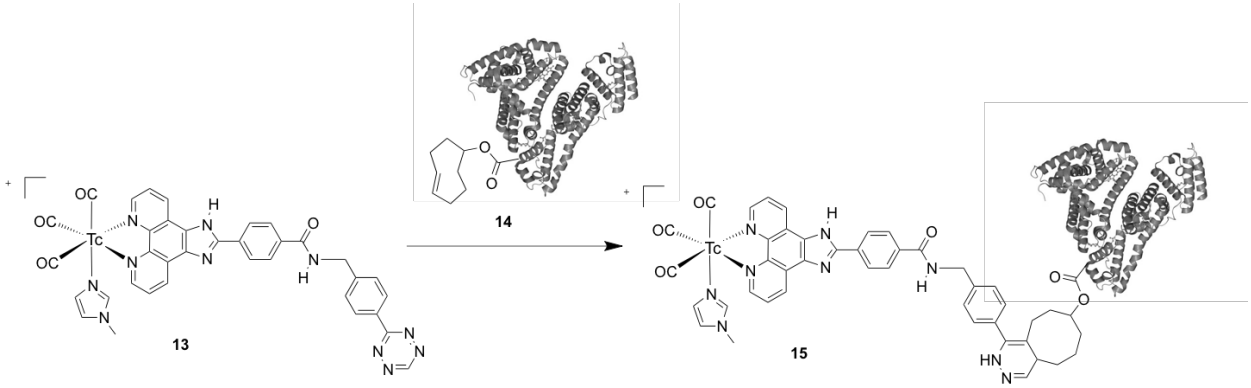

Scheme 2.8 Reaction of [^{99m}Tc]Tc-tetrazine **13** with TCO-BSA **14**.

2.5 Conclusions

A series of phenyl imidazole-fused phenanthroline (PIP) ligands were synthesized and the corresponding [2+1] ^{99m}Tc(I) and Re(I) complexes generated. The Re(I) complexes exhibit optical properties that are comparable to other Re(I) compounds that have been used as cellular dyes. The ^{99m}Tc(I) analogues can be prepared in good yield and under mild conditions, where products were sufficiently stable for use *in vivo*. Boronic acid and tetrazine derivatives were prepared allowing for further functionalization and bioconjugation. In the case of the tetrazine-PIP derivatives, a turn-on type Re(I) complex was developed, where the ^{99m}Tc analogue can be readily conjugated to TCO-modified biomolecules, including TCO-derived albumin, offering a convenient route to developing targeted multi-modal probes.

2.6 Experimental

Supplementary figures can be found in **APPENDIX I.**

Materials, instrumentation and general methods

All reagents and solvents were ACS grade and were purchase from commercial suppliers and used without further purification. (Benzotriazol-1-yloxy)tripyrrolidinophosphonium hexafluorophosphate (PyBOP) was purchased from Advanced ChemTech. (4-(1,2,4,5-Tetrazin-3-yl)phenyl)methanamine hydrochloride, and *(E)*-4-cycloocten-1-yl 2,5-dioxo-1-pyrrolidinyl ester carbonic acid were purchased from Conju-probe. Toluene, acetone, *N,N*-dimethylformamide, dimethyl sulfoxide and methanol were purchased from Caledon. Distilled water was used for all experiments. Deuterated solvents for NMR samples were purchased from Cambridge Isotope Laboratories. Sodium borate and potassium sodium tartrate were purchased from Anachemia Canada Inc. Sodium carbonate was purchased from EM science. Bovine serum albumin was purchased from Sigma. Purification performed by column was done using silica gel 60 (particle size 0.04-0.063 mm) purchased from EMD chemicals. ^{99m}Tc was obtained as [^{99m}Tc]TcO_4^- from a ^{99}Mo/^{99m}Tc generator (Lantheus Medical Imaging) in saline (0.9 % NaCl). *Caution: ^{99m}Tc is a γ-emitter (E_γ = 140 keV, $t_{1/2}$ = 6 h) and should only be used in a licensed and appropriately shielded facility.* All other reagents were purchased from Sigma Aldrich.

^{1}H and ^{13}C NMR spectra were recorded on a Bruker Avance AV-600 instrument at 300 K. High Resolution Mass Spectra (HRMS) were collected on a Waters/Micromass Q-Tof Global Ultima spectrometer. BSA samples were analyzed by mass spectrometry MALDI Bruker Ultraflextreme spectrometer. Microwave reactions were performed using a Biotage Initiator 60 instrument. Solvents were evaporated using either a Bioatage V10 system or under reduced pressure with a rotary

evaporator. Compounds were dried using a VirTis Benchtop lyophilizer equipped with an Edwards RV5 pump. Dialysis was performed using dialysis kit (Spectra/Por 1 Dialysis Tubing, 132645; 6-8 kD MWCO).

High Performance Liquid Chromatography (HPLC) was performed using a Waters XBridge analytical column (5 μm, 4.6 × 100 mm) or C18 preparative column (5 μm, 10 × 100 mm) with a Waters 1525 system connected to a Bioscan γ detector and a 2998 photodiode array detector monitoring at 254 nm operated using the Empower software package. Flow rates were 1 mL/min. (analytical) or 4 mL/min. (preparative) using the following methods: Method A: Solvent A: H_2O + 0.1% TFA; Solvent B: Acetonitrile + 0.1% TFA. Gradient: 10% B (0-2 min.), 100% B (2-12 min.), 100% B (12-14 min.), 10 % B (14-15 min.). Method B: Solvent A: 0.4% ammonium formate (w/v) in H_2O; Solvent B: Acetonitrile. Gradient: 10% B (0-2 min.), 100% B (2-12 min.), 100% B (12-14 min.), 10% B (14-15 min.). Method C: Solvent A: H_2O + 0.1% TFA, Solvent B: Acetonitrile + 0.1% TFA. Gradient: 10-70% B (0-14 min), 70% B (14-15 min), 70-100% B (15-17 min), 100-10% B (17-18 min). Method D: Solvent A: H_2O, Solvent B: Acetonitrile. Gradient 10-70% B (0-14 min), 70% B (14-15 min), 70-100% B (15-17 min), 100-10% B (17-18 min). Method E: Solvent A: H_2O, Solvent B: Acetonitrile. Gradient 10-70% B (0-14 min), 70% B (14-15 min), 70-100% B (15-17 min), 100-10% B (17-18 min), 10% B (18-23 min). Phenomenex PolySep-GFC-P Linear LC Column (300 x 7.8 mm) was also used with the following method: Method F: Solvent: H_2O. Isocratic, 20 min.

Synthetic procedures

2-Phenyl-1H-imidazo[4,5-f][1,10]phenanthroline, 3a. In a round bottomed flask, 1,10-phenanthroline-5,6-dione (52 mg, 0.25 mmol), benzaldehyde (40 mg, 0.38 mmol) and ammonium acetate (423 mg, 5.50 mmol) were added and the flask flushed with Ar for 10 min. To this mixture, degassed glacial acetic acid (10 mL) was added and the mixture heated at 125 °C for 3 h under Ar. The resulting solution was then cooled, diluted with water (20 mL) and neutralized with concentrated

NH_4OH whereupon a pale peach coloured precipitate formed. The precipitate was collected by filtration, washed with water and dried under vacuum. Yield: 67 mg (89%). ^{1}H NMR (DMSO-d_6, 600 MHz): δ (ppm) 13.71 (s, 1H, Ar-NH); 8.98 (dd, 2H, Ar-H); 8.87 (m, 2H, Ar-H); 8.24 (dd , 2H, Ar-H); 7.78 (s, 2H, Ar-H); 7.56 (m, 2H, Ar-H); 7.47 (m, 1H, Ar-H). ^{13}C NMR (DMSO-d_6, 150 MHz): δ (ppm) 150.6, 147.8, 143.6, 130.2, 129.6, 129.0, 126.2, 123.3. HRMS: m/z calcd for $C_{19}H_{13}N_4$: 297.1140, found: 297.1153. HPLC (UV 254 nm): R_t = 7.2 min.

2-(4-Carboxyphenyl)-1H-imidazo[4,5-f][1,10]phenanthroline, 3b. The ligand was synthesized according to the procedure followed for **3a** using 4-formylbenzoic acid (57 mg, 0.38 mmol) in place of benzaldehyde, to give a yellow solid. Yield: 93 mg (72%). ^{1}H NMR (DMSO-d_6, 600 MHz): δ (ppm) 9.07 (bs, 2H, Ar-H); 8.96 (bs, 2H, Ar-H); 8.43 (bs, 2H, Ar-H); 8.20 (bs, 2H, Ar-H); 7.88 (m, 2H, Ar-H). ^{13}C NMR (DMSO-d_6, 150 MHz): δ (ppm) 166.9, 151.1, 149.5, 148.1, 143. 8, 130.1, 129.7, 126.2. HRMS: m/z calcd for $C_{20}H_{13}N_4O_2$: 341.1039, found: 341.1034. HPLC (UV 254 nm): R_t = 6.5 min.

2-(4-Methoxyphenyl)-1H-imidazo[4,5-f][1,10]phenanthroline, 3c. The ligand was synthesized according to the procedure followed for **3a** using 4-methoxybenzaldehyde (52 mg, 0.38 mmol) in place of benzaldehyde to give a pale yellow solid. Yield: 99 mg (80%). ^{1}H NMR (CD_3OD, 600 MHz): δ (ppm) 8.94 (dd, 3H, Ar-H); 8.77 (s, 1H, Ar-H); 8.07 (d, 2H, Ar-H); 7.72 (q, 2H, Ar-H); 7.06 (d, 2H, Ar-H); 3.82 (s, 3H, -OCH_3). ^{13}C NMR (CD_3OD, 150 MHz): δ (ppm) 148.9, 144.9, 131.4, 129.4, 124.7, 115.6, 56.0. HRMS: m/z calcd for $C_{20}H_{15}N_4O$: 327.1233, found: 327.1233. HPLC (UV 254 nm): R_t = 7.3 min.

2-(4-Nitrophenyl)-1H-imidazo[4,5-f][1,10]phenanthroline, 3d. The ligand was synthesized according to the procedure followed for **3a** using 4-nitrobenzaldehyde (57 mg, 0.38 mmol) in place of benzaldehyde to give a bright yellow solid. Yield: 110 mg (85%). ^{1}H NMR (DMSO-d_6, 600 MHz): δ

(ppm) 8.99 (dd, 2H, Ar-H); 8.87 (dd, 2H, Ar-H); 8.47 (dd, 2H, Ar-H); 7.79 (m, 2H, Ar-H). ^{13}C NMR (DMSO-d_6, 150 MHz): δ (ppm) 148.3, 147.5, 144.1, 136.2, 129. 8, 127.0, 124.5, 123.5. HRMS: m/z calcd for $C_{19}H_{11}N_5O_2$: 342.0984, found: 342.0984. HPLC (UV 254 nm): R_t = 7.7 min.

2-(4-Cyanophenyl-1H-imidazo[4,5-f][1,10]phenanthroline, 3e. The ligand was synthesized according to the procedure followed for **3a** using 4-formylbenzonitrile (49 mg, 0.38 mmol) in place of benzaldehyde to give an orange precipitate. Yield: (76 mg, 93%). TLC R_f = 0.46 (70% DCM/MeOH + 0.01% TFA). ^{1}H NMR (DMSO-d_6, 600 MHz): δ (ppm) 14.06 (bs, 1H, Ar-NH); 9.07 (dd, 2H, Ar-H), 8.95 (d, 2H, Ar-H), 8.48 (d, 2H, Ar-H), 8.12 (d, 2H, Ar-H), 7.87 (bs, 2H, Ar-H). ^{13}C NMR (DMSO-d_6, 150 MHz): δ (ppm) 148.2, 143.9, 133.1, 129.7, 126.6, 123.4. HRMS: m/z calcd for $C_{20}H_{11}N_5$: 322.3039, found: 322.1084. HPLC (UV 254 nm): R_t = 4.4 min.

2-(-Phenyl boronic acid-1H-imidazo[4,5-f][1,10]phenanthroline, 3f. In a round bottom flask, 1,10-phelanthroline-5,6-dione (50 mg, 0.24 mmol), 4-formylphenyl boronic acid (54 mg, 0.36 mmol), and ammonium acetate (403 mg, 5.24 mmol) were combined and the flask flushed with Ar for 10 min. Degassed glacial acetic acid (10 mL) was added and the solution heated to reflux (125 °C) under Ar for 3 h. After cooling to RT, water (20 mL) was added and the resulting precipitate collected by filtration and washed with DI water. The solid was further dried under vacuum yielding a brownish-yellow solid. Yield: (72mg, 88%) ^{1}H NMR (DMSO-d_6, 600 MHz: δ (ppm) 13.78 (bs, 1H, Ar-NH); 9.00 (d, 4H, Ar-H), 8.25 (d, 4H, Ar-H), 8.03 (s, 2H, OH), 7.86 (d, 2H, Ar-H). ^{13}C NMR (DMSO-d_6, 150 MHz: δ (ppm) 150.6, 147.9, 143.7, 135.8, 134.7, 131.2, 129.7, 125.1, 123.8, 123.5, 123.2, 119.3. HRMS: m/z calcd for $C_{19}H_{13}BN_4O_2$: 341.1213, found: 341.1205. HPLC (UV 254 nm): R_t = 5.6 min.

General synthesis of [Re(CO)$_3$(L)Cl]. To [Re(CO)$_5$Cl] (36 mg, 0.1 mmol) in toluene (5 ml), the corresponding bidentate ligand L (0.12 mmol) in toluene (2 mL) was added and the mixture heated to reflux for 2 h. A precipitate formed during the course of the reaction, which was collected by filtration

and dried under vacuum. The solid was dissolved in DMSO and the desired product isolated by HPLC (method A) to give a yellow solid. Yield: 76-80%.

[Re(CO)$_3$(3a)Cl], 4a. ^{1}H NMR (DMSO-d_6, 600 MHz): δ (ppm) 14.33 (s, 1H, Ar-NH); 9.38 (d, 2H, Ar-H); 9.30 (d, 2H, Ar-H); 8.33(d, 2H, Ar-H); 8.19 (bs, 2H, Ar-H); 7.67 (m, 2H, Ar-H); 7.60 (m, 1H, Ar-H). ^{13}C NMR (DMSO-d_6, 150 MHz): δ (ppm) 198.0, 190.3, 151.6, 133.1, 130.6, 129.4, 126.7. HRMS: m/z calcd for $C_{22}H_{12}ClN_4O_3Re$: 601.0069, found: 601.0073.

[Re(CO)$_3$(3b)Cl], 4b. ^{1}H NMR (DMSO-d_6, 600 MHz): δ (ppm) 9.39 (d, 2H, Ar-H); 9.30 (d, 2H, Ar-H); 8.45 (d, 2H, Ar-H); 8.22 (d, 2H, Ar-H); 8.18 (q, 2H, Ar-H). ^{13}C NMR (DMSO-d_6, 150 MHz): δ (ppm) 197.8, 190.0, 166.8, 155.1, 151.5, 144.0, 132.9, 130.7, 126.7, 126.5. HRMS: m/z calcd for $C_{23}H_{12}ClN_4O_5Re$: 644.9967, found: 644.9971.

[Re(CO)$_3$(3c)Cl], 4c. ^{1}H NMR (DMSO-d_6, 600 MHz): δ (ppm) 14.15 (s, 1H, Ar-NH); 9.37 (dd, 2H, Ar-H); 9.28 (dd, 2H, Ar-H); 8.28 (d, 2H, Ar-H); 8.17 (bs, 2H, Ar-H); 7.23 (m, 2H, Ar-H), 3.90 (s, 3H, -CH_3). ^{13}C NMR (DMSO-d_6, 150 MHz): δ (ppm) 197.8, 190.1, 161., 152.9, 151.1, 143.5, 132.7, 128.9, 128.2, 126.4, 125.3, 121.9 114.6, 55.4. HRMS: m/z calcd for $C_{23}H_{14}ClN_4O_5Re$: 631.0175, found: 631.0192.

[Re(CO)$_3$(3d)Cl], 4d. ^{1}H NMR (DMSO-d_6, 600 MHz): δ (ppm) 14.70 (s, 1H, Ar-NH); 9.42 (d, 2H, Ar-H); 9.31 (m, 2H, Ar-H); 8.57 (m, 4H, Ar-H); 8.21 (bs, 2H, Ar-H). ^{13}C NMR (DMSO-d_6, 150 MHz): δ (ppm) 197.8, 190.1, 152.7, 151.8, 151.5, 132.9, 130.4, 129.3, 127.5, 126.5, 124.6. HRMS: m/z calcd for $C_{22}H_{11}ClN_5O_5Re$: 645.9919, found: 645.9931.

[Re(CO)$_3$(3e)Cl], 4e. ^{1}H NMR (DMSO-d_6 600 MHz): δ (ppm) 14.61 (s, 1H); 9.40 (d, 2H); 9.30 (d, 2H); 8.51 (d, 2H); 8.20 (m, 4H). ^{13}C NMR (DMSO-d_6, 150 MHz): δ (ppm). 197.6, 189.9, 151.6, 150.5, 144.0, 141.1, 133.2, 133.1, 132. 8, 132.7, 129.0, 128.3, 126.9, 126.6, 118.4, 112.1. HRMS: m/z calcd for $C_{23}H_{11}ClN_5O_3Re$: 626.0021, found: 626.0008.

General method for the preparation of $[Re(CO)_3(L)(MeIm)]OTf$

$[Re(CO)_3(L)Cl]$ (30 mg, 0.05 mmol) in acetone (5 mL) was mixed with AgOTf (12.8 mg, 0.05 mmol) in 1 mL acetone, and the mixture heated at 70 °C for 2 h. A precipitate formed during the course of the reaction, which was collected by filtration. To the filtrate, NMI (16 mg, 0.2 mmol) was added at room temperature and the mixture stirred overnight. The solvent was removed by rotary evaporation and the resulting solid was dissolved in DMSO and the desired product obtained by HPLC (method A) as a yellow solid. Yield: 51-80%.

$[Re(CO)_3(4a)(Melm)]OTf$, 5a. ^{1}H NMR (CD_3OD, 600 MHz): δ (ppm) 9.56 (dd, 2H, Ar-H); 9.30 (dd, 2H, Ar-H); 8.22 (d, 2H, Ar-H); 8.16 (q, 2H, Ar-H); 7.66 (s, 1H, Ar-H); 7.55 (md, 3H, Ar-H); 6.89 (s, 1H, Ar-H); 6.57 (s, 1H, Ar-H); 3.49 (s, 3H, -CH_3). ^{13}C NMR (DMSO-d_6, 150 MHz): δ (ppm) 150.0, 142.2, 140.5, 133.2, 128.5, 128.0, 126.4, 126.1, 122.9, 33.9. HRMS: m/z calcd for $C_{26}H_{18}N_6O_3Re$: 649.0999, found: 649.0994.

$[Re(CO)_3(4b)(MeIm)]OTf$, 5b. ^{1}H NMR (CD_3OD, 600 MHz): δ (ppm) 9.44 (dd, 2H, Ar-H); 9.11 (d, 2H, Ar-H); 8.18 (d, 2H, Ar-H); 8.07 (m, 4H, Ar-H); 7.53 (s, 1H, Ar-H); 6.77 (t, 1H, Ar-H); 6.45 (t, 1H, Ar-H); 3.37 (s, 3H, -CH_3). ^{13}C NMR (CD_3OD, 150 MHz): δ (ppm) 168.9, 162.2, 154.3, 153.5, 146.0, 141.9, 134.9, 133.8, 131.6, 129.8, 128.2, 127.9, 123.9, 34.5. HRMS: m/z calcd for $C_{26}H_{18}N_6O_3Re$: 693.089, found: 693.0889.

$[Re(CO)_3(4c)(MeIm)]OTf$, 5c. ^{1}H NMR (CD_3CN, 600 MHz): δ (ppm) 12.09 (s, 1H,Ar-NH); 9.47 (d, 2H, Ar-H); 8.24 (d, 2H, Ar-H); 8.12 (dd, 2H, Ar-H); 7.24 (s, 1H, Ar-H); 7.21 (d, 2H, Ar-H); 6.77 (s, 1H, Ar-H); 6.54 (s, 1H, Ar-H); 3.94 (s, 3H, -CH_3); 3.39 (s, 3H, CH_3). ^{13}C NMR (CD_3CN, 150 MHz): δ (ppm) 161.4, 153.3, 151.8, 151. 5, 140.0, 128.4, 128.0, 126. 7, 122.2, 121.4, 114.4, 55.0, 33.6. HRMS: (ESI+) calcd for $C_{26}H_{18}N_6O_3Re$: 679.1105, found: 679.1087.

[Re(CO)$_3$(4e)(MeIm)]OTf, 5e. ^{1}H NMR (CD_3OD, 600 MHz): δ (ppm) 9.48 (dd, 2H); 9.25 (s, 2H); 8.76 (s, 1H); 8.38 (dd, 2H); 8.10 (q, 2H); 7.90 (dd, 2H); 7.55 (s, 1H); 7.46 (d, 2H); 6.77 (t, 1H); 6.44 (t, 1H); 3.85 (s, 3H, CH_3). HRMS: m/z calcd for $C_{27}H_{17}N_7O_3Re$: 674.0952, found: 674.0943. HPLC (UV 254 nm): R_t = 12.9 min.

Synthesis of 5f. [$Re(CO)_3(H_2O)Br$] (25 mg, 0.077 mmol) was dissolved in 1:1 v/v methanol-water (2 mL). N-methylimidazole was then added (0.03 mL, 0.385 mmol) and the mixture heated in a microwave for 5 min at 110 °C. Compound **3f** (31 mg, 0.092 mmol) was added and the solution heated in the microwave for an additional 5 min at 110 °C. The desired product was obtained using semi-prep HPLC (Method D) yielding a yellow precipitate. Yield: (10 mg, 19%). ^{1}H NMR (CD_3OD, 600 MHz): δ (ppm) 9.57 (dd, 2H), 9.35 (dd, 2H), 8.26 (bs, 2H), 8.19 (q, 2H), 7.89 (bs, 2H), 7.66 (s, 1H), 6.89 (t, 1H), 6.56 (t, 1H), 3.50 (s, 3H). ^{13}C NMR (CD_3OD, 150 MHz): δ (ppm) 142.0, 130.4, 122.9, 34.4, 0.6. HRMS: m/z calcd for $C_{26}H_{19}BN_6O_5Re$: 693.1073, found: 693.1097. HPLC (UV 254 nm): R_t = 11.2 min.

Synthesis of Tetrazine-functionalized PIP ligand, 9. 4-(1,2,4,5-Tetrazin-3-yl)phenyl)methanamine hydrochloride (42 mg, 0.19 mmol) was dissolved in DMF (2 mL) and DIPEA (48 mg, 0.37 mmol) was added and the resulting solution stirred for 15 min. The solution was then added **3b** (38 mg, 0.11 mmol) and PyBOP (105 mg, 0.2 mmol) in DMF (2 mL) and the mixture stirred for 2 h. Water (20 mL) was added and the resulting precipitate was collected by centrifugation, which was re-dissolved in DMSO and the desired product isolated as a pink powder by HPLC (Method C). Yield: 38 mg (68 %). ^{1}H NMR (DMSO-d_6, 700 MHz): δ (ppm) 10.57 (s, 1H); 9.41 (t, 1H); 9.31 (d, 2H); 9.16 (dd, 2H); 8.48 (d, 2H); 8.35 (d, 2H); 8.23 (m, 2H); 8.15 (d, 2H); 7.65 (d, 2H); 4.67 (d, 2H). ^{13}C NMR (DMSO-d_6, 176 MHz): δ (ppm) 166.01, 159.15, 158.94, 158.73, 158.56, 151.72, 145.78, 145.33,

135.73, 132.05, 130.88, 128.57, 126.74, 126.23, 43.11. HRMS: m/z calcd for $C_{29}H_{19}N_9O$: 510.17, found: 510.1785

Tetrazine-functionalized PIP Re complex, 10. (4-(1,2,4,5-Tetrazin-3-yl)phenyl)methanamine hydrochloride (19 mg, 0.1 mmol) was dissolved in DMF (1 mL) and DIPEA (26 mg, 0.2 mmol) was added and the resulting solution stirred for 15 min. The solution was added **5b** (32 mg, 0.05 mmol) and PyBOP (52 mg, 0.1 mmol) in DMF (1 mL) and the mixture stirred for 2 h. Water (20 mL) was added and the resulting precipitate collected by centrifugation, dissolved in DMSO and the desired product isolated as an orange powder by HPLC (Method C). Yield: 30 mg (37%). ^{1}H NMR (DMSO-d_6, 600 MHz): δ (ppm) 10.60 (s, 1H, Ar-H); 9.40 (dd, 3H, Ar-H); 9.33 (dd, 2H, Ar-H); 8.52 (d, 2H, Ar-H); 8.46 (d, 2H, Ar-H); 8.23 (d, 3H, Ar-H); 7.68 (d, 2H, Ar-H); 4.70 (s, 2H, -CH_2-). ^{13}C NMR (DMSO-d_6, 176 MHz): δ (ppm) 198.31, 190.47, 166.28, 165.88, 158.62, 152.22, 151.98, 145.26, 144.47, 135.83, 133.36, 132.26, 130.91, 128.73, 128.37, 127.14, 126.87. HRMS: m/z calcd for $C_{32}H_{19}ClN_9O_4Re$: 814.0720, found: 814.0737 (with Re + Cl isotope pattern).

TCO-functionalized BSA, 14. *trans*-4-Cycloocten-yl 2,5-dioxo-1-pyrrolidinyl ester carbonic acid (9.3 mg, 0.061 mmol) was dissolved in DMSO (0.2 mL), and the solution added to bovine serum albumin (200 mg, 0.003 mmol) in water (2 mL). The reaction mixture was left to shake at 4 °C for 12 h. The product was then purified via dialysis against MilliQ water for 12 h. The product was obtained following lyophilization as a white solid. It was determined by MALDI-TOF MS that there were 2.7 TCO per BSA molecule.

Radiochemistry

General Synthesis of [^{99m}Tc(CO)$_3$(L)Cl] and [^{99m}Tc(CO)$_3$(L)NMI]Cl. Sodium boranocarbonate (10.0 mg, 0.07 nmol), sodium carbonate (15.0 mg, 14.0 mmol), sodium borate (20 mg, 0.05 mmol) and sodium potassium tartrate (22 mg, 0.08 mmol) were placed in a microwave vial

and purged with argon for 10 min. To this mixture, Na[^{99m}TcO$_4$] (1 mL, 1.85 GBq) was added and the vial was heated in a microwave at 110 °C for 3.5 min to form [^{99m}Tc(CO)$_3$(H$_2$O)$_3$]$^+$. After cooling to room temperature, the pH was adjusted to 2 with 0.1 M HCl (0.2 mL) and the solution added to **3a-d** (1 mg, 6 mmol) under argon. The solution was stirred at 40 or 65 °C for 1 h where the formation of **6a-d** was confirmed by analytical HPLC (Method B) and through comparison of retention times of the co-injected Re analogue. **6a**: R_t = 10.2 min, RCY = 63% (n = 3); **6b**: R_t = 7.9 min, RCY = 82% (n = 3); **6c**: R_t = 10.4 min, RCY = 57% (n = 2); **6d**: R_t = 10.2 min, RCY = 64% (n = 2). The N-methylimidazole (NMI) derivatives **6a-d** were prepared by adding NMI (50 μL, 0.75 mmol) to the solution containing **6a-d** under argon where the mixture was stirred at 40 °C for 1 h. The formation of products **7a-d** was confirmed was confirmed by analytical HPLC (Method B) and through comparison of retention times of the co-injected Re analogue. **7a**: R_t = 10.7 min, RCY = 77% (n = 3); **7b**: R_t = 8.3 min, RCY = 89% (n = 3); **7c**: R_t = 9.7 min, RCY = 66% (n = 3); **7d**: R_t =10.7 min, RCY = 54% (n = 3).

One-pot Synthesis of 7e. Compound **3e** (1 mg), NMI (50 μL) and [^{99m}Tc(CO)$_3$(OH$_2$)$_3$]$^+$ (2 mL) were added to a microwave vial, sealed, and heated to 40 °C under Ar for 1 h. The mixture was analyzed for purity using analytical HPLC method C to confirm formation of the product. R_t = 13.1 min, RCY = 55% (n = 2).

One-pot Synthesis of 7f. Compound **3f** (1 mg), NMI (50 μL) and [^{99m}Tc(CO)$_3$(OH$_2$)$_3$]$^+$ (2 mL) were added to a microwave vial, sealed, and heated to 40 °C under Ar for 1 h. The mixture was analyzed for purity using analytical HPLC to confirm formation of the product. R_t = 11.3 min, RCY = 49% (n=2).

Two-step Synthesis of 13. Compound **9** (41 mg) and [^{99m}Tc(CO)$_3$(OH$_2$)$_3$]$^+$ (2 mL) were added to a microwave vial, sealed, and heated to 40 °C under Ar for 3 h. The product **12** was purified from the

reaction mixture via HPLC (Method E R_t = 12.5 min, RCY = 35 % (n = 2). To the purified final product **13**, NMI (50 μL) was added and heated to 40 °C under Ar for 1 h (Method E R_t = 13 min, RCY = 24% (n =1).

2.7 References

(1) Ametamey, S. M.; Honer, M.; Schubiger, P. A. Molecular Imaging with PET. *Chem Rev.* **2008**, 1501–1516.

(2) Herschman, H. R. Molecular Imaging : Looking at Problems. *Science (80).* **2003**, *302*, 605–608.

(3) Kim, J.; Piao, Y.; Hyeon, T. Multifunctional Nanostructured Materials for Multimodal Imaging , and Simultaneous Imaging and Therapy. *Chem. Soc. Rev.* **2009**, *38*, 372–390.

(4) Paeng, J. C.; Lee, D. S. Multimodal Molecular Imaging. *Open Nucl. Med. J.* **2010**, *2*, 145–152.

(5) Thorp-Greenwood, F. L.; Coogan, M. P. Radiopharmaceuticals for Imaging and Therapy Current Applications and Prospects for Development of New Agents Complexes. *Dalt. Trans* **2011**, *40*, 6129–6143.

(6) Bhushan, K. R.; Misra, P.; Liu, F.; Mathur, S.; Lenkinski, R. E.; Frangioni, J. V. Detection of Breast Cancer Microcalcifications Using a Dual-Modality SPECT/NIR Fluorescent Probe. *J. Am. Chem. Soc.* **2008**, *130* (52), 17648–17649.

(7) Jennings, L. E.; Long, N. J.; Jennings, L.; Long, N. ' Two Is Better than One '— Probes for Dual-Modality Molecular Imaging. *Chem Comm* **2009**, 3511–3524.

(8) Morais, G. R.; Santos, I. Organometallic Complexes for SPECT Imaging and / or Radionuclide Therapy. *Organometallics* **2012**.

(9) Pitchumony, T. S.; Banevicius, L.; Janzen, N.; Zubieta, J.; Valliant, J. F. Isostructural Nuclear and Luminescent Probes Derived from Stabilized [2 + 1] Rhenium(I)/Technetium(I) Organometallic Complexes. *Inorg. Chem.* **2013**, *52* (23), 13521–13528.

(10) Spagnul, C.; Alberto, R.; Gasser, G.; Ferrari, S.; Pierroz, V.; Bergamo, A.; Gianferrara, T.; Alessio, E. Novel Water-Soluble 99m Tc (I)/ Re (I) -Porphyrin Conjugates as Potential Multimodal Agents for Molecular Imaging. *J. Inorg. Biochem.* **2013**, *122*, 57–65.

(11) Yazdani, A.; Janzen, N.; Banevicius, L.; Czorny, S.; Valliant, J. F. Imidazole-Based [2 + 1] Re(I)/99mTc(I) Complexes as Isostructural Nuclear and Optical Probes. *Inorg. Chem.* **2015**, *54* (4), 1728–1736.

(12) Boonstra, M. C.; Prakash, J.; Van De Velde, C. J. H.; Mesker, W. E.; Kuppen, P. J. K.; Vahrmeijer, A. L.; Sier, C. F. M. Stromal Targets for Fluorescent-Guided Oncologic Surgery. *Front. Oncol.* **2015**, *5* (November), 1–8.

(13) Miwa, S.; Matsumoto, Y.; Hiroshima, Y.; Yano, S.; Uehara, F.; Yamamoto, M.; Zhang, Y.; Kimura, H.; Hayashi, K.; Yamamoto, N.; et al. Fluorescence-Guided Surgery of Prostate Cancer Bone Metastasis. *J. Surg. Res.* **2014**, *192* (1), 124–133.

(14) Mondal, S. B.; Gao, S.; Zhu, N.; Liang, R.; Gruev, V.; Achilefu, S. *NIH Public AccessReal-Time Fluorescence Image-*

Guided Oncologic Surgery; 2015.

(15) Nguyen, Q. T.; Tsien, R. Y. Fluorescence-Guided Surgery with Live Molecular Navigation-a New Cutting Edge. *Nat. Rev. Cancer* **2013**, *13* (9), 653–662.

(16) Vahrmeijer, A. L.; Hutteman, M.; van der Vorst, J. R.; van de Velde, C. J. H.; Frangioni, J. V. Image-Guided Cancer Surgery Using near-Infrared Fluorescence. *Nat. Rev. Clin. Oncol.* **2013**, *10* (9), 507–518.

(17) Yan, R.; El-emir, E.; Rajkumar, V.; Robson, M.; Jathoul, A. P.; Pedley, R. B. One-Pot Synthesis of an 125 I-Labeled Trifunctional Reagent for Multiscale Imaging with Optical and Nuclear Techniques. *Angew. Chemie* **2011**, 6925–6927.

(18) Zhou, Y.; Kim, Y.; Yan, X.; Jacobson, O.; Chen, X.; Liu, S. Cu-Labeled Lissamine Rhodamine B : A Promising PET Radiotracer Targeting Tumor Mitochondria. *Mol. Pharm.* **2011**, 1198–1208.

(19) Duheron, V.; Moreau, M.; Collin, B.; Sali, W.; Bernhard, C.; Goze, C.; Gautier, T.; Barros, J. P. De. Dual Labeling of Lipopolysaccharides for SPECT-CT Imaging and Fluorescence Microscopy. *ACS Chem. Biol.* **2014**.

(20) Ghosh, S. C.; Ghosh, P.; Wilganowski, N.; Robinson, H.; Hall, M. A.; Dickinson, G.; Pinkston, K. L.; Harvey, B. R.; Sevick-muraca, E. M.; Azhdarinia, A. Multimodal Chelation Platform for Near-Infrared Fluorescence/ Nuclear Imaging. *J Med Chem* **2013**.

(21) Heinrich, T. K.; Gottumukkala, V.; Snay, E.; Dunning, P.; Fahey, F. H.; Treves, S. T.; Packard, A. B. Synthesis of Fluorine-18 Labeled Rhodamine B : A Potential PET Myocardial Perfusion Imaging Agent. *Appl. Radiat. Isot.* **2010**, *68* (1), 96–100.

(22) Hendricks, J. A.; Keliher, E. J.; Wan, D.; Hilderbrand, S. A. NIH Public Access. *Angew. Chem. Int. Ed. Engl.* **2013**, *51* (19), 4603–4606.

(23) Li, S.; Zhang, C.; Huang, S.; Hu, F.; Yin, J.; Lui, S. H. RSC Advances Highly Selective Colorimetric and Fluorescent Sensors for the Fluoride Anion. *RSC Adv.* **2012**, *2*, 4215–4219.

(24) Liu, S.; Lin, T.; Li, D.; Leamer, L.; Shan, H.; Li, Z.; Gabbaï, F. P.; Conti, P. S. Lewis Acid-Assisted Isotopic 18 F-19 F Exchange in BODIPY Dyes : Facile Generation of Positron Emission Tomography / Fluorescence Dual Modality Agents for Tumor Imaging. *Theranostics* **2013**, *3* (3).

(25) Priem, T.; Camporese, D.; Brune, X.; Hardouin, J.; Romieu, A.; Renard, P. Biomolecular Chemistry. *Org. Biomol. Chem.* **2013**, *11*, 469–479.

(26) Ting, R.; Aguilera, T. A.; Crisp, J. L.; Hall, D. J.; Eckelman, W. C.; Vera, D. R.; Tsien, R. Y. Fast 18 F Labeling of a Near-Infrared Fluorophore Enables Positron Emission Tomography and Optical Imaging of Sentinel Lymph

Nodes. *Bioconjugate Chem* **2010**, *21*, 1811–1819.

(27) Yazdani, A.; Janzen, N.; Czorny, S.; Ungars, R.; Miladinovic, T.; Singh, G.; Valliant, J. F. Preparation of Tetrazine-Containing [2+1] Complexes of 99mTc and in Vivo Targeting Using Bioorthogonal Inverse Electron Demand Diels-Alder Chemistry. *Dalt. Trans* **2017**.

(28) Azad, B. B. Development of Single and Multimodality Imaging Probes for PET, SPECT and Fluorescence Imaging, 2011.

(29) Botchway, S.; Dilworth, R.; Salichou, M. One and Two Photon Fluorescent Complexes of Rhenium and Their Technetium Analogues †. *Dalt. Trans* **2010**, *5*, 5219–5220.

(30) Connell, T. U.; Hayne, D. J.; Ackermann, U.; Tochon-danguy, H. J.; White, J. M.; Donnelly, P. S. Rhenium and Technetium Tricarbonyl Conjugated to a Targeting RGD Peptide ††. *Label. Compd. Radiopharm.* **2014**, No. August 2013.

(31) Faulkner, S.; Long, N.; College, I.; Thorp-greenwood, F. L.; Coogan, M. P.; Correia, J. D. G.; Paulo, A.; Raposinho, P. D.; Santos, I.; Yong, K.; et al. Radiopharmaceuticals for Imaging and Therapy Current Applications and Prospects for Development of New Agents Complexes First Dinuclear Re / Tc Complex as a Potential Bimodal Optical / SPECT Molecular Imaging Agent †. *Dalt. Trans* **2011**, No. 23.

(32) Ranyuk, E.; Lebel, R.; Berub-lauziere, Y.; Klarskov, K.; Lecomte, R.; Lier, J. E. Van; Guerin, B. Ga/DOTA- and 64 Cu/NOTA-Phthalocyanine Conjugates as Fluorescent/PET Bimodal Imaging Probes. *Bioconjug. Chem.* **2013**, *24*, 1624–1633.

(33) Lo, K. K.-W.; Choi, A. W.-T.; Law, W. H.-T. Applications of Luminescent Inorganic and Organometallic Transition Metal Complexes as Biomolecular and Cellular Probes. *Dalt. Trans.* **2012**, *41* (20), 6021.

(34) Alfonso, M.; Alberto, T. Ferrocene-Based Heteroditopic Receptors Displaying High Selectivity toward Lead and Mercury Metal Cations through Different Channels. **2011**, No. 4, 939–947.

(35) Kaur, N.; Alreja, P. A Novel 1,10-Phenanthroline Based Chemosensor for Differential Metal Ion Sensing and Constructing Molecular Logic Gates. *Tetrahedron Lett.* **2015**, *56* (1), 182–186.

(36) Resendiz, M. J. E.; Noveron, J. C.; Disteldorf, H.; Fischer, S.; Stang, P. J. LETTERS A Self-Assembled Supramolecular Optical Sensor for Ni (II), Cd (II), and Cr (III). **2004**, No. II, 4–6.

(37) Sun, D.; Liu, Y.; Yu, Q.; Zhou, Y.; Zhang, R.; Chen, X.; Hong, A.; Liu, J. The Effects of Luminescent Ruthenium(II) Polypyridyl Functionalized Selenium Nanoparticles on BFGF-Induced Angiogenesis and AKT/ERK Signaling. *Biomaterials* **2013**, *34* (1), 171–180.

(38) Hardouin-lerouge, M.; Chesneau, B.; Allain, M. Dual Signaling System with an Extended-Tetrathiafulvalene − Phenanthroline Dyad Acting as an Electrooptical Cation Chemosensor. **2012**.

(39) Wu, C.; Lu, H.; Chen, L.; Lin, Y. Synthesis and Ion-Sensing Phenomena of Two New Helical Conjugated Oligomers Containing 1 , 10-Phenanthroline and Oligo-Alkylthiophene. **2007**, 1586–1597.

(40) Shi, L.; Li, B. A Series of Cu I Complexes Containing 1 , 10-Phenanthroline Derivative Ligands : Synthesis , Characterization , Photophysical , and Oxygen-Sensing Properties. **2009**, 2294–2302.

(41) Yin, H. J.; Liu, Y.-J.; Gao, J.; Wang, K.-Z. A Highly Sensitive and Selective Visible-Light Excitable Luminescence Probe for Singlet Oxygen Based on a Dinuclear Ruthenium Complex. *Dalt. Trans.* **2017**, 3325–3331.

(42) Yi, X.; Zhao, J.; Wu, W.; Huang, D.; Ji, S.; Sun, J. Rhenium(i) Tricarbonyl Polypyridine Complexes Showing Strong Absorption of Visible Light and Long-Lived Triplet Excited States as a Triplet Photosensitizer for Triplet–Triplet Annihilation Upconversion. *Dalt. Trans.* **2012**, *41* (29), 8931.

(43) Qasim, S. S.; Ali, S. S.; Ahmed, S. K.; June, A. Research Journal of Pharmaceutical , Biological and Chemical. *Res. J. Pharm. Biol. Chem. Sci.* **2011**, *2* (2), 423–428.

(44) Miyaura, N.; Suzuki, A. Palladium-Catalyzed Cross-Coupling Reactions of Organoboron Compounds. *Chem. Rev.* **1995**, *95* (7), 2457–2483.

(45) Pappin, B.; Kiefel, M. J.; Houston, T. a. Boron-Carbohydrate Interactions. *Carbohydrates - Compr. Stud. Glycobiol. Glycotechnol.* **2012**, 1–50.

(46) Lazarova, N.; James, S.; Babich, J.; Zubieta, J. A Convenient Synthesis, Chemical Characterization and Reactivity of [Re(CO)3(H2O)3]Br: The Crystal and Molecular Structure of [Re(CO)3(CH3CN)2Br]. *Inorg. Chem. Commun.* **2004**, *7* (9), 1023–1026.

(47) Abou-Hatab, S.; Spata, V. A.; Matsika, S. Substituent Effects on the Absorption and Fluorescence Properties of Anthracene. *J Phys Chem A* **2017**, *121*, 1213–1222.

(48) Alberto, R.; Ortner, K.; Wheatley, N.; Schibli, R.; Schubiger, A. P. Synthesis and Properties of Boranocarbonate : A Convenient in Situ CO Source for the Aqueous. **2001**, *3* (12), 3135–3136.

(49) Alberto, R.; Schibli, R.; Schubiger, A. P.; Di, V.; Abram, U.; Dresden, D.-; Kaden, T. A. A Novel Organometallic Aqua Complex of Technetium for the Labeling of Biomolecules : Aqueous Solution and Its Reaction with a Bifunctional Ligand. **1998**, *3* (13), 7987–7988.

(50) Simms, R. W.; Causey, P. W.; Weaver, D. M.; Sundararajan, C.; Stephenson, K. A.; Valliant, J. F. Preparation of Technetium-99m Bifunctional Chelate Complexes Using a Microfluidic Reactor: A Comparative Study with

Conventional and Microwave Labeling Methods. *J. Label. Compd. Radiopharm.* **2012**, *55* (1), 18–22.

(51) Rossin, R.; van den Bosch, S. M.; ten Hoeve, W.; Carvelli, M.; Versteegen, R. M.; Lub, J.; Robillard, M. S. Highly Reactive Cyclooctene Tags with Improved Stability for Diels-Alder Chemistry in Living Systems. *Bioconjug. Chem.* **2013**.

(52) Choi, A. W.-T.; Tso, K. K.-S.; Yim, V. M.-W.; Liu, H.-W.; Lo, K. K.-W. Modification of 1,2,4,5-Tetrazine with Cationic Rhenium(I) Polypyridine Units to Afford Phosphorogenic Bioorthogonal Probes with Enhanced Reaction Kinetics. *Chem. Commun.* **2015**, *51* (16), 3442–3445.

(53) Lo, K. K.; Tsang, K. H.; Hui, W.; Zhu, N.; Road, P.; Kong, H. Photophysical , and Protein-Binding Properties of Luminescent Rhenium (I) Diimine Indole Complexes. *Chem comm* **2003**, 2704–2705.

(54) Bilton, H. A.; Ahmad, Z.; Janzen, N.; Czorny, S.; Valliant, J. F. Preparation and Evaluation of 99mTc-Labeled Tridentate Chelates for Pre-Targeting Using Bioorthogonal Chemistry. **2017**, No. 120, e55188.

(55) Devaraj, N. K.; Weissleder, R. Biomedical Applications Fo Tetrazine Cycloadditions. *Acc Chem Res.* **2011**, *44* (9), 816–827.

(56) Zeglis, B. .; Sevak, K. K.; Reiner, T.; Mohindra, P.; Carlin, S. D.; Zanzonico, P.; Weissleder, R.; Lewis, J. S. A Pretargeted PET Imaging Strategy Based on Bioorthogonal Diels-Alder Click Chemistry. *J. Nucl. Med.* **2013**, *54* (8), 1389–1396.

(57) Meyer, J. P.; Kozlowski, P.; Jackson, J.; Cunanan, K. M.; Adumeau, P.; Dilling, T. R.; Zeglis, B. M.; Lewis, J. S. Exploring Structural Parameters for Pretargeting Radioligand Optimization. *J. Med. Chem.* **2017**, *60* (19), 8201–8217.

(58) Blackman, M. L.; Royzen, M.; Fox, J. M. The Tetrazine Ligation: Fast Bioconjugation Based on Inverse-Electron-Demand Diels-Alder Reactivity NIH Public Access. *J Am Chem Soc* **2008**, *130* (41), 13518–13519.

(59) Van Der Heyde, H. C.; Bauer, P.; Sun, G.; Chang, W. L.; Yin, L.; Fuseler, J.; Granger, D. N. Assessing Vascular Permeability during Experimental Cerebral Malaria by a Radiolabeled Monoclonal Antibody Technique. *Infect. Immun.* **2001**, *69* (5), 3460–3465.

(60) Yao, L.; Xue, X.; Yu, P.; Ni, Y.; Chen, F. Evans Blue Dye: A Revisit of Its Applications in Biomedicine. *Contrast Media Mol. Imaging* **2018**, *2018*, 18–24.

Chapter 3: Synthesis, Characterization and Preliminary Testing of a Near Infrared PIP Derivative

3.1 Overview and Background

The applicability of compound **9** (synthesized in Chapter 2) as a platform for the creation of targeted SPECT/OI was investigated. The initial step was to assess the distribution of its ^{99m}Tc(I) complex *in vivo*. Ultimately, as presented below, the ^{99m}Tc complex of **9** showed significant retention in non-target tissues, consequently a second-generation compound was developed by linking the PIP ligand to a cyanine dye. Cyanine dyes have been shown previously to bind albumin which can improve pharmacokinetics.[1–5] Sulfonated cyanine dyes are also readily soluble in aqueous solutions addressing another limitation of the PIP ligands which are generally only soluble in DMSO. The dye selected was IR783, which is structurally similar to ICG and has well characterized albumin binding properties.[6] IR783 has the added advantage that it can also be used as a photoacoustic (PA) dye to provide real time high resolution images to go along with whole-body images generated using SPECT and the ^{99m}Tc labelled derivative.

3.2 Results and Discussion

3.2.1 Distribution of PIP-Tz

Compound **13** (developed in Chapter 2) is a general-purpose platform for linking PIP complexes to biomolecules using biorthogonal chemistry. Prior to evaluating its distribution *in vivo*, radiolabelling was optimized. First, compound **9** was heated at 50 °C with $[^{99m}Tc(CO)_3(OH_2)_3]^+$ for 1 hour to afford **12**. Following purification of **12**, NMI was added and the mixture heated again to 50 °C for 30 minutes providing **13** in 89% radiochemical yield (RCY). The final product (**13**) was isolated via HPLC (Figure 3.1 & 3.2).

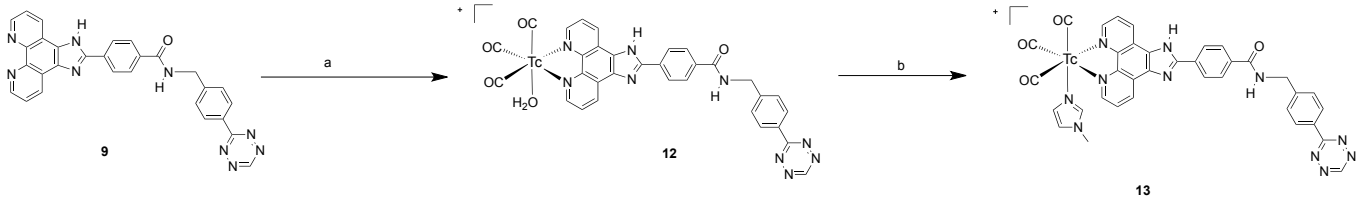

Scheme 3.1 Radiolabeling of **9**. Reagents and conditions: a) $[^{99m}Tc(CO)_3(OH_2)_3]^+$, 50 °C, 1 h, RCY = 77%; b) NMI, 50 °C, 30 min, RCY = 89%.

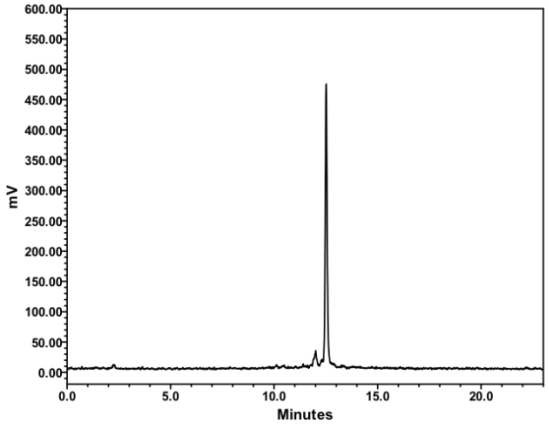

Figure 3.1 Gamma HPLC trace of **13** (HPLC method A).

With the labelled probe in hand, a biodistribution study was conducted in healthy mice to determine the clearance route and to assess the extent of binding and retention to non-target tissues (liver, kidneys, etc.). At 1 hour post-injection, high liver (94 %ID/g), lung (101 %ID/g) and spleen (32 %ID/g) uptake were seen, likely due to the lipophilic nature of the metal complex (Figure 3.2). It is also possible that the complex is not stable *in vivo*, resulting in the loss of the monodentate ligand.

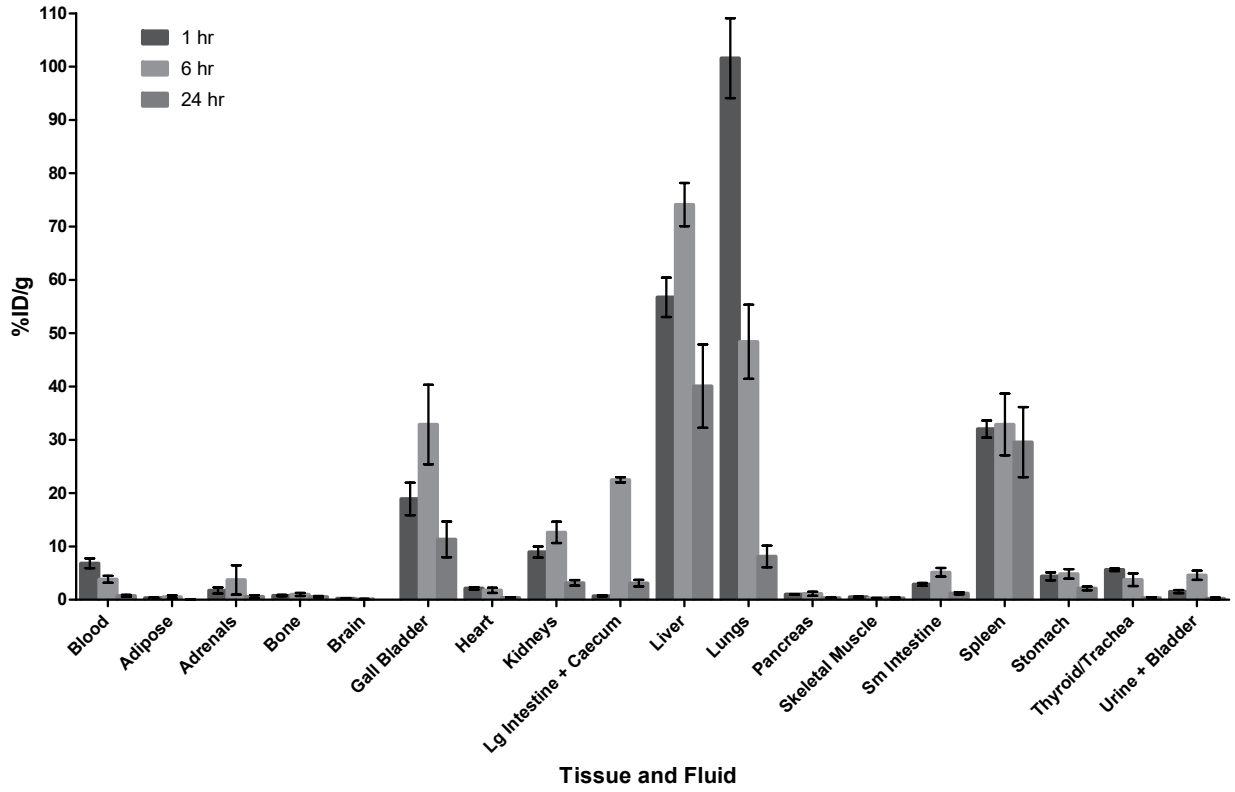

Figure 3.2 Biodistribution data for selected fluids and tissues for **13**. Experiments were performed using Balb/c mice (n=3 per time point) and tissues and fluids were collected at 1, 6, and 24 h post administration. Data is expressed as the mean percent injected dose per gram (%ID/g) ± SEM.

To determine if loss of the monodentate ligand was a major factor in the high liver and lung uptake, a second biodistribution study was conducted with excess NMI in the formulation. Adding an excess of NMI has been previously shown to stabilize [2+1] ^{99m}Tc complexes and prevent the loss of the monodentate ligand *in vivo*.[7] The addition of excess NMI did reduce the uptake in the liver by 52% and the spleen by 13%, however there was still a high overall accumulation in these organs and an increase in the lung uptake by 171% (Figure 3.3). The less than desirable biodistribution is most likely due to the hydrophobic nature of the compound despite the measured log P (0.013).

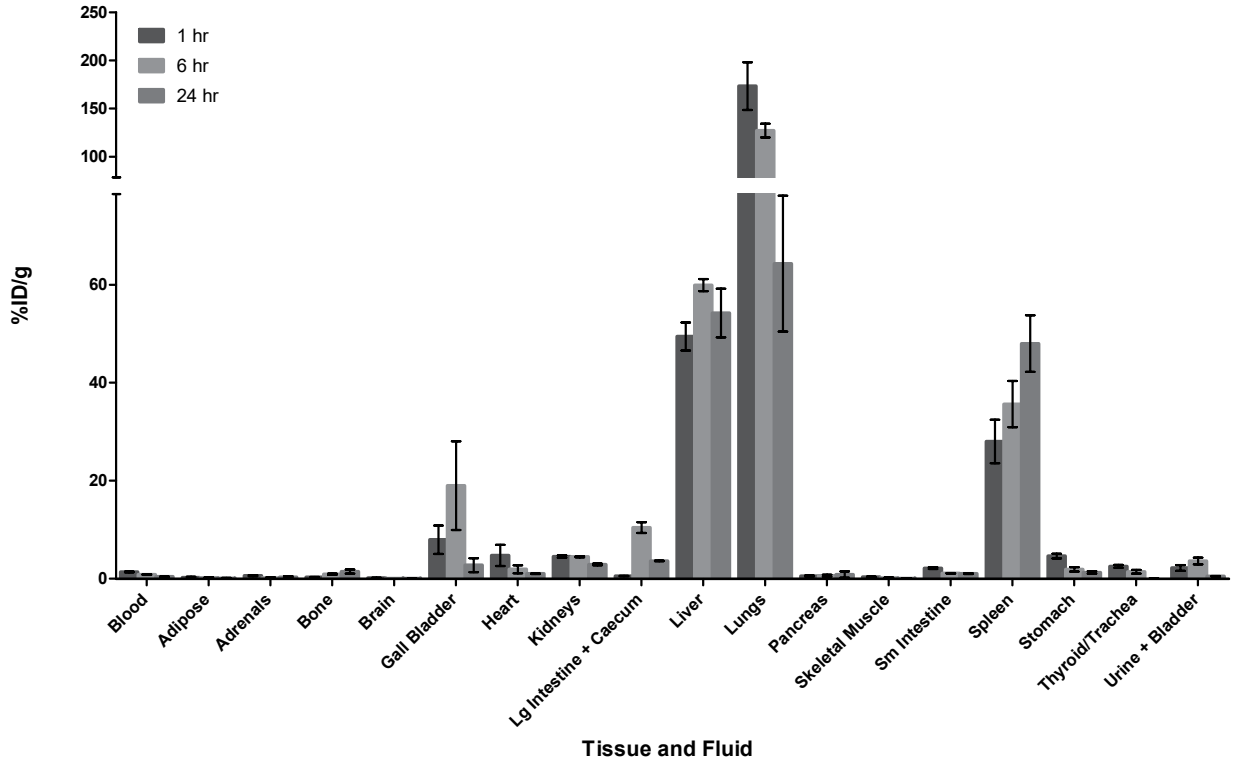

Figure 3.3 Biodistribution data for selected fluids and tissues for **13** in the presence of excess NMI. Experiments were performed using Balb/c mice (n=3 per time point) and tissues and fluids were collected at 1, 6, and 24 h post administration. Data is expressed as the mean percent injected dose per gram (%ID/g) ± SEM.

While the nature of the monodentate ligand can in theory be changed to tune the pharmacokinetics of **13**, an alternative strategy was pursued. Here, a NIR dye was coupled to the PIP ligand. Incorporation of the NIR dye, particularly one with sulfonate groups, should reduce the lipophilic nature of the ligand and it can promote albumin binding to improve pharmacokinetics. With the choice of the right NIR dye, the approach also has the advantage that it creates the opportunity to use PA imaging rather than OI and the ability to generate images with higher resolution and greater depth of penetration.

There are a wide range of commercially available fluorescent dyes, but only a limited number of these dyes emit in the NIR, and of those, only a handful have been used previously for targeted *in vivo* applications. The optimal selection for linking to PIP would involve a construct that is water-

soluble, exhibit a high quantum yield for optical imaging or high PA signal for PA imaging, and is stable *in vitro* and *in vivo*. Of particular interest are cyanine dyes which have these desired properties while also being amenable to further derivatization. A previous member of the Valliant group reported derivatizing IR780 with a prosthetic group suitable for labelling with ^{18}F. The PET tracer showed long circulation times *in vivo* likely due to albumin binding.[8] Building on this work, a PIP derivative of IR783, a more polar dye, was prepared and the corresponding metal complex tested *in vitro* and *in vivo*.

3.2.2 Synthesis and characterization of NIR Derivatives

The overall strategy involved preparing a PIP ligand directly from a benzaldehyde derivative of an IR dye. This required the synthesis of previously unknown cyanine dyes (**19** & **20**, Scheme 3.2). To this end 4-formylphenyl boronic acid (4-FBA, **18**) was used to optimize the conditions needed to derivatize IR780 (**16**) and subsequently the more water soluble IR783 (**17**). Following extensive testing (Table 3.1), the optimal conditions for IR780 were identified as $Pd(PPh_3)_4$, DIPEA, and the aldehyde (**18**) mixed at 100 °C for 12 hours in THF and water. The product was isolated as a green solid via HPLC in 16% yield (Scheme 3.2). The synthesis of the more water soluble derivative was also optimized (Table 3.2) and success realized by combining IR783 and 4-formylphenylboronic acid in the presence of $Pd(PPh_3)_4$ and Cs_2CO_3 with heating at 100 °C for 4 hours. The product was readily purified by HPLC in superior yield to that observed with IR780 (96%) as a green solid. The difference in observed yield is likely due to the increased solubility of IR783.

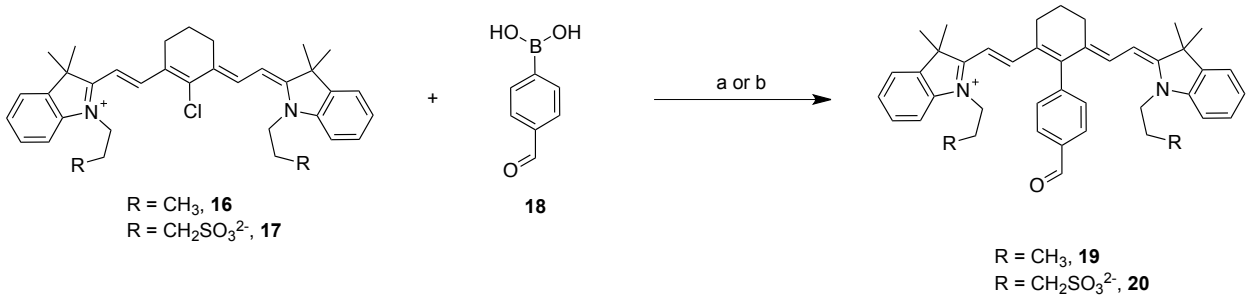

Scheme 3.2 Synthesis of compounds **19** and **20** (a = $Pd(PPh_3)_4$, DIPEA, THF/H_2O, 12 h, 100 °C; b = $Pd(PPh_3)_4$, Cs_2CO_3, H_2O, 4 h, 100 °C).

Table 3.7 Conditions evaluated to convert compound **16** to compound **19**.

Entry	16 (eq)	18 (eq)	Catalyst	Base	Solvent	Temp (°C)	Time	Yield
Literature Method[8]	1	1.2	$Pd(OAc)_2$ 10 mol% & t-BuxPhos 20 mol%	K_3PO_4	H_2O/EtOH	100	12 h	Trace
1	1	5	$Pd(OAc)_2$ 10 mol% & t-BuxPhos 20 mol%	K_3PO_4	EtOH	100	24 h	Trace
2	1	50	$Pd(OAc)_2$ 10 mol% & t-BuxPhos 20 mol%	K_3PO_4	EtOH	100	12 h	Trace
3	1	2.2	$Pd(PPh_3)_4$ 1.2 eq	Et_3N	H_2O/MeOH	RT	12 h	Trace
4	1	2.2	$Pd(PPh_3)_4$ 1.2 eq	Et_3N	H_2O/MeOH	100	12 h	Trace
5	1	8	$Pd(PPh_3)_4$ 4 eq	DIPEA	THF/H_2O	100	12 h	16%
6	1	1.2	$Pd(PPh_3)_4$ 4 mol%	Cs_2CO_3	DMF/H_2O	100	48 h	Trace

Table 3.8 Conditions screened to convert **17** to **20**.

Entry	17 (eq)	18 (eq)	Catalyst	Base	Solvent	Temp (°C)	Time	Yield
Literature Method[9]	1	2.3	$Pd(PPh_3)_4$ 7 mol%	-	DMF/H_2O	120	5 h	n.p.
1	1	1.3	$Pd(OAc)_2$ 10 mol% & t-BuxPhos 20 mol%	K_3PO_4	$EtOH/H_2O$	100	12 h	Trace
2	1	1.9	$Pd(PPh_3)_4$ 8 mol%	Cs_2CO_3	H_2O	100	4 h	96%

With the functionalized IR dye **20** in hand, the next step was to generate the PIP ligand. The conventional method used to prepare PIP ligands which involves heating 1,10-phenanthroline-5,6-dione (**21**), NH_4OAc, and a benzaldehyde in glacial acetic acid for 3 hours failed to convert **20** to the desired product **22**. After screening multiple reaction conditions and catalysts (Table 3.3) a successful route was found by combining **20**, **21**, NH_4OAc, and $SnCl_2$ and allowing the mixture to stir at 80 °C

overnight (Scheme 3.3). This reaction yielded a green product in 40% yield which was isolated in high purity using HPLC.

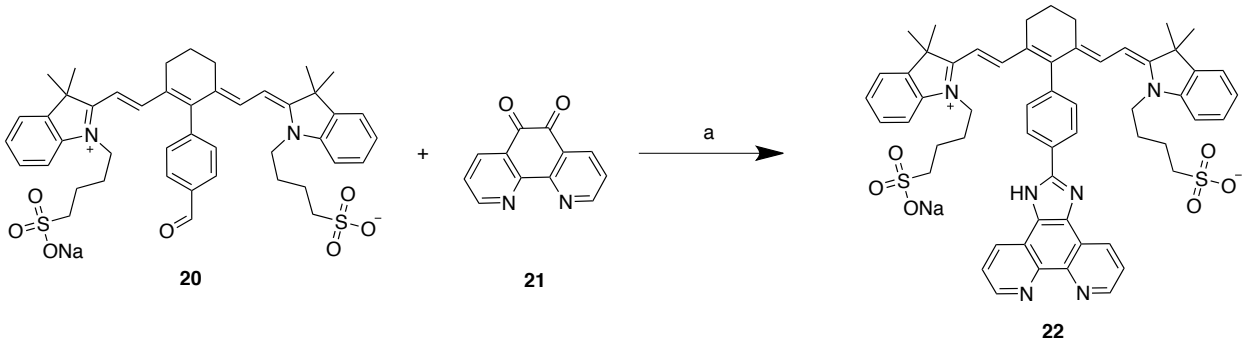

Scheme 3.3 Synthesis of **22**. Reagents and conditions: a) NH_4OAc, $SnCl_2$, MeOH, 80 ˚C, 12 h, 42%.

Table 3.3 Conditions tested for the synthesis of **22**.

Entry	Solvent	Catalyst	Conventional (C) or microwave (MW) heating	Temperature (˚C)	Time (h)	Yield (%)
1	Methanol	$SnCl_2$	-	RT	12	Trace
2	Methanol	$SnCl_2$	MW	60	0.3	Trace
3	Methanol	$SnCl_2$	C	80	12	42%
4	Methanol	$SnCl_2$	C	60	12	30%
5	DMF	$SnCl_2$	MW	60	0.3	Trace
6	H_2O	$SnCl_2$	MW	60	0.3	Trace
7	Methanol	$InCl_3$	-	RT	12	Trace
8	Methanol	$InCl_3$	C	80	12	Trace

3.2.3 Optical and photoacoustic properties

The absorbance and emission spectra of **20** and **22** were evaluated in DMF, methanol, and 10% v/v ethanol-water (Table 3.3). The spectra showed ideal absorbance and emission wavelengths for *in vivo* imaging ranging from 760 nm to 774 nm and 786 nm to 820 respectively for **20** and 758 nm to 776 nm and 775 nm to 794 nm for **22**. A hypsochromic shift of compound **22** in both the absorbance and emission spectra was observed in all solvents compared to the parent IR783 dye (**17**) likely due to the electron withdrawing nature of the aldehyde and PIP ligand.[10] When temperatures were changed, there was no real shift in the maxima and there was also no sensitivity to biologically

relevant pH changes. There was a slight shift in the absorbance and emission maxima in various solvents due to the solvent effect where polar aprotic solvents elicit a bathochromic shift.

Table 3.4 Absorbance and emission data for **17**, **20** and **22** in various solvents and temperatures.

	MeOH				**DMF**				**10% EtOH in H_2O**				**10% EtOH in PBS**					
	25 ˚C		37 ˚C		25 ˚C		37 ˚C		25 ˚C		37 ˚C		pH 5.5		pH 6.5		pH 7.4	
	λ_{ex}	λ_{em}	λ_{ex}	λ_{em}	λ_{ex}	λ_{em}	λ_{ex}	λ_{em}	λ_{ex}	λ_{em}	λ_{ex}	λ_{em}	λ_{ex}	λ_{em}	λ_{ex}	λ_{em}	λ_{ex}	λ_{em}
17	780	802	782	802	794	816	792	818	778	800	776	802	778	805	778	803	778	801
20	764	789	760	764	772	820	774	800	762	798	760	786	762	787	762	785	762	787
22	768	791	766	790	776	792	772	794	760	781	758	780	760	781	760	775	760	777

Next, the ability of **22** to bind albumin was evaluated using an established assay.[6] Albumin is the predominant protein in blood and it makes up half of total serum protein. It is known to control levels of Ca^{2+} and Mg^{2+} in the blood as well as transport fatty acids within the body through non-covalent interactions. By binding to albumin (soluble protein), otherwise insoluble fatty acids can be carried to tissues where they can dissociate by plasma membrane transporters. Albumin, which has a half-life of 19 days and is made in liver hepatocytes,[11] has a tertiary structure composed of three domains each with 2 subdomains.

There are two main binding sites (I and II) sites that are relevant to drug development. Site I binds large heterocyclic compounds and dicarboxylic acids (warfarin, and bilirubin) mainly through hydrophobic interactions. Site I (in subdomain IIA) contains a single tryptophan residue (Trp214) which is commonly referred to as the warfarin binding site. Site II interacts with molecules through a combination of hydrophobic, H-bonding, and electrostatic interactions. IR783, binds through electrostatic interactions in site II. Albumin site II binds aromatics with peripherally located charges as well as smaller molecules (indoles and diazepam). The sulfonate groups on the cyanine dye interacts with the cationic and polar residues of the cavity rim forming electrostatic and H-bonds.

To determine the effect binding with albumin had on photophysical properties, increasing concentrations of BSA were mixed with 3 μM sample of **22**, then after heating at 37 ˚C and shaking gently for one hour, the absorbance and emission spectra were obtained (Figure 3.4). The absorbance

data showed that as the dye binds to albumin there is a shift from the aggregate peak (698 nm) to a dimer (716 nm) and monomer peak (778 nm). There was also a hyperchromic change in the molar absorptivity when increasing concentrations of BSA were used. The emission spectra showed suppressed signal without the presence of albumin, which can be attributed to aggregation of the dye causing self-quenching. As the concentration of BSA was increased, disaggregation took place and the signal was restored. To prove a similar effect will be seen in the blood, a 0.1 mM sample of **22** was added to murine blood. Compared to **22** in saline, there was a 5-fold increase in PA signal intensity when in blood (Figure 3.5). There was also a bathochromic shift from disaggregation from the dimer to the monomer species.

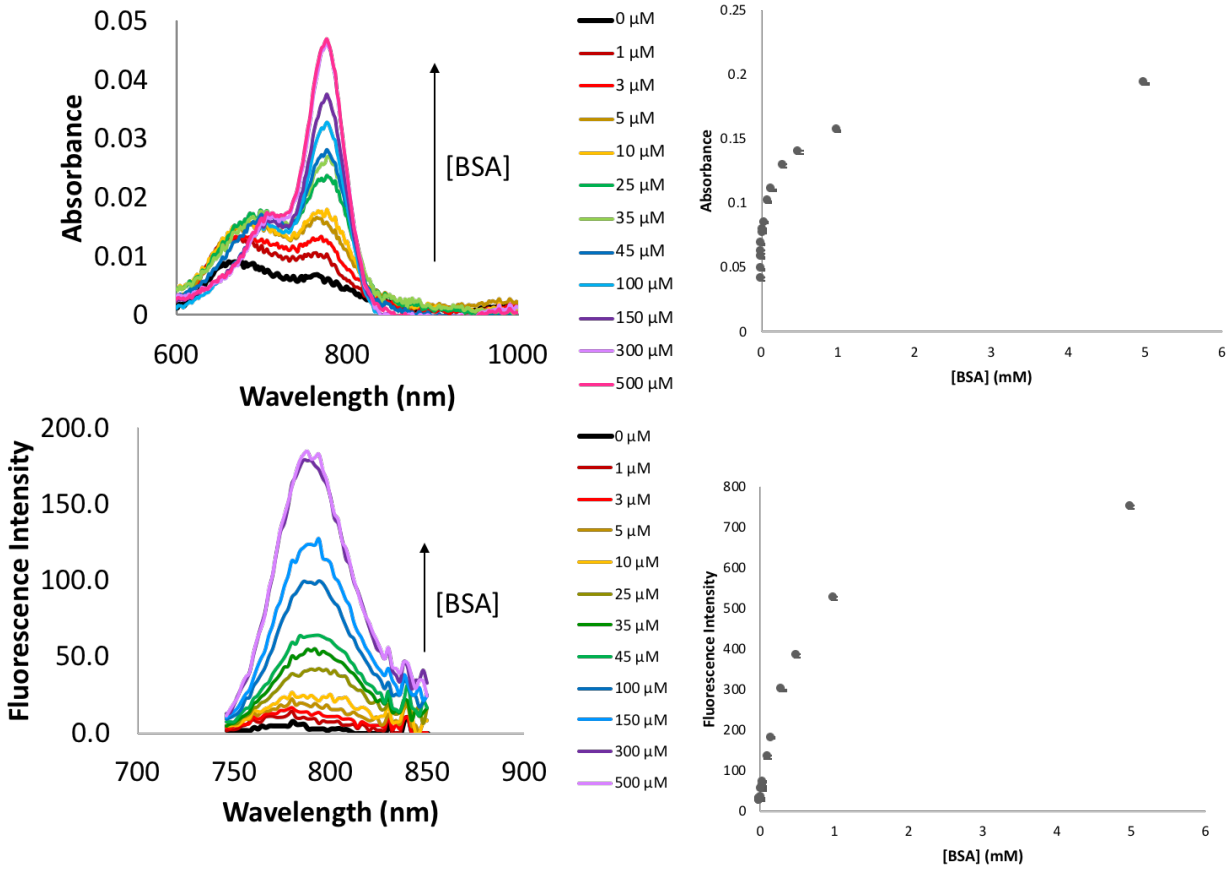

Figure 3.4 Top left: Absorption spectra of a solution of **22** dissolved in 10% ethanol and saline (3 µM) with increasing concentrations of BSA. Top right: Absorbance at 778 nm versus concentration of BSA. Bottom left: Fluorescence emission spectra of **22** (3 µM) with increasing concentrations of BSA (λ_{ex} = 736 nm). Bottom right: Fluorescence emission intensity at 792 nm versus concentration of BSA.

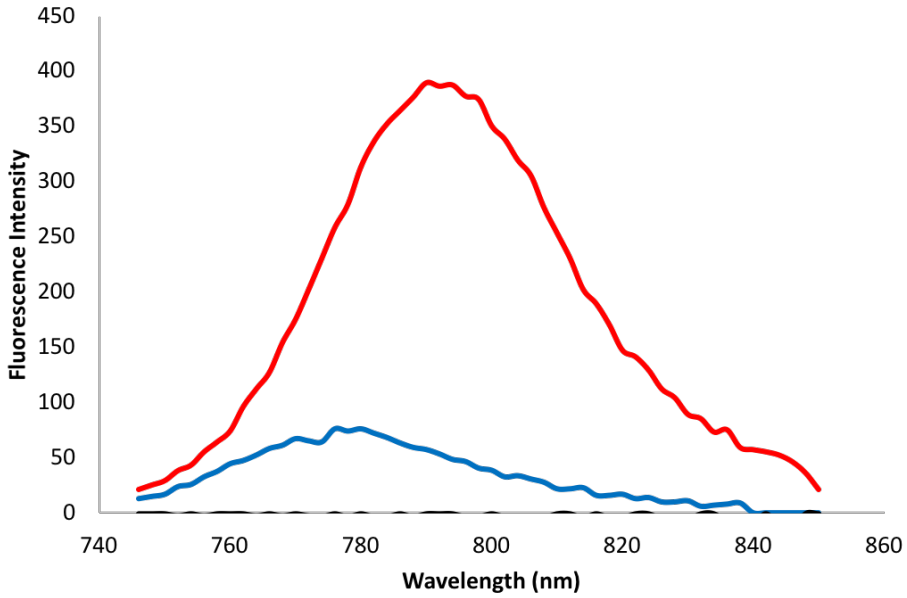

Figure 3.5 Fluorescence emission of 0.1 mM **22** in saline (blue), 0.1 mM **22** in blood (red), and blood alone (black).

Compound **22** was subsequently evaluated in a photoacoustic imaging phantom (Figure 3.6). For photoacoustic imaging, the arising signal from blood, which is mostly from oxy- and deoxyhemoglobin, and **22** need to be separable. To determine if this was possible, samples of **22** in saline and blood were imaged in a phantom and compared to blood alone. Figure 3.7 shows the PA signal arising from **22** in green and signal from blood in red where in Figure 3.7B only signal of the **22** is seen. In Figure 3.7C there is a mix of **22** and blood, and in 3.7D there is only signal from the blood. Interestingly, as the concentration of **22** was increased, there was a concomitant decrease in the PA average threshold likely due to aggregation. Notwithstanding, the ability to selectively detect the PA signal from **22** supported advancing to *in vivo* studies.

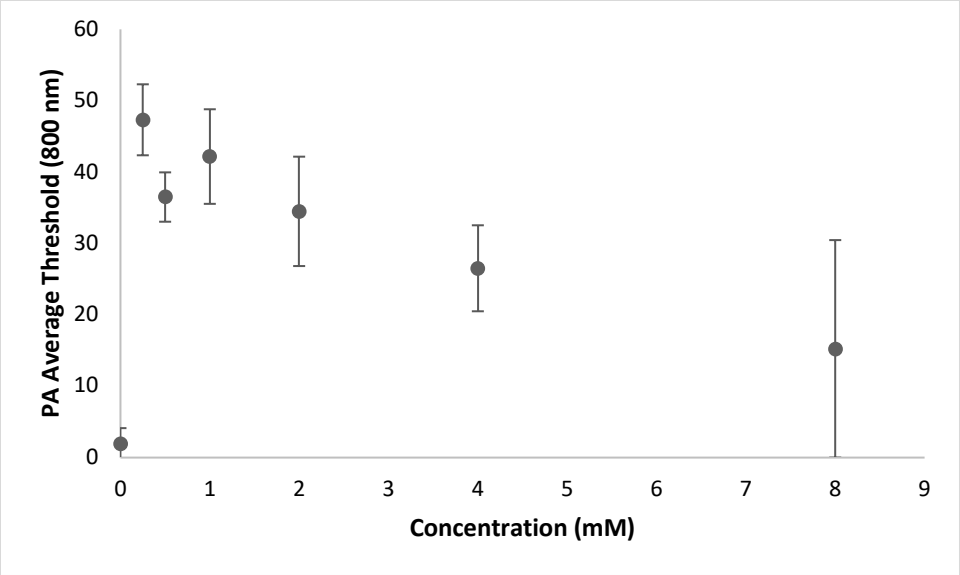

Figure 3.6 Photoacoustic signal intensity at 800 nm versus the concentration of **22** in 10% ethanol and saline.

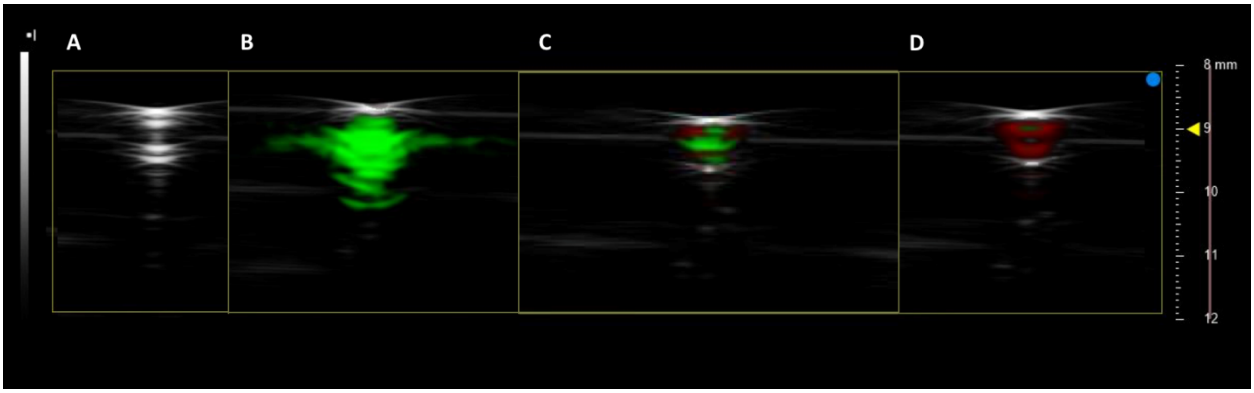

Figure 3.7 PA and US images of A) saline alone B) 0.1 mM **22** in saline C) 0.1 mM **22** in blood D) Blood alone. Red = oxyhemoglobin, Blue = deoxyhemoglobin, Green= **22**.

3.2.4 Metal Sensing

A second potential use of **22** was explored notably the ability of the cyanine dye-PIP complex to act as a metal sensor. Metal sensors are being developed to evaluate trace metal levels in biological as well as ecological samples. Phenanthroline-based ligands have been used as chemosensors for different metal ions including Na^{+}, K^{+}, Al^{3+}, Ni^{2+}, Cu^{2+}, Fe^{2+}, Fe^{3+}, Zn^{2+}, Cd^{2+}, Hg^{2+}, Mn^{2+}, Ag^{+}, Cr^{3+}, Pb^{2+}, Co^{2+}, and Co^{3+}.[12–21] To assess the potential impact of metal coordination on the optical properties of **22**, a series of mono- and divalent metal ions were added to the ligand and changes in

absorbance (significant increase or decrease in signal intensity) or a shift in emission wavelength were noted. The metals used in the study are given in Table 3.4, and include those involved in key biological processes including signaling immune cells (calcium)[22], a cofactor in DNA processing in enzymatic systems (magnesium)[23], an essential biofactor in the central nervous system (zinc)[24], and transportation of oxygen in heme (iron)[25].

Table 3.5 Mono- and divalent metal ions added to **17** and **22** in a 1:1 mole ratio (50 μM)

	Source	**Cation**
1	$NiCl_2$	Ni^{2+}
2	$MnCl_2$	Mn^{2+}
3	$FeCl_2$	Fe^{2+}
4	$CuCl_2$	Cu^{2+}
5	$ZnCl_2$	Zn^{2+}
6	$MgCl_2$	Mg^{2+}
7	NaCl	Na^{+}
8	Cs_2CO_3	Cs^{+}
9	$NaCH_3COO$	Na^{+}
10	$CaSO_4$	Ca^{2+}
11	$CaCO_3$	Ca^{2+}

As a control, the study utilized IR783. In the corresponding absorbance spectra, there was a general decrease in the absorbance intensity for all metal ions. For the emission spectra, there were no major shifts in maxima upon addition of metals as was expected given the absence of a metal binding ligand. The change in the intensity of the absorbance spectrum is likely due to nonspecific binding.

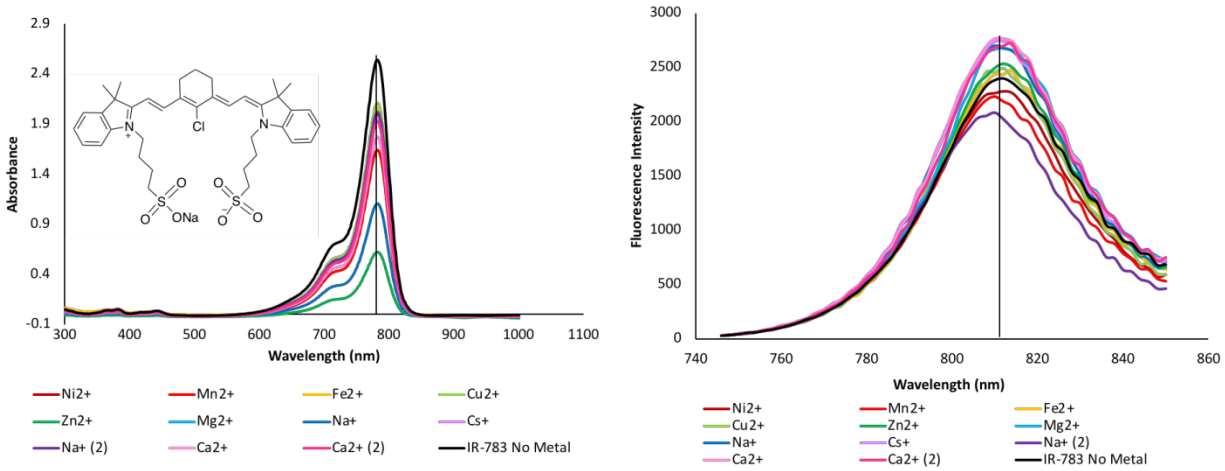

Figure 3.8 Metal binding with **17** in a 1:1 mole ratio (50 μM in methanol or water/methanol mixture). Left: Absorbance spectra of **17** with various metal ions. Right: Fluorescence emission of **17** with various metal ions. The black line indicates the location of the maxima of **17** alone.

With the presence of a metal binding chelate provided by the phenanthroline, there is the potential to have a shift in the emission wavelength upon formation of a metal complex (Figure 3.9). Again, in the absorbance spectra there was a decrease in signal intensity for all metals. For the emission spectra there was no quenching effects seen, rather there was an increase in fluorescence intensity and a hypsochromic shift. Unfortunately, the shift is present for all metals with no significant discernable difference indicating this dye could not work as a selective metal sensor. The blue shift likely indicates metal binding as it was not seen with the dye alone. Although there is an increase (2×), the change in intensity is not significant enough for **22** to act as a biological sensor.

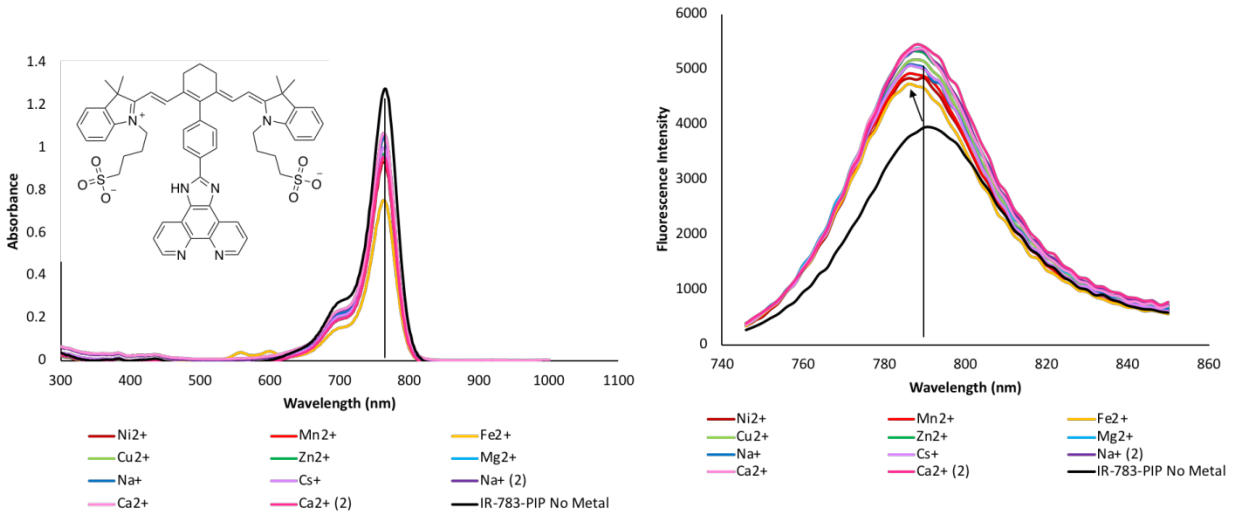

Figure 3.9 Optical data associated with metal binding studies with **22** in a 1:1 ratio mole ratio (50 μM, in methanol or water/methanol mixture). Left: Absorbance spectra of **22** with various metal ions. Right: Fluorescence emission of **22** with various metal ions. The vertical black lines indicate the location of the absorbance and emission maxima of **22**. The black arrow highlights the extent of the shift of the emission maxima.

3.2.5 Radiolabelling compound 22

While compound **22** was not an effective metal sensor, the attractive PA properties warranted developing a means of producing the ^{99m}Tc labelled analogue to study the distribution of the dye-ligand conjugate *in vivo*. A 2-step labelling procedure was developed where **22** was added to $[^{99m}Tc(CO)_3(OH_2)_3]^+$ and heated in a microwave at 80 °C for 30 minutes (Scheme 3.4). Several other reaction temperatures and times were attempted which failed to convert a significant amount (<6%) of $[^{99m}Tc(CO)_3(OH_2)_3]^+$ to **23**. The complex **23** was isolated by HPLC (Figure 3.10) in 41% yield. Following the isolation of **23**, NMI as a model monodentate ligand, was added to **23** and the mixture heated in a microwave at 60 °C for 30 minutes and the product **24** isolated by HPLC in 41% yield (Scheme 3.4/Figure 3.11). The yield was lower than that observed with simpler PIP ligands and may be due to steric hinderance introduced by the dye or more likely the electron withdrawing nature of cyanine group.

Next, the synthesis of an analogue of **24** was prepared which could be linked to targeting molecules. The approach taken involved bioorthogonal chemistry which are a class if reactions that can occur selectively in living systems without affecting native biological processes.[26] These reactions are highly selective, proceed under physiological conditions, and can be used to study, target, and manipulate biological systems. Several prominent examples include the Staudinger ligations, strain-promoted azide-alkyne cycloadditions (SPAAC) and the inverse-electron demand Diels-Alder cycloaddition (IEDDA).[27] The Staudinger ligation is between an azide and a phosphine or phosphite to produce an iminophosphorane. Although the reaction is selective and irreversible, it has poor kinetics ($k < 1\ M^{-1}s^{-1}$) which limit the *in vivo* applications.[28] Typical azide-alkyne cycloadditions require high temperatures or the presence of a Cu(I) catalyst to proceed. However, if ring strain is introduced (18 kcal/mol) to the alkyne component, the reaction can occur at room temperature without the need for a catalyst.[29]

IEDDA relies on the reactivity of electron withdrawing dienes with dienophiles in protic solvents. One example is the reaction between tetrazine (Tz) and *trans*-cyclooctene (TCO). IEDDA reactions involving Tz and TCO are rapid ($k_2 = 10^6\ M^{-1}s^{-1}$) and catalyst free. These reactions are selective, modular, orthogonal, and rapid and allow for coupling at very low concentrations. The insensitivity of the Tz-TCO reaction to nucleophiles present in biological systems (amino, thiol, and hydroxide), and its compatibility in aqueous media and catalyst free conditions make this reaction suitable for *in vivo* use.[30] IEDDA chemistry has been used to great success with radiolabelled tetrazines derived from ^{18}F[31–34], ^{111}In[33,35], ^{64}Cu[33,35,36], ^{177}Lu[37], ^{99m}Tc[7,37–39] and a range of different TCO-derived targeting vectors. This work showed that through the IEDDA reaction, the TCO-derived targeting vector can be injected first, allowed to accumulate at the target of interest and clear from non-target tissues, whereupon administration of the radiolabelled tetrazine the compounds react selectively *in*

vivo. This approach, called pre-targeting, is usually employed with targets with long circulation time, such as antibodies, which require time to clear before adequate contrast is achieved.

To create a tetrazine derivative of **22**, a new N-substituted imidazole-tetrazine (ImTz, **25**) monodentate ligand was needed (Scheme 3.4). The ImTz ligand was prepared following a literature procedure.[7] The conditions used previously to prepare **24** were then used to generate **26** (Figure 3.12/Scheme 3.4) which was isolated by HPLC in 32% yield. Unfortunately, this complex was not stable and showed signs of degradation. This may be due to loss of the monodentate ligand or reaction between the tetrazine and the technetium complex.

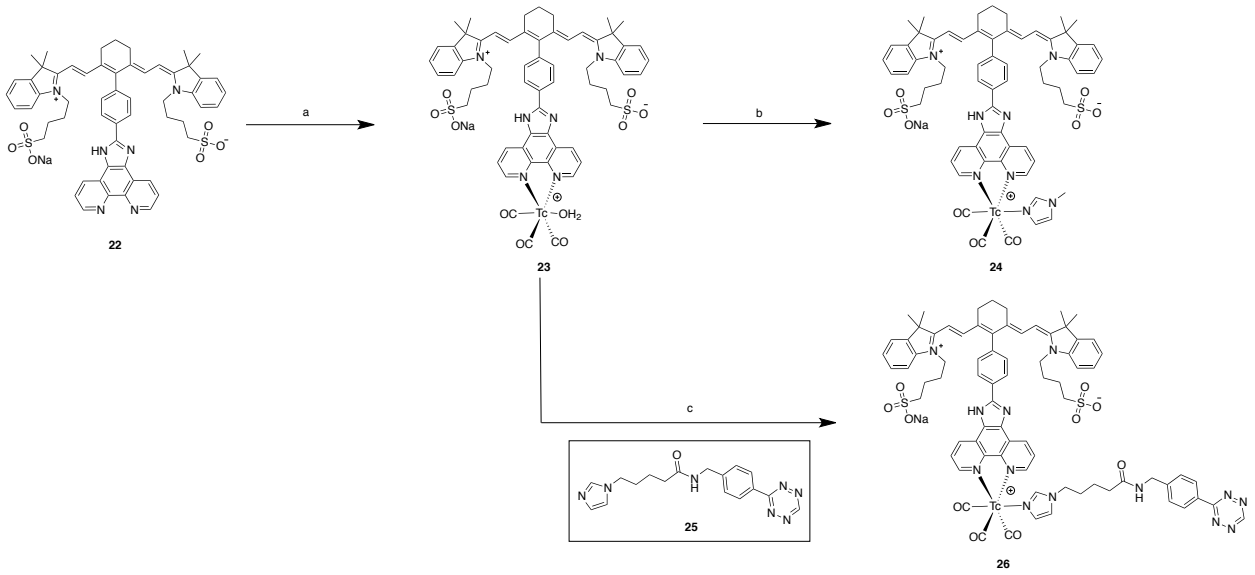

Scheme 3.4 Radiolabelling of **22** with ^{99m}Tc(I). Reagents and conditions: a) $[^{99m}Tc(CO)_3(OH_2)_3]^+$, 80 °C, 30 min, RCY = 41%; b) NMI, 60 °C, 30 min, RCY = 41% c) Im-Tz **25**, 60 °C, 30 min, RCY = 32%.

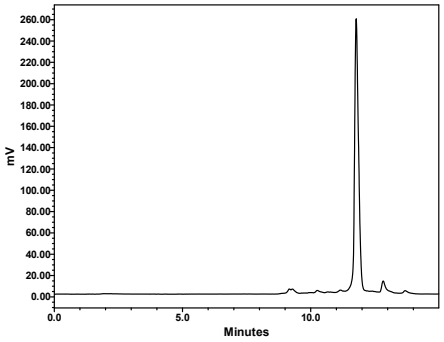

Figure 3.10 Gamma HPLC trace of **23** (HPLC method B).

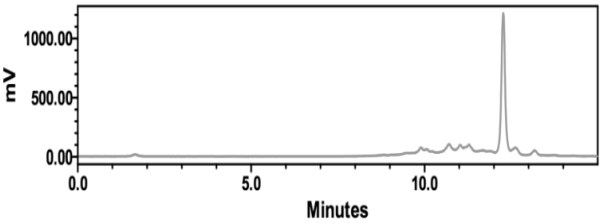

Figure 3.11 Gamma HPLC trace of **24** (HPLC method B).

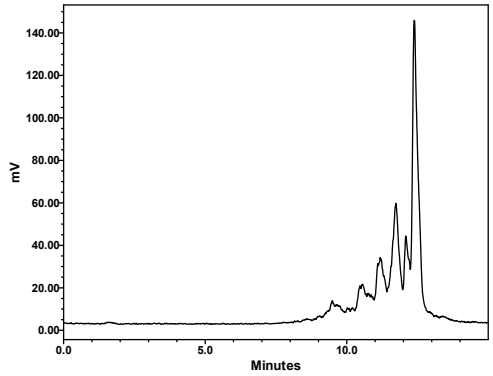

Figure 3.12 Gamma HPLC trace of **26** (HPLC method B).

3.3 Summary and Conclusions

A new cyanine dye derivative that can be labelled with ^{99m}Tc was developed. Specifically a PIP ligand capable of binding the $[Tc(CO)_3]^+$ core was linked to a new IR783 derivative creating a platform for generating bimodal SPECT/PA probes. The PIP derivative was shown to have attractive PA imaging properties that should translate *in vivo* and it was labelled in high yield with ^{99m}Tc. It was possible to add a simple monodentate ligand (NMI) however when a bifunctional ligand containing a

tetrazine was added a mixture of products formed. The positive impact on imaging and pharmacokinetics created by adding the IR783 and with access to the IR783 aldehyde **20**, the subsequent strategy involved focusing on creating a simpler tetrazine derivative that can be used to create targeted PA agents and multi-probes through IEEDA chemistry with the appropriate TCO derivative.

3.4 Experimental

Supplementary figures can be found in **APPENDIX II**.

General considerations. All reagents and solvents were ACS grade and were purchase from commercial suppliers and used without further purification. (4-(1,2,4,5-Tetrazin-3-yl)phenyl)methanamine hydrochloride, and *(E)*-4-cycloocten-1-yl 2,5-dioxo-1-pyrrolidinyl ester carbonic acid were purchased from Conju-probe. Methanol was purchased from Caledon. Distilled water was used for all experiments. Deuterated solvents for NMR samples were purchased from Cambridge Isotope Laboratories. Bovine serum albumin was purchased from Sigma. ^{99m}Tc was obtained as [^{99m}Tc]TcO_4^- from a ^{99}Mo/^{99m}Tc generator (Lantheus Medical Imaging) in saline (0.9 % NaCl). *Caution: ^{99m}Tc is a γ-emitter (E_γ = 140 keV, $t_{1/2}$ = 6 h) and should only be used in a licensed and appropriately shielded facility*. All other reagents were purchased from Sigma Aldrich.

^{1}H and ^{13}C NMR spectra were recorded on a Bruker Avance AV-600 instrument at 300 K. High Resolution Mass Spectra (HRMS) were collected on a Waters/Micromass Q-Tof Global Ultima spectrometer. Microwave reactions were performed using a Biotage Initiator 60 instrument. Solvents were evaporated using either a Bioatage V10 system or under reduced pressure with a rotary evaporator. Compounds were dried using a VirTis Benchtop lyophilizer equipped with an Edwards RV5 pump.

High Performance Liquid Chromatography (HPLC) was performed using a Waters XBridge analytical column (5 μm, 4.6 × 100 mm) or Phenomenex Polar-RP column (4μm, 250 × 10 mm) with a Waters 1525 system connected to a Bioscan *γ* detector and a 2998 photodiode array detector monitoring at 254 nm operated using the Empower software package. Flow rates were 1 mL/min (analytical) using the following method: Method A: Solvent A: H_2O + 0.1% TFA; Solvent B:

Acetonitrile + 0.1% TFA. Gradient: 10% B (0 min.), 70% B (0-14 min.), 70% B (14-15 min.), 100% B (15-17 min), 10% B (17-18 min), 10% B (18-23 min). Method B: Solvent A: H_2O + 0.1% TFA; Solvent B: Acetonitrile + 0.1% TFA. Gradient: 10% B (0 min.), 70% B (0-14 min.), 70% B (14-15 min.). Flow rates were 4 mL/min using the following method: Method C: (Solvent A: H_2O + 0.1% TFA, Solvent B: Acetonitrile + 0.1% TFA) 0-1 min 90% B, 1-20 min 10% B, 20-21 min 10-90% B).

Synthetic Procedures

Synthesis of IR780-benzaldehyde (19). In a round bottom flask IR-780 iodide (16) (50 mg, 0.09 mmol), $Pd(PPh_3)_4$ (427 mg, 0.37 mmol), DIPEA (0.27 mL, 1.57 mmol), and 4-formylphenylboronic acid (111 mg, 0.74 mmol) were dissolved in THF/H_2O (3:1) and heated to 80 °C for 12 h. The product was purified by HPLC (Method C) yielding a green solid. Yield: (9 mg, 16%) Crude ^{1}H NMR (Methanol-d_4, 600 MHz): δ (ppm) 9.99 (s, 2H); 8.45 (d, 2H); 7.87 (d, 5H); 7.80 (m, 2H); 7.53 (d, 2H); 7.43 (m, 2H); 7.34 (d, 2H); 7.29 (m, 2H); 6.29 (d, 2H); 4.16 (t, 4H); 2.73 (t, 4H); 1.96 (m, 2H); 1.89 (m, 4H); 1.74 (s, 12H); 1.06 (t, 6H). HRMS (ES^-) m/z calculated for $C_{43}H_{49}N_2O$: 609.3845 [M-H$^-$], found 609.3828.

Synthesis of IR783-benzaldehyde (20). Described and characterized in Chapter 4.

Synthesis of IR-783-PIP (22). In a round bottom flask IR-783-BA (20) (50 mg, 0.06 mmol), 1,10-phenanthroline (21) (11 mg, 0.06 mmol), NH_4OAc (24 mg, 0.31 mmol), and $SnCl_2$ (2 mg, 0.01 mmol) were dissolved in methanol and heated to 80 °C for 24 h. The product was purified by HPLC (Method C) yielding a green solid. Yield: (26 mg, 42%) Crude ^{1}H NMR (Methanol-d_4, 600 MHz): δ (ppm) 9.13 (m, 2H); 9.07 (m, 2H); 7.92 (m, 2H); 7.56 (m, 2H); 7.28 (m, 9H); 7.08 (m, 2H); 6.28 (m, 2H); 4.12 (s, 4H); 2.87 (m, 4H); 2.79 (m, 4H); 2.10(s, 2H); 1.93 (m, 8H); 1.23 (m, 12H). Crude ^{13}C NMR (DMSO-d_6, 150 MHz): δ (ppm) 173.41, 149.20, 143.64, 142.15, 133.01, 132.12, 131.92, 129.75, 128.71, 127.97,

125.96, 125.44, 123.33, 111.92, 101.39, 51.86, 49.87, 44.79, 28.07, 27.25, 25.74, 23.62, 22.56. HRMS (ES^-) m/z calculated for $C_{57}H_{57}N_6O_6S_2$: 985.3775 [$M-H^-$], found 985.3786.

Radiochemistry

Synthesis of $[^{99m}Tc(CO)_3(OH_2)]^+$ Sodium boranocarbonate (10.0 mg, 0.07 nmol), sodium carbonate (15.0 mg, 14.0 mmol), sodium borate (20 mg, 0.05 mmol) and sodium potassium tartrate (22 mg, 0.08 mmol) were placed in a microwave vial and purged with argon for 10 min. To this mixture, $Na[^{99m}TcO_4]$ (1 mL, 1.85 GBq) was added and the vial was heated in a microwave at 110 °C for 3.5 min to form $[^{99m}Tc(CO)_3(H_2O)_3]^+$. After cooling to room temperature, the pH was adjusted to 3 with 0.1 M HCl (0.2 mL).

Synthesis of $[^{99m}Tc(CO)_3$(9)NMI$]^+$ (13) $[^{99m}Tc(CO)_3(OH_2)]^+$ was added to a solution of **9** (6 mg, 0.01 mmol) dissolved in 0.2 mL DMSO under argon. The solution was heated in a microwave at 50 °C for 1 h where the formation of **12** was detected by analytical HPLC (Method A). **12**: R_t = 11.9 min, RCY = 77%. The N-methylimidazole (NMI) derivative **13** were prepared by adding NMI (50 μL, 0.75 mmol) to the solution containing **12** under argon where the mixture was heated in a microwave at 50 °C for 30 min. The formation of product **13** was seen by analytical HPLC (Method A). **13**: R_t = 12.5 min, RCY = 89%.

Synthesis of $[^{99m}Tc(CO)_3$(22)NMI$]^+$ (24) and $[^{99m}Tc(CO)_3$(22)Im-Tz$]^+$ (25) $[^{99m}Tc(CO)_3(OH_2)]^+$ was added to a solution of **22** (1 mg, 0.001 mmol) dissolved in 0.2 mL ethanol under argon. The solution was heated in a microwave at 80 °C for 30 min where the formation of **23** was detected by analytical HPLC (Method B). **23**: R_t = 11.8 min, RCY = 50%. The N-methylimidazole (NMI) derivative **24** or imidazole-tetrazine (Im-Tz) derivative **25** were prepared by adding NMI (50 μL, 0.75 mmol) or Im-Tz (1 mg, 0.003 mmol) dissolved in 0.2 mL ethanol to the solution containing **23** under argon where the mixture was heated in a microwave at 60 °C for 30 min. The formation of

products **24** and **25** were seen by analytical HPLC (Method B). **24**: R_t = 12.3 min, RCY = 41%; **25**: R_t = 11.3 min, RCY = 40%.

3.5 References

[1] T. Peters, *All About Albumin*, **1995**.

[2] J. C. Rasmussen, I. C. Tan, M. V. Marshall, C. E. Fife, E. M. Sevick-Muraca, *Curr. Opin. Biotechnol.* **2009**, *20*, 74–82.

[3] I. Gregersen, A. Rawson, *Am. J. Physiol* **1942**, *138*, 698–707.

[4] C. A. Davies-venn, B. Angermiller, N. Wilganowski, P. Ghosh, B. R. Harvey, G. Wu, S. Kwon, M. B. Aldrich, E. M. Sevick-muraca, *Mol. Imaging Biol.* **2012**, *14*, 301–314.

[5] G. R. Cherrick, S. W. Stein, C. M. Leevy, C. S. Davidson, *J Clin Invest* **1959**, *39*, 592–600.

[6] A. D. Watson, Binding Studies of Near Infrared Cyanine Dyes with Human Serum Albumin and Poly-L-Lysine Using Optical Spectroscopy Methods By, **2008**.

[7] A. Yazdani, N. Janzen, S. Czorny, R. Ungars, T. Miladinovic, G. Singh, J. F. Valliant, *Dalt. Trans* **2017**, DOI 10.1039/C7DT01497J.

[8] S. Al-Karmi, S. A. Albu, A. Vito, N. Janzen, S. Czorny, L. Banevicius, M. Nanao, J. Zubieta, A. Capretta, J. F. Valliant, *Chem. - A Eur. J.* **2016**, *13244*, 1–6.

[9] E. A. Rodriguez, Y. Wang, J. L. Crisp, D. R. Vera, R. Y. Tsien, *Bioconj Chem* **2016**, *27*, 1390–1399.

[10] N. S. James, Y. Chen, P. Joshi, T. Y. Ohulchanskyy, M. Ethirajan, M. Henary, L. Strekowski, R. K. Pandey, *Theranostics* **2013**, *3*, 692–702.

[11] T. Peters, in *Adv. Protein Chem.*, **1985**, pp. 161–245.

[12] S. Li, C. Zhang, S. Huang, F. Hu, J. Yin, S. H. Lui, *RSC Adv.* **2012**, *2*, 4215–4219.

[13] N. Kaur, P. Alreja, *Tetrahedron Lett.* **2015**, *56*, 182–186.

[14] F. Wang, C. Wang, Z. Yu, K. Xu, X. Li, Y. Fu, *Polyhedron* **2016**, *105*, 49–55.

[15] X. Liu, X. Zhou, X. Shu, J. Zhu, **2009**, 7634–7637.

[16] M. C. Aragoni, M. Arca, F. Demartin, F. A. Devillanova, F. Isaia, A. Garau, V. Lippolis, F. Jalali, U. Papke, M. Shamsipur, et al., **2002**, *41*, 6623–6632.

[17] S. Sangeetha, G. Sathyaraj, D. Muthamilselvan, V. G. Vaidyanathan, B. U. Nair, *Dalt. Trans.* **2012**, *41*, 5769–5773.

[18] M. Hardouin-lerouge, B. Chesneau, M. Allain, **2012**.

[19] G. M. Cockrell, G. Zhang, D. G. Vanderveer, R. P. Thummel, R. D. Hancock, **2008**, 1420–1430.

[20] M. Alfonso, T. Alberto, **2011**, 939–947.

[21] T. Korzeniak, C. Mathonière, A. Kaiba, P. Guionneau, M. Koziel, B. Sieklucka, *Inorganica Chim. Acta* **2008**, *361*, 3500–3504.

[22] J.-P. Kinet, M. Vig, *Nat. Immunol.* **2009**, *10*, 21–7.

[23] A. Hartwig, *Mutat. Res.* **2001**, *475*, 113–121.

[24] S. D. Gower-Winter, C. W. Levenson, *Biofactors* **2013**, *38*, 186–193.

[25] P. Ponka, *Am. J. Med. Sci.* **1999**, *318*, 241.

[26] H. C. Hang, C. Yu, D. L. Kato, C. R. Bertozzi, *PNAS* **2003**, *100*, 14846–14851.

[27] D. M. Patterson, L. A. Nazarova, J. A. Prescher, *ACS Chem. Biol.* **2014**, *9*, 592–605.

[28] H. C. Kolb, M. G. Finn, K. B. Sharpless, *Angew. Chemie - Int. Ed.* **2001**, *40*, 2004–2021.

[29] N. J. Agard, J. A. Prescher, C. R. Bertozzi, *JACS* **2004**, *126*, 15046–15047.

[30] N. K. Devaraj, R. Weissleder, *Acc Chem Res.* **2011**, *44*, 816–827.

[31] J. Zhu, S. Li, C. Wängler, B. Wängler, R. Bruce Lennox, R. Schirrmacher, *Chem. Commun.* **2015**, *51*, 12415–12418.

[32] C. Denk, D. Svatunek, T. Filip, T. Wanek, D. Lumpi, J. Fröhlich, C. Kuntner, H. Mikula, *Angew. Chem. Int. Ed. Engl.* **2014**, 1–6.

[33] T. Reiner, B. M. Zeglis, *J. Label. Compd. Radiopharm.* **2013**, DOI 10.1002/jlcr.3149.

[34] M. Pretze, D. Pietzsch, C. Mamat, *Molecules* **2013**, *18*, 8618–8665.

[35] R. Rossin, M. S. Robillard, *Curr. Opin. Chem. Biol.* **2014**, *21*, 161–169.

[36] B. . Zeglis, K. K. Sevak, T. Reiner, P. Mohindra, S. D. Carlin, P. Zanzonico, R. Weissleder, J. S. Lewis, *J. Nucl. Med.* **2013**, *54*, 1389–1396.

[37] A. Yazdani, H. Bilton, A. Vito, A. R. Genady, S. M. Rathmann, Z. Ahmad, N. Janzen, S. Czorny, B. M. Zeglis, L. C. Francesconi, et al., *J. Med. Chem.* **2016**, *59*, 9381–9389.

[38] J. Le, A. Zlitni, H. A. Bilton, M. Yin, A. Farhadi, N. R. Janzen, M. G. Shapiro, J. F. Valliant, F. S. Foster, *Mol. imaging Biol.* **2017**, *20*, 230–239.

[39] H. A. Bilton, Z. Ahmad, N. Janzen, S. Czorny, J. F. Valliant, **2017**, e55188.

Chapter 4: An Albumin-Binding Tetrazine-Derived Near-Infrared Dye as a Facile Reagent for Developing Targeted Photoacoustic Imaging Agents

S.R. Slikboer, Z. Naperstkow, N. Janzen, A. Faraday, Y. Soenjaya, J. Le Floc'h, S. Al-Karmi, C.E.M Demore, F.S Foster, J.F. Valliant.

4.1 Description of Contributions

The following chapter is written in the form of a manuscript that will shortly be submitted. S.R. Slikboer was responsible for the development and execution of the majority of the work described in this paper including drafting the initial manuscript and experimental. Z. Naperstkow aided in the preliminary synthetic work. Tumour inoculation was performed by N. Janzen and A. Faraday. Y. Soenjaya and J. Le Floc'h aided in preliminary photoacoustic imaging. Dr. Demore, Dr. Foster, and Dr. Valliant were the primary investigators and led the research efforts.

4.2 Abstract

A new photoacoustic dye was developed as a simple to use reagent for creating targeted optoacoustic imaging agents. The lead molecule was prepared via an efficient two step synthesis from an inexpensive commercially available starting material. The resulting tetrazine-derived dye was engineered to non-covalently bind albumin which fosters tumour localization and gives the dye an optimal biological half-life and distribution profile. The presence of the tetrazine in turn makes it possible to link the albumin binding optoacoustic signaling agent to a wide range of targeting molecules. To demonstrate the utility and ease of use of the platform, a novel photoacoustic probe for imaging calcium accretion was generated using a single step bioorthogonal coupling reaction where high-resolution photoacoustic images of the knee joint in mice were obtained as early as one hour post-injection. Whole-body distribution was determined subsequently by labelling with ^{99m}Tc and

performing tissue counting following necropsy. These studies, along with tumour imaging and *in vitro* binding studies, revealed that the core photoacoustic contrast agent has attractive biological and imaging properties to go along with the straightforward way it can be linked to targeting molecules.

4.3 Introduction

Photoacoustic imaging is an emerging modality that assuages the limited depth of penetration associated with traditional optical methods. The technique involves the generation of acoustic waves following irradiation of suitable contrast agents with rapid laser pulses. These pulses cause endogenous tissue chromophores or exogeneous contrast agents to rapidly expand and contract, producing acoustic waves at megahertz frequencies.[1] Photoacoustic imaging can penetrate several centimeters while having ~100 μm resolution, and is used preclinically to evaluate tumour models and test new therapies,[2,3] and clinically as an experimental alternative to methods that utilize ionizing radiation for imaging breast, and head and neck cancers.[4]

There have been extensive efforts to develop photoacoustic imaging agents derived from nanomaterials and low molecular weight dyes.[4–8] One active area of research is to create contrast agents that are capable of targeting specific cancer biomarkers.[9–11] To this end, low molecular weight photoacoustic imaging dyes have been linked to cancer cell-seeking small molecules and antibodies to concentrate the contrast agent selectively within tumours.[10,12,13] Work to date has largely been accomplished using indocyanine green (ICG) and conventional ligation chemistry. There is a limited toolbox of general-purpose strategies available for creating targeted photoacoustic imaging probes that can be employed by the broader scientific community who may not have access to synthetic chemistry experts. Herein, we describe the development of a convenient reagent for the preparation of targeted photoacoustic probes based on a tetrazine functionalized cyanine dye. The new dye creates the opportunity to employ the selectivity and versatility of inverse electron demand Diels-Alder

(IEEDA) chemistry between tetrazines and *trans*-cyclooctenes (TCO) to create novel photoacoustic contrast agents. This approach leverages the fact that methods to create TCO-derived targeting molecules from small molecules and antibody conjugates, are well established and straight-forward.[14–19]

4.4 Results and Discussion

The preparation of functionalized cyanine dyes is non-trivial and often low yielding. Consequently, to ensure general utility and accessibility, an efficient synthetic route to the target tetrazine was sought (Scheme 4.1). To this end, compound **28** was prepared from the commercially available dye IR-783, which is known to produce a strong photoacoustic signal and bind albumin. The latter is attractive because it can be used to promote tumour localization and prolong the circulation of any dye conjugates while retaining kidney localization and rapid excretion where the first step involves the preparation of the IR783-aldehyde **20** which was done successfully using a Suzuki-Miyaura coupling between **17** and **18** in the presence of $Pd(PPh_3)_4$ and Cs_2CO_3. A significant number of different catalysts, bases and reaction conditions were screened to maximize the yield of **20** (96%). The aldehyde was subsequently coupled to tetrazine **27**, prepared using a literature procedure,[20] to form the hydrazone **28**. Following characterization by NMR, HRMS and HPLC, the stability of **28** in plasma was evaluated. The dye-tetrazine conjugate showed no signs of degradation out to 24 h in murine plasma at 37 °C (Figure S4.7, Supporting Information) and the tetrazine remained reactive towards TCO-derivatives during that time.

Photoacoustic properties of **28** in saline were assessed initially in a Vevo Phantom imaging chamber (Fujifilm VisualSonics Inc., Toronto) scanning over a wavelength range of 680-970 nm. The photoacoustic spectrum and absorbance spectrum of **28** were nearly identical (Figure S4.13, Supporting Information) where the optimal wavelength for imaging was 775 nm, which should be distinguishable from the photoacoustic signals arising from oxygenated and deoxygenated hemoglobin

(684, 750 and 870 nm). To test this, the photoacoustic spectra of **28** and a TCO-conjugate **30** (*vide infra*) in saline (0.1 mM), and blood (0.1 mM) were compared to that for whole blood alone (Figure 4.1A). It was evident that the dyes were readily detected in both saline and blood (shown in green) and not in the control sample of blood alone (Figure 4.1B). Interestingly, the intensity of the image in blood was greater than in saline, which is consistent with binding to albumin. The photoacoustic signal was measured in triplicate over a range of concentrations which showed increasing intensity with increasing amounts of **28** (Figure S4.13, Supporting Information). This was evident visually when cotton swabs were dipped in increasing concentrations of **30** and then imaged on the photoacoustic imaging scanner (Figure 4.1C).[21]

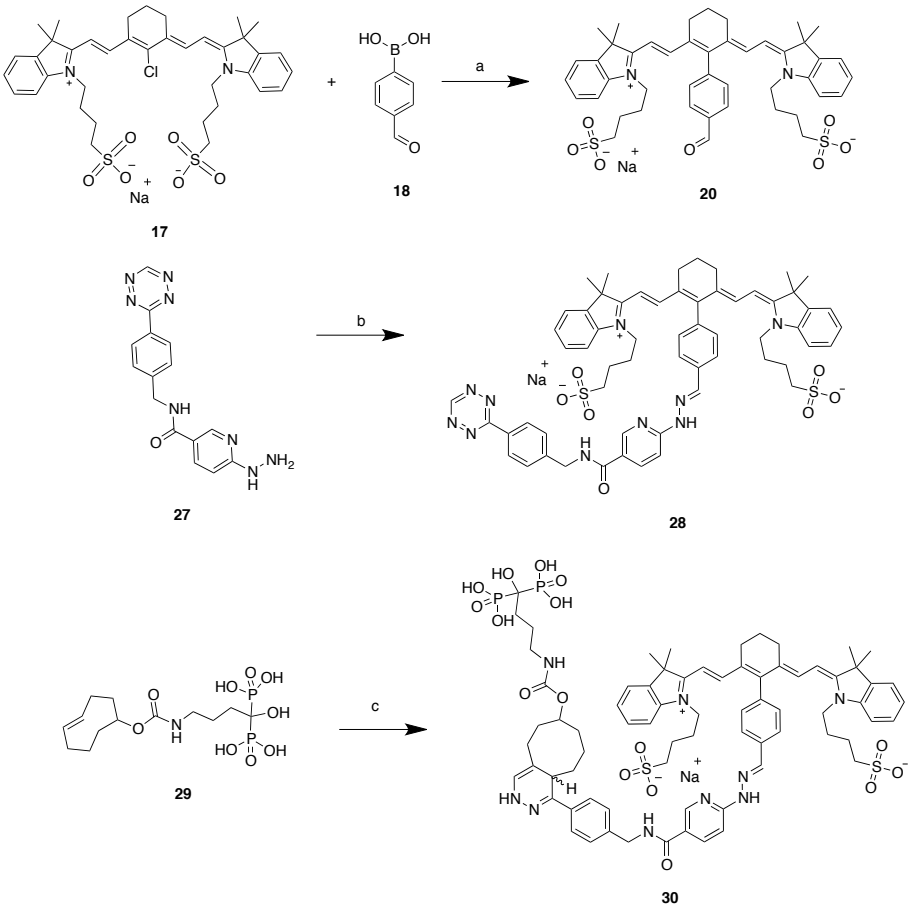

Scheme 4.1 Synthesis of the tetrazine derived cyanine dye **28** and bisphosphonate derivative **30**. Reagents and conditions: a) $Pd(PPh_3)_4$, Cs_2CO_3(aq), 4 h, 100 °C, 96%; b) **20**, aniline, EtOH, N_2, 12 h, RT, 35%; c) **28**, 10% EtOH/saline, RT, 10 min, 35%.

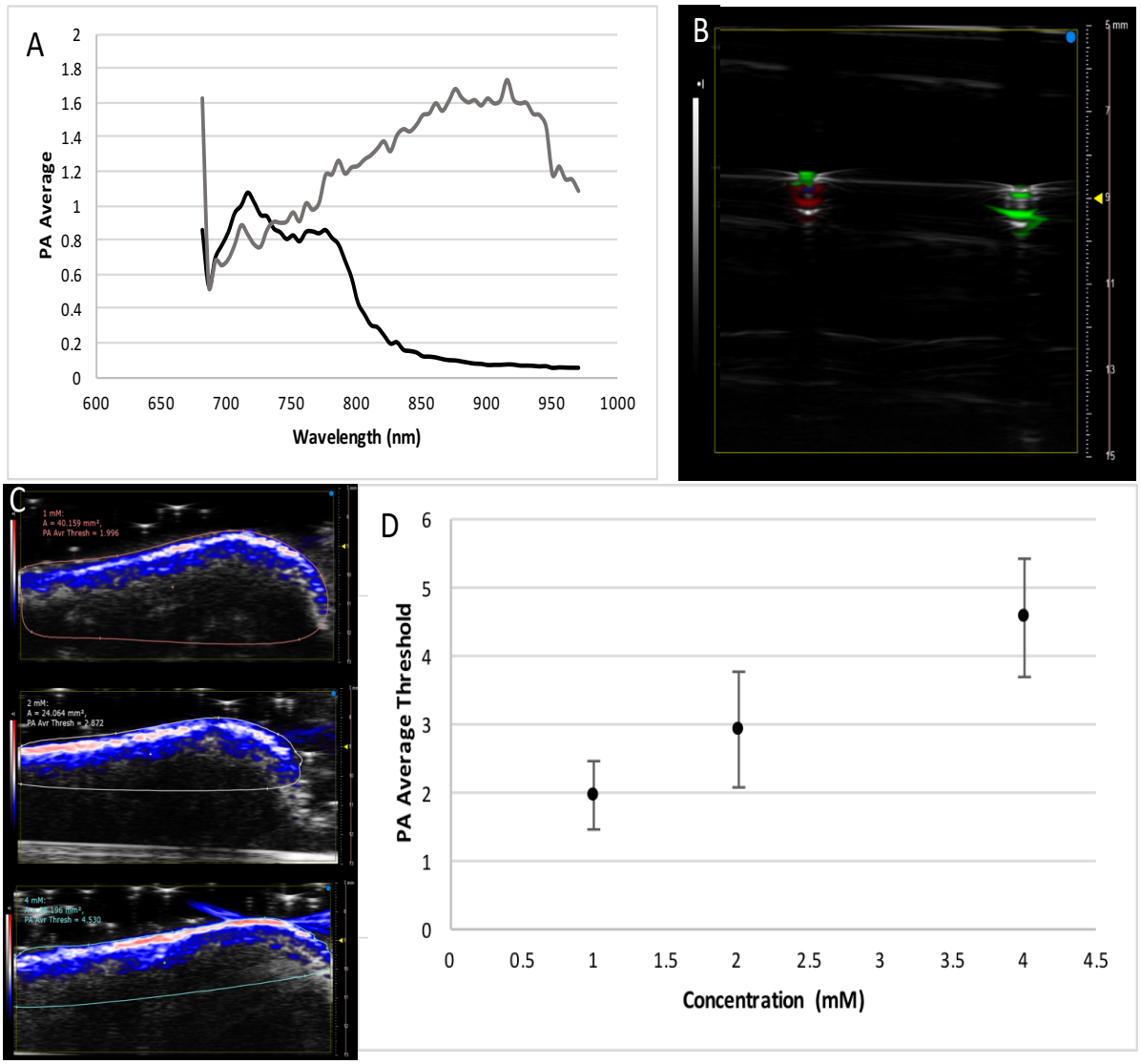

Figure 4.1 A) Photoacoustic spectra of 0.1 mM **30** in saline (black) and blood (grey). B) B-Mode and photoacoustic images of 0.1 mM **30** in blood (left), and saline (right). C) Photoacoustic image of cotton swabs dipped in increasing concentrations of **30** (1 mM (top), 2 mM (middle), and 4 mM (bottom)) (red is the most intense signal, blue is the least intense signal). D) A plot of the average photoacoustic signal at 714 nm vs concentration for the cotton swabs imaged in C.

Prior to developing and testing a targeted derivative, *in vivo* imaging studies were performed with **28** and 143B human osteosarcoma xenografts; leveraging reports that have shown albumin binding ligands including certain cyanine dyes localize to tumours via macromolecule formation when

bound with albumin being taken up by the enhanced permeability and retention (EPR) effect.[22–28] Compound **28** was soluble in 10% ethanol in saline and formulated at a concentration of 5 mg mL^{-1}, which conveniently is higher than what can be achieved for ICG (1 mg mL^{-1}). Prior to injection, tumours were imaged in order to separate the signals arising from oxygenated and deoxygenated hemoglobin, and **28**, which are shown in red, blue and green respectively in Figure 4.2. Following administration of 200 μL of **28** (1 mg), signal arising from **28** was clearly visible in the tumour as early as 1 hour post-injection (Figure 4.2B). Mice were sacrificed and the tumours were imaged *ex vivo* (Figure 4.2C) where uptake of the dye within the tumour was clearly evident. Analysis of the signal intensity from the *in vivo* images showed a 2.3× increase in signal intensity in the tumour at 1 hour post injection versus the background signal in the tumour before the injection (Figure 4.2D).

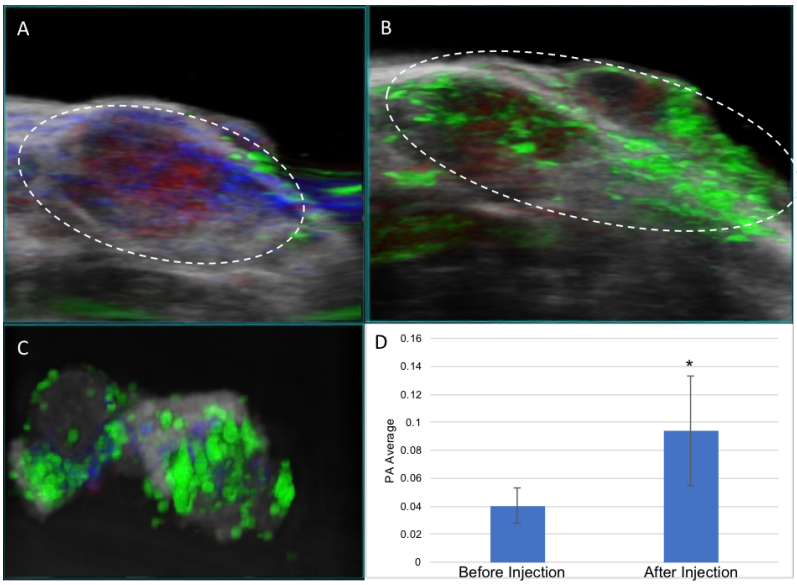

Figure 4.2 Photoacoustic images of a 143B human osteosarcoma mouse xenograft tumour A) prior to administration and B) 1 hour after administration of **28**. C) Photoacoustic image of the same tumour shown in B) ex vivo 1 hour after injection. D) Graph of the average signal intensity in the tumour before and after administration of **28** showing a 2.3× increase over background. The * indicates significance ($P < 0.01$). Red = oxyhemoglobin, Blue = deoxyhemoglobin and Green = **28**. The dashed white lines outline the tumour.

There are a number of TCO-derived molecules, including antibodies and small molecules, that are available for use as targeting vectors.[14,16,19,29] For the proof of concept study, compound **28** was combined with a TCO-derived bisphosphonate (TCO-BP (**29**)). TCO-BP has been used successfully to target radiolabelled tetrazines to sites of high calcium accretion. Conveniently, the compound allows testing to be performed in inexpensive healthy mouse models since tetrazine derivatives coupled to TCO-BP should localize to elbow and knee joints where there is elevated turnover of calcium.[14,30,31] Compound **30** was prepared by mixing compounds **28** and **29** at room temperature for 10 min in quantitative yield; highlighting the ease with which new photoacoustic imaging agents can be prepared using this approach.

For *in vivo* studies, a group of Balb/c mice were administered the parent tetrazine **28** and a second group received the bisphosphonate derivative **30**. Imaging of the knee was performed for both groups at 1 hour post-injection where the same timepoint was used in studies using radiolabelled tetrazines and TCO-BP.[14] The photoacoustic images of animals administered **28** did not show any significant signal in the knee or shoulder joints, which was expected given that the dye is not targeted to bone. In contrast, mice given compound **30** showed a significant signal in the knee joints (Figure 4.3). Images taken of the leg *ex vivo* confirmed the results where intense uptake was observed only for animals who were treated with **30**.

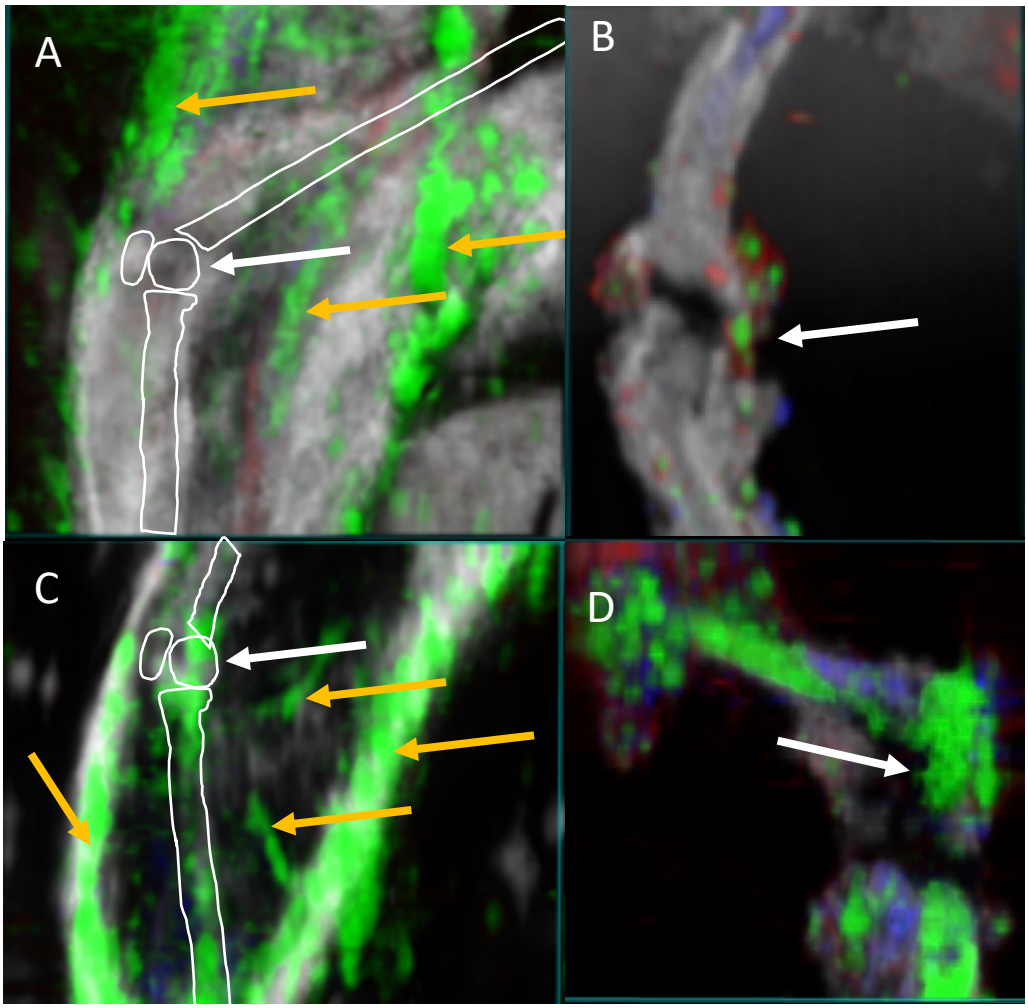

Figure 4.3 Photoacoustic images of A) a mouse leg focusing on the knee joint at 1 hour after injection of **28**. B) The same mouse leg ex vivo. C) A mouse leg 1 hour after injection of **30** and D) Photoacoustic image of the same mouse leg from C) ex vivo. The white arrows indicate the knee joint and yellow arrows indicate blood vessels.

An additional benefit to using TCO-BP is that the bisphosphonate can be labelled with ^{99m}Tc (**31**) and the product coupled to **28** so that the whole-body biodistribution of the photoacoustic imaging dye can be determined quantitatively. ^{99m}Tc labelling of TCO-BP was performed following a literature procedure[14] where radio-TLC (Figure S4.8, Supporting Information) showed the presence

of the product and a small amount of pertechnetate. Compound **28** was then added to **31** and the solution allowed to mix at room temperature for 20 min giving **32** in high yield (>99%) (Scheme 4.2).

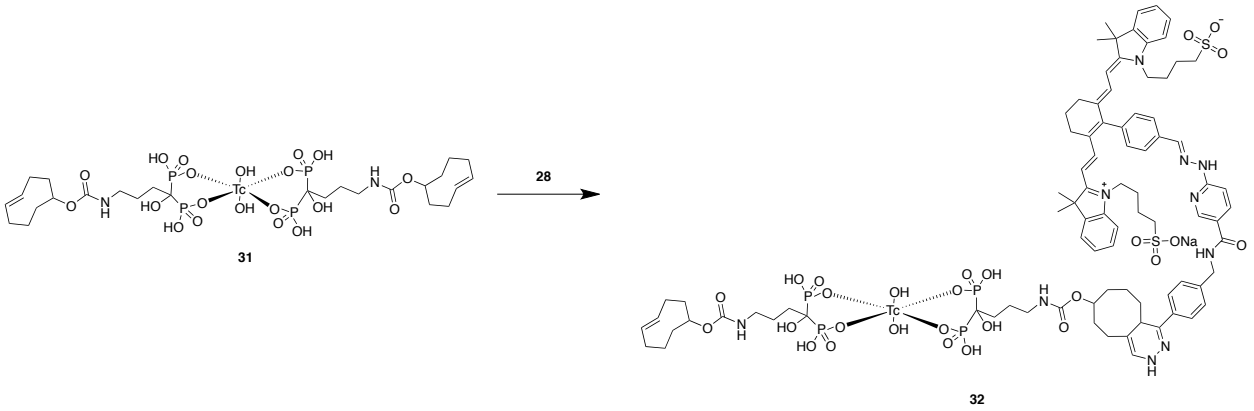

Scheme 4.2 IEDDA reaction between **28** and [^{99m}Tc]Tc-TCO-BP (**31**).

Mice were administered **32** (518 kBq) and sacrificed at 1, 3, 6, and 24 h post injection where fluids, bone (knee, shoulder), and other key tissues were collected, weighed, and counted in a gamma counter. The resulting data is shown in Figure 3 and expressed as percent injected dose per gram of tissue or fluid (%ID g^{-1}). The shoulder and knee showed 3-5%ID g^{-1} (6-10%ID O^{-1}) which remained constant over 24 hours. The compound also exhibited some level of localization in all major tissues and organs with high uptake in the thyroid and stomach being associated with the presence of pertechnetate. Activity was detected in both the kidneys and liver suggesting dual routes of excretion are likely. Due to the albumin binding properties, at the 1 h timepoint, over 15% ID g^{-1} was found in the blood, which was 20× higher than that observed for [^{99m}Tc]Tc-TCO-BP alone (0.78 %ID g^{-1}) at the same time point which increased to 187× higher at 6 h (Figure 4.5).

Based on the high blood concentrations, a subsequent plasma binding study was performed on **32** which showed 50% of the activity was present in the pellet containing the proteins and 50% in the supernatant after 1 hour (Figure S4.11, Supporting Information). A parallel study was also

performed where the fluorescence intensity arising from the cyanine dye in blood following administration of **32** to the Balb/c mice was measured at 1, 3, 6, and 24 h. The blood half-life of the dye (3.8 h) was similar to that determined using radioactive counting (3.2 h) where the small difference is likely due to dissociation of the ^{99m}Tc, which is known to happen *in vivo* particularly at the modest concentrations of ligand used in this study.

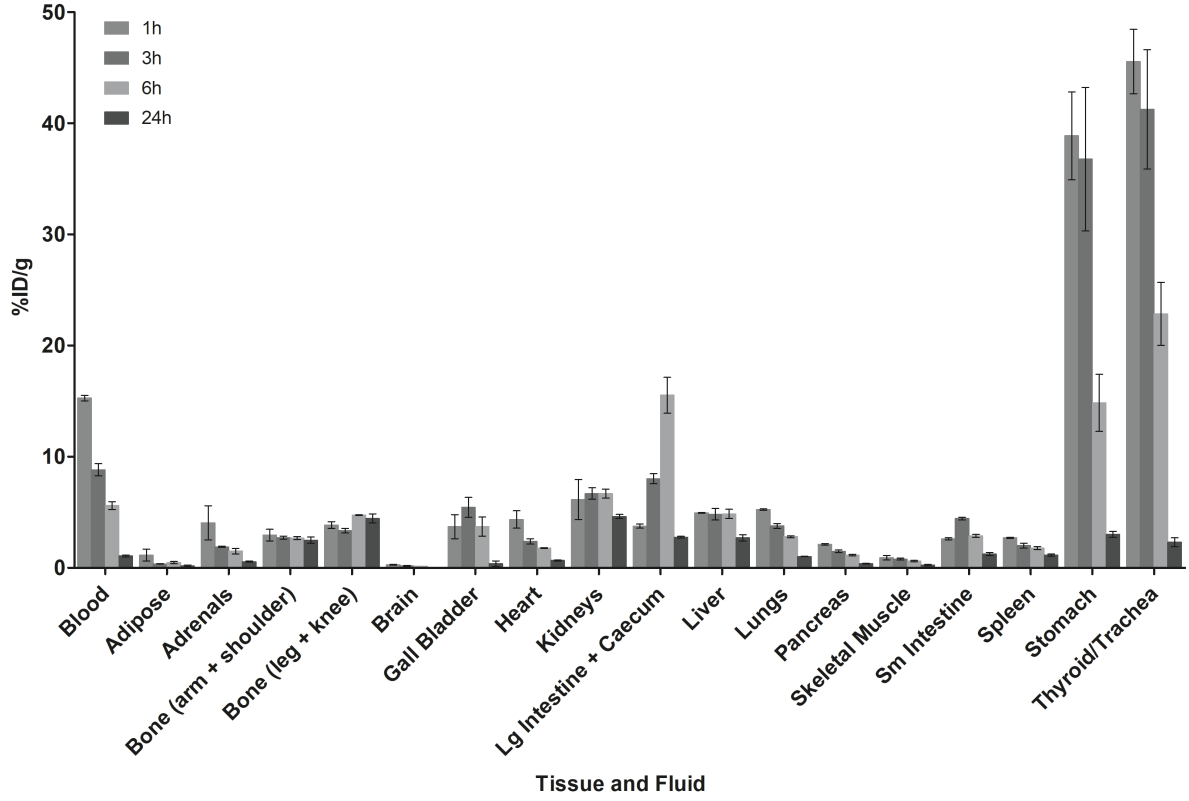

Figure 4.4 Biodistribution data for selected fluids and tissues for **32**. Experiments were performed using Balb/c mice (n=3 per time point) and tissues and fluids were collected at 1, 3, 6, and 24 h post administration. Data are expressed as the mean percent injected dose per gram (%ID g^{-1}) ± SEM.

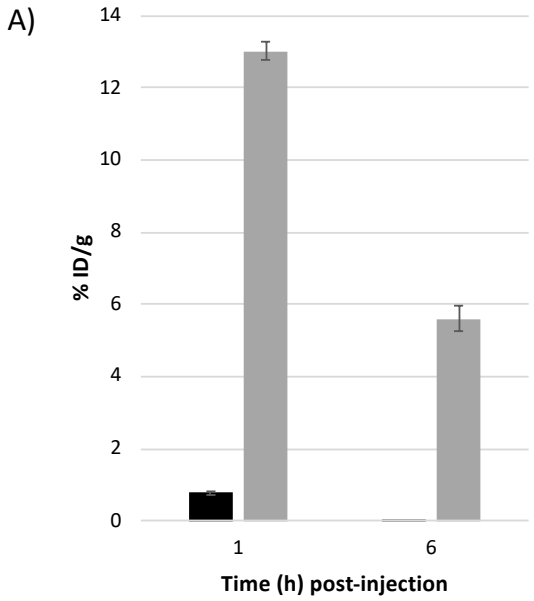

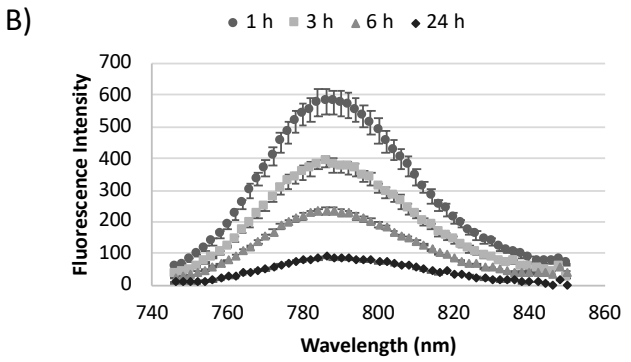

Time (h)	FI @ 786 nm	Amount in blood (µmol)	% of total amount injected
1	580 ± 39	0.025	13.7 %
3	388 ± 17	0.017	9.3 %
6	234 ± 11	0.011	6.0 %
24	88 ± 2.8	0.005	2.7 %

Figure 4.5 A) Blood concentrations expressed as percent injected dose per gram (%ID g^{-1}) for **31** (black) and **32** (grey) at 1 and 6 h p.i. B) Fluorescence spectra and intensity and concentration data for blood samples (n=3 for each time point) following the administration of **32** taken at 1, 3, 6, and 24 h p.i.

There is significant interest in bifunctional molecules that bind blood proteins such as albumin as a way to prolong circulation of drugs that are rapidly excreted.[32–36] As was noted, sulfonated cyanine dyes have been shown to non-covalently bind to the hydrophobic pockets of albumin.[37] For the tetrazine-IR-783 derivative, a preliminary albumin binding study was performed looking at the absorbance and emission of **28** with varying concentrations of BSA. The absorbance spectrum (Figure 4.6) exhibited a band around 650 nm, which is indicative of H-band aggregates with stacked dipoles.[38] Upon the addition of albumin, the absorbance maxima shifts to that for a dimer, seen at 700 nm, and a monomer (774 nm) which is indicitive of disaggregation. When experiments were performed at high dye concentrations, aggregation completely quenches the fluorescence signal, which can be restored through the addition of albumin. This is indicative of cut-on fluorescence and the dye binding to a hydrophobic binding site of albumin.[37]

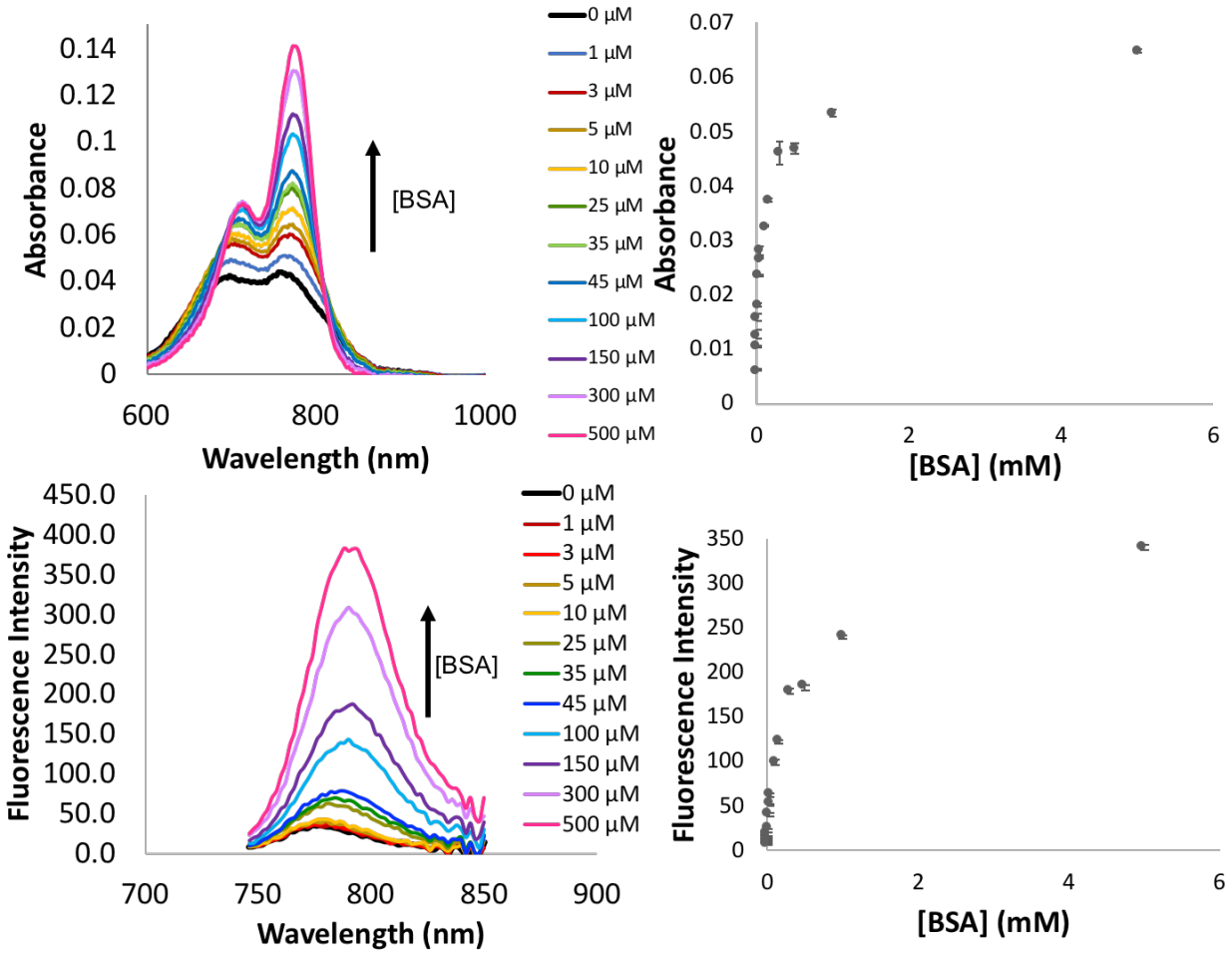

Figure 4.6 Top left: Absorption spectra of **28** (3 µM) with increasing concentrations of BSA. Top right: Absorbance at 776 nm versus concentration of BSA. Bottom left: Fluorescence intensity of **28** (3 µM) with increasing concentrations of BSA (λ_{ex} = 736 nm). Bottom right: Fluorescence intensity at 786 nm versus concentration of BSA.

4.5 Conclusion

In summary, a new tetrazine-derived cyanine dye that can be used to create targeted photoacoustic imaging probes through IEEDA chemistry was reported. The ability to rapidly and effectively couple the dye to a TCO-derivative was demonstrated using a TCO-bisphosphonate and a ^{99m}Tc labelled analogue where the product was used to visualize the knee joint of mice. The platform can not only be used to create new photoacoustic probes, it can also be used to promote albumin

binding of molecules attached to the dye. While active targeting was used in this report, there is also the opportunity to employ pre-targeting strategies where a TCO-derivative is administered first, and once optimal target uptake achieved, the tetrazine can be injected, localizing at the site of interest through IEEDA coupling *in vivo*. This approach would benefit from the pharmacokinetics and stability observed for **28**.

4.6 Experimental

Supplementary figures can be found in **APPENDIX III.**

Materials. Unless otherwise noted, all reagents and solvents were ACS grade and were purchased from commercial suppliers and used without further purification. 6-(2-(tert-butoxycarbonyl) hydrazinyl)nicotinic acid was purchased from Ontario Chemicals Inc. *(E)*-cyclooct-4-enol (TCO-OH), *(E)*-4-cycloocten-1-yl-2,5-dioxo-1-pyrrolidinyl ester carbonic acid (TCO-NHS), and(4-(1,2,4,5-tetrazin-3-yl)phenyl)methanamine hydrochloride were purchaced from Conju-Probe. *N,N*-dimethylformamide, and methanol were purchased from Caledon. Distilled water was used for all experiments. Deuterated solvents for NMR samples were purchased from Cambridge Isotope Laboratories. Sodium borate and potassium sodium tartrate ($KNaC_4H_4O_6 \bullet 4H_2O$) were purchased from Anachemia Canada-VWR. Sodium carbonate was purchased from EM Science. All other compounds were purchased from Sigma-Aldrich. ^{99m}Tc was obtained as TcO_4^- from a ^{99}Mo/^{99m}Tc generator (Lantheus Medical Imaging) in saline (0.9 % NaCl). *Caution: ^{99m}Tc is a γ-emitter (E_γ = 140 keV, $t_{1/2}$ = 6 h) and should only be used in a licensed and appropriately shielded facility.*

^{1}H and ^{13}C NMR spectra were recorded on a Bruker Avance AV-600 instrument at 300 K. High Resolution Mass Spectra (HRMS) were collected on a Waters/Micromass Q-Tof Global Ultima spectrometer. Microwave reactions were performed using a Biotage Initiator 60 instrument. High Performance Liquid Chromatography (HPLC) was performed using a Phenomenex Polar-RP column (4μm, 250 × 10 mm) operating at a flow rate of 4.0 mL/min was used with a Waters 1525 system connected to a Bioscan *γ* detector and a 2998 photodiode array detector monitoring at 350 nm and 700 nm operated using the Empower software package. Flow rates were 1 mL/min. (analytical) or 4 mL/min. (preparative) using the following methods: Method 1 (Solvent A: H_2O + 0.1% TFA, Solvent B: Acetonitrile + 0.1% TFA) 0-1 min 90% B, 1-20 min 10% B, 20-21 min 10-90% B). Solvents were

evaporated using either a Bioatage V10 system or under reduced pressure with a rotary evaporator. Compounds were dried using a VirTis Benchtop lyophilizer equipped with an Edwards RV5 pump.

Methods

Cells and Culture Methods. 143B (CRL-8303) cells were cultured in MEM, NEAA no glutamine, 0.015 mg/mL 5-bromo-2'deoxyuridine supplemented with 10% FBS, and 1% penicillin streptomycin. The cell line was maintained at 37 °C under 5% CO_2.

Animal Care. Female BALB/c immunocompetent mice (Charles River Laboratories, Kingston, NY) at 4-6 weeks of age were sterile housed and maintained at 24 °C with a 12 h light/dark cycle and were provided autoclaved food and water *ad libitum*. All procedures were conducted according to the guidelines of the Committee for Research and Ethical Issues of the International Association for the Study of Pain, and guidelines established by the Canadian Council on Animal Care and the McMaster University Animal Research Ethics Board. 143B (CRL-8303) cells were purchased from ATCC. Female 10-11 week old BALB/c nu/nu mice (Charles River Laboratories, Kingston, NY) were injected with 2.0×10^6 143B cells in Matrigel:DPBS (1:1) subcutaneously into the right flank. Photoacoustic studies were performed 10 days following tumour inoculation.

Biodistribution Studies. Biodistribution studies were performed using female Balb/c mice (Charles River, Kingston, NY) at the indicated time points. The mice were administered the agents via tail vein injection with the final volume not exceeding 200 μL. A 5 mg/mL solution of compound **28** in 10% ethanol in saline was administered at a dose of 20 mg/kg to all mice (approximately 518 kBq of **28**). For all studies, at 1, 3, 6, or 24 h post-injection of the labelled compound, the animals were euthanized by cervical dislocation. Fluids, bone (knee and shoulder), and select tissues were collected, weighed, and counted in a PerkinElmer Wizard 1470 automatic gamma counter. Decay correction was used to

normalize organ activity measurements to time of dose preparation for data calculations. Data is expressed as percent injected dose per gram tissue or fluid (%ID/g) or percent injected dose per organ (%ID/O).

Photoacoustic Imaging Studies. Photoacoustic imaging was performed using Vevo LAZR-X (FUJIFILM VisualSonics Inc., Toronto, ON, Canada) Imaging system equipped with a 680-970 nm laser. Mice were anaesthetized with isofluorane and set up on a platform that monitored the respiration rate and the heart rate of the mouse. The hair on the hindlimb was removed while the mouse was anaesthetized. A 30-MHz, linear array ultrasound transducer with integrated fiber optic light delivery (LZ-400 and MX-400, FUJIFILM VisualSonics, Inc.) was positioned laterally overtop the hindlimb knee joint. The integrated fiber bundle delivered 15 to 20 mJ/cm^2 of light to the hindlimb of the mouse.

Synthetic Procedures

Synthesis of 20 In a round bottom flask, IR-783 (80 mg, 0.11 mmol), 4-formylphenylboronic acid (31 mg, 0.21 mmol), $Pd(PPh_3)_4$ (10 mg, 8 mol%), and Cs_2CO_3 (20 mg, 50 mol%) were dissolved in water (10 mL) and heated at 100 °C for 4 hours. The product was then dried and purified by HPLC (Method 1) yielding a teal solid.

Yield: (71 mg, 96%) ^{1}H NMR (600 MHz, $(CD_3)_2SO$): δ (ppm) 10.22 (s, 1H), 8.18 (d, 2H), 7.56 (d, 2H), 7.45 (d, 2H), 7.35 (m, 4H), 7.16 (d, 2H), 6.99 (d, 2H), 6.28 (d, 2H), 4.13 (t, 4H), 2.72 (t, 5H), 1.98 (t, 2H), 1.74 (dd, 9H), 1.08 (d, 14H). ^{13}C NMR (150 MHz, $(CD_3)_2SO$): δ (ppm) 193.48, 171.68, 159.78, 147.08, 146.06, 142.55, 141.11, 136.14, 130.99, 130.79, 130.09, 128.93, 125.10, 122.85, 111.65, 100.91, 51.24, 48.65, 43.92, 27.46, 26.54, 24.57, 22.96, 21.30. HRMS (ES$^-$) m/z calculated for $C_{45}H_{51}N_2O_7S_2$: 795.3143 [M-H$^-$], found 795.3143.

Synthesis of 28 In a round bottomed flask **20** (90 mg, 0.113 mmol), HYNIC-tetrazine (44mg, 0.136 mmol), and aniline (62 μL, 0.681 mmol) were added with 10 mL absolute ethanol and the flask was sealed. This mixture, was allowed to stir at RT for 12 h. The product was isolated by HPLC Method 1, dried under vacuum yielding a green solid. Yield: 30 mg (35%). ^{1}H NMR ((CD_3OD), 600 MHz): δ (ppm) 10.33 (s,1H), 8.67 (d, 1H), 8.59 (d, 2H), 8.54 (dd, 1H), 8.45 (s, 1H), 8.23 (d, 2H), 7.66 (d, 2H), 7.43 (d, 2H), 7.34 (m, 2H), 7.29 (d, 2H), 7.26 (d, 2H), 7.23 (s, 1H), 7.16 (t, 2H), 6.23 (d, 2H), 4.09 (t, 4H), 3.20 (m, 2H), 2.84 (t, 4H), 2.76 (t, 4H), 2.07 (m, 2H), 1.93 (s, 2H), 1.87 (m, 7H), 1.31 (t, 4H), 1.22 (s, 12H). ^{13}C NMR ($(CD_3)_2SO$), 150 MHz): δ (ppm) 171.09, 165.42, 158.08, 142.11, 140.61, 132.02, 131.49, 131.43, 130.74, 130.32, 129.78, 128.78, 128.70, 128.40, 128.18, 128.08, 127.81, 100.22, 50.76, 28.09, 27.06, 26.03, 22.51. HRMS (ES^-) m/z calculated for $C_{60}H_{63}N_{10}O_7S_2$: 1099.4323 [$M-H^-$], found 1099.4289.

4.7 References

[1] L. V Wang, J. Yao, *Nat. Methods* **2016**, *13*, DOI 10.1038/nmeth.3925.

[2] A. Needles, A. Heinmiller, J. Sun, C. Theodoropoulos, D. Bates, D. Hirson, M. Yin, F. S. Foster, *IEEE Trans. Ultrason. Ferroelectr. Freq. Control* **2013**, *60*, 888–897.

[3] A. Bar-zion, M. Yin, D. Adam, F. S. Foster, *Cancer Res.* **2016**, *76*, 4320–4332.

[4] J. Weber, P. C. Beard, S. E. Bohndiek, *Nat. Publ. Gr.* **2016**, *13*, 639–650.

[5] E. C. Experience, J. K. Willmann, **2016**, *280*.

[6] S. Y. Emelinov, P.-C. Li, M. O'Donnell, *Phys Today* **2010**, *62*, 34–39.

[7] M. Mehrmohammadi, S. J. Yoon, D. Yeager, S. Y. Emelianov, *Curr Mol Imaging* **2013**, *2*, 89–105.

[8] S. Zackirsson, S. M. W. . van de Ven, S. S. Gambhir, *Cancer Res* **2015**, *74*, 979–1004.

[9] K. E. Wilson, S. V. Bachawal, L. Abou-Elkacem, K. Jensen, S. Machtaler, L. Tian, J. K. Willmann, *Theranostics* **2017**, *7*, 1463–1476.

[10] K. E. Wilson, S. V Bachawal, J. K. Willmann, *Clin. Cancer Res.* **2018**, clincanres.0417.2018.

[11] H. K. Zhang, Y. Chen, J. Kang, A. Lisok, I. Minn, M. G. Pomper, E. M. Boctor, *J. Biophotonics* **2018**, e201800021.

[12] M. Capozza, F. Blasi, G. Valbusa, P. Oliva, C. Cabella, F. Buonsanti, A. Cordaro, L. Pizzuto, A. Maiocchi, L. Poggi, *Photoacoustics* **2018**, *11*, 36–45.

[13] C. Zhang, Y. Zhang, K. Hong, S. Zhu, J. Wan, *Nat. Publ. Gr.* **2017**, 1–9.

[14] A. Yazdani, H. Bilton, A. Vito, A. R. Genady, S. M. Rathmann, Z. Ahmad, N. Janzen, S. Czorny, B. M. Zeglis, L. C. Francesconi, et al., *J. Med. Chem.* **2016**, *59*, 9381–9389.

[15] A. Yazdani, N. Janzen, S. Czorny, R. Ungars, T. Miladinovic, G. Singh, J. F. Valliant, *Dalt. Trans* **2017**, DOI 10.1039/C7DT01497J.

[16] R. Rossin, T. Lappchen, S. M. van den Bosch, R. Laforest, M. S. Robillard, *J. Nucl. Med.* **2013**, *54*, 1989–1995.

[17] R. Rossin, M. S. Robillard, *Curr. Opin. Chem. Biol.* **2014**, *21*, 161–169.

[18] B. M. B. M. Zeglis, K. K. Sevak, T. Reiner, P. Mohindra, S. D. Carlin, P. Zanzonico, R. Weissleder, J. S. Lewis, *J. Nucl. Med.* **2013**, *54*, 1389–1396.

[19] B. M. Zeglis, C. Brand, D. Abdel-Atti, K. E. Carnazza, B. E. Cook, S. Carlin, T. Reiner, J. S. Lewis, *Mol. Pharm.* **2015**, *12*, 3575–3587.

[20] A. Vito, H. Alarabi, S. Czorny, O. Beiraghi, J. Kent, N. Janzen, A. R. Genady, S. A. Alkarmi, S. Rathmann, Z. Naperstkow, et al., *PLoS One* **2016**, *11*, e0167425.

[21] K. Okumura, K. Yoshida, K. Yoshioka, S. Aki, N. Yoneda, D. Inoue, A. Kitao, T. Ogi, K. Kozaka, T. Minami, et al., *Eur. Radiol. Exp.* **2018**, *2*, DOI 10.1186/s41747-018-0036-7.

[22] S. Onoe, T. Temma, Y. Shimizu, M. Ono, H. Saji, *Cancer Med.* **2014**, *3*, 775–786.

[23] N. S. James, Y. Chen, P. Joshi, T. Y. Ohulchanskyy, M. Ethirajan, M. Henary, L. Strekowski, R. K. Pandey, *Theranostics* **2013**, *3*, 692–702.

[24] J. Fang, H. Nakamura, H. Maeda, *Adv. Drug Deliv. Rev.* **2011**, *63*, 136–151.

[25] R. Tian, S. Zhu, Q. Zeng, L. Lang, Y. Ma, D. Kiesewetter, Y. Liu, X. Fu, J. Lau, G. Zhu, et al., *Bioconjug. Chem.* **2019**, acs.bioconjchem.9b00258.

[26] Z. Liu, X. Chen, *Chem. Soc. Rev.* **2016**, *45*, 1432–1456.

[27] A. Becker, B. Riefke, B. Ebert, U. Sukowski, H. Rinneberg, W. Semmler, K. Licha, *Photochem. Photobiol.* **2000**, *72*, 234–41.

[28] H. Maeda, H. Nakamura, J. Fang, *Adv. Drug Deliv. Rev.* **2013**, *65*, 71–79.

[29] H. J. Chung, T. Reiner, G. Budin, C. Min, M. Liong, D. Issadore, H. Lee, R. Weissleder, *ACS Nano* **2011**, *5*, 8834–8841.

[30] T. S. T. Wang, R. A. Fawwaz, L. Johnson, G. E. Mojdehi, P. M. Johnson, **n.d.**, *21*, 767–771.

[31] K. Ogawa, T. Mukai, Y. Inoue, M. Ono, H. Saji, *J. Nucl. Med.* **2006**, *47*, 2042–2047.

[32] J. Chen, D. S. Hage, **2006**, *78*, 2672–2683.

[33] J. M. Kelly, A. Amor-coarasa, A. Nikolopoulou, W. Till, P. Barelli, D. Kim, C. W. Jr, X. Zheng, C. Bi, B. Hu, et al., **2017**, *58*, 1442–1450.

[34] M. Karimi, S. Bahrami, S. B. Ravari, P. Sahandi, H. Mirshekari, M. Bozorgomid, S. Shahreza, M. Sori, M. R. Hamblin, *Expert Opin. Drug Deliv.* **2016**, *13*, 1609–1623.

[35] R. Li, H. Yang, D. Jia, Q. Nie, H. Cai, Q. Fan, L. Wan, L. Li, X. Lu, *J. Control. Release* **2016**, *228*, 96–106.

[36] M. Cristina, H. Struthers, C. Winiger, K. Zhernosekov, R. Schibli, *J. Nucl. Med.* **2013**, *54*, 124–132.

[37] A. D. Watson, Binding Studies of Near Infrared Cyanine Dyes with Human Serum Albumin and Poly-L-Lysine Using Optical Spectroscopy Methods By, **2008**.

[38] A. Mishra, R. K. Behera, P. K. Behera, B. K. Mishra, G. B. Behera, *Chem Rev* **2011**, *100*, 1973–2011.

Chapter 5: Cyanine Dye-Gas Vesicle Conjugates as Dual-Modality Contrast Agent for Combined Ultrasound and Photoacoustic Imaging

5.1 Description of Contributions

Samantha Slikboer in collaboration with Holly Bilton were responsible for the development and execution of the experimental work described in this paper including drafting the initial manuscript and experimental section. Yohannes Soenjaya was responsible for preparing the gas vesicles and undertaking imaging studies. Prof. Valliant was the primary investigator and led the research efforts.

5.2 Introduction

A new generation of echogenic contrast agents based on naturally occurring nanostructures called gas vesicles (GVs) were reported recently by Shaprio *et al*.[1] GV's are produced by many species of aquatic bacteria to provide buoyancy to access light and nutrients.[2,3] Thes GV's are harvested from two main strains of bacteria *Anabanea flos-aquae* (Ana) and *Halobacterrium NRC-1* (Halo). They have been widely studied over the last century, are well characterized[2–5] and easily isolated via hypo-osmotic shock. They are biconical gas-filled protein-shelled nanostructures ranging in size from 45-250 nm wide and 100-600 nm long and are permeable only to gas (Figure 5.1).[2,3]

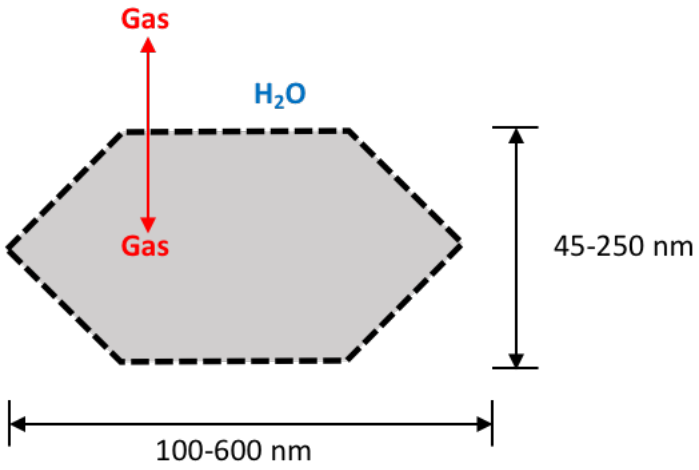

Figure 5.1 Schematic showing the approximate shape and size of a halo gas vesicle (GV).

As contrast agents, GVs were shown to enhance ultrasound signal and exhibit non-linear ultrasonic properties due to buckling. They have unique ultrasound-relevant properties due to their echogenicity, small size, and stability differentiating them from conventional US contrast agents which are typically 400 to 800 μm in size.[1,6,7] GV's are able to take advantage of the enhanced permeability and retention (EPR) effect to access extravascular targets due to their size. In addition, the availability of amino groups on their protein shell provide an opportunity to create a new generation of molecularly targeted US contrast agents. With respect to toxicology, no adverse effects were noted when studies were performed in mice using 13-30 OD formulations.[8]

As an alternative to simple amine conjugation strategies to create targeted GVs, *trans*-cyclooctene, through *trans*-cyclooctene-N-hydroxysuccinimide ester (TCO-NHS), can be added to the protein shell. The resulting-TCO-linked carbamates can be used as an attachment point for tetrazine derivatives through IEEDA chemistry like that used successfully in Chapter 4 to created targeted PA agents. Previously, a multimodal US/SPECT platform was developed which linked the TCO-conjugated Halo-GVs (TCO-GVs) to a radiolabelled tetrazine. In a healthy mouse model, uptake of was seen through the reticuloendothelial system (RES) 20 minutes after injection. Since there was no

disease site to accumulate at, it is likely that the macrophages in the RES removed the ^{99m}Tc labelled GVs from the blood stream similarly to what has been observed for various nanoparticles.[8] Of particular interest here is the development of a combined PA and US imaging agent, which would afford a unique technology to visualize both anatomical features and molecular markers of disease. The GVs enhance echogenicity (by orders of magnitude) creating a clear difference in signal between regions containing the contrast agent and surrounding tissue and fluids. The PA dye would allow for high resolution images to be obtained and contrasted with the US images.

Currently in the literature, GVs have been used to image the liver, and colon where they are able to provide stable contrast at sub-nanomolar concentrations. The GV's produce high resolution contrast-enhanced ultrasound (CEUS) images[1,9,10] of anatomy and tumours that take up the GVs through the EPR effect. The EPR effect is a phenomenon whereby molecules of certain sizes (liposomes, nanoparticles, proteins, drug-polymer conjugates, micelles, DNA polyplexes, and lipid particles and macromolecular drugs) accumulate in tumour tissue much more than they do in normal tissue due to leaky vasculature and poor lymphatic drainage.[11–17] In order for tumour cells to grow quickly, they must stimulate the production of blood vessels. The tumour cells aggregate and start to become dependent on the blood supply carried by the neovasculature for their nutritional and oxygen supply. The resulting "leaky" vasculature allows nanosized (<100 nm) drugs and imaging agents with long circulation times to extravasate into tumour tissues.[18] The reduced lymphatic drainage associated with many tumours also causes these compounds to be retained. Molecules larger than 40 kDa, particles or protein bound compounds (i.e. Evans Blue bound to albumin)[19,20] are above the size threshold for renal clearance allowing for slow clearance and prolonged circulation which increases the uptake through the EPR effect.[20]

There are a limited number of examples of PA/CEUS probes for imaging tumours. Those that have been reported are microbubbles that incorporate dyes or inks into the protein shell or

encapsulate the PA agent.[21–24] Many dye or ink incorporated microbubbles that exist possess sub-optimal pharmacokinetics and are not targeted, therefore they are less than ideal for tumour imaging.[24–26] As shown in Chapter 4, IR783 possess an innate ability to accumulate in tumours through albumin binding and the EPR effect which could be used to promote tumour uptake of GVs .[27] Herein we describe the synthesis and evaluation of a new generation multimodal PA-US agent.

5.3 Results and Discussion

To create the multi-modal US/PA probe, the IEDDA chemistry used successfully in Chapter 4 was employed. More specifically the tetrazine-linked cyanine dye IR783-HYNIC-Tz (**28**) was combined with the TCO-functionalized GVs. The dye-GV complex (**34**) was synthesized using TCO-GVs (Halo) (**33**) produced using the method we reported previously[8] and gently shaking them with IR783-HYNIC-Tz (**28**) prepared as described in Chapter 4. The mixture containing **28** and **33** was agitated gently at 4 °C for 30 min (Scheme 5.1). Following extensive optimization of the purification procedure, the newly functionalized GV's (**34**) were isolated by centrifugation, where due to their buoyant nature, they float to the surface of the centrifuge tube.[10] The amount of dye present has a significant impact on the purification duration as well as the PA signal produced where adding 45.5 nmol to 15-30 optical density (OD) GVs produced the optimal results.

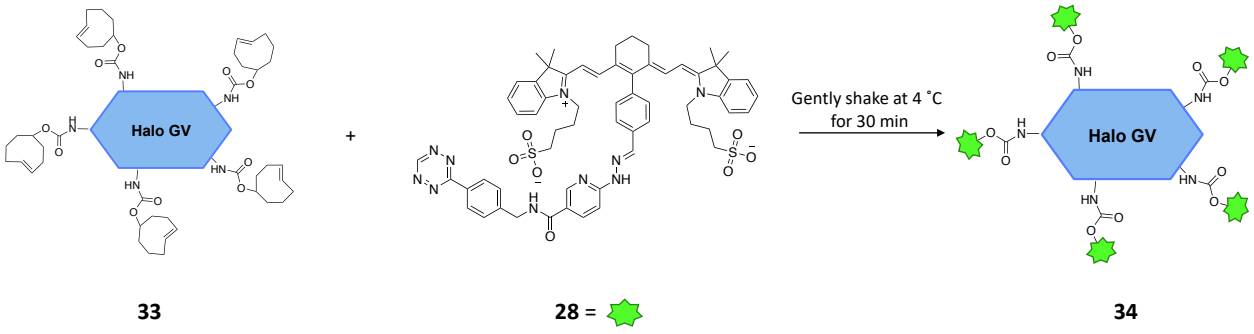

Scheme 5.1 Synthesis of **34.**

Figure 5.2 shows the absorbance spectra of compounds **28**, **33**, and **34**. The absorbance maxima were observed for **28** at 670 and 780 nm which overlapped with the absorbance maxima seen for **34**, indicating the GVs were successfully tagged with the tetrazine-dye complex without significantly altering the PA/absorbance properties. One concern is that there could be non-specific binding however there was a significant colour change between **33** and **34** provides additional evidence the reaction between the dye-tetrazine and the TCO-GV had taken place. After several rounds of centrifugal purification, the supernatant appears clear and colorless indicating free **28** has been removed. The reduction in intensity between **28** and **34** is due to decrease in concentration of the dye in **34** and the increase in mass of the coupled product.

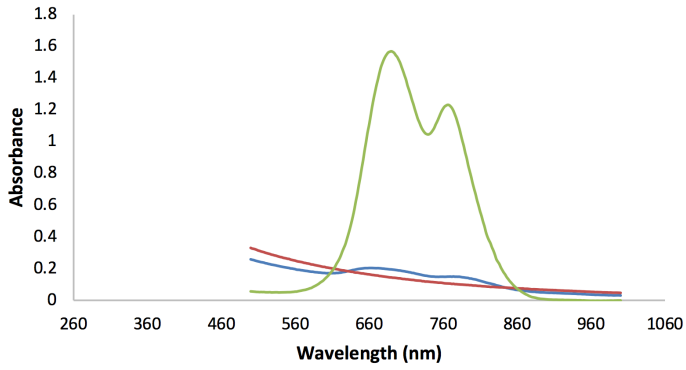

Figure 5.2 Absorbance spectra of **28** (green), **33** (red), and **34** (blue).

The photoacoustic signals (Figure 5.3) of the intact dye-GVs (**34**) and TCO-GVs (**33**) showed a decrease in signal of both when samples of gas vesicles were "popped", which was done by increasing the US power from 1 to 100%. There was a 15× decrease in signal with **3** versus only 5× decrease of **1**. The major decrease in PA signal is likely due in part to the fact that when the GVs pop they create a small air bubble which prevents any of the remaining solution from refilling the void in the phantom tubing. In a living system, where there is dynamic blood flow, there would be a wash-in once the GVs were popped which would maintain a signal from the dye to go along with the loss of the US contrast associated with the destruction of the GVs.

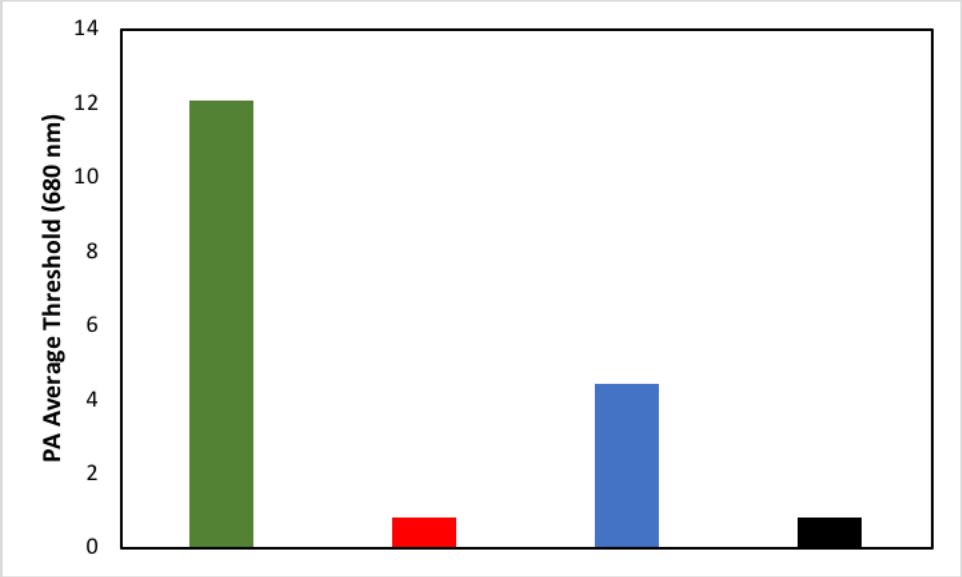

Figure 5.3 Photoacoustic average threshold intensities for: **34** intact (green), **34** popped (red), **33** intact (blue), and **33** popped (black).

In order to determine the optimal amount of tetrazine required to maximize the yield of conjugated dye-GVs, a loading study was performed. Increasing amounts of **28** were added to **33** and the mixtures shaken for 30 min at 4 °C to allow sufficient time for complete conversion. This was followed by centrifugation for 1 hour at 300 rpm. The supernatant was then collected and the absorbance was measured to determine if any unreacted dye was present. Figure 5.4 illustrates the increase in signal with increasing dye concentration. The two lowest mass amounts showed little to no dye present in the supernatant meaning most of the available TCO groups had been consumed where adding more dye after this point did not result in higher yield. This is better visualized in Figure 5.5 where the absorbance signal (698 nm) is plotted versus the amount of **28** added to each sample. A colour gradient is seen in each sample (Figure 5.6) before centrifugation. Furthermore, the size of the unreacted dye pelleted after centrifugation changes as does the intensity of the colour of the extracted dye-GVs after isolation and washing.

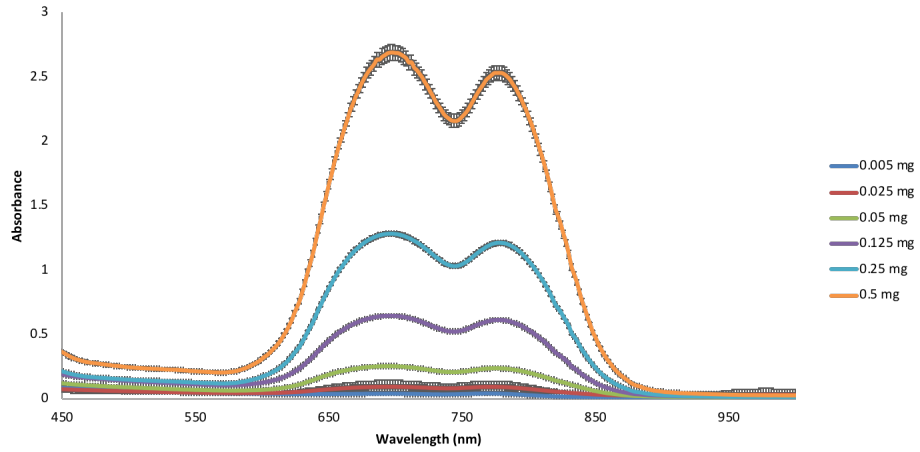

Figure 5.4 Absorbance of the supernatant in the dye loading study (adding increasing amounts of **28** to 30 OD **33**).

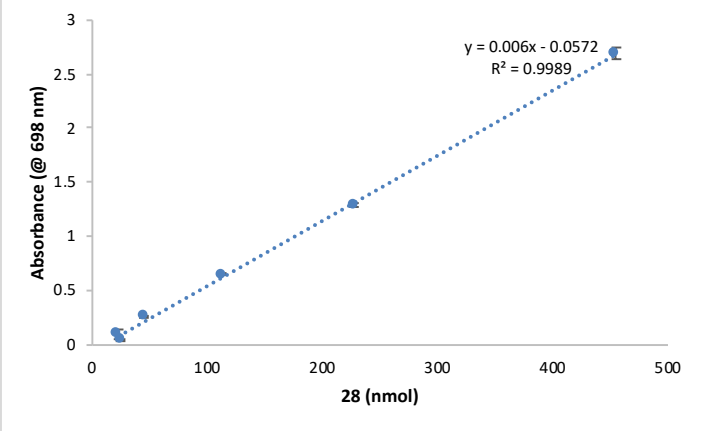

Figure 5.5 A plot of the absorbance at 698 nm found in the supernatant versus the amount of **28** added.

The PA signal of each isolated sample of **34** from the dye loading study was evaluated showing an increase in signal with an increase in the mass of dye loaded. Unsurprisingly, the sample with the highest concentration of dye produced the strongest signal (Figure 5.6). From these experiments it was concluded that the optimal mass of **28** to add was 0.05 mg because it produced an adequate signal with the smallest amount small amount of unreacted dye remaining thereby requiring fewer cycles of centrifugation. Prolonged purification requiring multiple rounds of centrifugation can burst the GVs leading to lower OD.

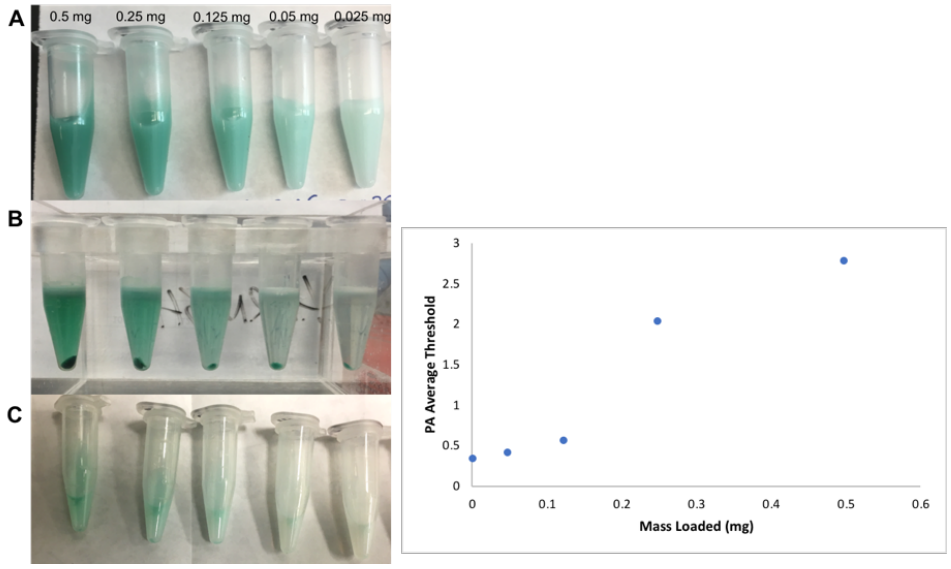

Figure 5.6 Left: Samples of the dye loaded GV's: A) before centrifugation B) after centrifugation and C) after isolation of **34**. Right: PA average signal of loading study samples.

In order to assess the concentration (OD) of dye-gas vesicles required to detect the contrast agent *in vivo* above background, various ODs of **34** were mixed with whole blood and PA images collected. The samples of **34** at 15 and 30 OD (signal of **34** shown in green in Figure 5.7) were seen above the background signal arising from blood (shown in red) which is consistent with the OD used literature for *in vivo* PA imaging (13-33 OD)[8] The signals from 3 and 0.3 OD were indiscernible from blood (Figure 5.7) making those concentrations too dilute for *in vivo* applications.

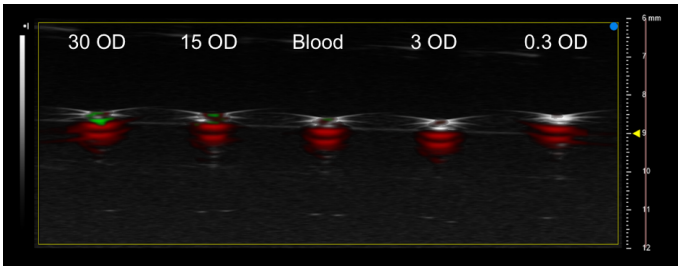

Figure 5.7 PA images of samples of **34** at various concentration in whole blood (green = **34**, red = oxy hemoglobin, blue = deoxy hemoglobin).

Further verifying these findings, the signal at each concentration was plotted and only 15 and 30 OD samples were distinguishable above background of blood (0 OD) (Figure 5.8).

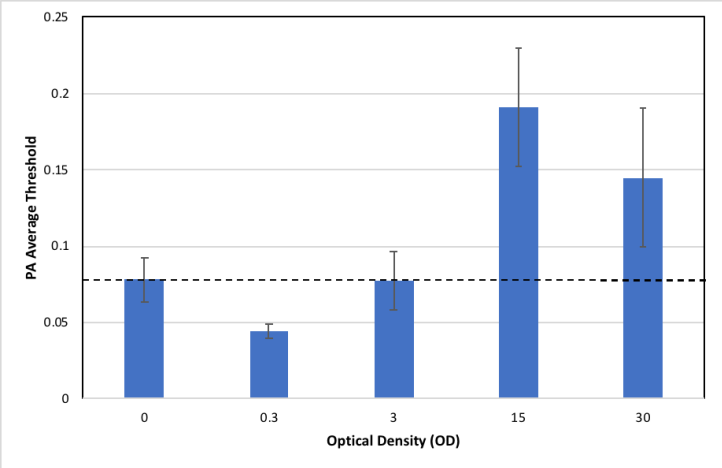

Figure 5.8 PA average threshold vs optical density of **34**. The dashed line indicates the background signal threshold.

To visualize and contrast the ultrasound and photoacoustic signals, **33** and **34** were injected into a gel phantom and both PA and US images collected. The gel phantom was utilized because the tubing used in the phantom has a high background US signal that can interfere with measurements. In Figure 5.9, a sample of **33** was injected with a needle into an Aquaflex® gel pad, where it was possible to visualize the needle track using US. Figure 5.9A shows the ultrasound signal from the GVs alone, and 5.9B shows the PA signal in red from the dye as well as the US signal from the GV component of **34** in white. These results illustrate the feasibility of using **34** multimodal PA and US imaging agent.

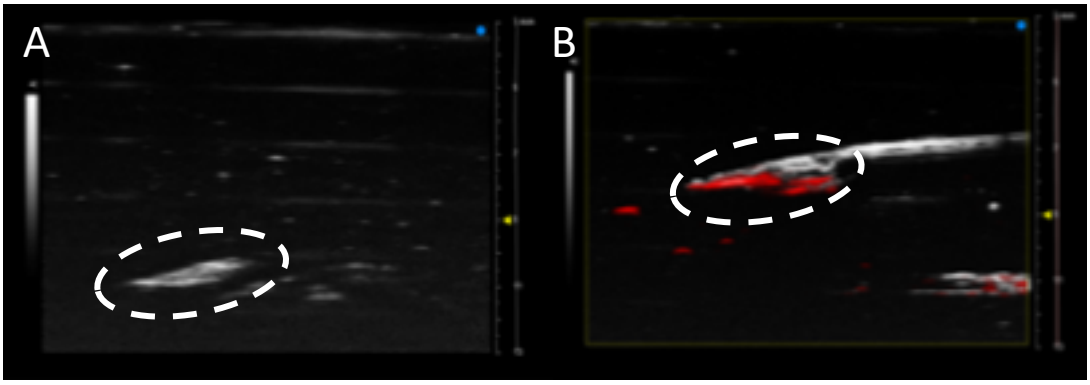

Figure 5.9 A) B-mode US image of **34** in a gel phantom. B) Overlaid PA and B-mode US images of **34** in a gel phantom (30 OD samples).

5.4 Conclusion

A method to prepare a multi-modal US and PA agent using gas vesicles was developed. TCO-modified GVs were combined with the IR783 dye-tetrazine derivative developed in Chapter 4. The dye functionalized GVs combine the strong PA signal of **28** with the CEUS signal of **33** which was evident in the multimodal images of phantoms containing **34**. The propensity of the GV's to collect in tumours via the EPR effect and the ability of the dye to bind albumin (and subsequently localize in tumours) may enable this new class of multimodal contrast agents to visualize cancers. Future work will focus on testing in preclinical models and developing ways to incorporate targeting molecules such as antibodies.

5.5 Experimental

Gas Vesicle Preparation

Gas vesicle culturing, isolation and purification methods were repeated in the same manner described previously.[1] Halobacteria sp. NCR-1 (Carolina Biological Supply, Burlington, NC) were cultured in high salt Carolina media at 42 °C in a shaking incubator at 100 rpm (Ecotron, Infors AG, Switzerland). GVs were isolated by TMC lysis buffer and purified by centrifugal floatation (5 to 6 rounds) at 300 rcf in a centrifuge maintained at 4 °C.

Functionalization of GVs with IR783-HYNIC-Tz

Trans-cyclooctene (TCO)-conjugated GVs (TCO-GVs) (**1**) were prepared as previously described.[8] (E)-cyclooct-4-enyl-2,5-diocopyrrolidin-1-yl carbonate (TCO-NHS) (750 μg, 2.8 μmol; Click Chemistry Tools, 1016-100) in dimethyl sulfoxide (DMSO, 100 μL) was added to a solution of GVs (OD_{500nm} = 77.2, 300 μL) in PBS and diluted with 477 μL of DI water. The solution was left on a shaker for 2.5 h in a cold room. The final TCO-GVs were purified by dialysis using a 6-8 kD dialysis membrane submerged in DI water overnight in a cold room (Spectra/Por 1 Dialysis Membrane, Spectrum Labs, USA). The TCO-GVs were then concentrated by centrifugal floatation at 300 rcf for 45 minutes.

Compound **2** dissolved in 100 μL DMSO was then added (1.5 mg, 1.4 μmol) to the solution of **1** (OD_{500nm} = 40, 300 μL) and left shaking in a cold room for 1 h. The IR-GVs were then washed with cold PBS and purified from any residual **2** using two rounds of centrifugal floatation at 300 rcf for 1 h, until the bottom PBS layer was colourless.

Photoacoustic Imaging Studies

Photoacoustic imaging was performed using Vevo LAZR-X (FUJIFILM VisualSonics Inc., Toronto, ON, Canada) imaging system equipped with a 680-970 nm laser. A 30-MHz, linear array ultrasound transducer with integrated fiber optic light delivery (LZ-400 and MX-400, FUJIFILM VisualSonics, Inc.) was used. The integrated fiber bundle delivered 15 to 20 mJ/cm^2 of light. B-mode 2-D power was set to 1% to prevent popping GVs while imaging. To intentionally pop GVs, the 2-D power was set to 100% and the dynamic range was increased to 100 dB.

Gel phantom studies were performed using Aquaflex ultrasound gel pads. The sample of interest was injected into the gel pad using a needle and imaged.

Blood Studies

Studies were performed in whole mouse blood treated with 10% EDTA to prevent clotting. 50 μL of blood was added to 50 μL of sample and inverted gently to mix.

5.6 References

[1] M. G. Shapiro, P. W. Goodwill, A. Neogy, M. Yin, F. S. Foster, D. V Schaffer, S. M. Conolly, *Nat. Nanotechnol.* **2014**, *9*, 311–316.

[2] A. E. Walsby, *Microbiol. Rev.* **1994**, *58*, 94–144.

[3] F. Pfeifer, *Nat. Rev. Microbiol.* **2012**, *10*, 705–715.

[4] D. E. M. K. Ochmann, F. S. T. F. Oster, M. I. G. S. Hapiro, *Ultrasound Med biol* **2017**, *43*, 1016–1030.

[5] A. E. Walsby, P. K. Hayes, *Biochem* **1989**, *264*, 313–322.

[6] A. Rev, C. Biomol, E. Downloaded, D. Maresca, A. Lakshmanan, M. Abedi, A. Bar-zion, A. Farhadi, G. J. Lu, J. O. Szablowski, et al., *Annu. Rev.* **2018**, *9*, 229–252.

[7] V. Paefgen, D. Doleschel, F. Kiessling, *Front. Pharmacol.* **2015**, *6*, 1–16.

[8] J. Le, A. Zlitni, H. A. Bilton, M. Yin, A. Farhadi, N. R. Janzen, M. G. Shapiro, J. F. Valliant, F. S. Foster, *Mol. imaging Biol.* **2017**, *20*, 230–239.

[9] R. W. Bourdeau, A. Lee-gosselin, A. Lakshmanan, A. Farhadi, S. R. Kumar, S. P. Nety, M. G. Shapiro, *Nat. Publ. Gr.* **2018**, *553*, 86–90.

[10] A. Rev, C. Biomol, E. Downloaded, D. Maresca, A. Lakshmanan, M. Abedi, A. Bar-zion, A. Farhadi, G. J. Lu, J. O. Szablowski, et al., *Annu. Rev.* **2017**, *9*, 2050–2080.

[11] H. Maeda, *Adv. Drug Deliv. Rev.* **2001**, *46*, 169–185.

[12] H. Maeda, *Adv. Enzyme Regul.* **2001**, *41*, 189–207.

[13] H. Maeda, G. Y. Bharate, J. Daruwalla, *Eur. J. Pharm. Biopharm.* **2009**, *71*, 409–419.

[14] A. K. Iyer, G. Khaled, J. Fang, H. Maeda, *Drug Discov. Today* **2006**, *11*, 812–818.

[15] H. Maeda, Y. Matsumura, *Cancer Res.* **1986**, *46*, 6387–6392.

[16] Y. Noguchi, J. Wu, R. Duncan, J. Strohalm, K. Ulbrich, T. Akaike, H. Maeda, *Japanese J. Cancer Res.* **1998**, *89*, 307–314.

[17] Ronit Satchi-Fainaro, Ruth Duncan, *Polymer Therapeutics I: Polymers as Drugs, Conjugates and Gene Delivery Systems*, **2006**.

[18] Y. Nakamura, A. Mochida, P. L. Choyke, H. Kobayashi, *Bioconjug. Chem.* **2016**, *27*, 2225–2238.

[19] M. Radu, J. Chernoff, **2013**, 2–5.

[20] J. Fang, H. Nakamura, H. Maeda, *Adv. Drug Deliv. Rev.* **2011**, *63*, 136–151.

[21] R. X. Xu, *Contrast Media Mol. Imaging* **2011**, *6*, 401–411.

[22] C. Kim, R. Qin, J. S. Xu, L. V. Wang, R. Xu, *J. Biomed. Opt.* **2010**, *15*, 010510.

[23] M. Jeon, W. Song, E. Huynh, J. Kim, J. Kim, B. L. Helfield, B. Y. C. Leung, D. E. Goertz, G. Zheng, J. Oh, et al., *J. Biomed. Opt.* **2014**, *19*, 016005.

[24] E. Huynh, B. Y. C. Leung, B. L. Hel, M. Shakiba, J. Gandier, C. S. Jin, E. R. Master, B. C. Wilson, D. E. Goertz, G. Zheng, *Nat. Nanotechnol.* **2015**, *10*, 325–332.

[25] D. Das, K. Sivasubramanian, C. Yang, M. Pramanik, *Sci. Rep.* **2018**, 1–10.

[26] W. Lv, Y. Shen, H. Yang, R. Yang, W. Cai, J. Zhang, L. Yuan, Y. Duan, L. Zhang, **2018**, *2018*, DOI 10.1155/2018/6202876.

[27] X. Yang, C. Shi, R. Tong, W. Qian, H. E. Zhau, R. Wang, G. Zhu, J. Cheng, V. W. Yang, T. Cheng, et al., *Clin Cancer Res* **2010**, *16*, 2833–2844.

Chapter 6: *In Vivo* Photoacoustic Imaging of Glioblastoma Multiforme

6.1 Description of Contributions

S.R. Slikboer was responsible for the development and execution of all of the imaging work and the design of the experiments. N. Tatari and C. Venugopal were responsible for creating the mouse model. Dr. J.M. Kwiecien provided the histopathology results. Dr. S. Singh and Dr. J. Valliant were the principal investigators.

6.2 Introduction

Glioblastoma multiforme (GBM) is the most common and aggressive primary brain tumour in adults where the prognosis is notoriously poor. Currently there are no curative options for GBM and treatment consists of surgical resection followed by chemo- and radiation therapy.[1,2] After treatment, patients usually relapse and have a median survival post-diagnosis of around 15 months and under 6% survive 5 years which is among the lowest survival rate of malignant brain tumours.[1,3] GBM tumours are grade IV astrocytomas, the most malignant form of astrocytoma and the most prevalent form of glioma. They are highly vascularized, heterogeneous, and are characterized by their infiltrative growth, which can make these cells nearly indistinguishable from normal brain tissue.[4–7] This makes distinguishing tumour margins extremely challenging and is believed to be one of the contributing factors to recurrence. To improve patient prognosis, there is an urgent need to develop new diagnostics for identifying tumour margins and residual GBM.

With photoacoustic imaging being a noninvasive and non-destructive high-resolution imaging technique, it has the potential to improve the detection of tumour margins and to be a tool to monitor response to treatment. PA imaging agents designed for selective uptake in GBM cells could provide surgeons with the ability to delineate GBM from normal brain tissue for guided resection and post-

treatment monitoring. Preclinically, PA imaging of the brain has been explored using a number of agents, such as targeted cyanine dyes like IRDye800-c(KRGDf)[8], gold nanoparticles[9], copper nanoparticles[10], organic nanoparticles[11], gold nanospheres[12,13], and MoS_2 nanosheets[14]. In all cases, GBMs were detected above background signal through the intact skull via i.v. injection.

Nanoparticles, with or without PA dyes, accumulate in the brain via the EPR effect and are optimally imaged after 1-2 days. Nanoparticles are highly "tunable" with respect to their optical properties due to their unique chemical and physical properties and their ability to carry molecular cargo (i.e. pharmaceuticals). In addition, they exhibit a large surface area to volume ratio that increases their sensitivity. However, nanoparticles have several noteworthy challenges including reproducibility during manufacturing, poor purification efficiency, inhomogeneity, slow clearance rates, as well as toxicity concerns.[15] In contrast, PA dyes have good tissue penetration, desirably fast clearance, and low toxicity. Unfortunately, PA dyes usually have solubility issues, are known to aggregate, and have a short circulation time which reduces target uptake. Compound **28** (Chapter 3) did not have these limitations noting that it is easily soluble in 10% ethanol and saline up to a concentration of 5 mg/mL. In addition, interaction with albumin in the blood prevents aggregation and prolongs the circulation time to several hours, allowing adequate time for the dye to accumulate in its target.

Wu *et al.* showed that IR783 crosses the blood-brain-barrier (BBB) and blood-tumour-barrier (BTB) through the EPR effect. This is likely due to fenestration of blood vessels and ventricles when tumour cells are present (depicted in Figure 6.1). IR783 was used successfully to shuttle the chemotherapeutic drug gemcitabine across the BBB, which cannot normally cross. In this study, mice bearing orthotopic U87 GBM xenografts were administered IR783 and IR783-gemtizumide intraperitoneally and imaged using whole-body and organ-specific fluorescence imaging.[16] Tumour uptake was seen after 1 h and persisted for 24 hours. Unfortunately, optical imaging does not possess sufficient depth of penetration to effectively delineate tumour margins, especially for sub-millimeter

lesions. Photoacoustic imaging, conversely, has micrometer resolution and with the appropriate contrast agent has the potential to delineate tumour margins especially when combined with anatomical information provided by ultrasonography. To this end, a study was initiated to evaluate compound **28** for imaging GBM in tumour xenografts.

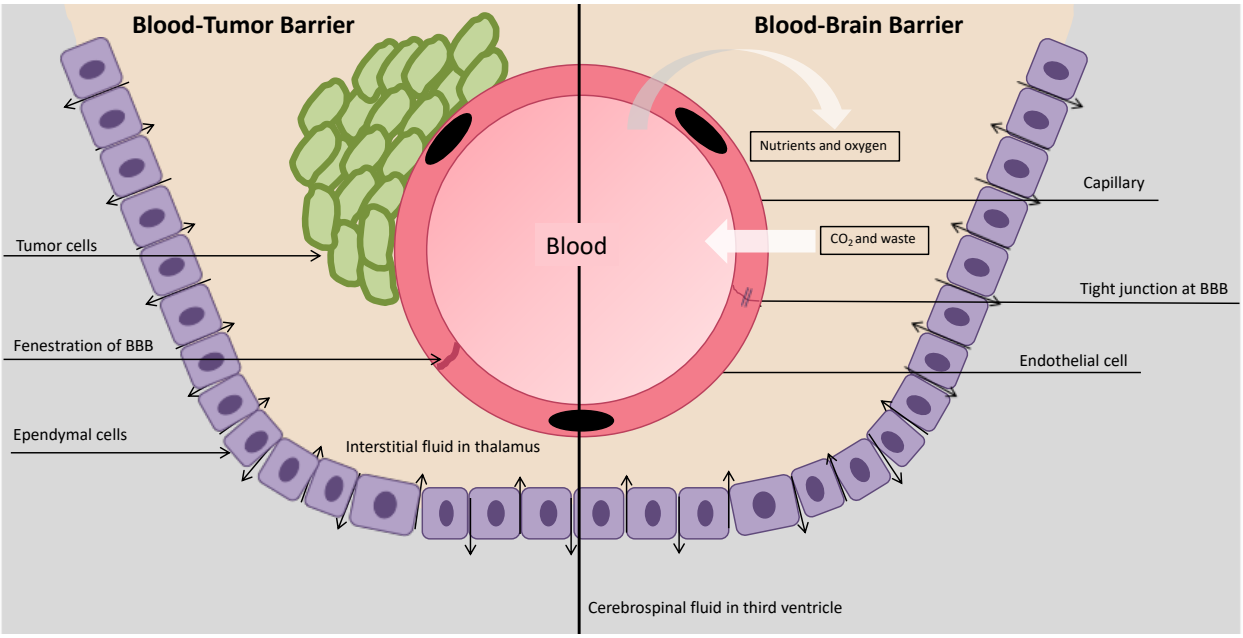

Figure 6.1 Schematic representation of the blood-brain barrier and blood-tumour barrier. This figure was generated using PowerPoint and is a modification and combination of two published figures.[17,18]

6.3 Results and Discussion

Prior to i.v. administration, preliminary tests were performed to determine if IR783-Tz (**28**) (Figure 6.2) could be detected in the brain through an intact mouse skull. First, the oxygenated and deoxygenated blood in the brain was imaged through the intact skull of a normal mouse prior to injection to acquire the background signal. After the mouse was sacrificed, a small sample of **28** (1 mg/mL) was injected through the skull and the brain was imaged again. As shown in Figure 6.3, the dye is easily visible as green signal and easily separable from oxy- and deoxyhemoglobin.

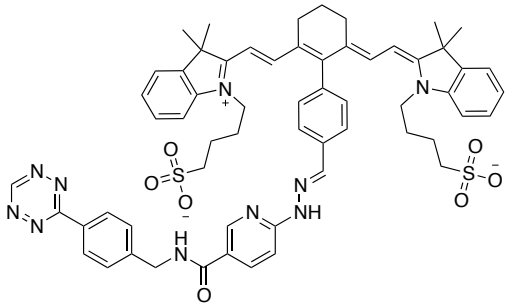

28

Figure 6.2 Structure of **28**.

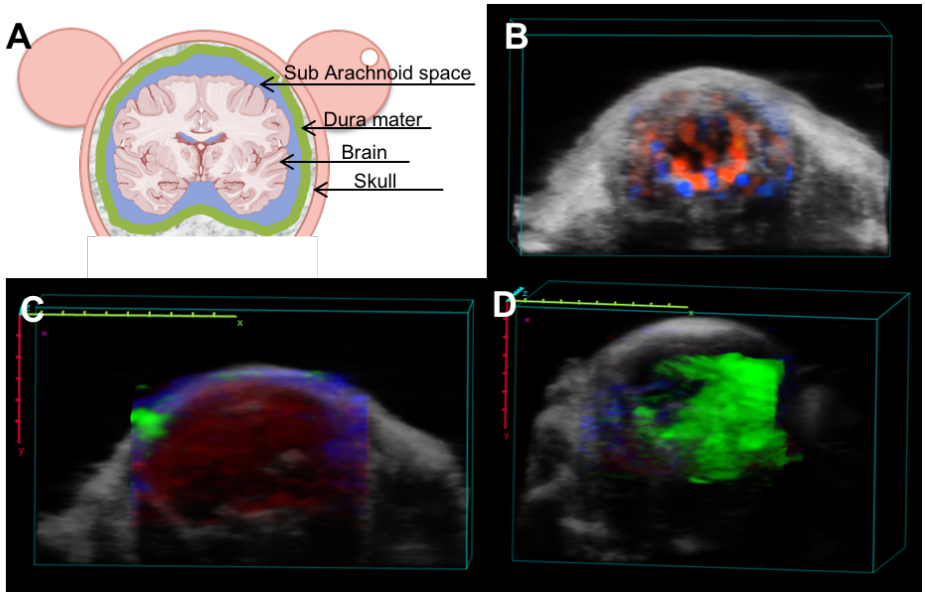

Figure 6.3 A: A schematic representation of the coronal section of the head of a mouse. (Figure generated in PowerPoint adapted from a published figure[19]). B: Colour doppler image of a mouse head. C: PA image of a mouse head showing the skull and brain before injection of **1** looking at oxyhemoglobin (red) and deoxyhemoglobin (blue). D: PA image of a mouse skull and brain after injection of **1** (green).

Next, accumulation of the dye administered via the tail vein was evaluated in an established, patient derived GBM model.[20] For this study, 5 NOD/SCID mice were implanted via bore hole in the right prefrontal cortex with patient derived GMB cells (5×10^5 cells) and allowed to grow for 12 days. Background images (with skulls intact) were acquired using PA imaging (Figure 6.4A). Mice were then injected with compound **28** (0.4 mg in 200 μL) via the tail vein. One hour after injection, mice

were imaged where compound **28** was mainly found in the sub arachnoid space (Figure 6.4). Mice were sacrificed and their brains imaged *ex vivo*. When the brain was removed, the subarachnoid space was separated from the brain, and only uptake within the brain can be seen. The *in vivo* images (Figure 6.4B) shows strong signal in the sub arachnoid space (shown by concentrated green signal), as well as in the lateral and third ventricles. The ventricle uptake can be seen more clearly in the *ex vivo* image (Figure 6.4C). The signal was quantified 1 hour after injection and compared to the background signal. A 1.8× increase in photoacoustic signal intensity was detected (Figure 6.5), which is depicted in Figure 6.4.

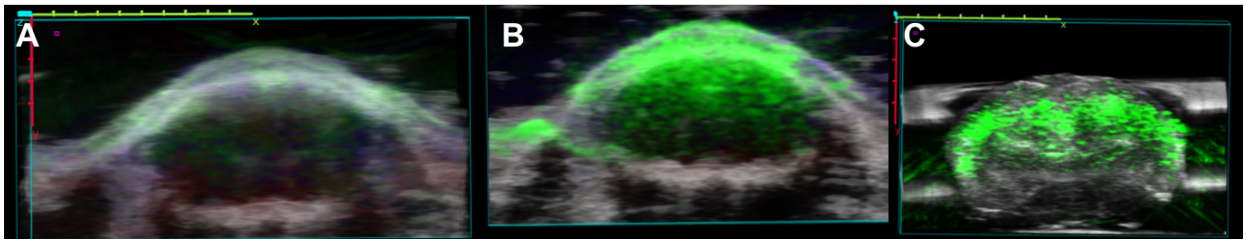

Figure 6.4 PA images overlaid with the B-mode US of the brain and skull in a murine glioblastoma model. A: Prior to administration, B: PA image of the same mouse 1 hour after injection **of 28** (1 mg/mL), C: *ex vivo* 1 hour after injection. Red = oxyhemoglobin, Blue = deoxyhemoglobin, Green= **28**.

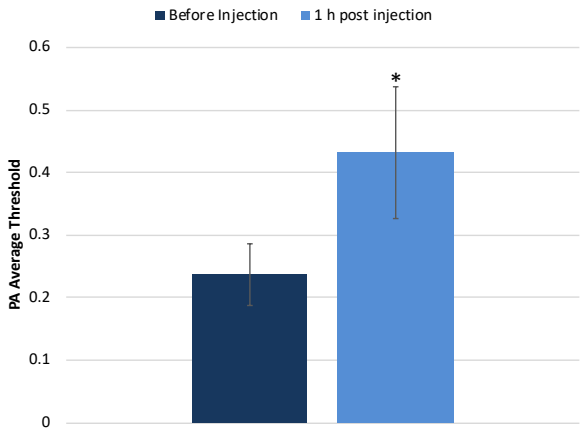

Figure 6.5 Graph of the average signal intensity in the brain before and 1 h after administration of **28** showing a 1.8× increase over background. The * indicates significance ($P < 0.05$).

To confirm that this increased signal was due to the presence of GBM cells, brains were fixed, sectioned, and stained for histopathology analysis. Histopathology confirmed the presence of cancer cells where the sections were stained with hematoxylin and eosin (H&E) alone or H&E counterstained

with luxol fast blue (LFB). H&E alone stains the nuclei of cells dark bluish-purple, cytoplasm pink, and red blood cells red, whereas LFB stains myelin fibers blue, neurophils pink, and nerve cells purple.[21,22] Two small masses (700×200 μm and 400×100 μm) were found on either side of the needle track in the striatum (Figure 6.7 & 6.8). Human tumour cells are much larger than native mouse brain cells, enabling clear differentiation (Figure 6.6B). There was another small aggregation of neoplastic cells in the 4th ventricle and in the basal meninges of the medulla (Figure 6.9). Histopathology verifies that while some tumour cells survived in the area of intracerebral injection, most cells escaped from the injection site into the adjacent cerebral ventricles and into the sub-arachnoid space. Notably, obliteration of the ependymal lining resulted in local infiltration of the subependymal white matter (white matter surrounding lateral ventricles) and is indicative of high malignant activity of the tumour capable of transgressing into the central nervous system (CNS). These findings agree with the corresponding PA images and show that even micrometer sized masses will accumulate compound **1** enabling detection and differentiation from the native mouse brain.

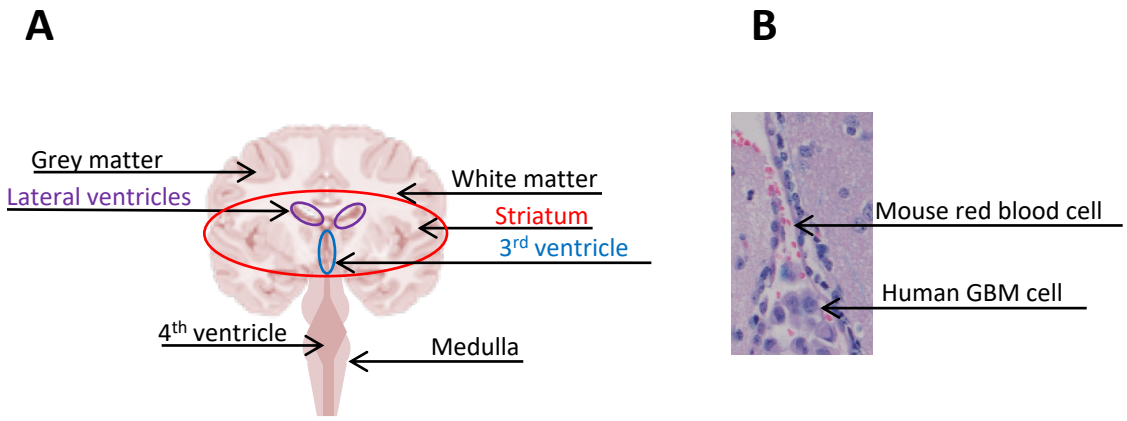

Figure 6.6 A) A schematic of basic brain anatomy highlighting areas of interest for histopathology (Figure generated in PowerPoint adapted from a published figure[23]). B) Representative image from histopathology showing mouse red blood cells (red) and human GBM cells (light purple with darker purple nuclei).

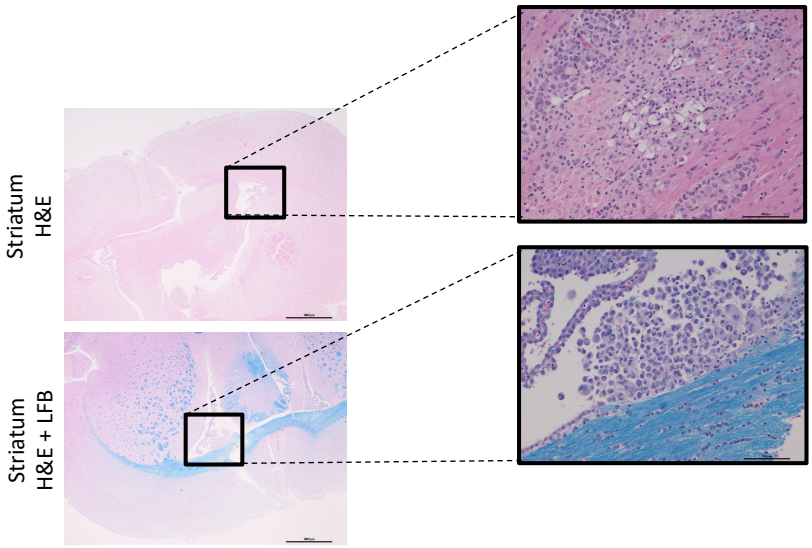

Figure 6.7 Histologic analysis of the infiltration of GBM cells in the striatum. Representative sections stained with H&E or H&E and LFB showing the tumour cells in the striatum. (Left: scale bar = 1000 μm; Right: scale bar = 100 μm).

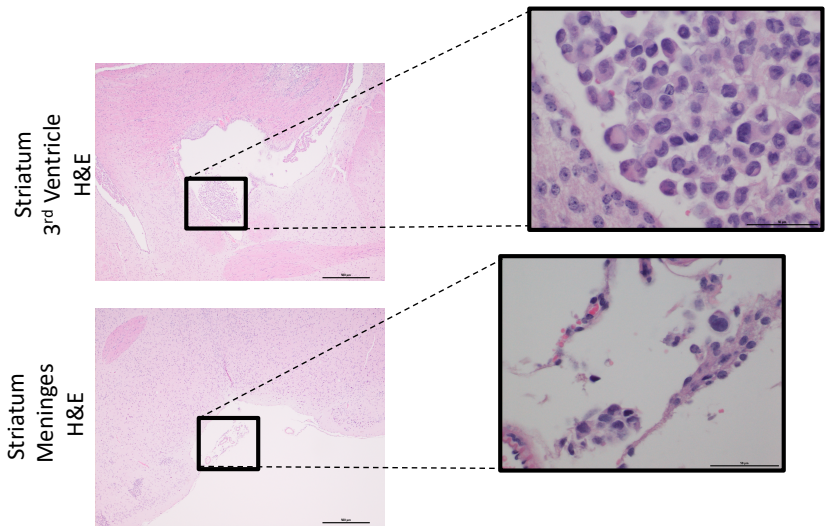

Figure 6.19 Histologic analysis of the infiltration of GBM cells in the striatum 3rd ventricle, and meninges. Representative sections stained with H&E or H&E and LFB showing the tumour cells in the striatum. (Left: scale bar = 500 μm; Right: scale bar = 50 μm).

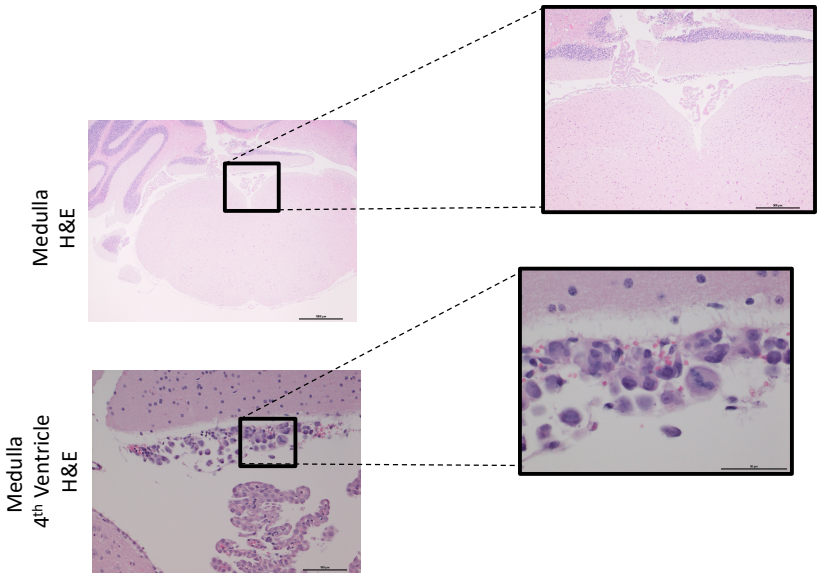

Figure 6.9 Histologic analysis of the infiltration of GBM cells in the Medulla, and 4th ventricle. Representative sections stained with H&E or H&E and LFB showing the tumour cells in the striatum. (Top left: scale bar = 1000 μm; Top right: scale bar = 500 μm; Bottom left: scale bar = 100 μm; Bottom right: scale bar = 50 μm).

6.4 Conclusion

PA imaging employing a new contrast agent was used to detect the presence of GBM cells *in vivo* where the results correlated with pathology. By showing that compound **28** can cross the BBB, localize selectively to GBM cells creates the opportunity to advance a new technology to support surgical guidance that leverages the depth of penetration, high resolution, and sensitivity of PA imaging. Furthermore, because compound **28** has a tetrazine, it can be readily linked to chemotherapeutics through the use of bioorthogonal chemistry as a way to promote crossing the BBB.

6.5 Experimental

Supplementary figures can be found in **APPENDIX IV**.

Animal care. Animals provided by Dr. Singh. Animal studies were performed according to guidelines under Animal Use Protocols of McMaster University Central Animal Facility. 500,000 BT 241 cells were intracranially injected into right frontal lobe of 6-8 week old immunocompromised NOD/SCID mice for tumour formation as previously described.[20] Briefly, mice were anaesthetized using 2.5% Isoflurane (gas anaesthesia). Using a 15-blade scalpel a 1.5 cm vertical midline incision was made on top of the skull. A small burr hole was then made (2-3 mm anterior to the coronal suture, 3 mm lateral to midline) using a drill held perpendicular to the skull. A Hamilton syringe was used to inject 5µl of cell suspension into the frontal lobe. The syringe was inserted through the burr hole at a 30° angle to a 5 mm depth. The incision was closed using interrupted stitches and sutures were sealed with a tissue adhesive. Mice were identified using ear notches, placed in recovery cages and were monitored weekly for signs of illness.

Photoacoustic Imaging Studies. Photoacoustic imaging was performed using Vevo LAZR-X (FUJIFILM VisualSonics Inc., Toronto, ON, Canada) Imaging system equipped with a 680-970 nm laser. Mice were anaesthetized with isofluorane and set up on a platform that monitored the respiration rate and the heart rate of the mouse. The hair on the head was removed while the mouse was anaesthetized. A 15-MHz, linear array ultrasound transducer with integrated fiber optic light delivery (LZ-400 and MX-201, FUJIFILM VisualSonics, Inc.) was positioned laterally overtop the head using the stereotactic frame to keep the head in position. The integrated fiber bundle delivered 15 to 20 mJ/cm^2 of light to the head of the mouse. The mice were administered the agent via tail vein injection

with the final volume not exceeding 200 μL. A 1 mg/mL solution of **28** in 10% ethanol in saline was administered at a dose of 20 mg/kg to all mice.

6.6 References

[1] A. Shergalis, A. Bankhead, U. Luesakul, N. Muangsin, N. Neamati, N. Campus, A. Arbor, A. Arbor, *Pharmacol. Rev.* **2018**, *70*, 412–445.

[2] M. Weller, B. Fisher, M. J. B. Taphoorn, K. Belanger, A. A. Brandes, C. Marosi, U. Bogdahn, J. Curschmann, R. C. Janzer, *N. Engl. J. Med.* **2005**, *352*, 987–997.

[3] J. A. Schwartzbaum, J. L. Fisher, K. D. Aldape, M. Wrensch, *Nat. Clin. Pract. Neurol.* **2006**, *2*, 494–503.

[4] A. G. Linkous, E. M. Yazlovitskaya, *Anticancer. Agents Med. Chem.* **2011**, DOI 10.2174/187152011797378643.

[5] L. Zhen, C. Yufeng, S. Zhenyu, X. Lei, *J Neurooncol* **2010**, *97*, 451–457.

[6] K. Urbańska, J. Sokołowska, M. Szmidt, P. Sysa, *Contemp Oncol* **2014**, *18*, 307–312.

[7] S. Karcher, H. Steiner, R. Ahmadi, S. Zoubaa, G. Vasvari, H. Bauer, *Int. J. Caner* **2006**, *118*, 2182–2189.

[8] B. M. Li, J. Oh, X. Xie, G. Ku, W. Wang, C. Li, G. Lungu, G. Stoica, L. V Wang, *Proceddings IEEE* **2008**, *96*, 481–489.

[9] M. F. Kircher, A. De Zerda, J. V Jokerst, C. L. Zavaleta, P. J. Kempen, E. Mittra, K. Pitter, R. Huang, C. Campos, F. Habte, et al., *Nat. Med.* **2012**, *18*, 829–834.

[10] G. Ku, M. Zhou, S. Song, Q. Huang, J. Hazle, C. Li, *ACS Nano* **2012**, *6*, 7489–7496.

[11] D. Wang, *Neurophotonics* **2019**, *3*, 1–9.

[12] W. Lu, M. P. Melancon, C. Xiong, Q. Huang, A. Elliott, S. Song, R. Zhang, L. G. F. Ii, J. G. Gelovani, L. V Wang, et al., *Cancer Res.* **2011**, *71*, 6116–6122.

[13] W. Lu, Q. Huang, G. Ku, X. Wen, M. Zhou, D. Guzatov, P. Brecht, R. Su, A. Oraevsky, L. V Wang, et al., *Biomaterials* **2010**, *31*, 2617–2626.

[14] J. Chen, C. Liu, D. Hu, F. Wang, H. Wu, X. Gong, X. Liu, *Adv. Funct. Mater.* **2016**, *26*, 8715–8725.

[15] J. Weber, P. C. Beard, S. E. Bohndiek, *Nat. Publ. Gr.* **2016**, *13*, 639–650.

[16] J. B. Wu, C. Shi, G. C. Chu, Q. Xu, Y. Zhang, J. S. Yu, H. E. Zhau, L. W. K. Chung, L. Angeles, L. Angeles, *Biomaterials* **2015**, *67*, 1–10.

[17] F. ELAmrawy, A. A. Othman, C. Adkins, A. Helmy, M. I. Nounou, *J. Cancer Metastasis Treat.* **2016**, *2*, 112.

[18] F. H. Martini, E. F. Bartholomew, J. L. Nath, in *Fundam. Anat. Physiol.*, **2012**.

[19] V. . Scanlon, T. Sanders, in *Essentials Anat. Physiol.*, **2007**.

[20] M. et al Qazi, in *Stem Cells Tissue Repair. Methods Mol. Biol. (Methods Protoc.*, **2014**.

[21] J. K. C. Chan, *Int. J. Surg. Pathol.* **2014**, *22*, 12–32.

[22] J. Bruce-Gregorios, *Histopathologic Techniques*, Goodwill Tradinc Co., Inc., **2006**.

[23] F. H. Martini, Ober, E. F. Bartholomew, J. L. Nath, in *Vis. Essentials Anat. Physiol.*, **2013**.

Chapter 7: Summary and Future Work

7.1 Summary

The overall objective was to develop a new platform for the preparation of targeted multi-modal contrast agents. In Chapter 2, methods to prepare and characterize a family of PIP ligands and their isostructural Re(I) and Tc(I) complexes were established. While the ligands offer a convenient way to develop novel ^{99m}Tc complexes, the biodistribution profiles were not ideal and the luminescence properties of the Re complexes were not suited for *in vivo* imaging. To address these issues, a cyanine dye was added to the scaffold, resulting in the production of IR783-PIP (**22**), which was engineered as a new platform for preparing SPECT and photoacoustic imaging agents. The NIR dye was attached to the bidentate PIP ligand in one step where the product was readily labelled with ^{99m}Tc. Unfortunately, the addition of a bifunctional monodentate ligand to these [2+1] complexes was not successful thereby precluding the development of targeted analogues.

Building on this work, a second PA imaging agent, IR783-HYNIC-Tz (**28**), was designed to provide a simple platform for generated targeted PA agents. Being synthesized in only two steps **28** was found to be an exceptionally useful agent for PA imaging. The tetrazine moiety provides a convenient method to link any TCO bound targeting vector such as TCO-bisphosphonate (TCO-BP) (**29**) that was used for imaging regions of calcium turnover in the skeleton. Compound **29** was labelled with ^{99m}Tc and the distribution of the cyanine dye-Tz adduct determined quantitatively. Through this approach, a multimodal probe for imaging microfracture and microcalcification detection was created. The precursor **28** was also found to have innate tumour targeting ability which was examined in multiple models including GBM. Compound **28** was able to target cancer cells as well as cross the BBB where PA imaging was performed with the intact skull. The presence of the tetrazine moiety in

28 will allow in the future for a drug payload to be attached and brought across the BBB which could improve the effectiveness of treatments.

Further application of the platform was explored with one promising avenue being the combination of **28** with TCO-derived gas vesicles. The amalgamation of these two concepts allows for both CEUS via the gas vesicles as well as PA imaging through the signals produced from IR783. This new multimodal agent has the potential to be used for tumour imaging as both components (GVs and IR783) have shown innate uptake into tumours through the EPR effect. Moving forward into *in vivo* models will show the practicality of this new multimodal probe for the detection and monitoring of cancer.

7.2 Future Work

7.2.1 Expanding testing across a greater breadth of disease models

While there is work that can be done on the PIP ligands, the focus of future work should be on studying the general utility of **28** as a PA probe. Firstly, its use to visualize cancer cells across a wider array of cancer models is a critical next step to understand the broader potential utility. Some models of interest include breast, colorectal, prostate, and pancreatic cancer. Breast and prostate are of interest due to the need for an agent to guide biopsies and surgical resection and for addressing limitations in existing diagnostic technologies particularly for women with dense breast tissue. The real time imaging that PA offers, as well as the combination with ultrasound, can provide superior information to confirm the presence of disease and to more accurately detect cancer cells in surrounding structures (i.e. lymph nodes). Pancreatic and colorectal cancers have poor outcomes as they are both difficult to detect before the cancer reaches an advanced stage. Having a targeted PA probe would allow for non-invasive screening of high-risk patients. The approach proposed would

allow the physician in real time to visualize the pancreas and colon using ultrasound and the cancer cells using PA.

Based on the work reported in Chapter 6, further studies in GBM should be pursued for its immediate value in preclinical research and clinically for the assessment of disease progression, responses to treatment and for surgical guidance. In the short term, an additional study will be performed with a control group with PBS injected instead of tumour cells in NOD/SCID mice (n=5) and mice bearing GBM (n=5) with tumours close to endpoint. The tumours will be imaged at select timepoints over 24-48 hours to visualize uptake and retention of the dye and find the optimal imaging window. Following the sacrifice of animals, histology and pathology on the brains will be completed to see if the signal correlates to the location of the disease. With success, strategies to translate this agent for clinical studies will be pursued.

Another possible avenue, which is starting to be explored in the group, is using the tetrazine in **28** to link to targeting antibodies. In collaboration with Kevin Wyszatko in the Valliant research group, an IR783-HYNIC-Tz-TCO-antibody conjugate that can bind to CD133 which is a biomarker found on cancer stem cells has been prepared. Having established binding *in vitro*, future work will focus on imaging studies in hind limb xenografts notably those derived from human colorectal tumour cells (HT-29) to verify the uptake and retention over time. Further applications using other antibodies or TCO-derived small molecules is clearly an opportunity to expand the impact of the work described here.

7.2.2 Utilizing non-covalent albumin binding

Utilizing the natural ability of the cyanine dye-tetrazine complex to non-covalently bind to albumin provides a unique opportunity to increase the circulation and bioavailability of diagnostics and therapeutics that exhibit rapid clearance. As a first step, the binding ratio and affinity between **28**,

mouse serum albumin (MSA) and human serum albumin (HSA) will be established through incubation of the dye with increasing amounts of protein. Subsequently, the amount of time required for complete binding will be determined through fluorescence detection by sampling the reaction mixture at various time points. The blood half-life will then be measured *in vivo* compared to **28** coupled to TCO-albumin. Assuming comparable distribution profiles, future work will focus on modifying pharmaceuticals that have poor retention with TCO and linking them to the dye-Tz construct. The blood retention and extent of accumulation at the site of interest versus the pharmaceutical alone will be assessed using PA. This would be followed by comparative efficacy studies of the free drug versus the albumin conjugate.

7.2.3 Development of an instant kit for producing targeted PA imaging agents

Developing a new targeted PA agent typically requires multiple synthetic steps and extensive optimization. This approach requires new synthesis and optimization efforts for each new PA probe which is a costly and time-consuming process. A simple and more general-purpose method for producing PA imaging agents is needed to further advance this field. IR783-HYNIC-Tz (**28**) offers a convenient way to quickly create a targeted PA agent in a single step. To facilitate this, lyophilized kits containing **28** will be prepared so that upon addition of TCO-antibodies, a targeted PA imaging agent will be generated in high yield (Figure 7.1). Ready in under an hour and accessible to scientists not experienced with complex synthetic chemistry, compound **28** will expand research and accelerate and expedite new therapeutic and imaging agents to the clinic. These types of "instant kits" are widely used to generate ^{99m}Tc labelled molecules, and a key driver behind it becoming the most widely used isotope in diagnostic nuclear medicine.[1]

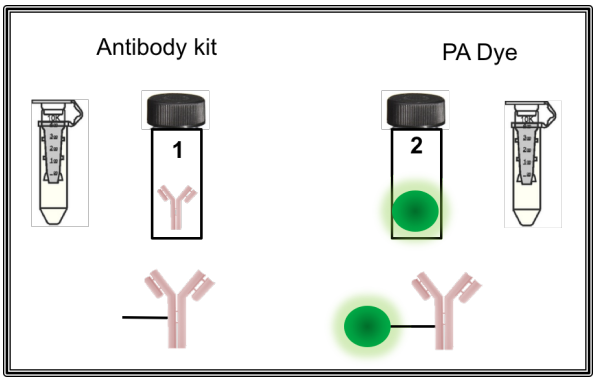

Figure 7.1 Photoacoustic imaging kit for commercialization.

7.3 References

[1] I. A. E. Agency, *Technetium-99m Radiopharmaceuticals: Manufacture of Kits*, **2008**.

Appendix I: Synthesis and Evaluation of Imidazole Fused Phenanthroline (PIP) Ligands as a Platform for the Preparation for Re(I) and ^{99m}Tc(I) Multimodal Probes

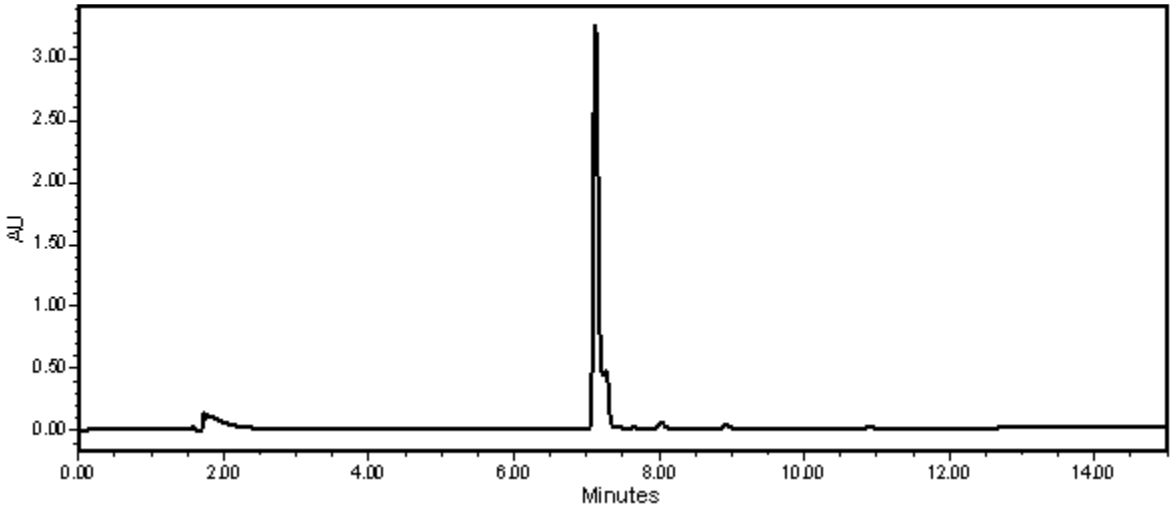

Figure S2.1 UV-HPLC trace of **3a** (Method B).

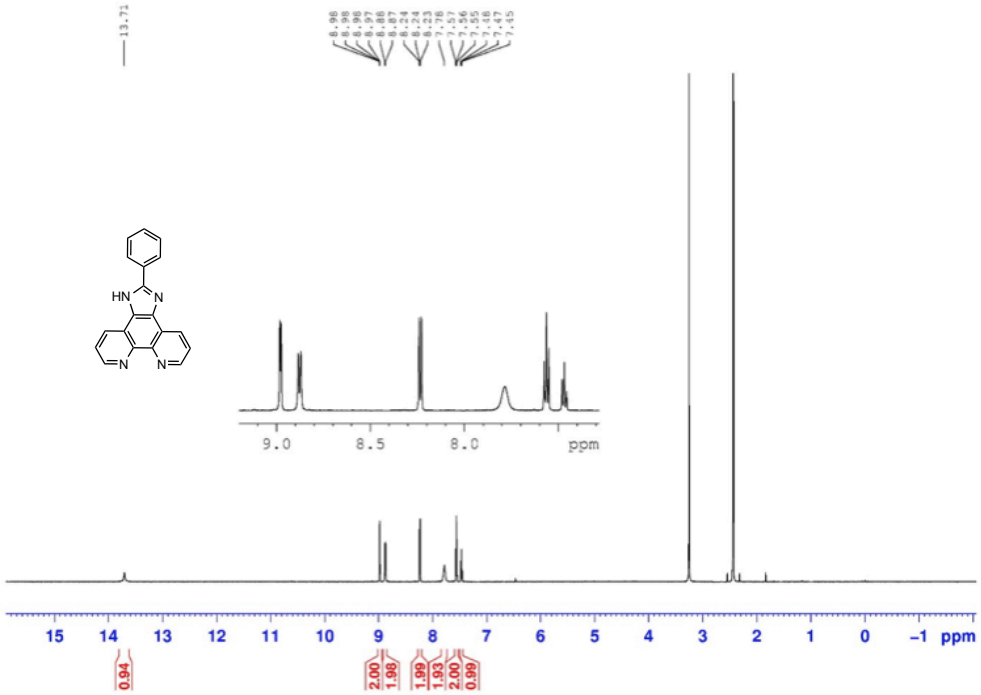

Figure S2.2 ^{1}H NMR spectrum ($(CD_3)_2SO$, 600 MHz) of **3a**.

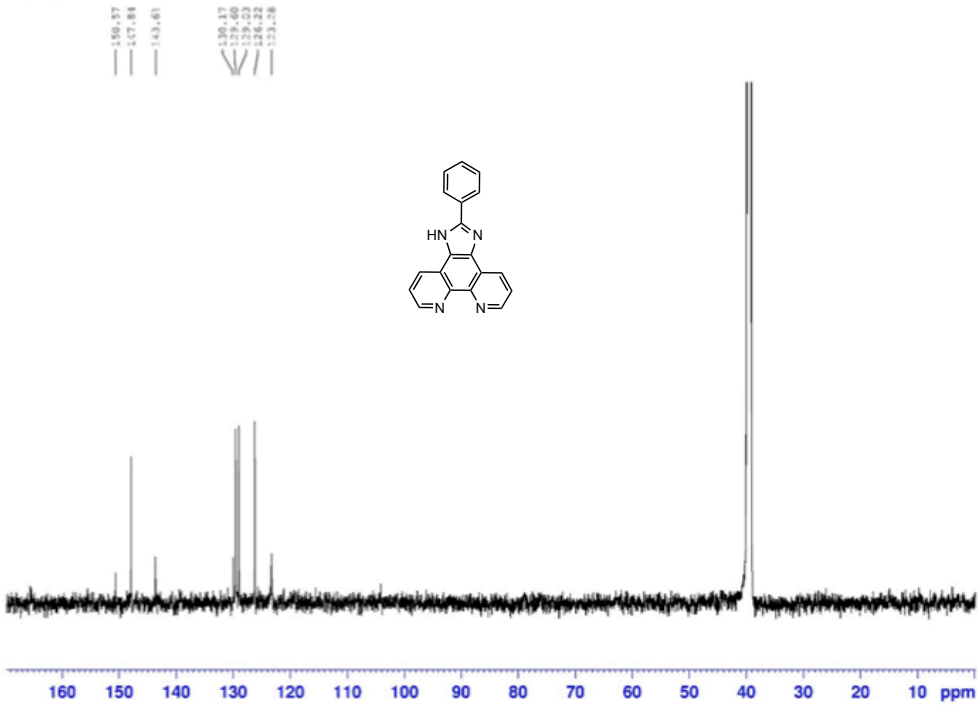

Figure S2.3 ^{13}C NMR spectrum ($(CD_3)_2SO$, 150 MHz) of the ligand **3a**.

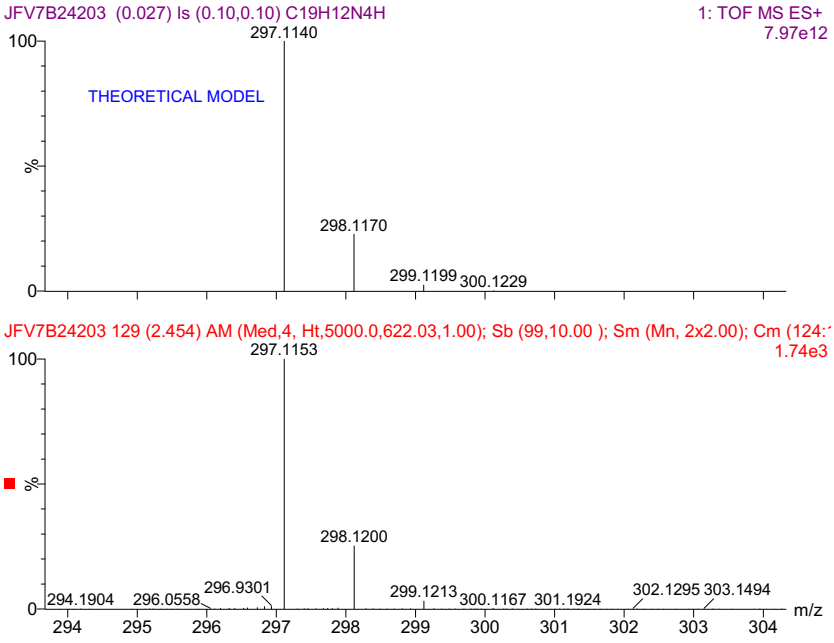

Figure S2.4 HRMS of **3a**.

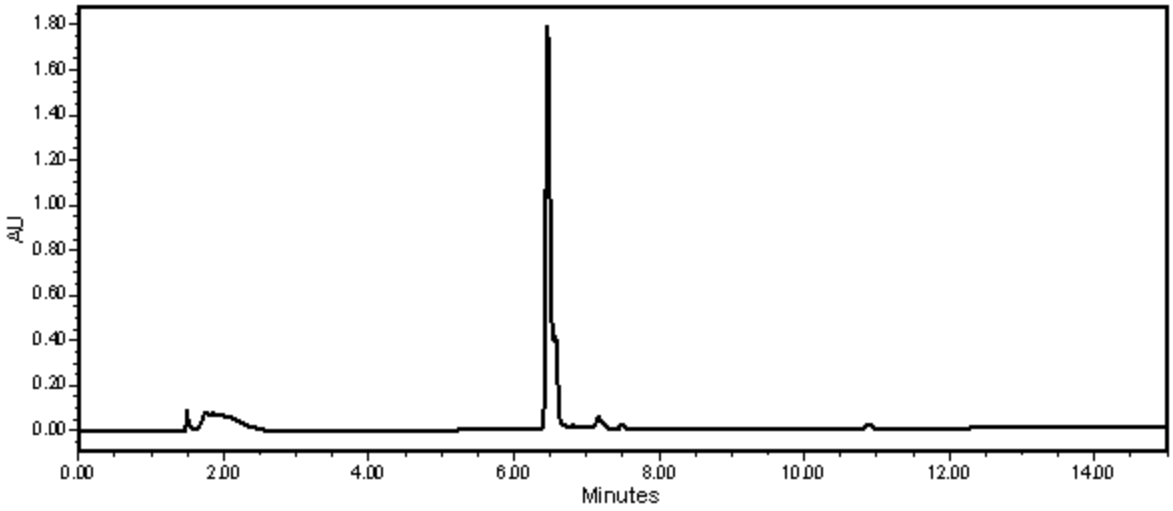

Figure S2.5 UV-HPLC trace of **3b** (Method B).

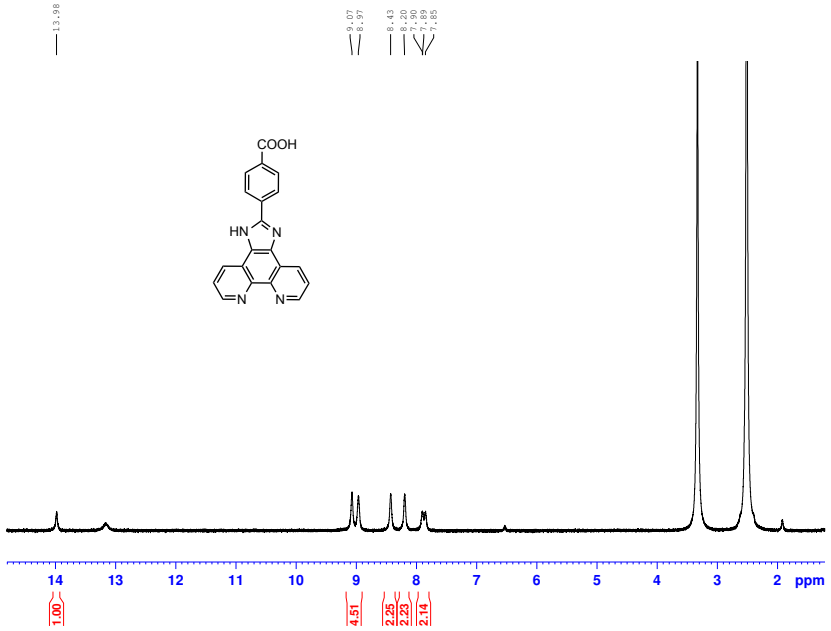

Figure S2.6 ^{1}H NMR spectrum ($(CD_3)_2SO$, 600 MHz) of **3b**.

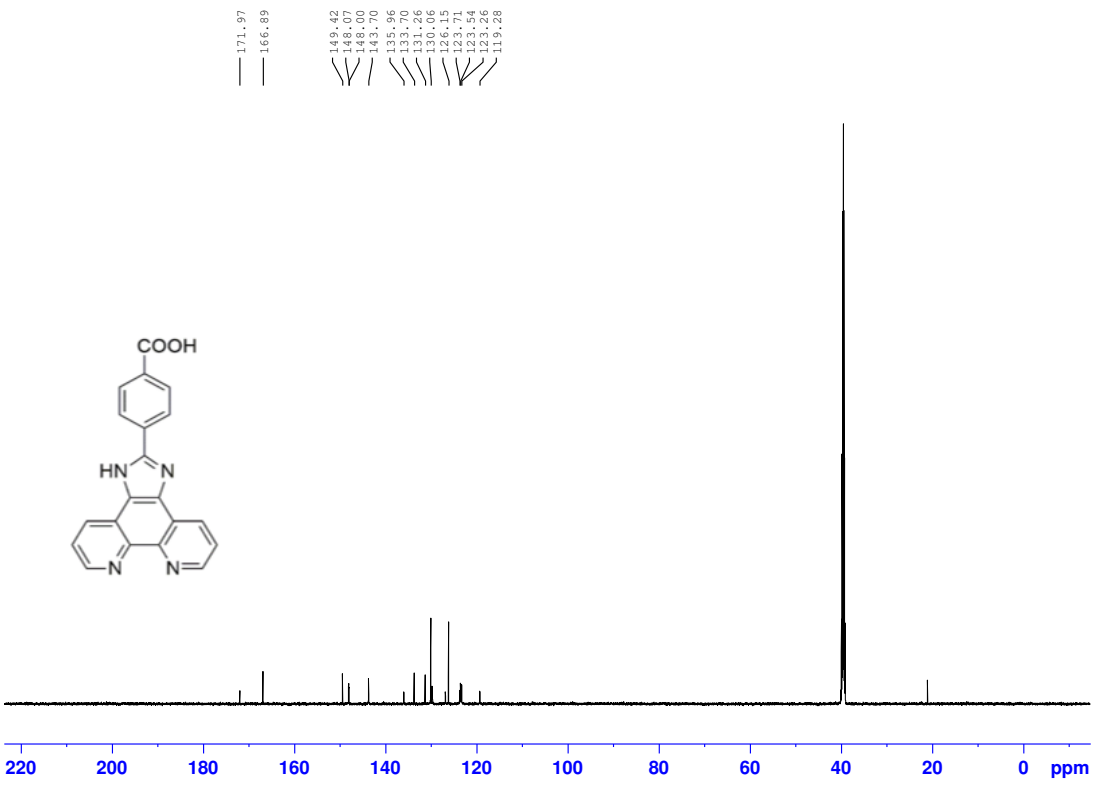

Figure S2.7 ^{13}C NMR spectrum ($(CD_3)_2SO$, 150 MHz) of **3b**.

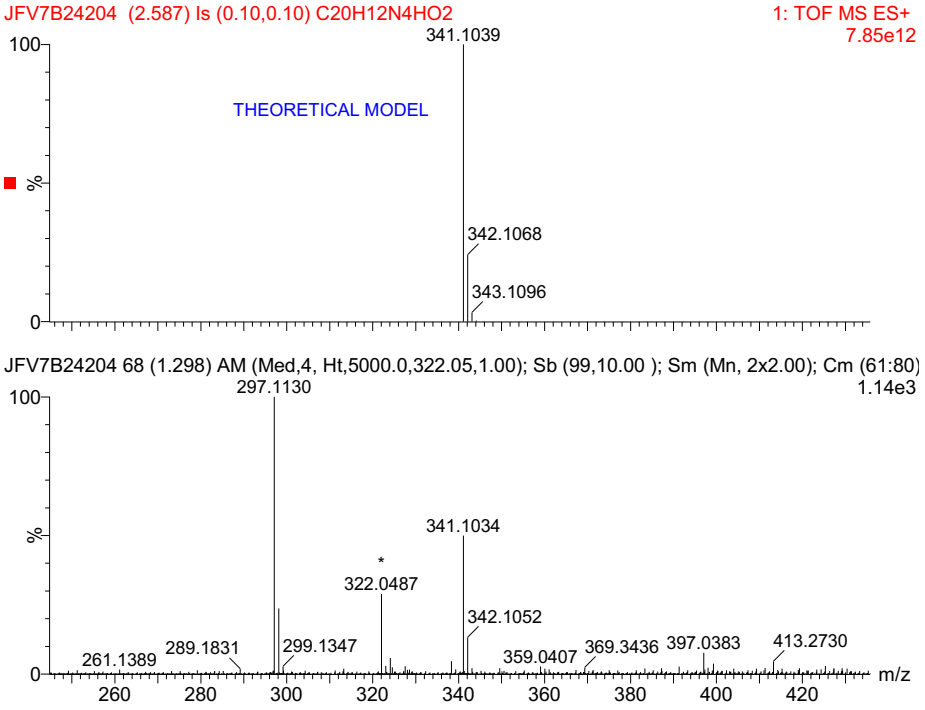

Figure S2.8 HRMS of **3b**.

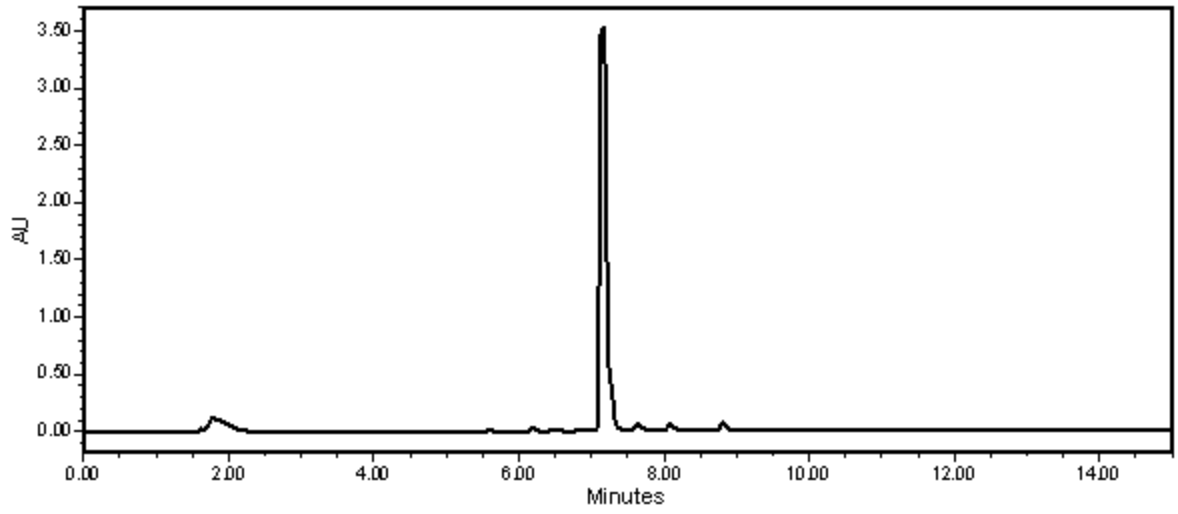

Figure S2.9 UV-HPLC trace of **3c** (Method B).

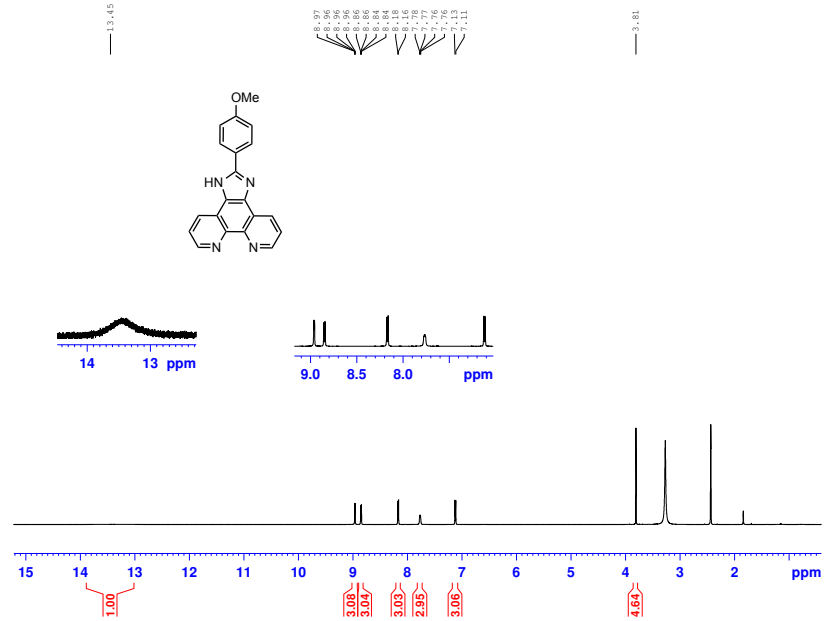

Figure S2.10 ^{1}H NMR spectrum (CD_3OD, 600 MHz) of **3c**.

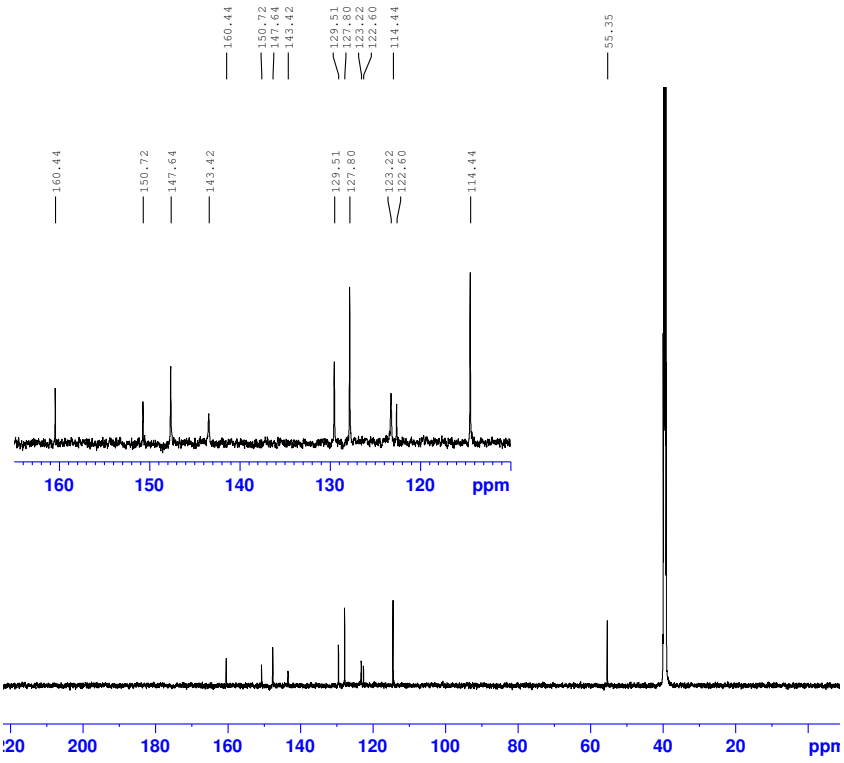

Figure S2.11 ^{13}C NMR spectrum (CD_3OD, 150 MHz) of **3c**.

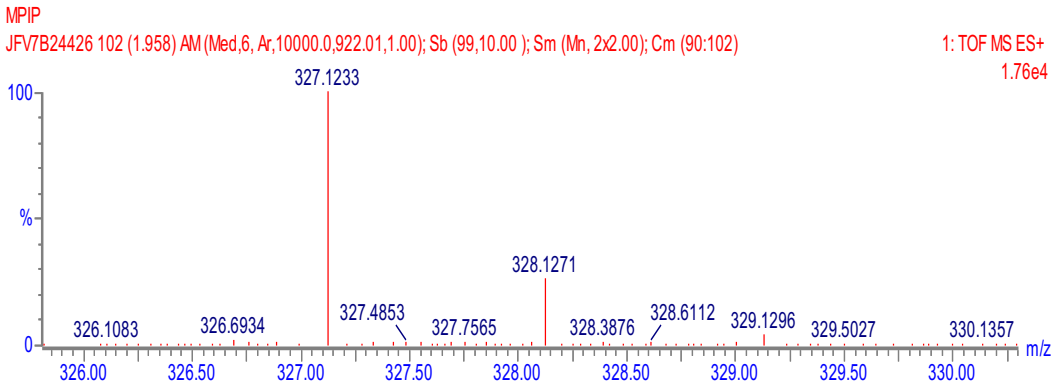

Figure S2.12 HRMS of **3c**.

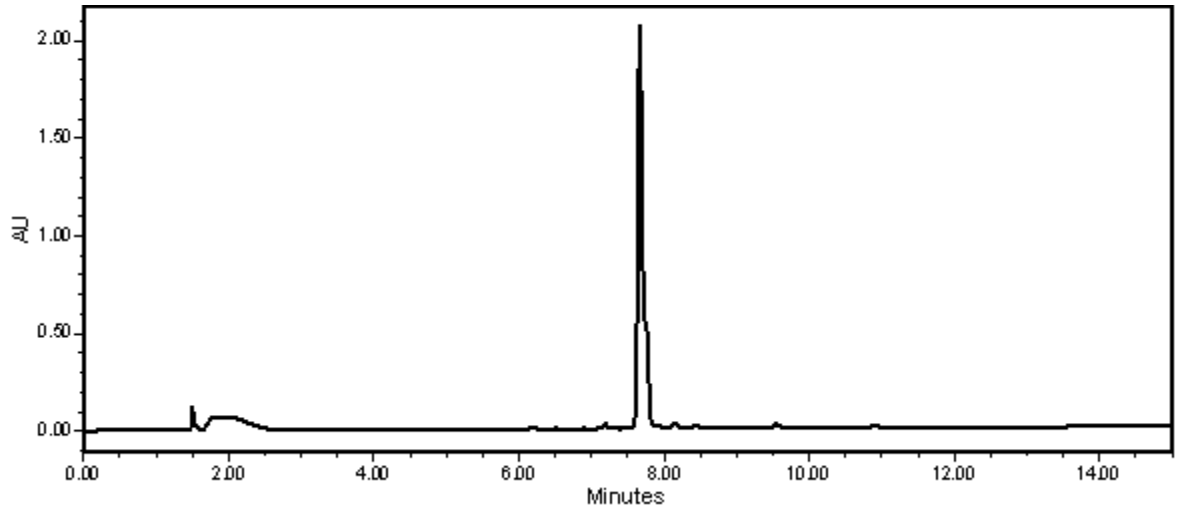

Figure S2.13 UV-HPLC trace of **3d** (Method B).

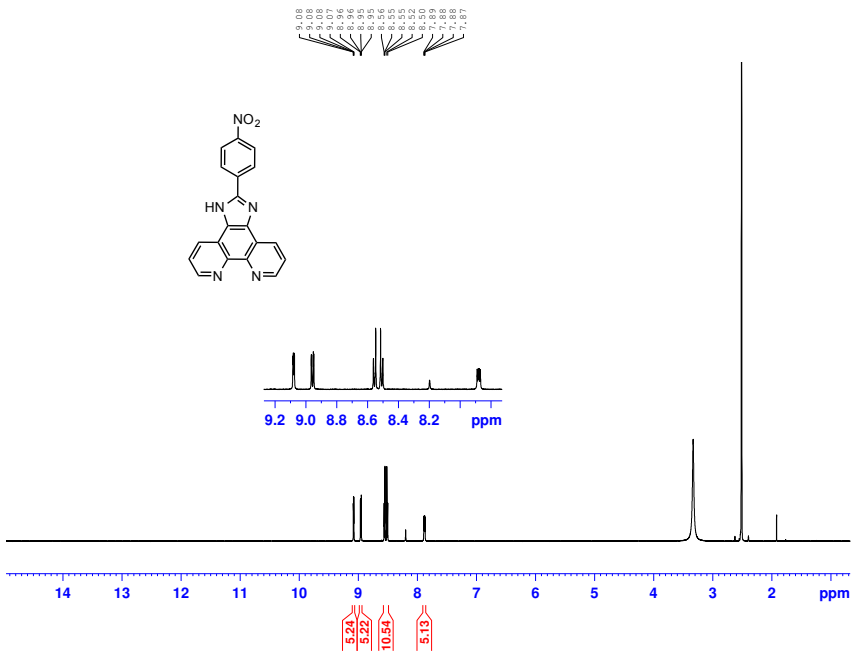

Figure S2.14 ^{1}H NMR spectrum ($(CD_3)_2SO$, 600 MHz) of **3d**.

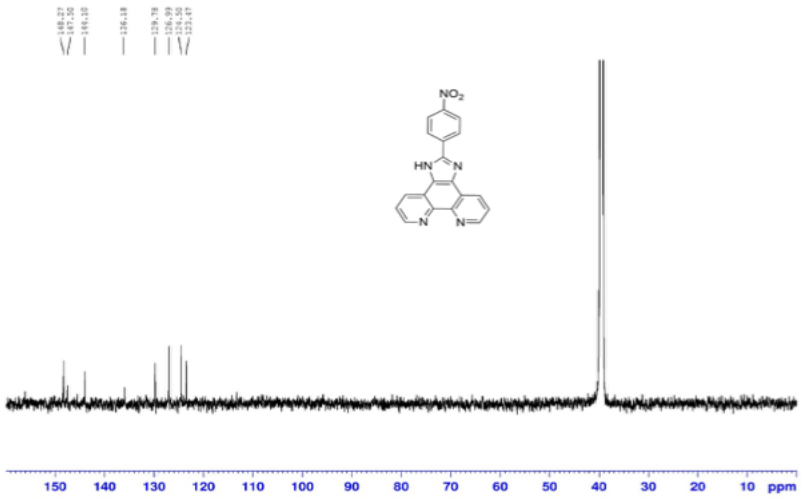

Figure S2.15 ^{13}C NMR spectrum ($(CD_3)_2SO$, 150 MHz) of **3d**.

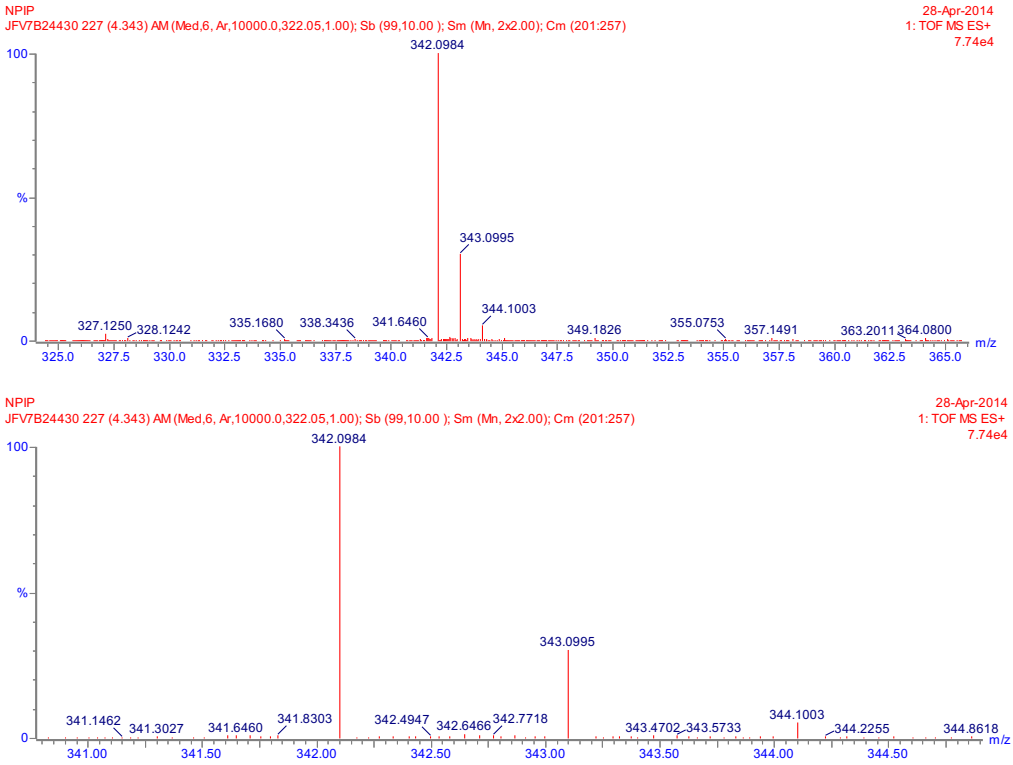

Figure S2.16 HRMS of **3d**.

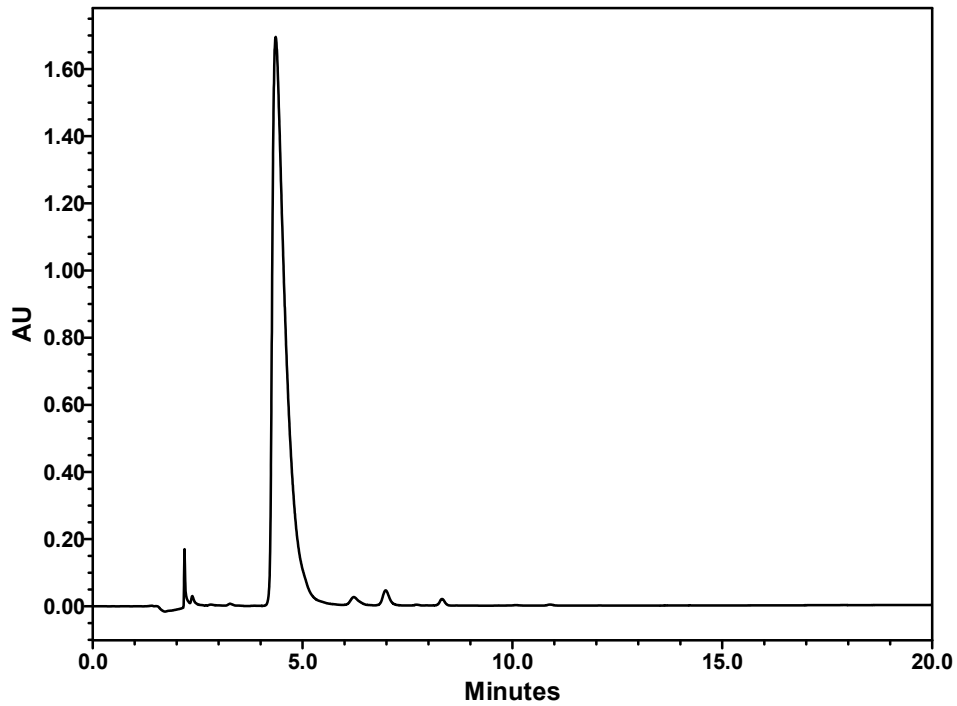

Figure S2.17 UV-HPLC trace of **3e** (Method C).

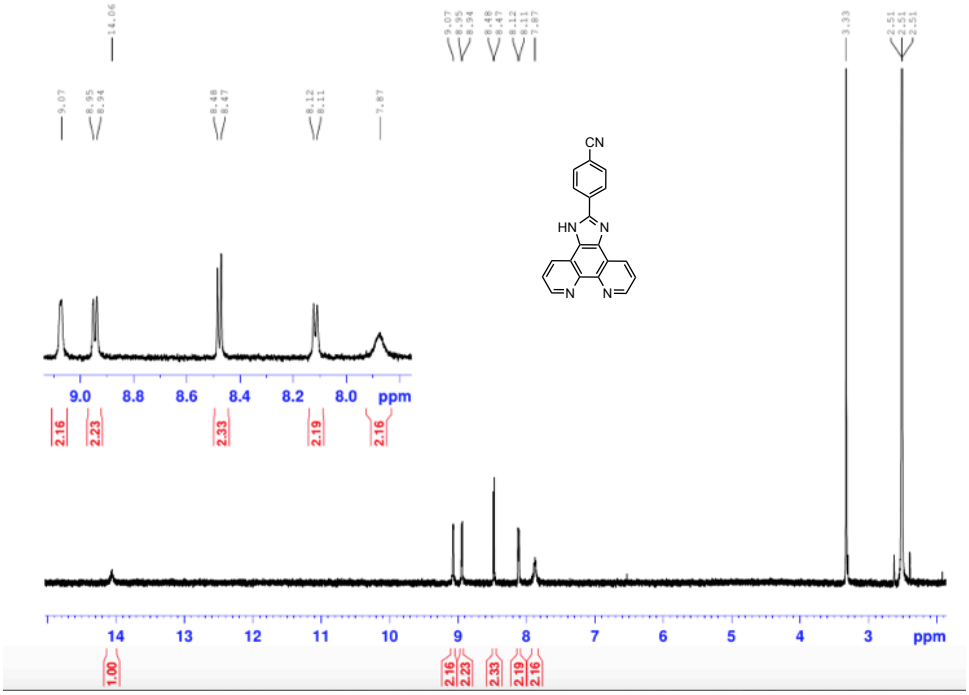

Figure S2.18 ^{1}H NMR spectrum ($(CD_3)_2SO$, 600 MHz) of **3e**.

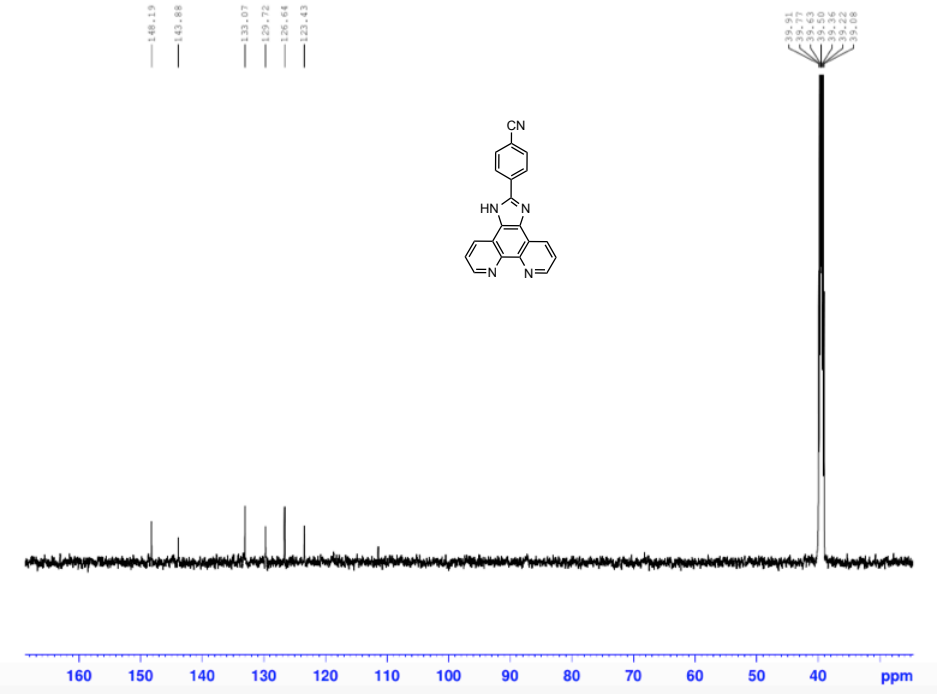

Figure S2.19 ^{13}C NMR spectrum ($(CD_3)_2SO$, 150 MHz) of 3e.

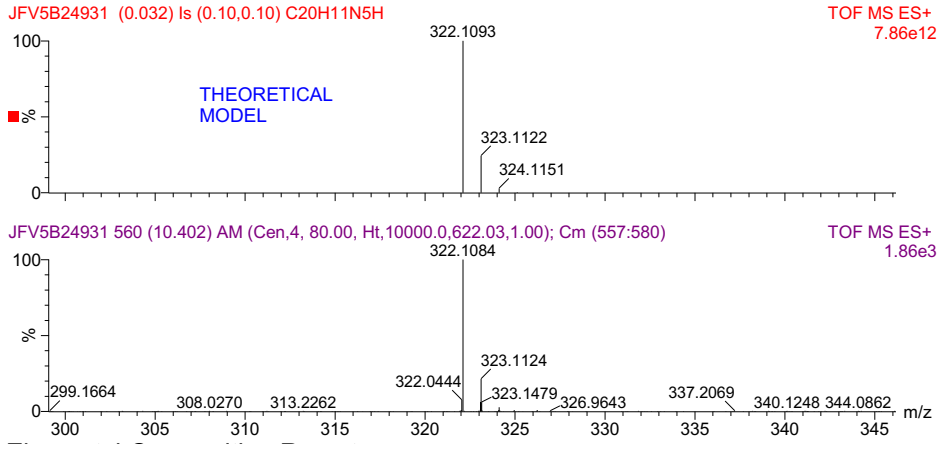

Figure S2.20 HRMS of 3e.

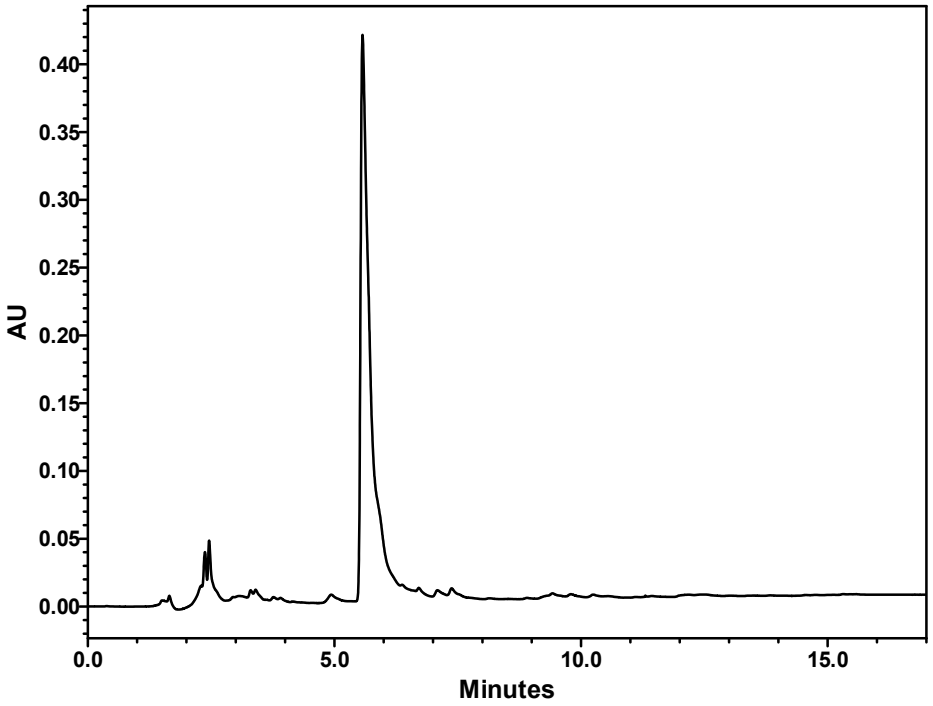

Figure S2.21 UV-HPLC trace of **3f** (Method C).

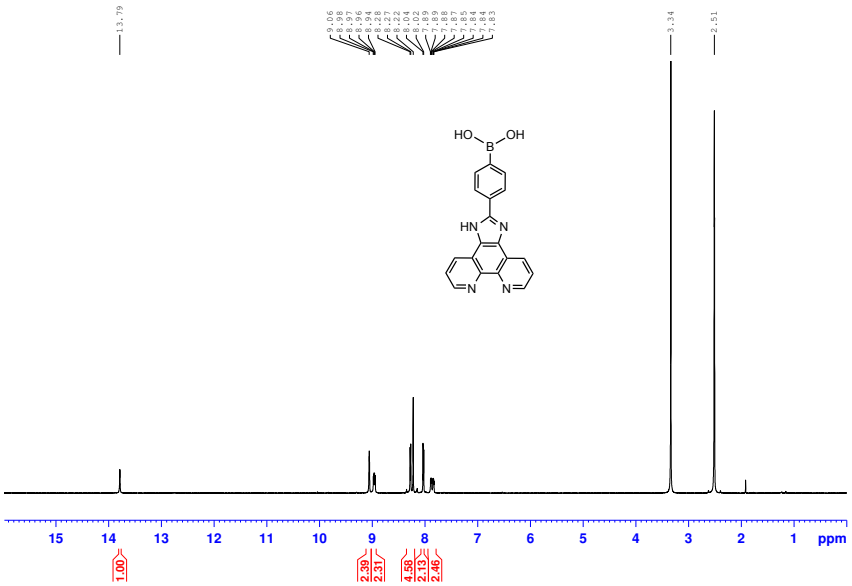

Figure S2.22 ^{1}H NMR ($(CD_3)_2SO$), 600 MHz) of **3f**.

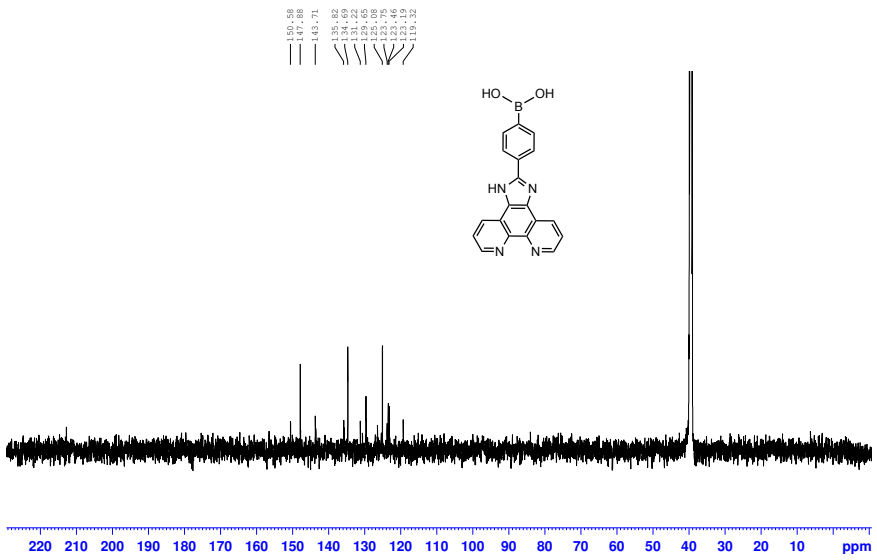

Figure S2.23 ^{13}C NMR ($(CD_3)_2SO$), 150 MHz) of **3f**.

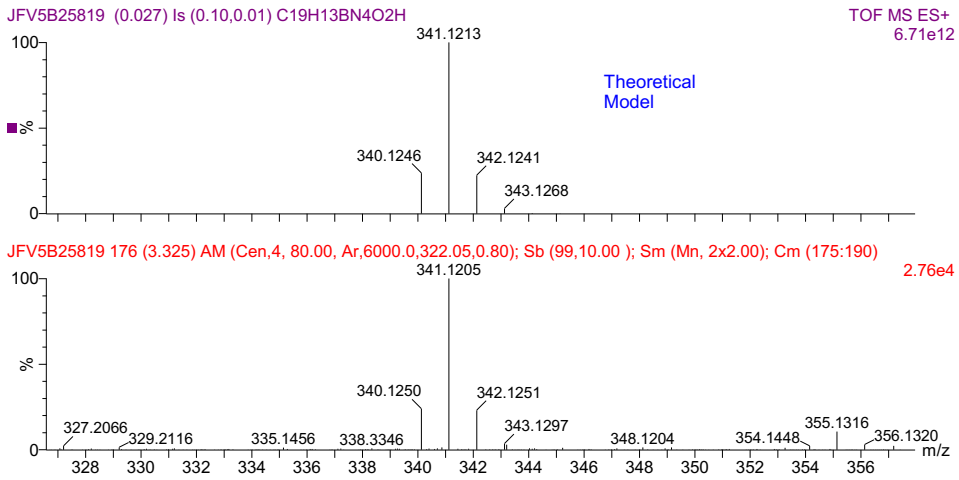

Figure S2.24 HRMS of **3f**.

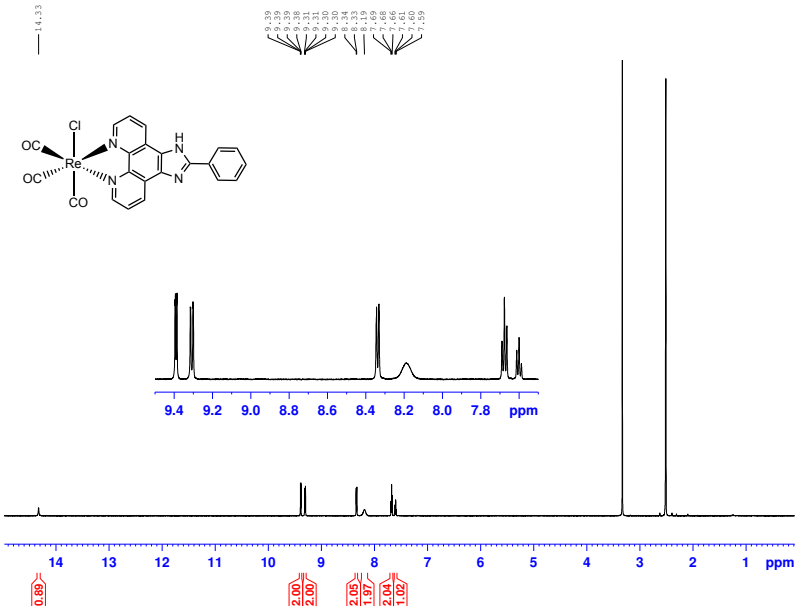

Figure S2.25 ^{1}H NMR spectrum ($(CD_3)_2SO$, 600 MHz) of **4a**.

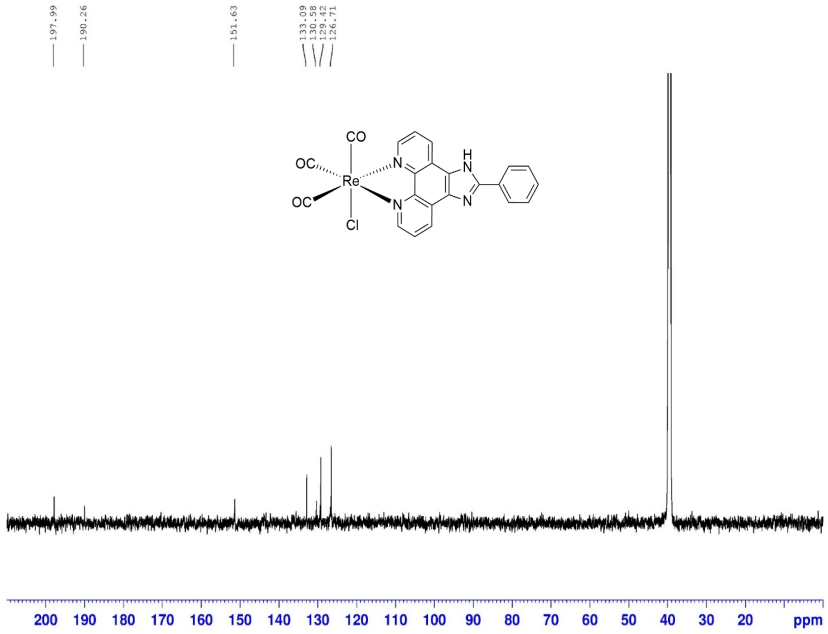

Figure S2.26 ^{13}C NMR spectrum ($(CD_3)_2SO$, 150 MHz) of **4a**.

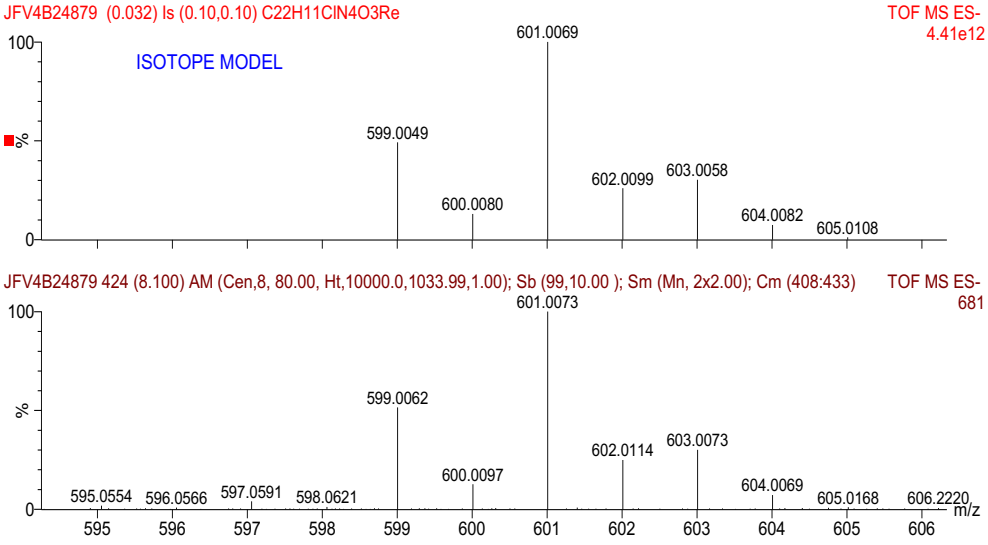

Figure S2.27 HRMS of **4a**.

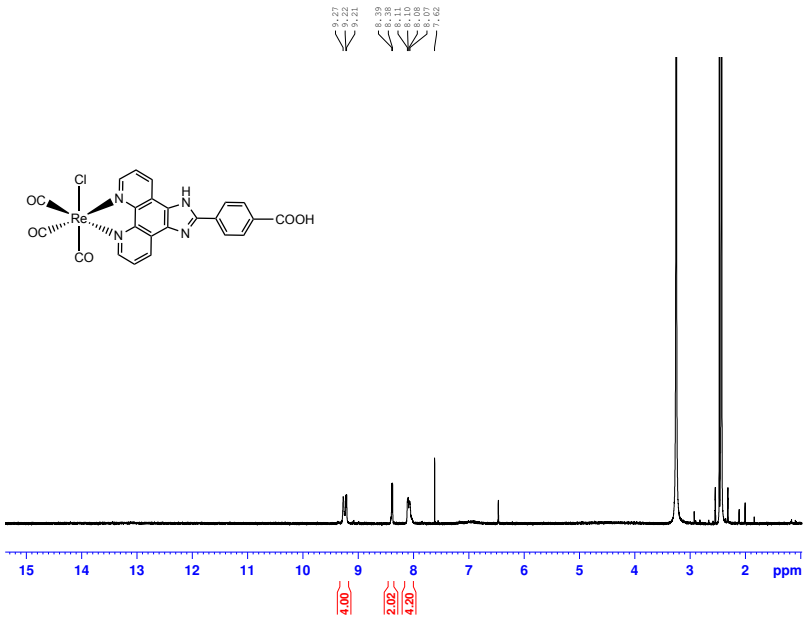

Figure S2.28 ^{1}H NMR spectrum ($(CD_3)_2SO$, 600 MHz) of **4b**.

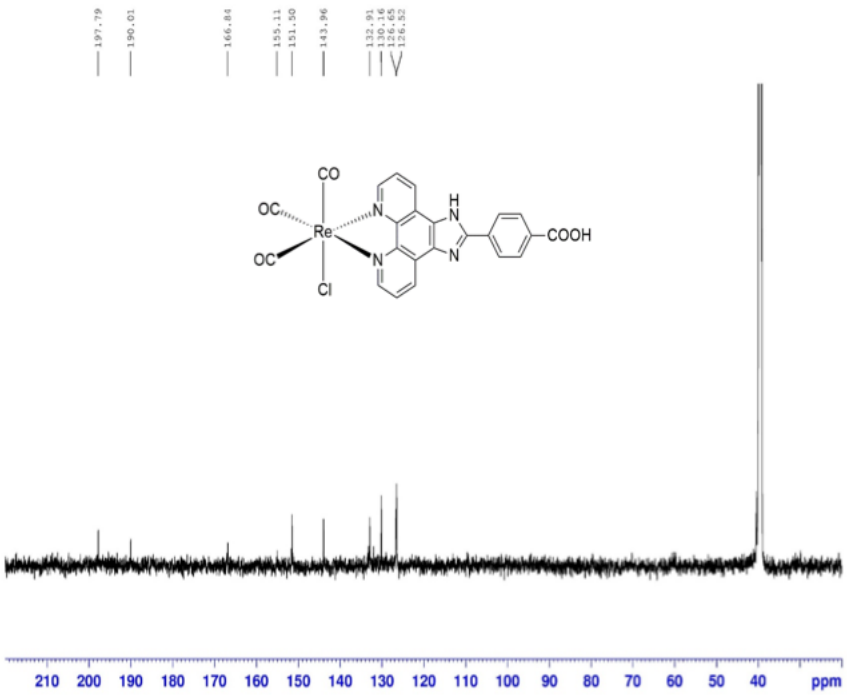

Figure S2.29 ^{13}C NMR spectrum ($(CD_3)_2SO$, 150 MHz) of **4b**.

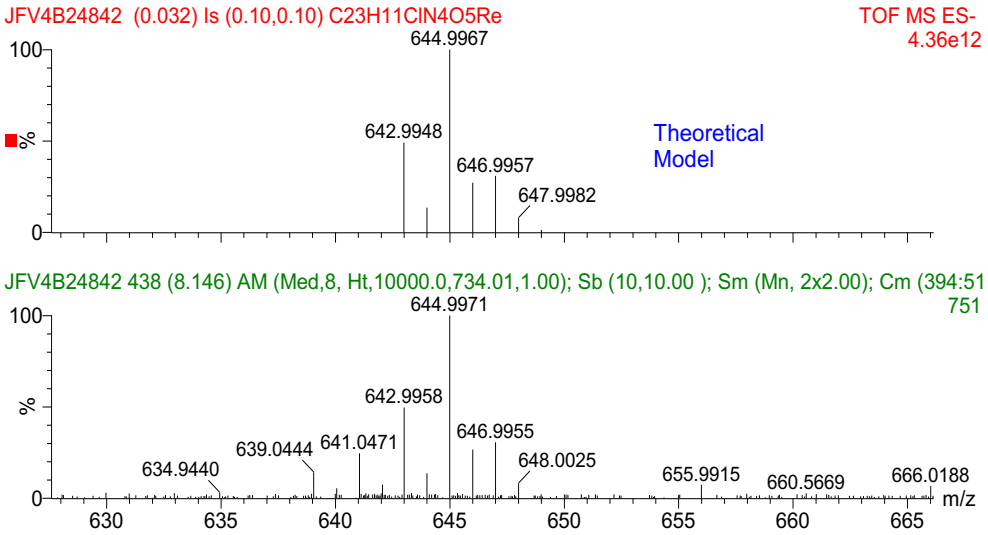

Figure S2.30 HRMS of **4b**.

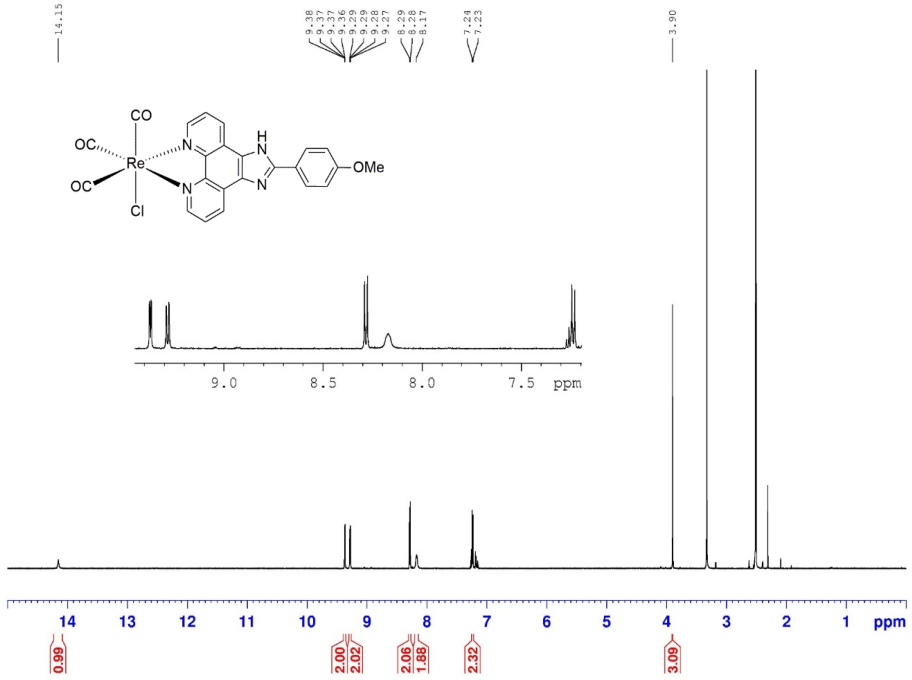

Figure S2.31 ^{1}H NMR spectrum ($(CD_3)SO$, 600 MHz) of **4c**.

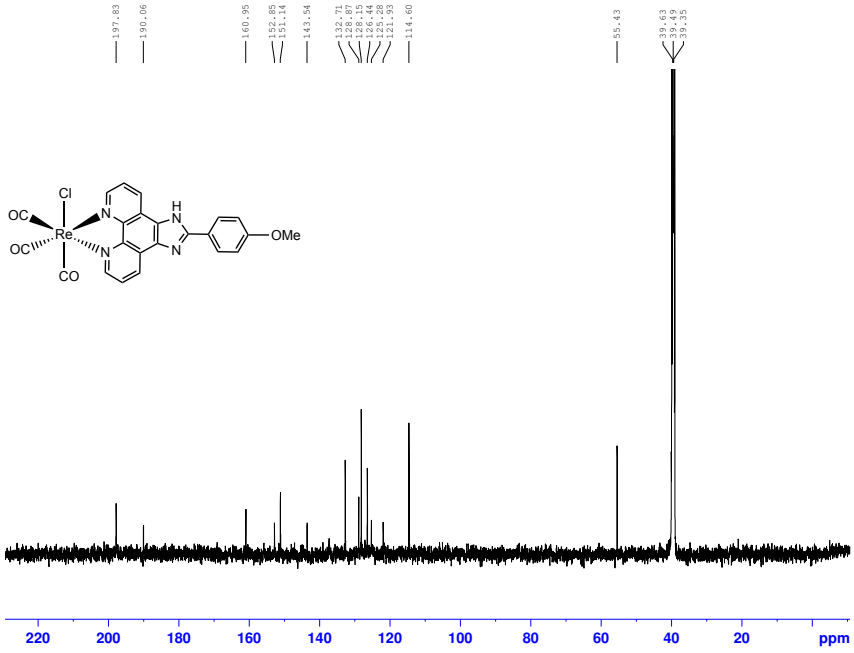

Figure S2.32 ^{13}C NMR spectrum ((CD$_3$)SO, 150 MHz) of **4c**.

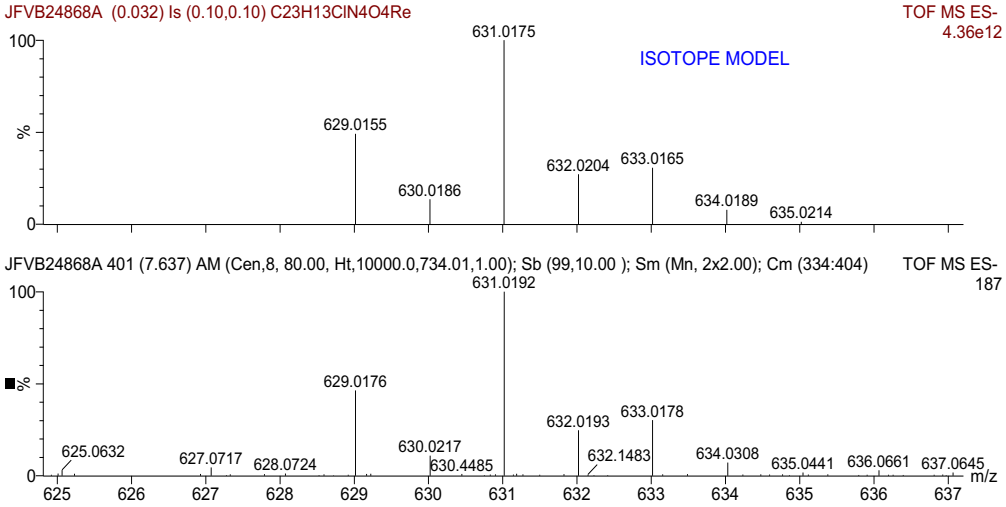

Figure S2.33 HRMS of **4c**.

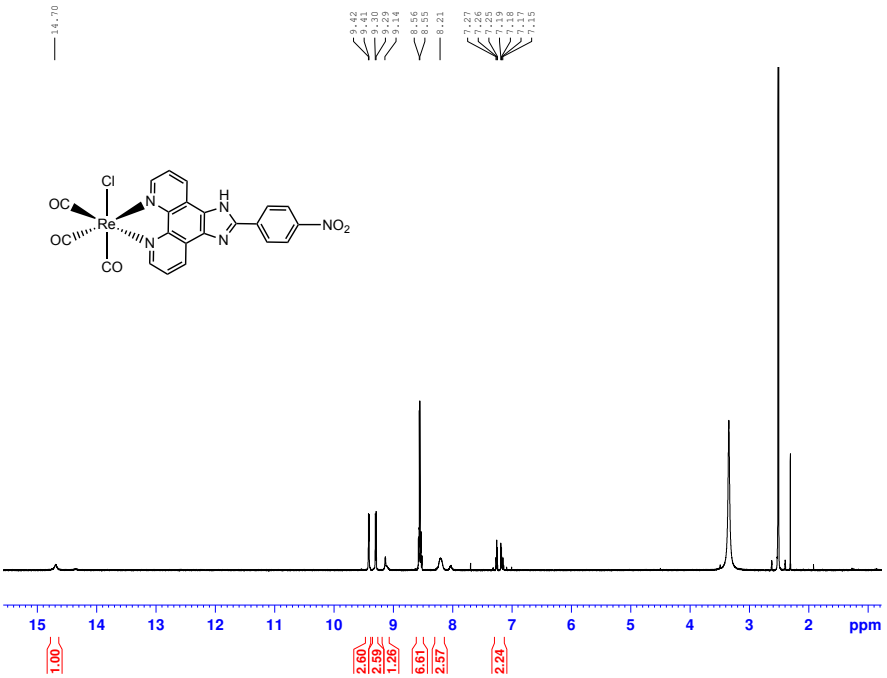

Figure S2.34 ^{1}H NMR spectrum ((CD$_3$)SO, 600 MHz) of **4d**.

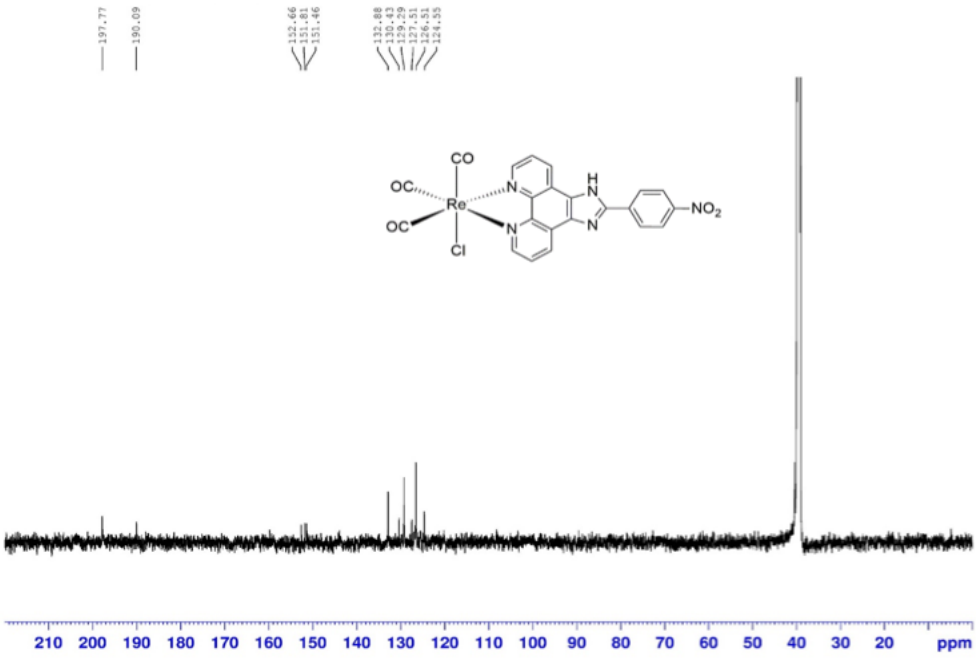

Figure S2.35 ^{13}C NMR spectrum ((CD$_3$)SO, 150 MHz) of **4d**.

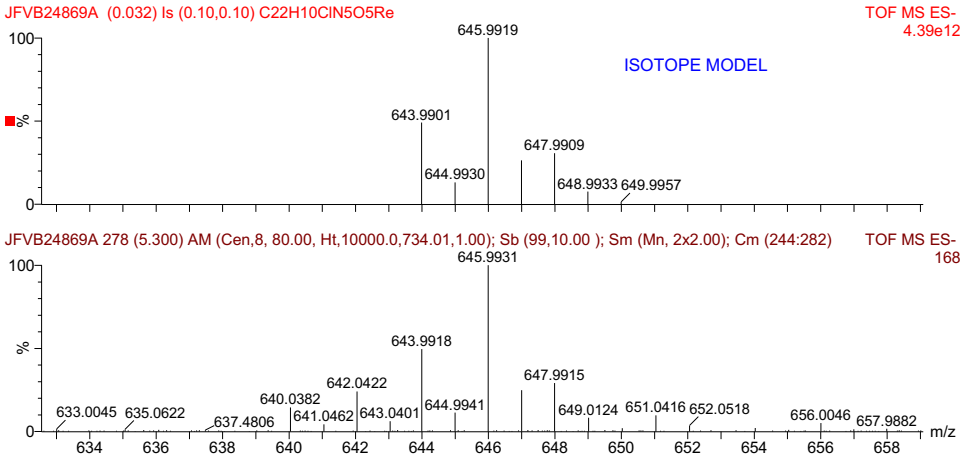

Figure S2.36 HRMS of **4d**.

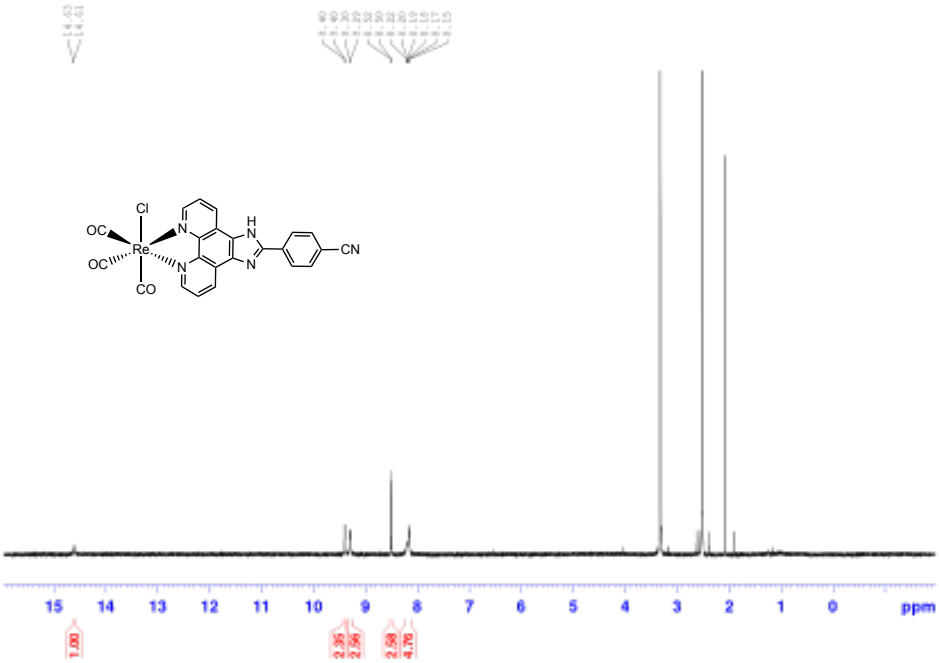

Figure S2.37 ^{1}H NMR spectrum ($(CD_3)_2SO$), 600 MHz) of **4e**.

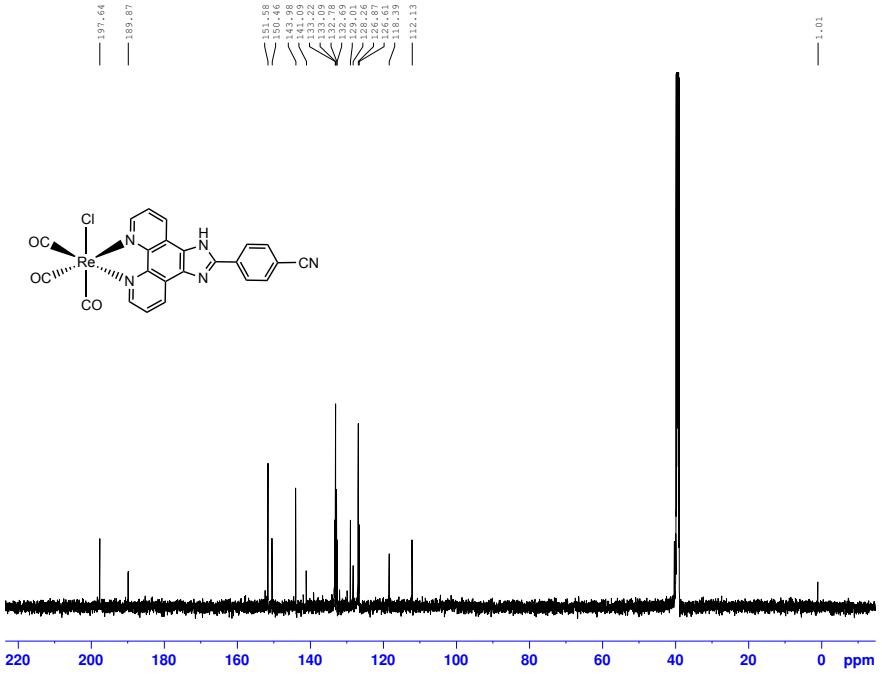

Figure S2.38 ^{13}C NMR spectrum ($(CD_3)_2SO$), 600 MHz) of **4e**.

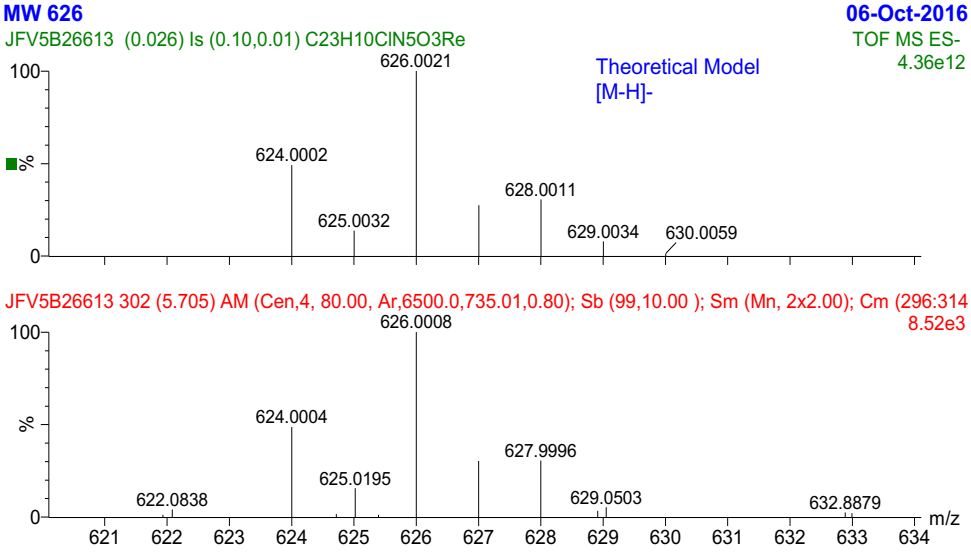

Figure S2.39 HRMS of **4e**.

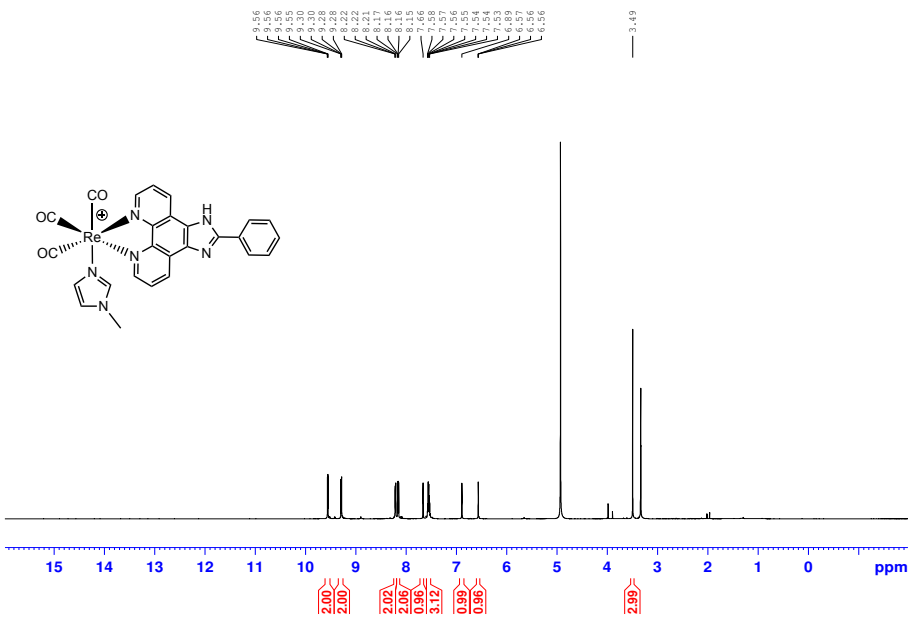

Figure S2.40 ^{1}H NMR spectrum (CD_3OD, 600 MHz) of **5a**.

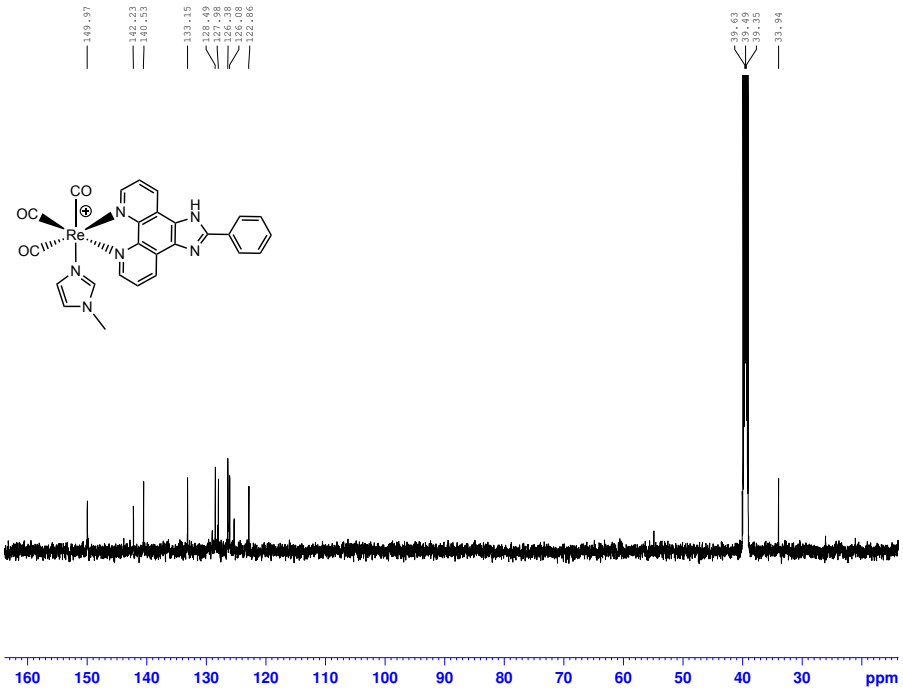

Figure S2.41 ^{13}C NMR spectrum ($(CD_3)_2SO$, 150 MHz) of **5a**.

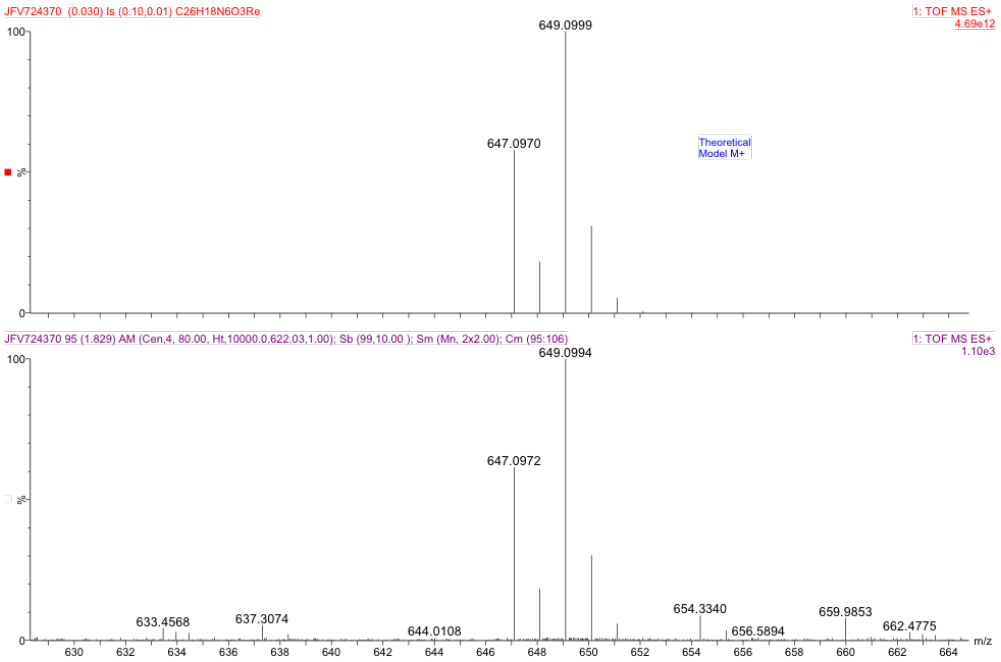

Figure S2.42 HRMS of **5a**.

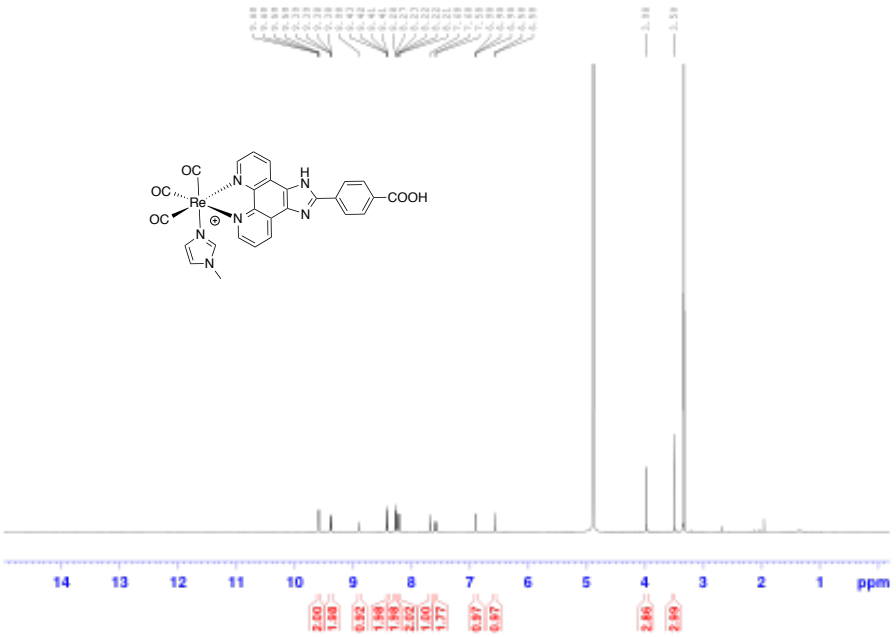

Figure S2.43 ^{1}H NMR spectrum (CD_3)D, 600 MHz) of **5b**.

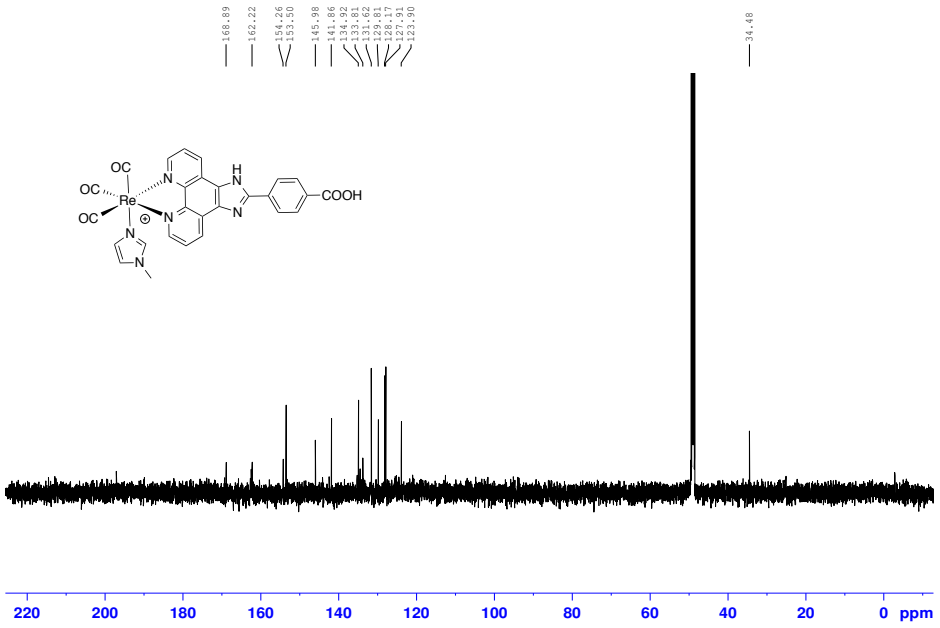

Figure S2.44 ^{13}C NMR spectrum (CD_3OD, 150 MHz) of 5b.

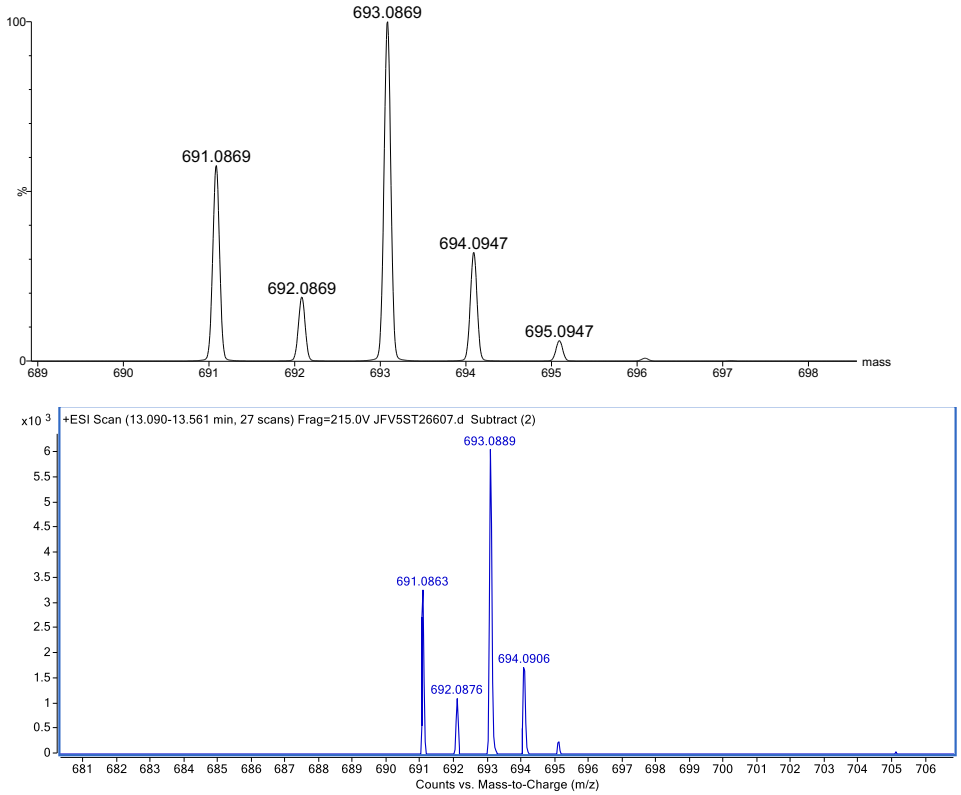

Figure S2.45 HRMS of 5b.

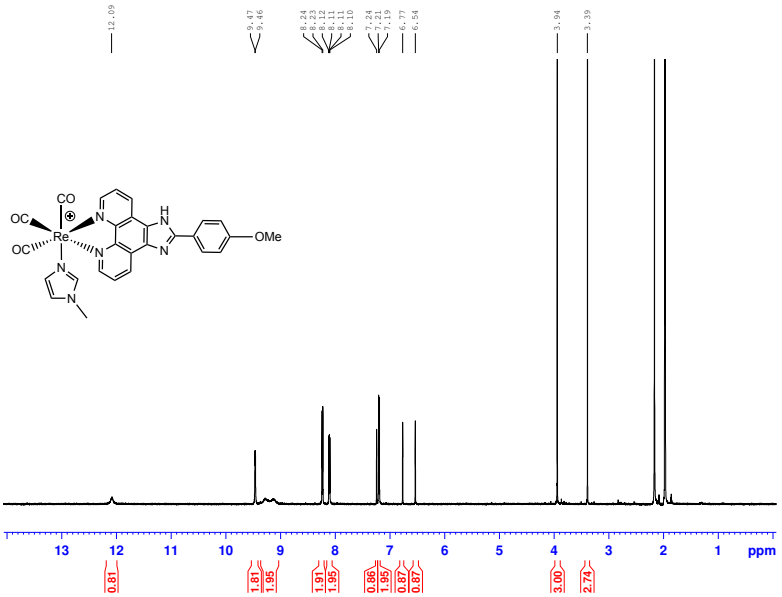

Figure S2.46 ^{1}H NMR spectrum (CD_3CN, 600 MHz) of **5c**.

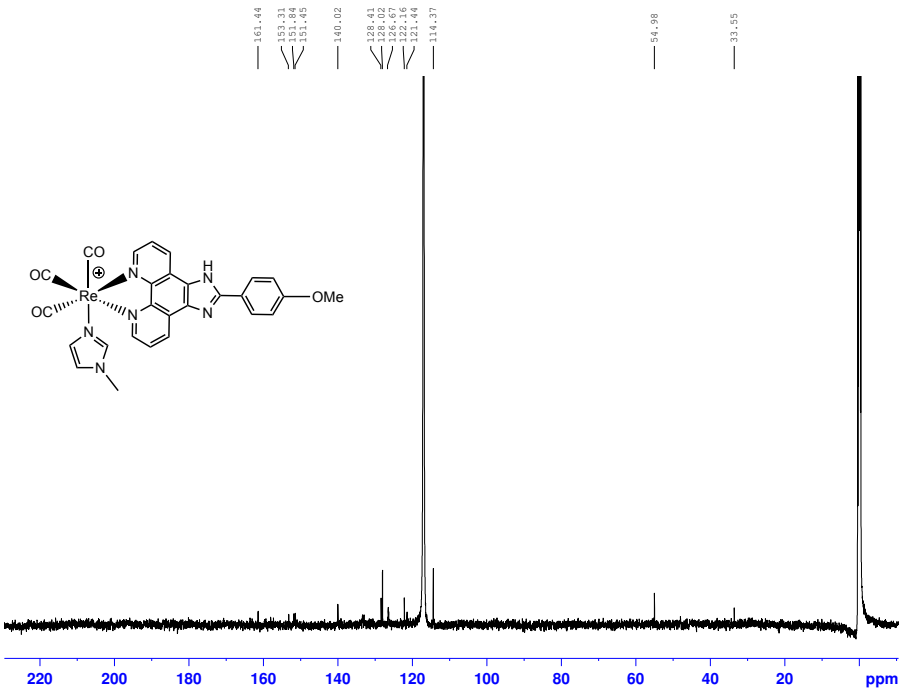

Figure S2.47 ^{13}C NMR spectrum (CD_3CN, 150 MHz) of **5c**.

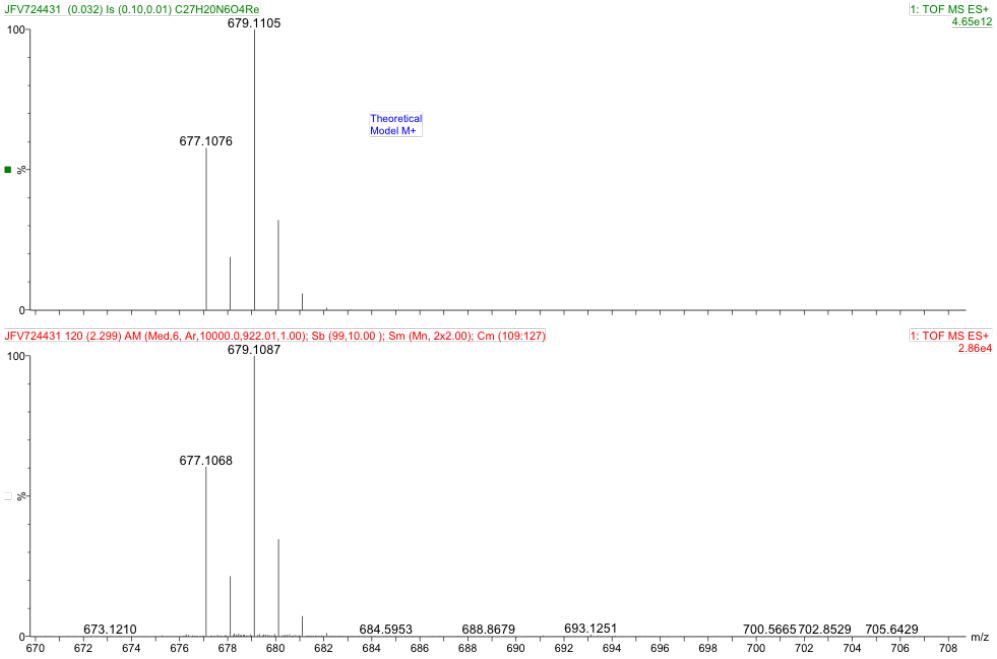

Figure S2.48 HRMS of **5c**.

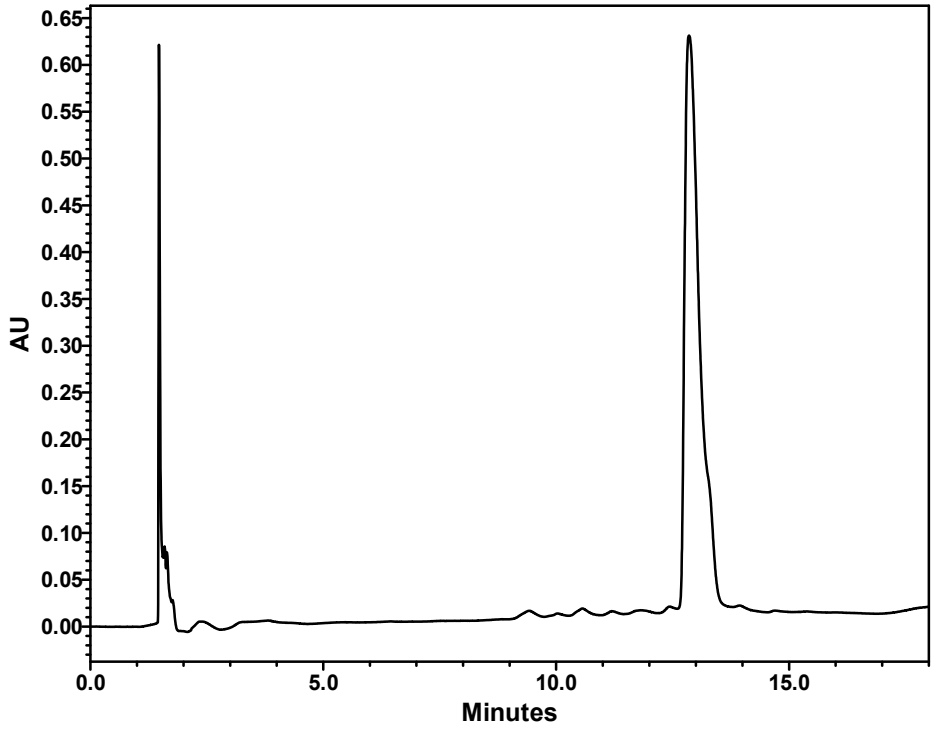

Figure S2.49 UV-HPLC trace of **5e** (Method D).

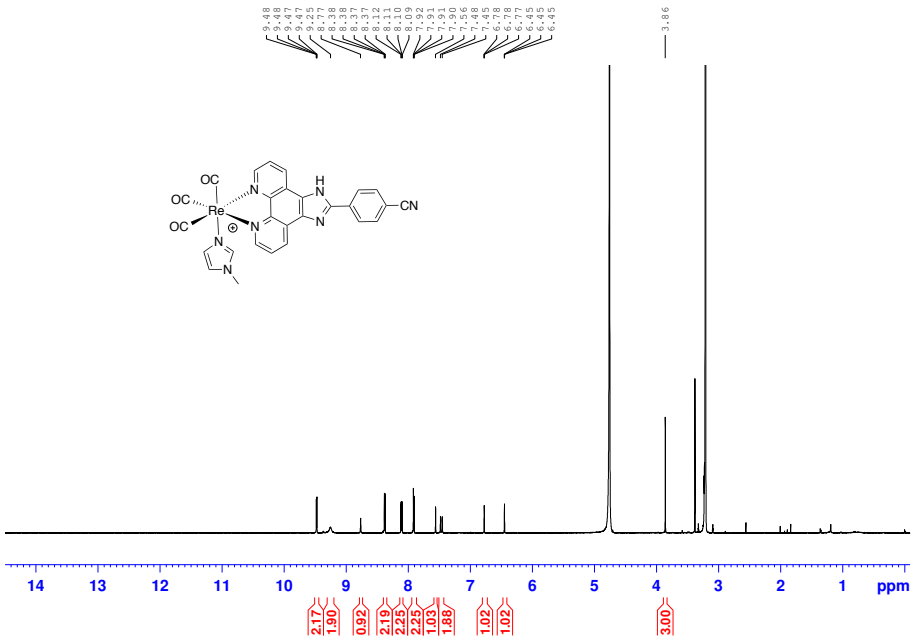

Figure S2.50 ^{1}H NMR spectrum (CD_3OD), 600 MHz) of **5e**.

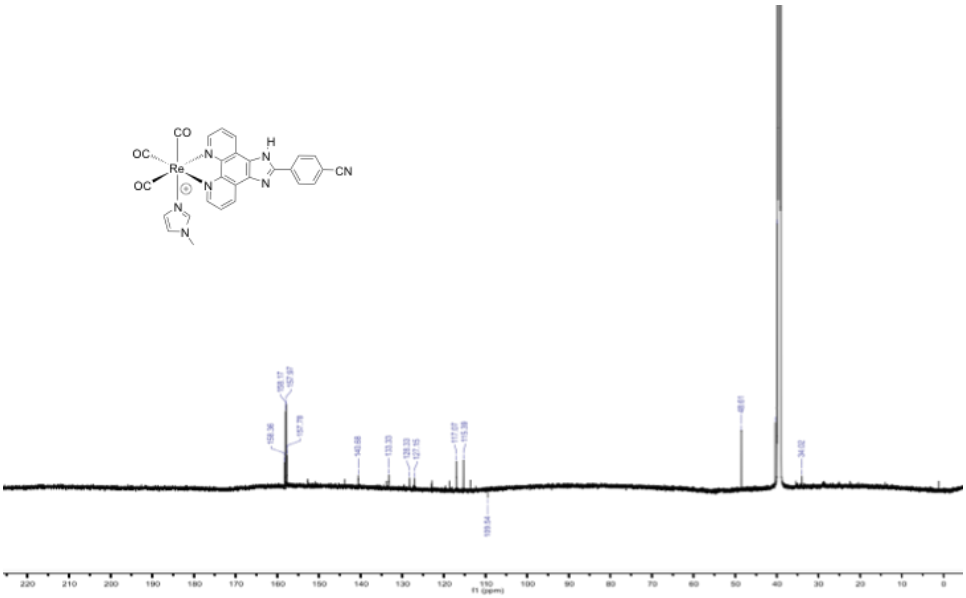

Figure S2.51 ^{13}C NMR Spectrum (CD_3OD), 150 MHz) of **5e**.

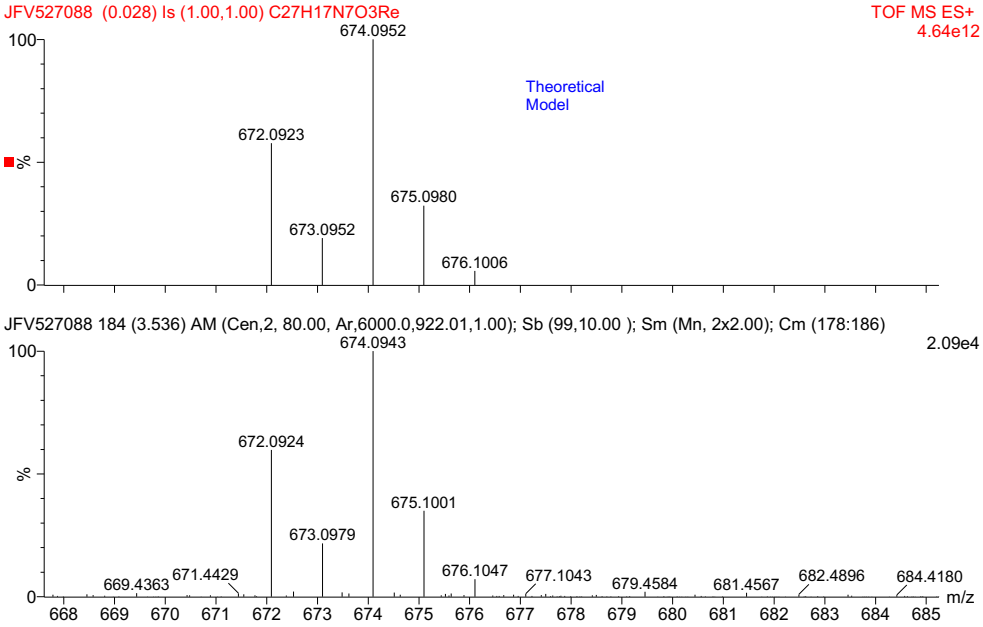

Figure S2.52 HRMS of **5e**.

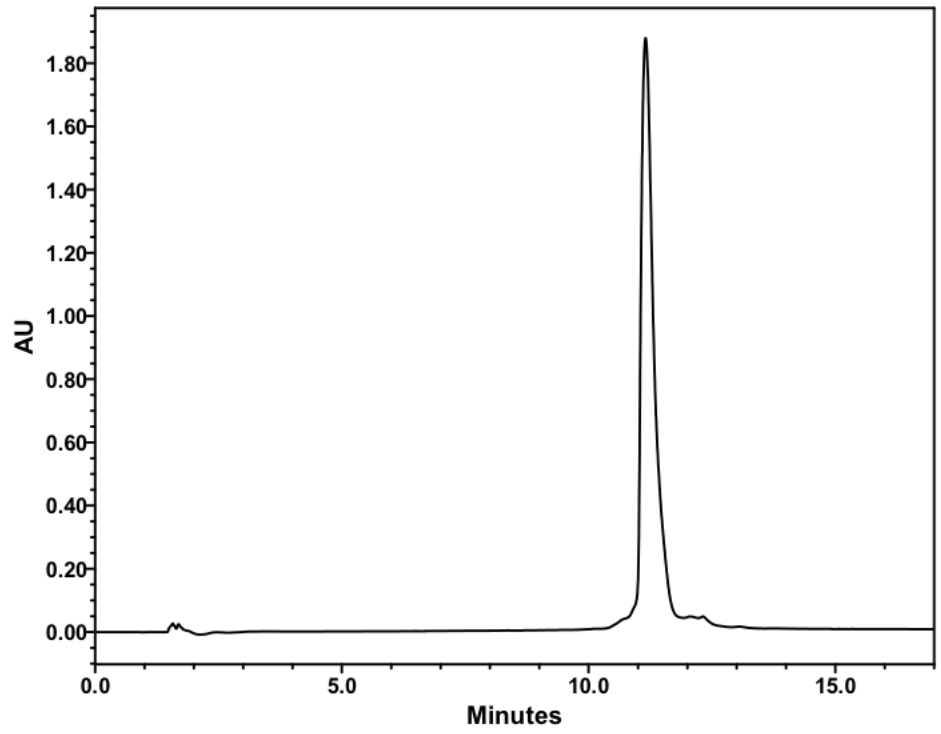

Figure S2.53 UV-HPLC trace of **5f** (Method D).

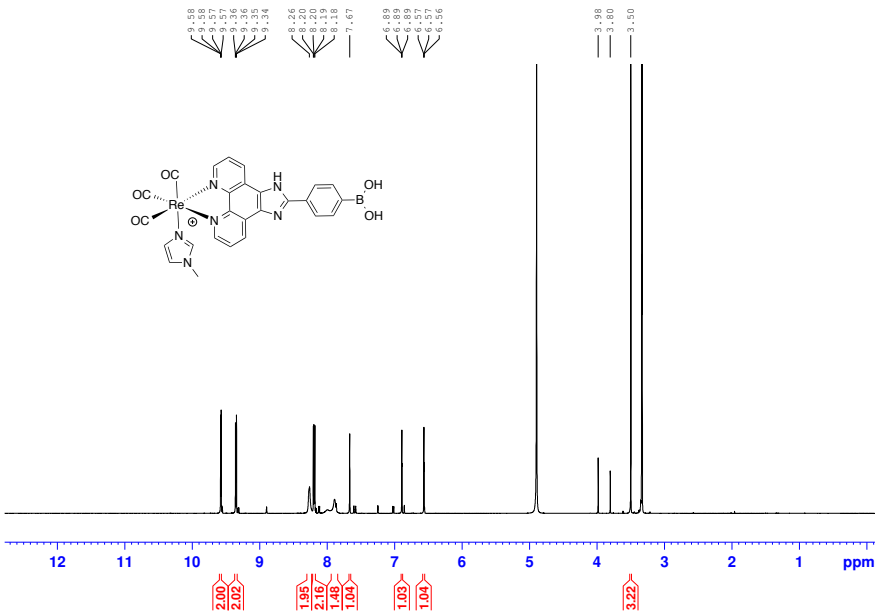

Figure S2.54 ^{1}H NMR spectrum (CH_3)D, 600 MHz) of **5f**.

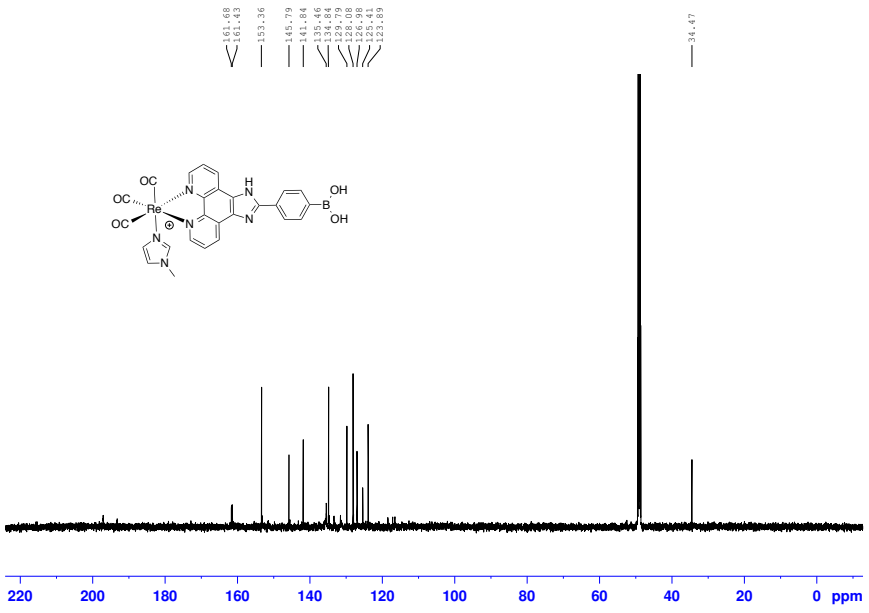

Figure S2.55 ^{13}C NMR spectrum (CD_3OD, 150 MHz) of **5f**.

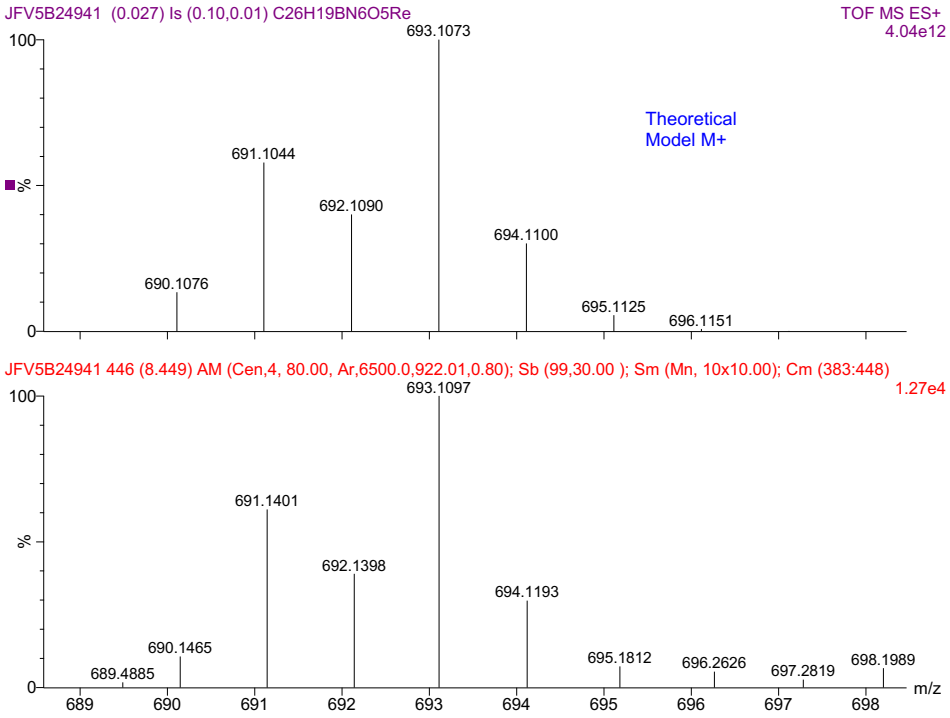

Figure S2.56 HRMS of **5f**.

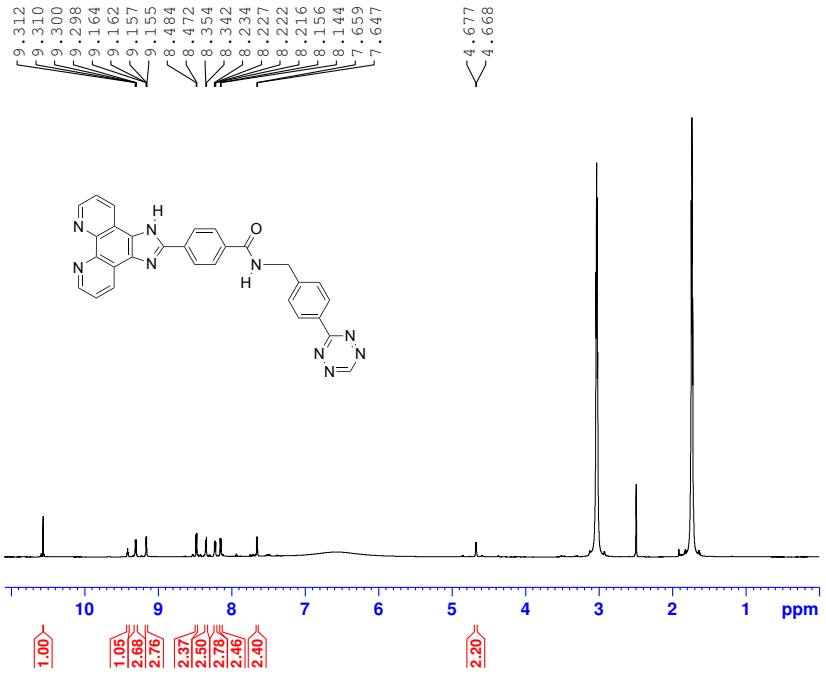

Figure S2.57 ^{1}H NMR spectrum ($(CD_3)_2SO$), 600 MHz) of **9.**

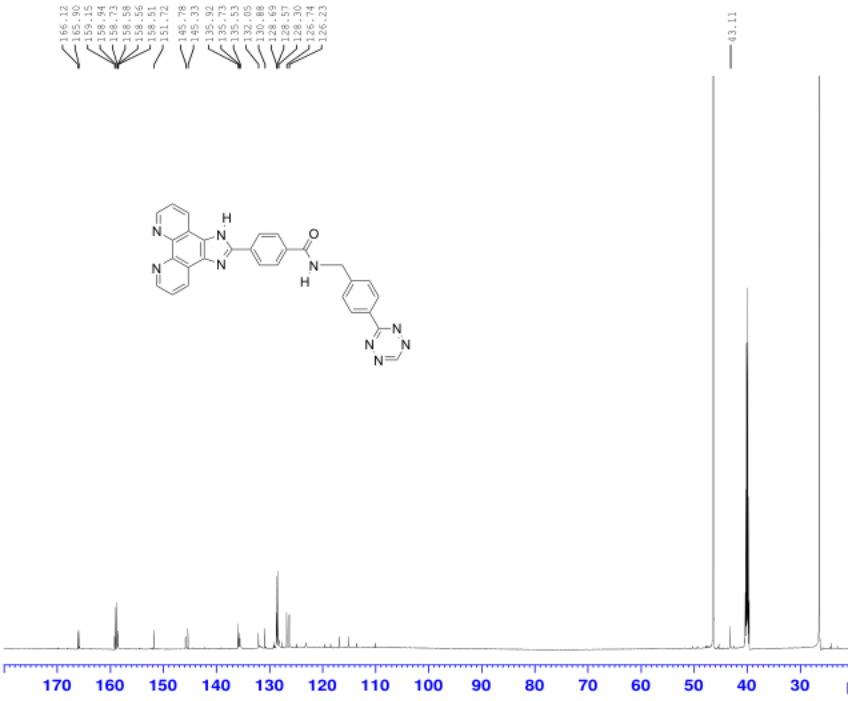

Figure S2.58 ^{13}C NMR spectrum ($(CD_3)_2SO$), 150 MHz) of **9.**

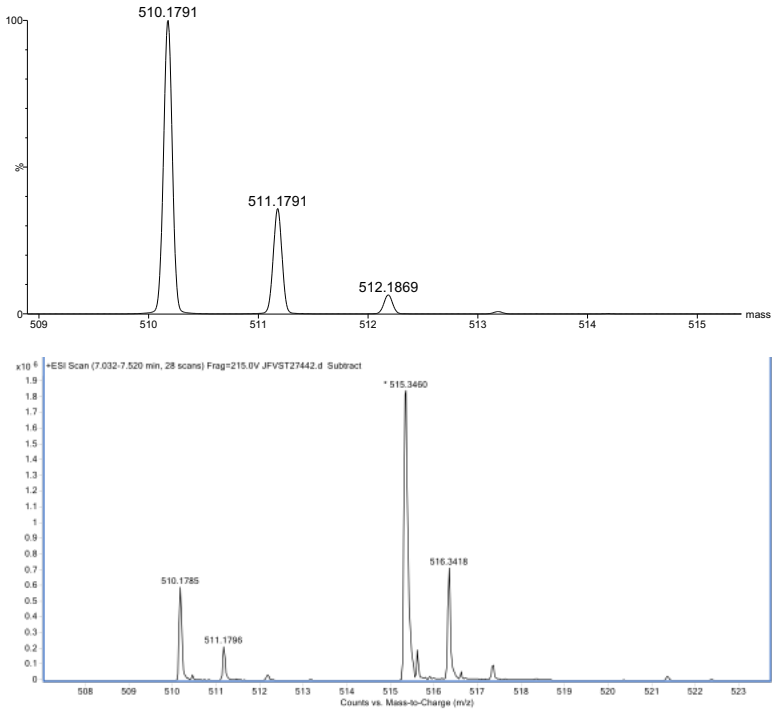

Figure S2.59 HRMS of **9**.

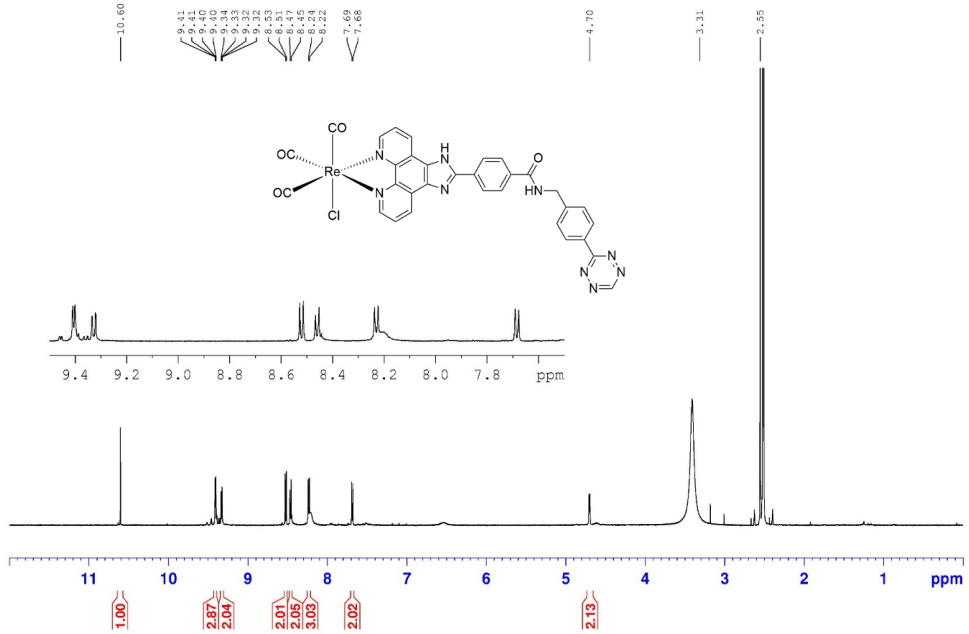

Figure S2.60 ^{1}H NMR spectrum ($(CD_3)_2SO$), 600 MHz) of **10.**

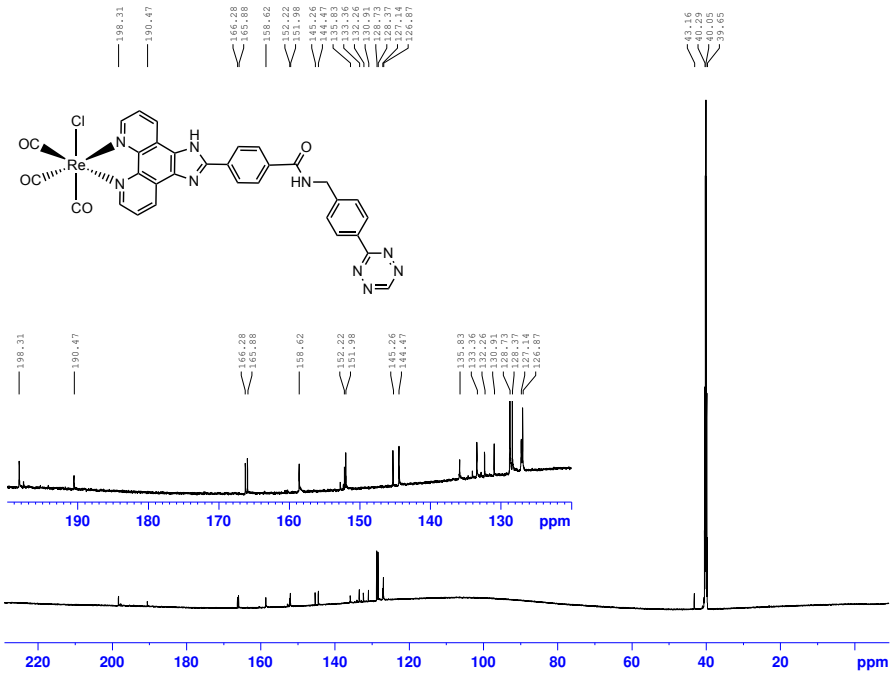

Figure S2.61 ^{13}C NMR spectrum ($(CD_3)_2SO$), 150 MHz) of **10.**

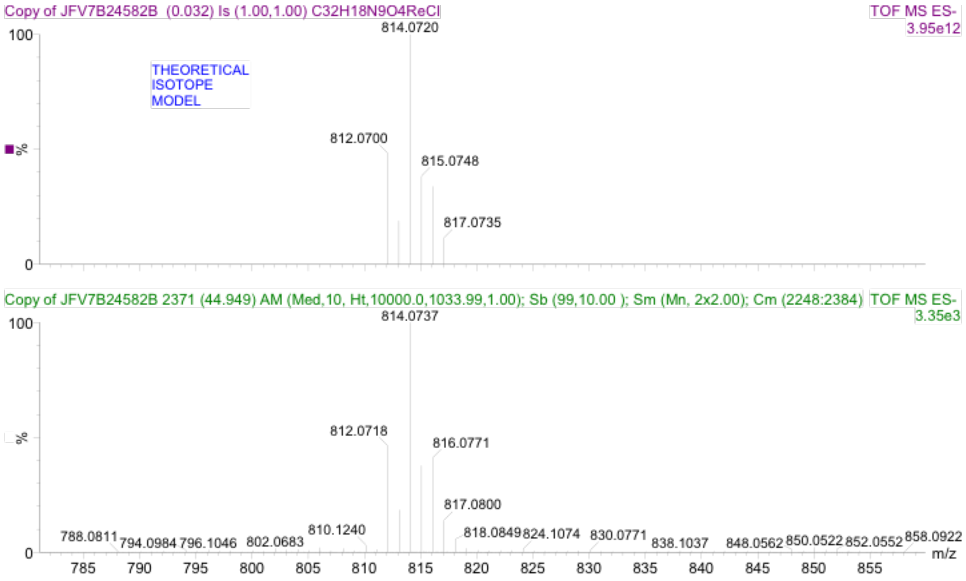

Figure S2.62 HRMS of **10**.

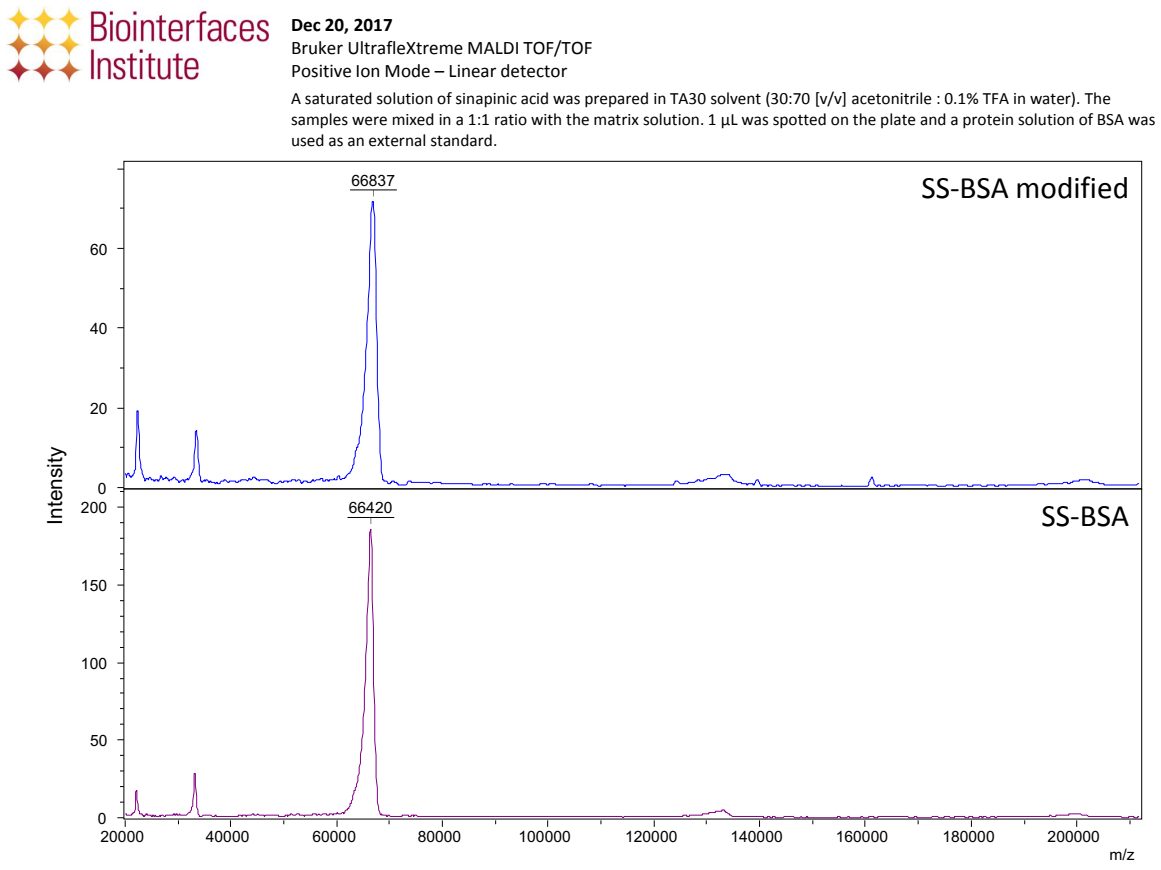

Figure S2.63 MALDI-TOF MS analysis of BSA samples top: **14** and bottom BSA.

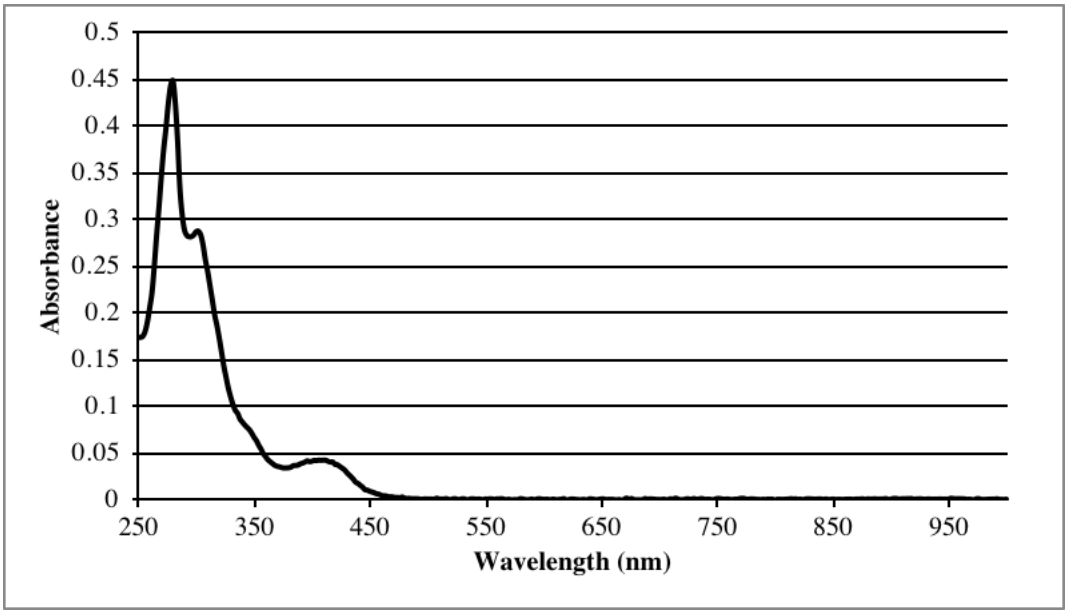

Figure S2.64 Absorbance spectrum of **4a** (278 nm, 0.44 a.u.; 304 nm, 0.28 a.u.; 406 nm, 0.39 a.u.)

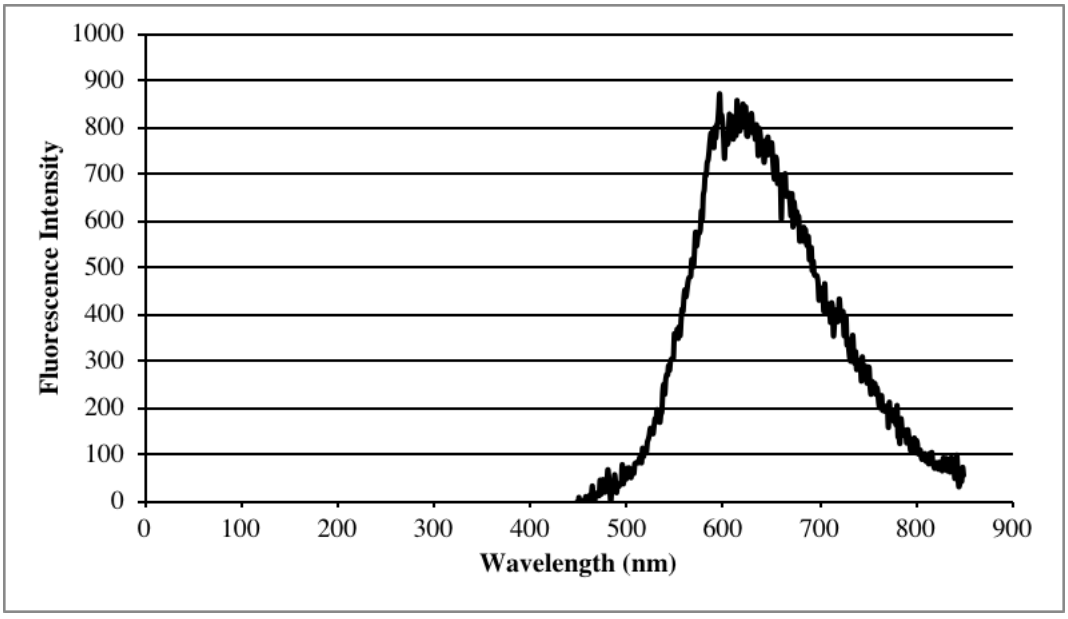

Figure S2.65 Fluorescence emission spectrum of **4a** (λ_{ex} = 460 nm; 612 nm, 782 a.u.)

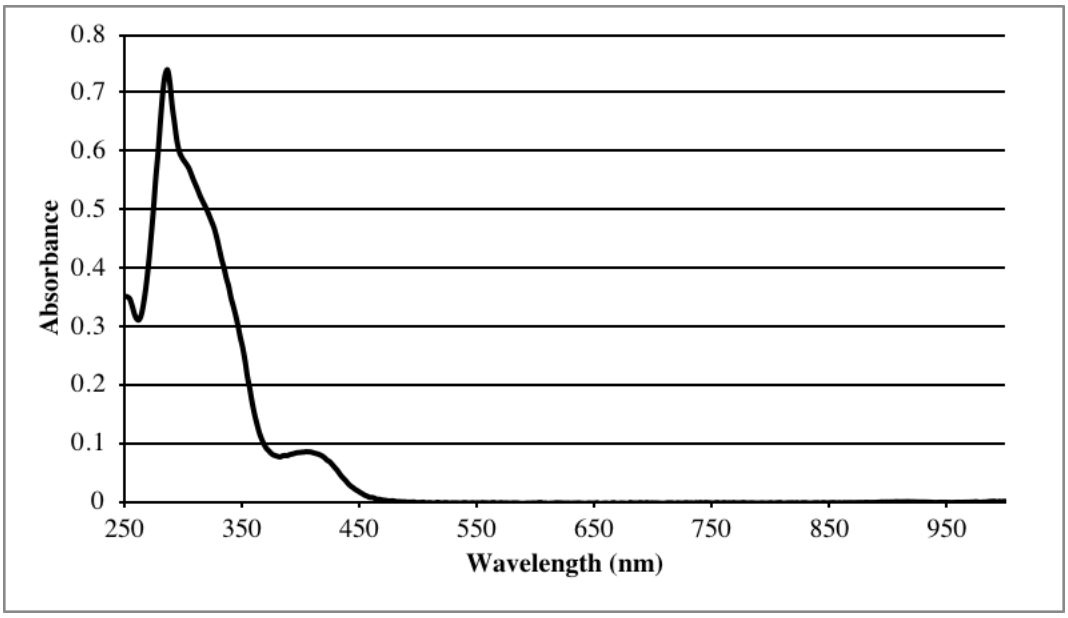

Figure S2.66 Absorbance spectrum of **4b** (284 nm, 0.73 a.u.; 302 nm, 0.58 a.u.; 404 nm, 0.087 a.u.)

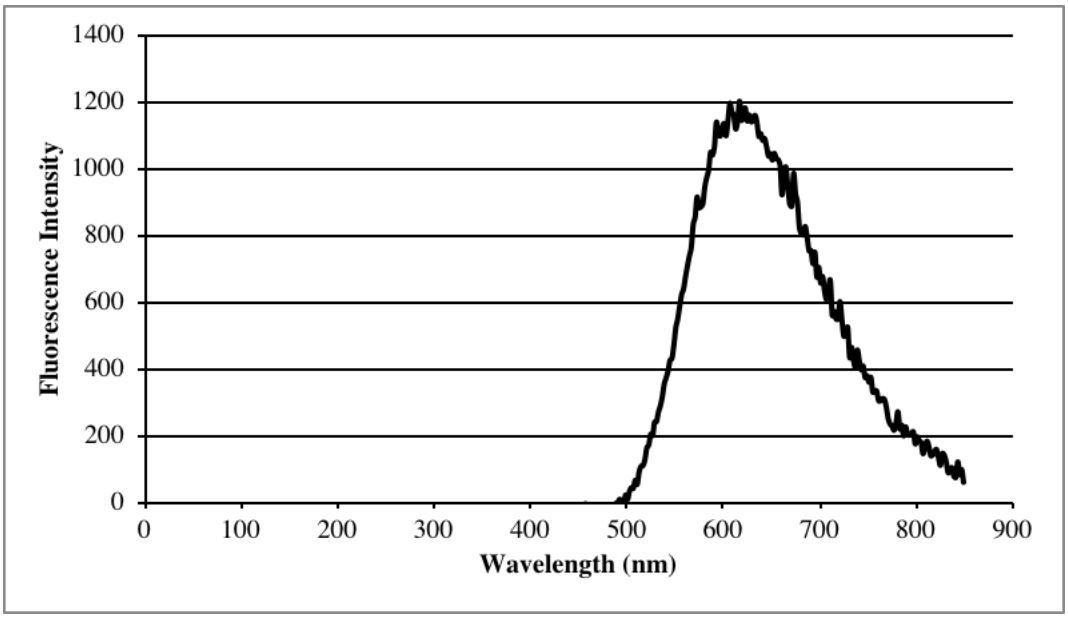

Figure S2.67 Fluorescence emission spectrum of **4b** (λ_{ex} = 406 nm; 596 nm, 1166 a.u.)

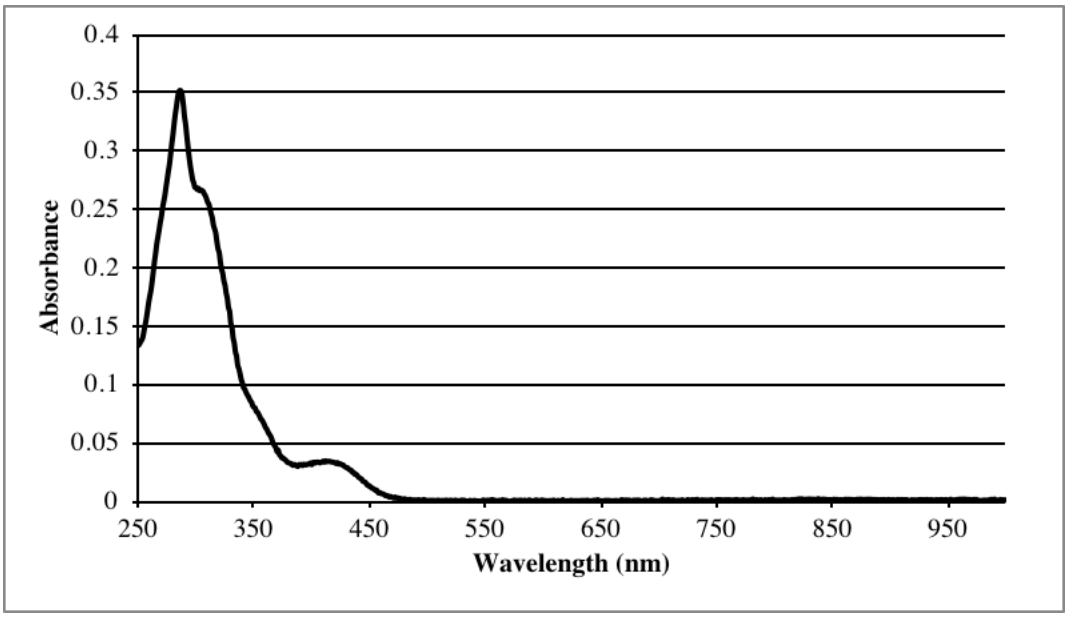

Figure S2.68 Absorbance spectrum of **4c** (283 nm, 0.34 a.u.; 303 nm, 0.27 a.u.; 412 nm, 0.034 a.u.).

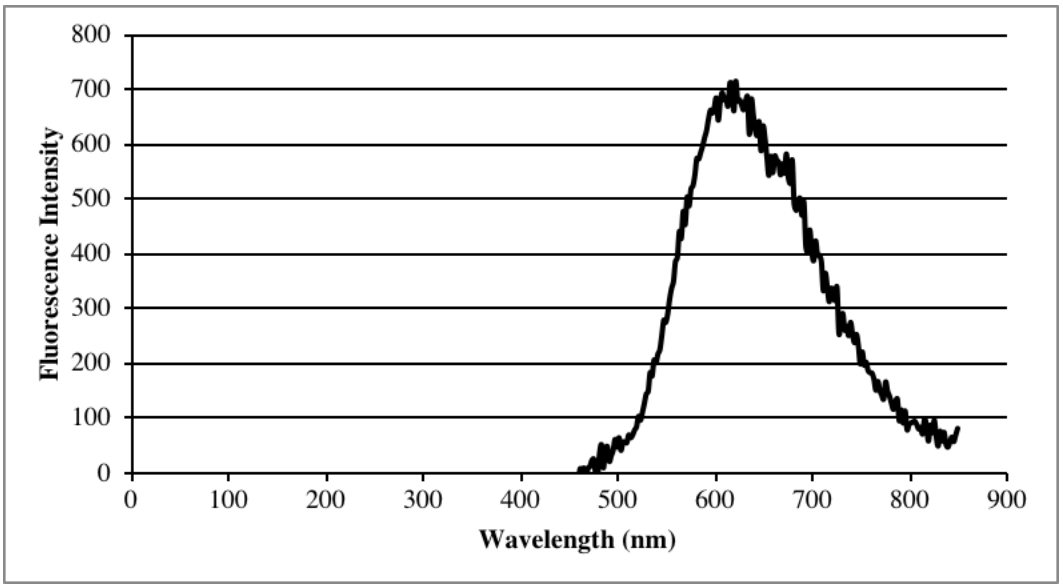

Figure S2.69 Fluorescence emission spectrum of **4c** (λ_{ex} = 410 nm; 616 nm, 713 a.u.).

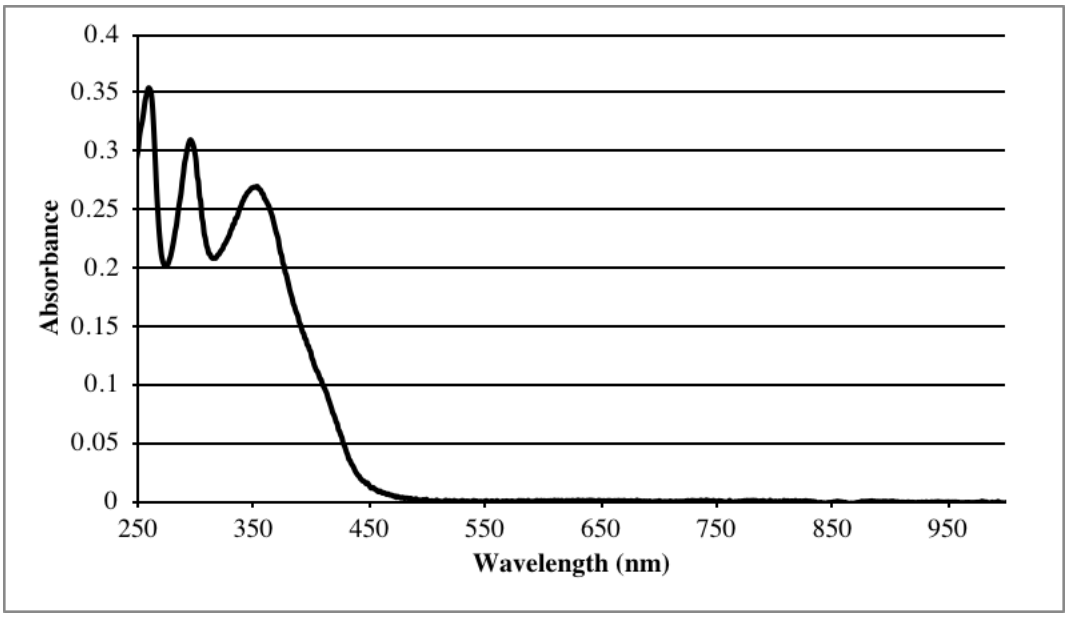

Figure S2.70 Absorbance spectrum of **4d** (259 nm, 0.35 a.u.; 293 nm, 0.304 a.u.; 344 nm, 0.26 a.u.; 351 nm, 0.094 a.u.).

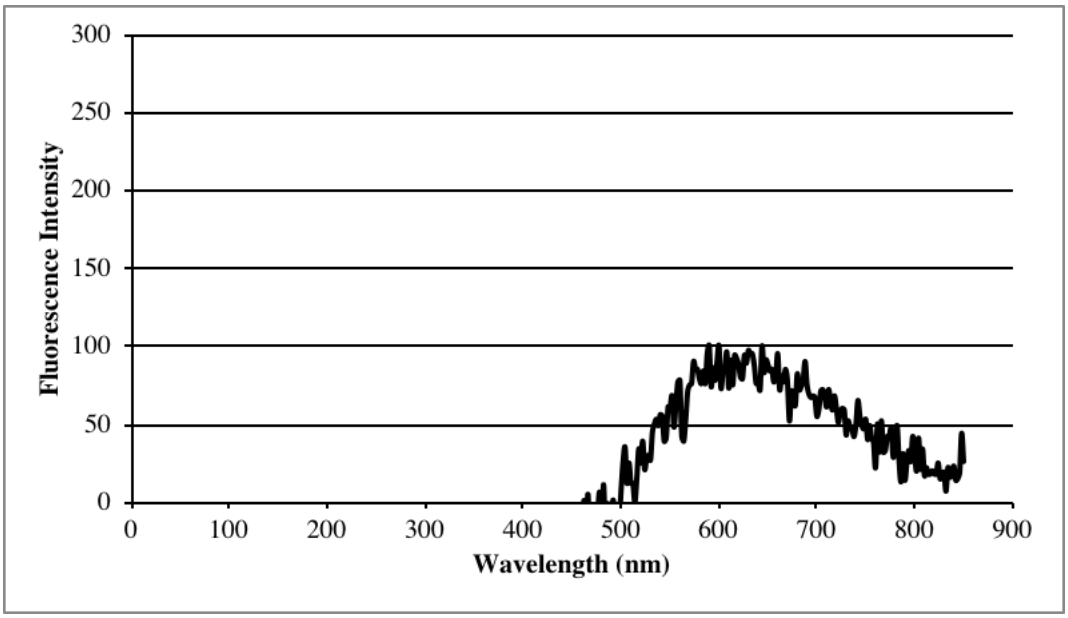

Figure S2.71 Fluorescence emission spectrum of **4d** (λ_{ex} = 351 nm; 649 nm, 69 a.u.).

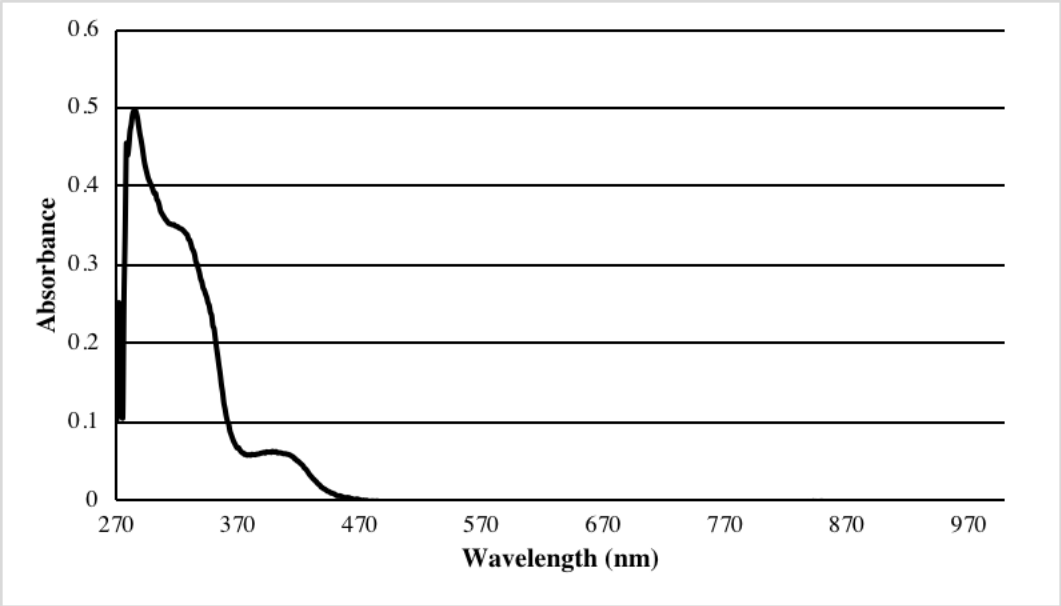

Figure S2.72 Absorbance spectrum of **4e** (286 nm, 0.497 a.u.; 324 nm, 0.35 a.u.; 399 nm, 0.061 a.u.).

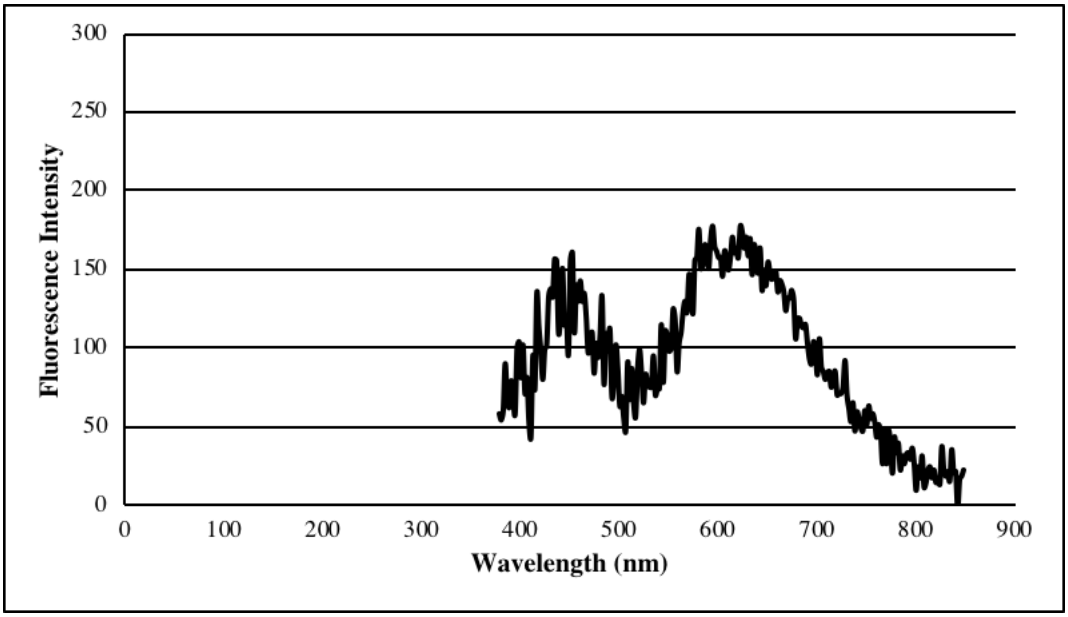

Figure S2.73 Fluorescence emission spectrum of **4e** (λ_{ex} = 365 nm; 451 nm, 156 a.u.; 611 nm, 150 a.u.).

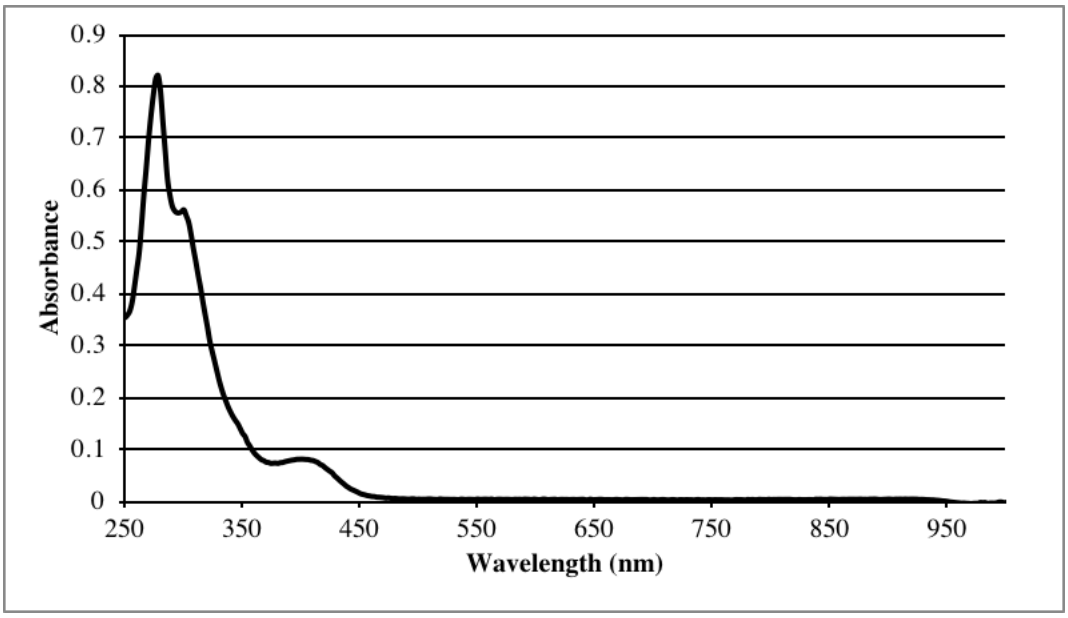

Figure S2.74 Absorbance spectrum of **5a** (276 nm, 0.81 a.u;/ 302 nm, 0.55 a.u.; 400 nm, 0.08 a.u.).

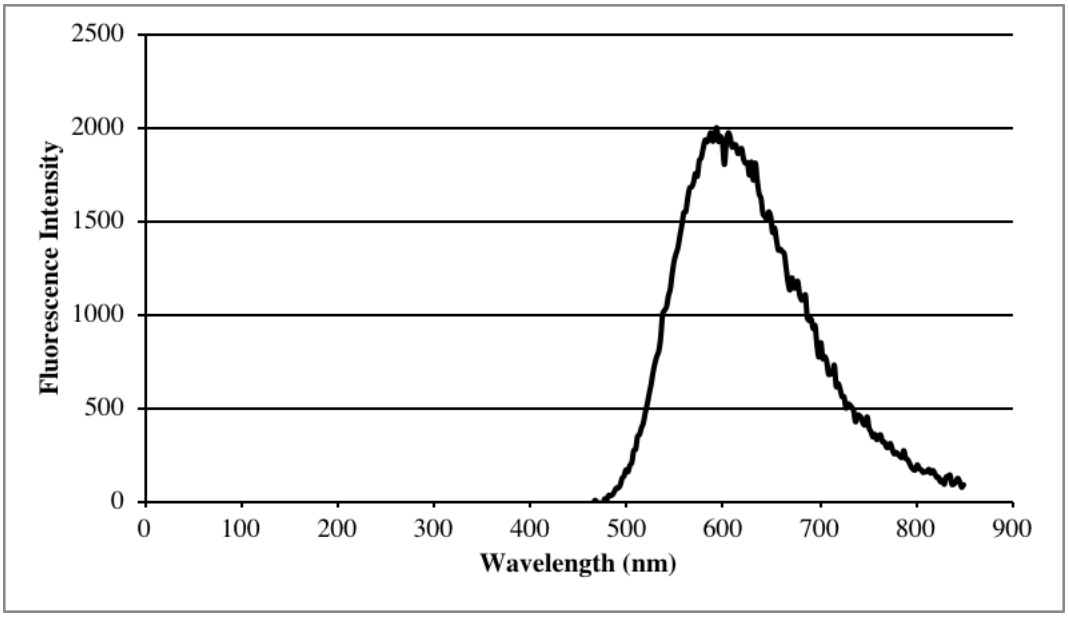

Figure S2.75 Fluorescence emission spectrum of **5a** (λ_{ex} = 400 nm; 594 nm, 1916 a.u.).

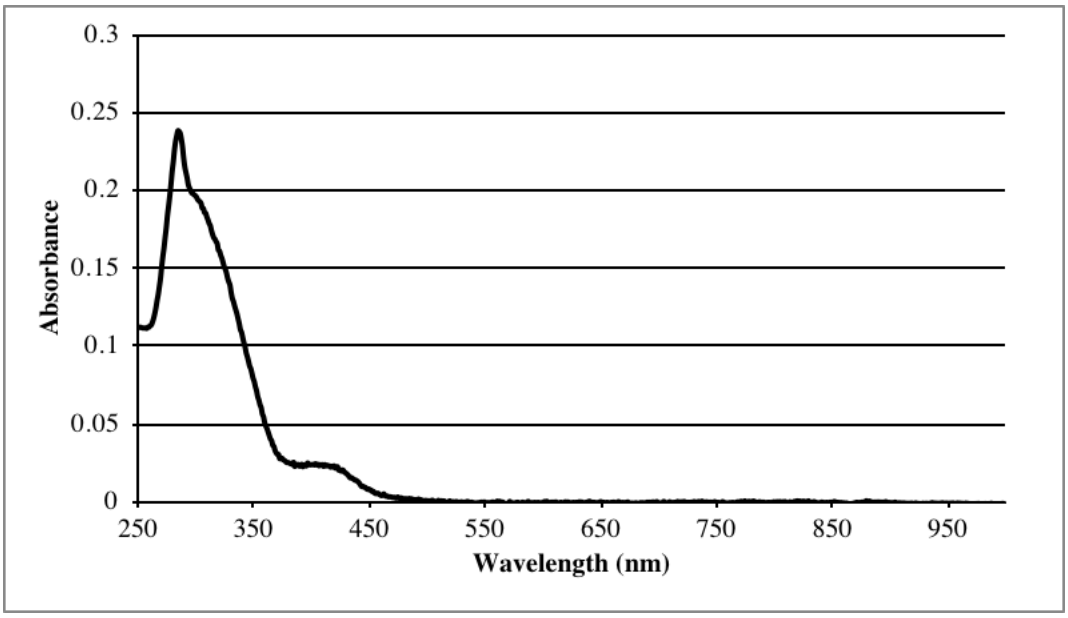

Figure S2.76 Absorbance spectrum of **5b** (282 nm, 0.23 a.u.; 302 nm, 0.19 a.u.; 407 nm, 0.024 a.u.).

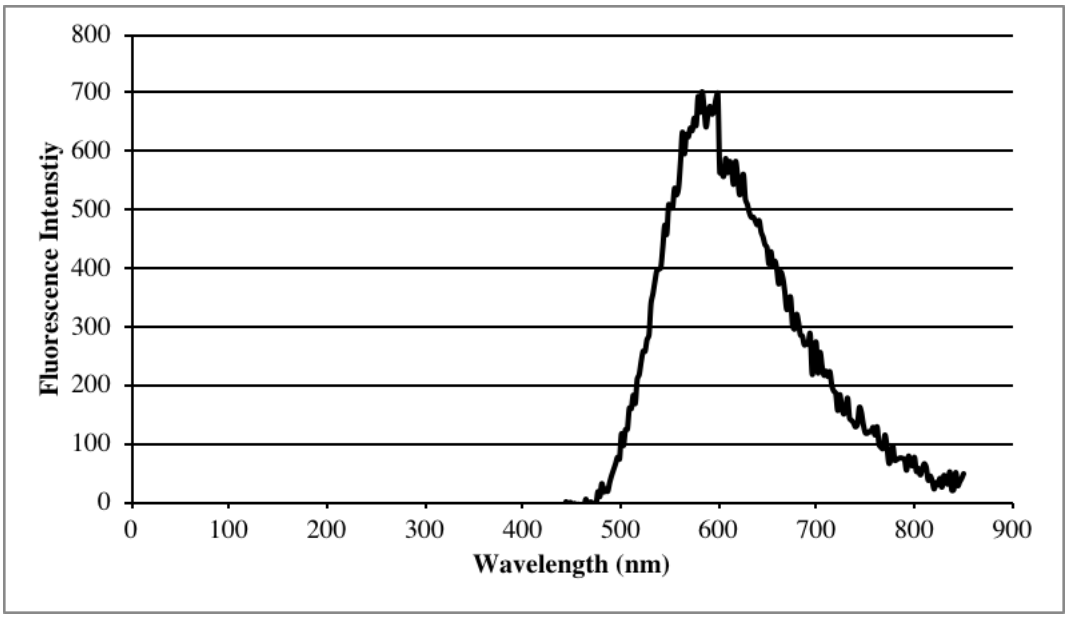

Figure S2.77 Fluorescence emission spectrum of **5b** (λ_{ex} = 407 nm; 595 nm, 667 a.u.).

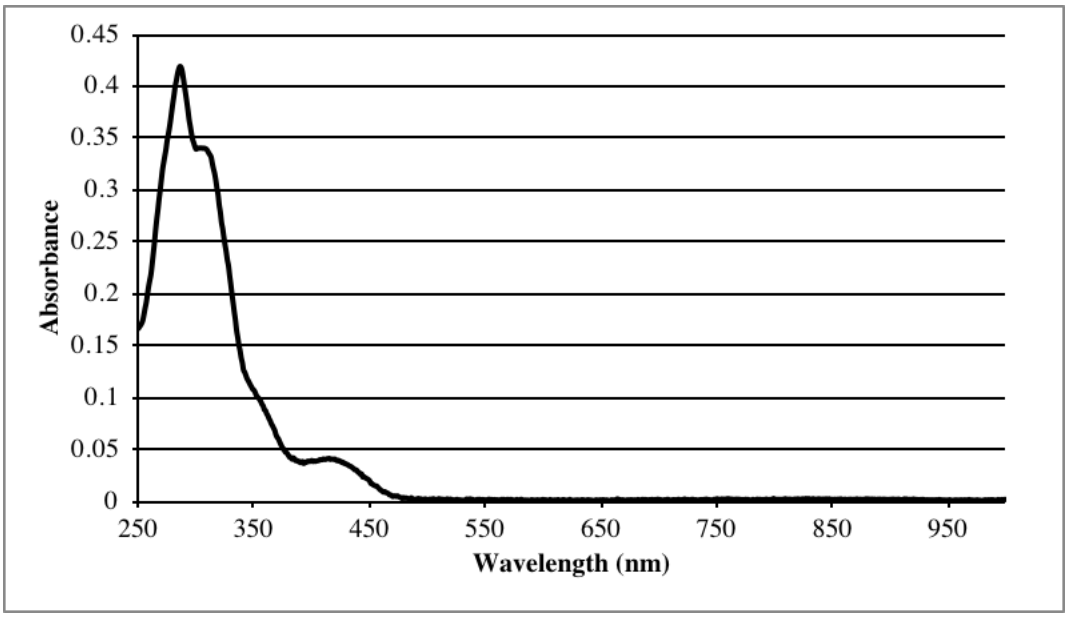

Figure S2.78 Absorbance spectrum of **5c** (283 nm, 0.40 a.u.; 299 nm, 0.34 a.u.; 414 nm, 0.039 a.u.).

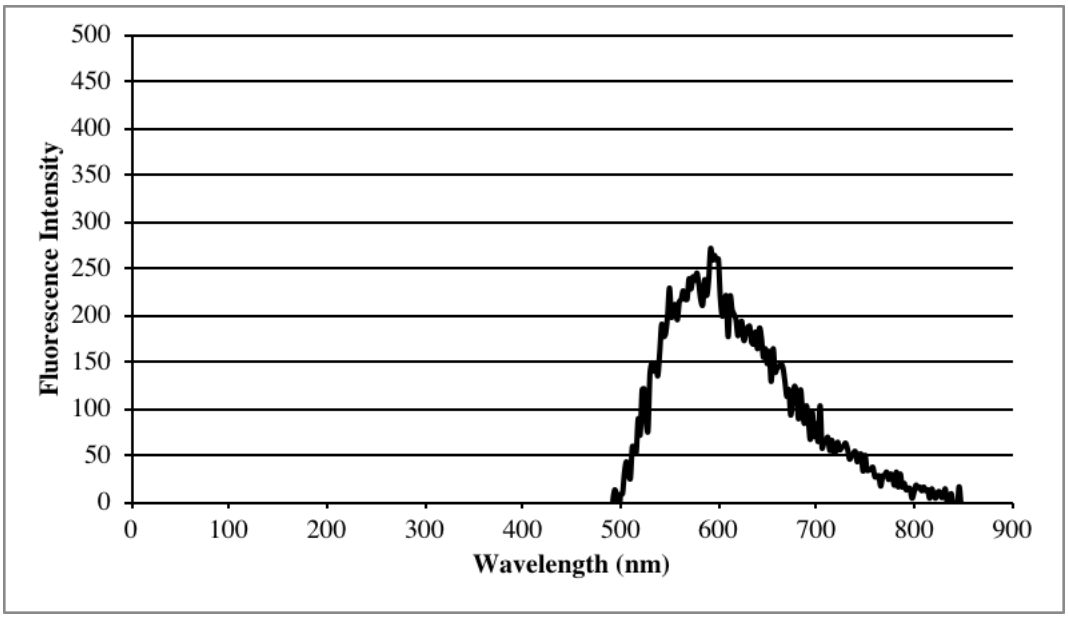

Figure S2.79 Fluorescence emission spectrum of **5c** (λ_{ex} = 422 nm; 574 nm, 213 a.u.).

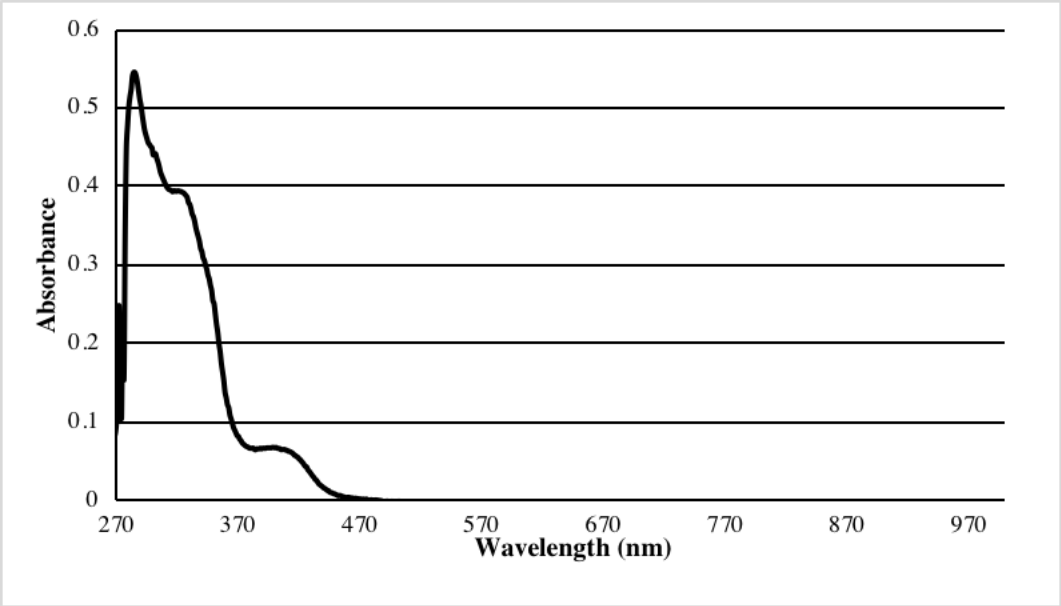

Figure S2.80 Absorbance spectrum of **5e** (284 nm, 0.54 a.u.; 314 nm, 0.40 a.u.; 399 nm, 0.068 a.u.).

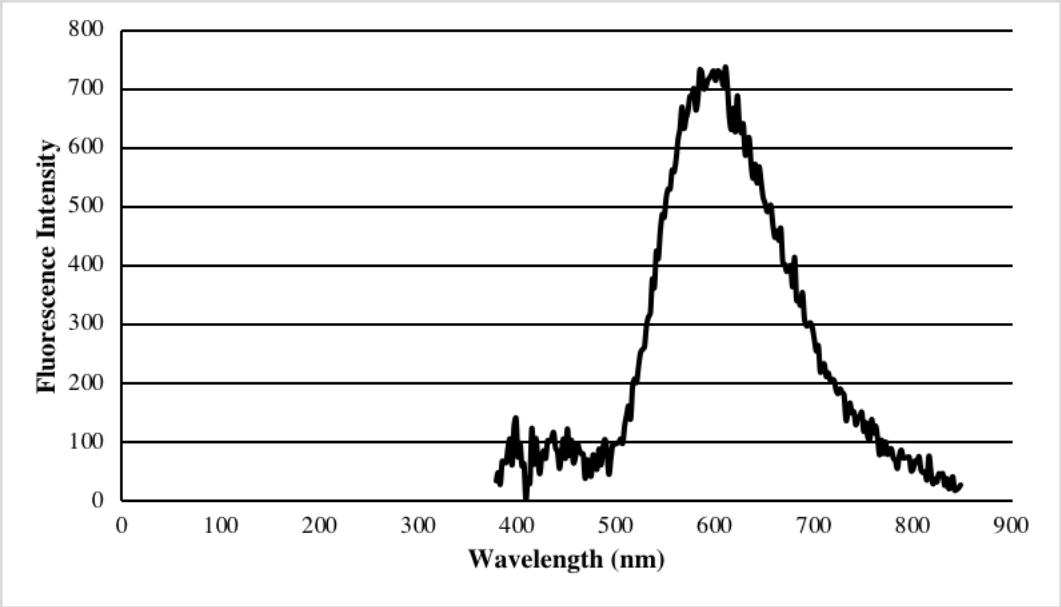

Figure S2.81 Fluorescence emission spectrum of **5e** (λ_{ex} = 365 nm; 611 nm, 735 a.u.).

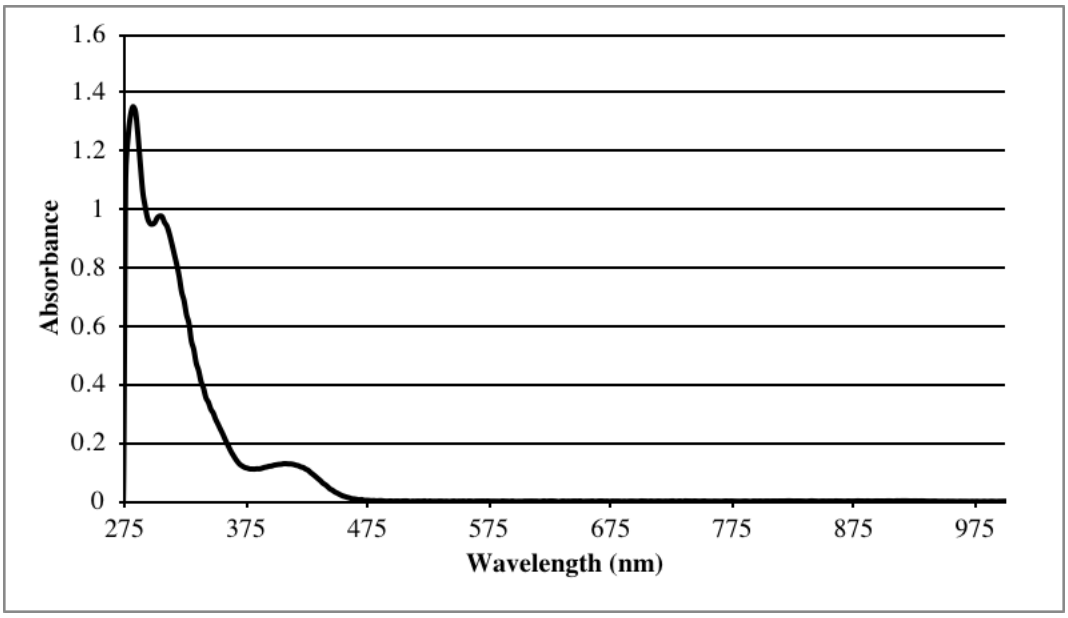

Figure S2.82 Absorbance spectrum of **5f** (282 nm, 1.35 a.u.; 306 nm, 0.97 a.u.; 406 nm, 0.128 a.u.).

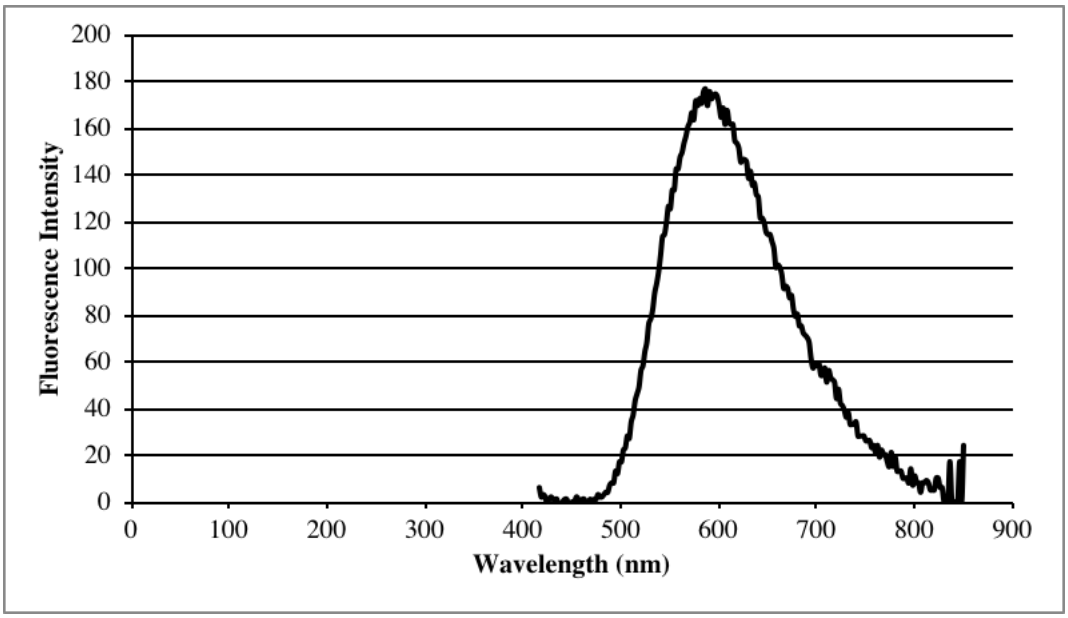

Figure S2.83 Fluorescence emission spectrum of **5f** (λ_{ex} = 406 nm; 586 nm, 176 a.u.).

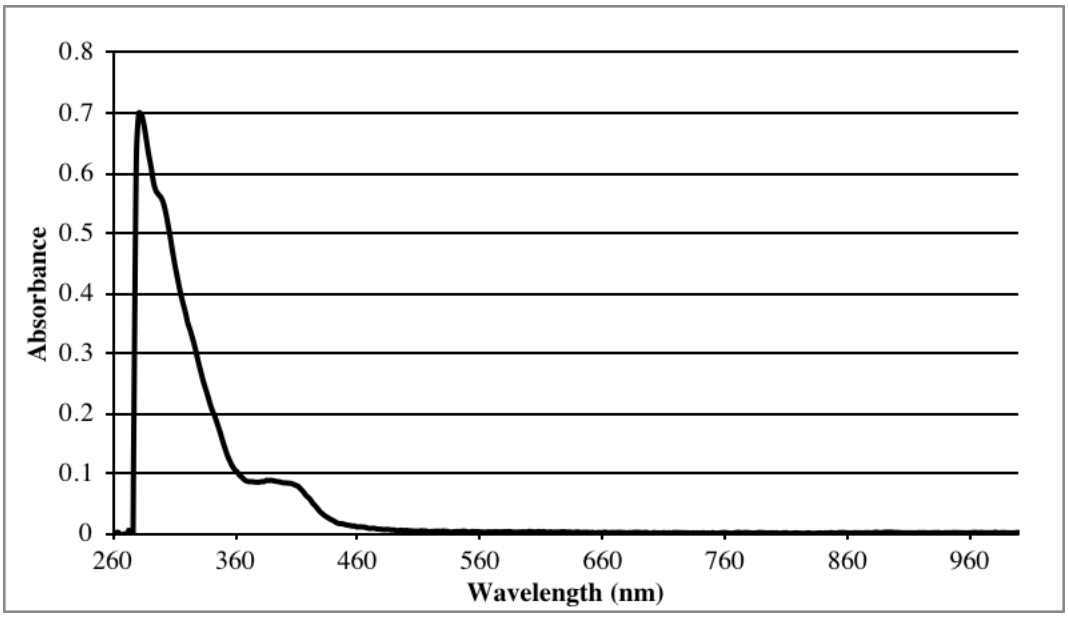

Figure S2.84 Absorbance spectrum of **9a** (282 nm, 0.70 a.u.; 300 nm, 0.56 a.u.; 402 nm, 0.084 a.u.).

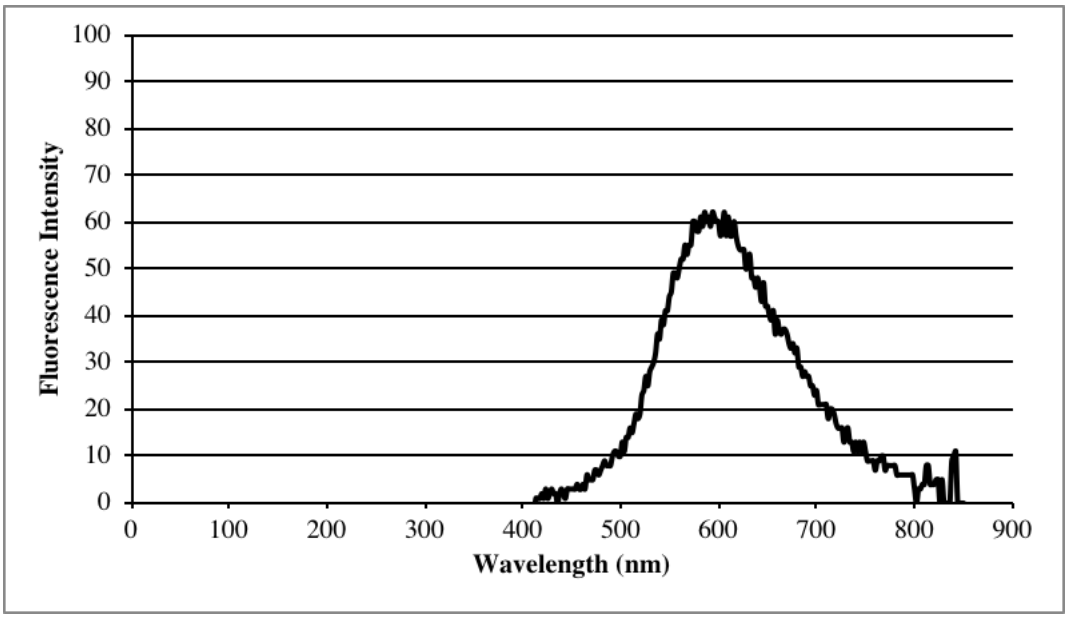

Figure S2.85 Fluorescence emission spectrum of **9a** (λ_{ex} = 402 nm; 594 nm, 62 a.u.).

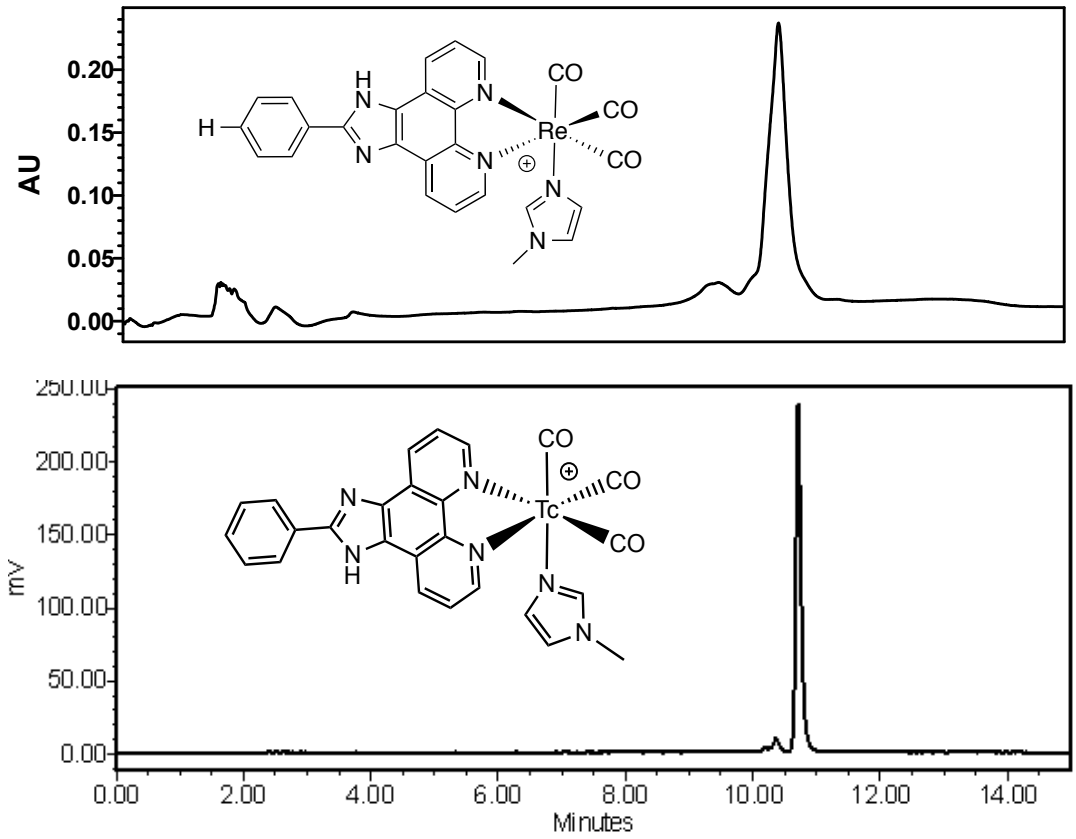

Figure S2.86 UV-HPLC trace of **5a** (top) and γ-HPLC trace of **7a** (bottom) (Method B).

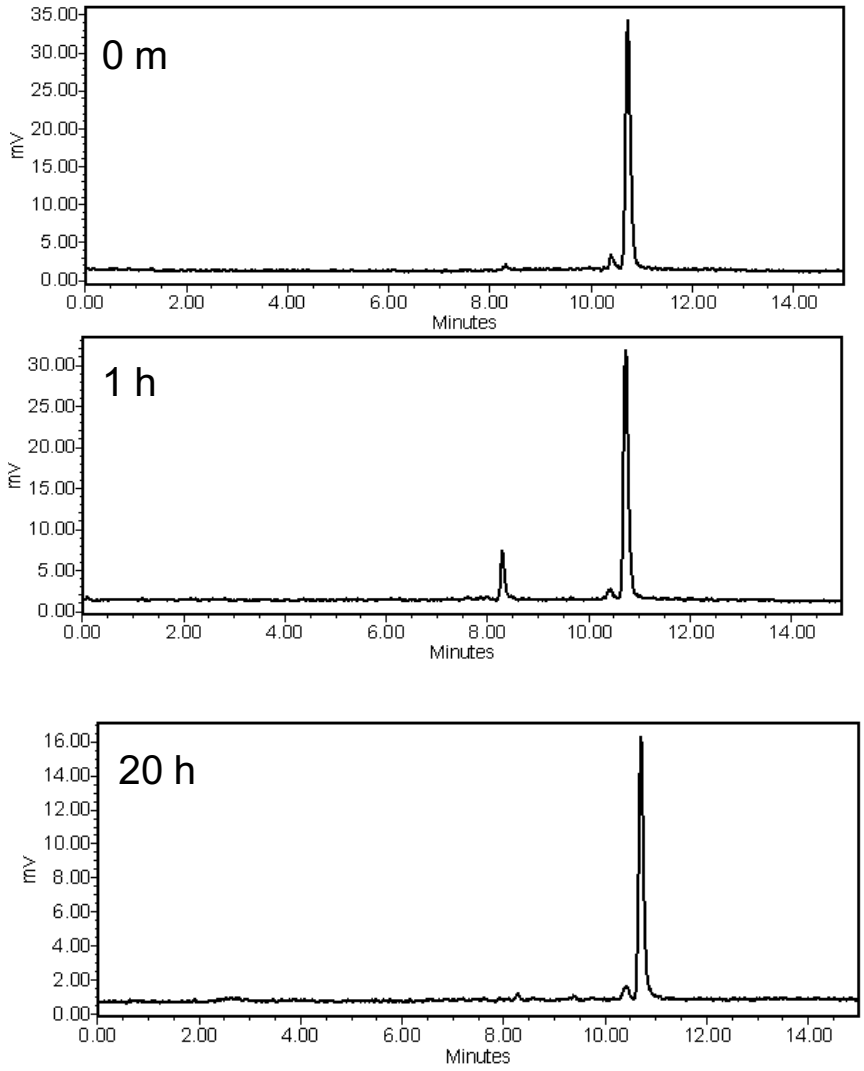

Figure S2.87 γ-HPLC trace of **7a** after 1 and 20 h in saline (Method B).

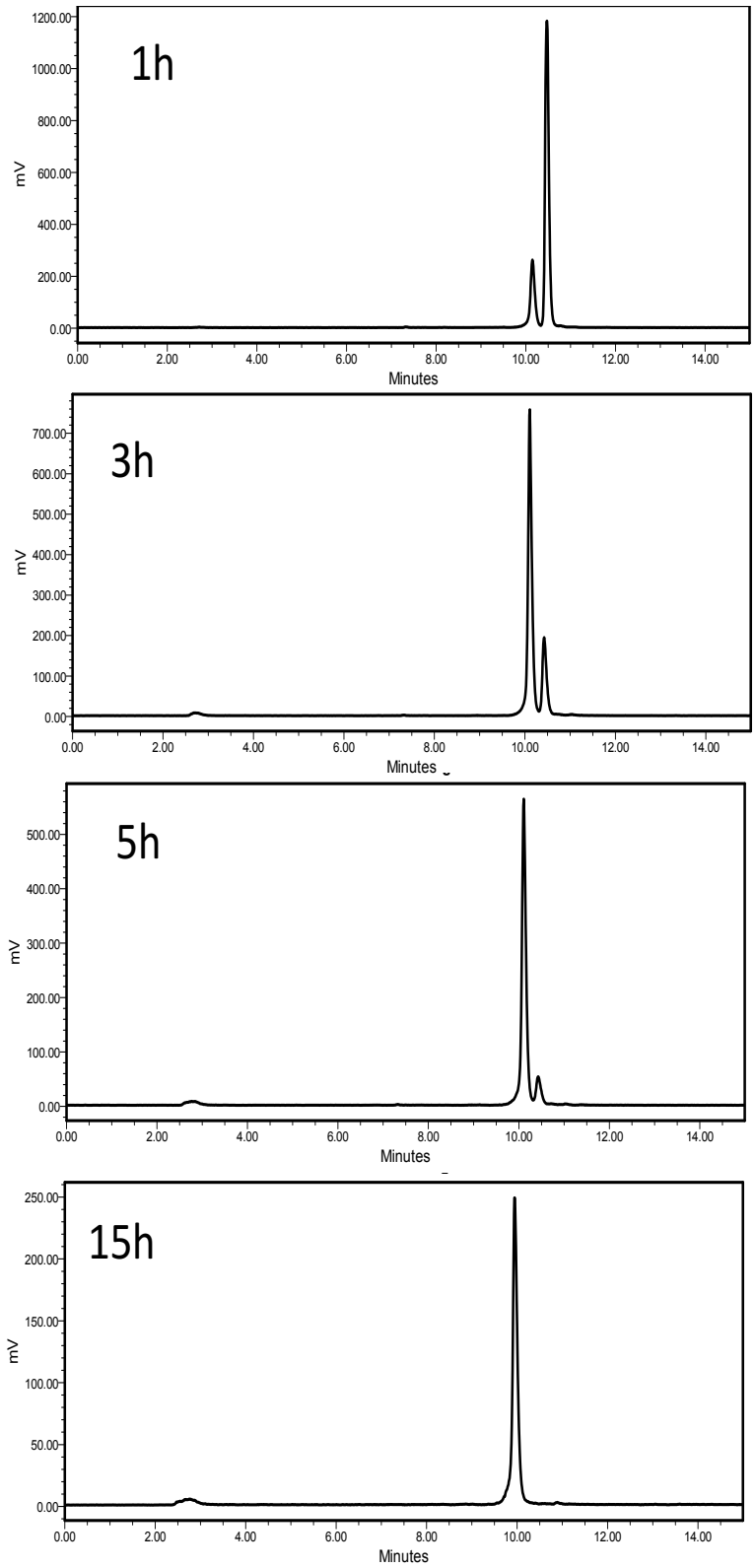

Figure S2.88 γ-HPLC trace of **7a** with histidine challenge (Method B).

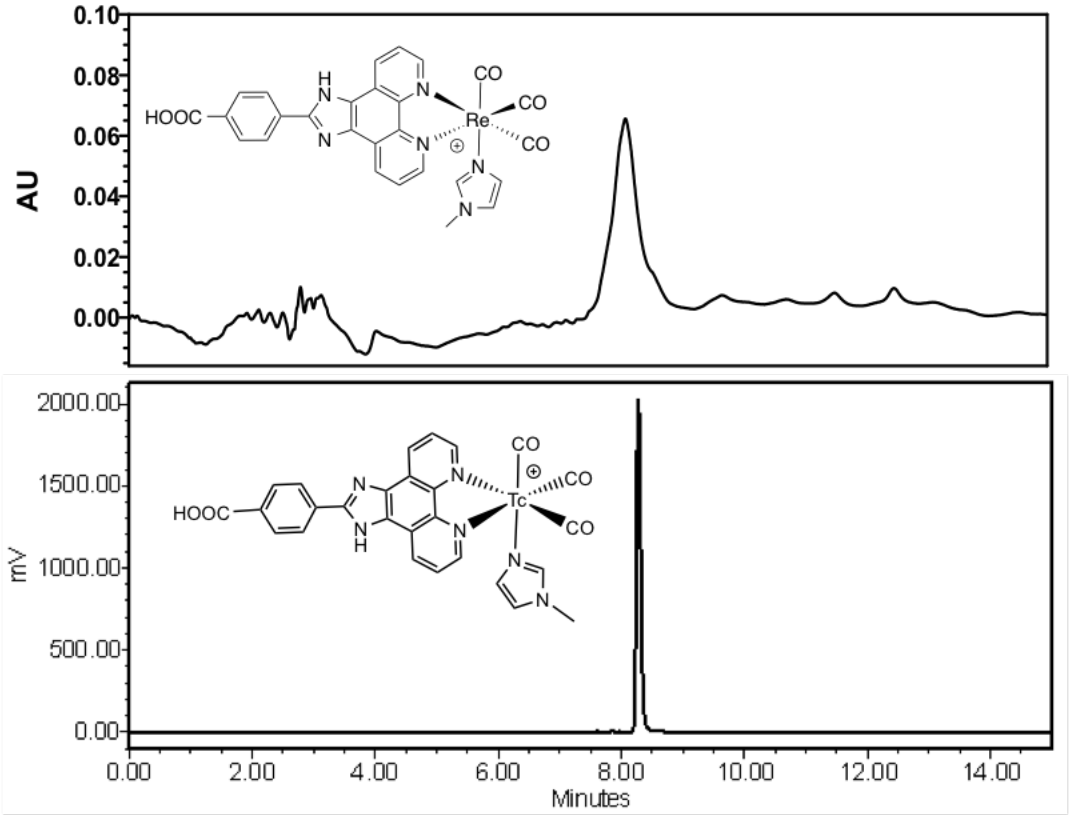

Figure S2.89 UV-HPLC trace of **5b** (top) and γ-HPLC trace of **7b** (bottom) (Method B).

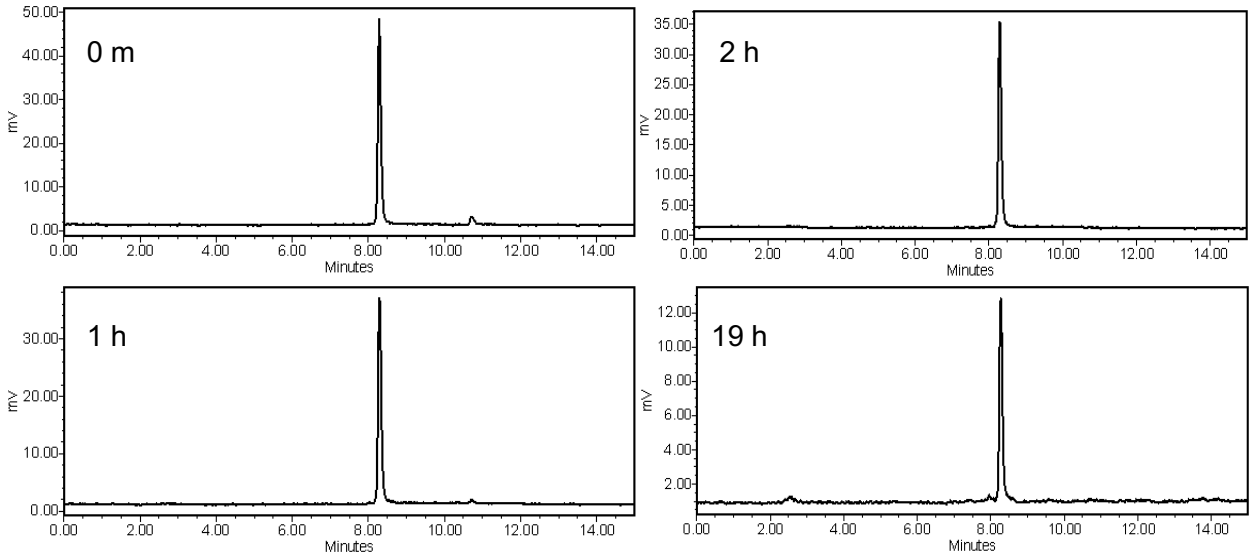

Figure S2.90 γ-HPLC trace of **7b** after 1, 2 and 19 h in saline (Method B).

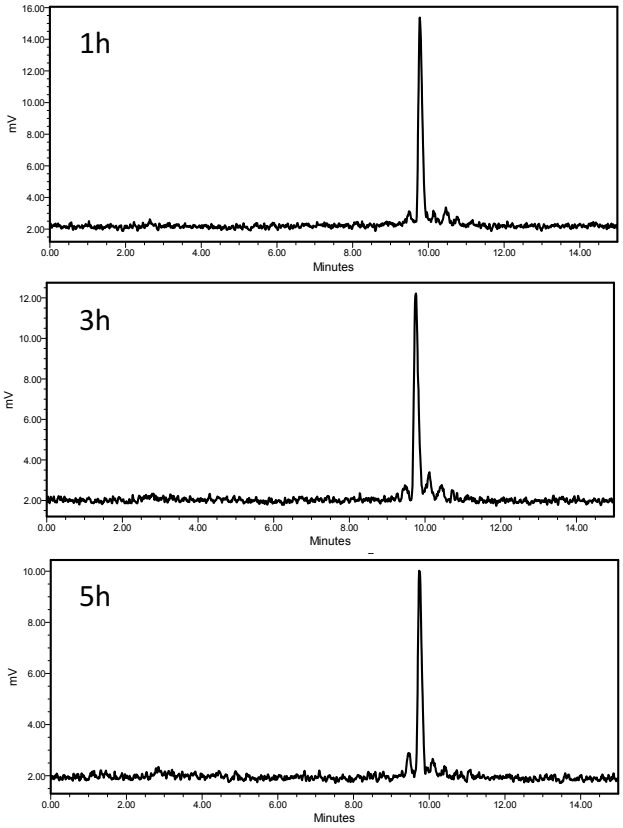

Figure S2.91 γ-HPLC trace of **7b** after 1, 3 and 5 h in histidine (Method B).

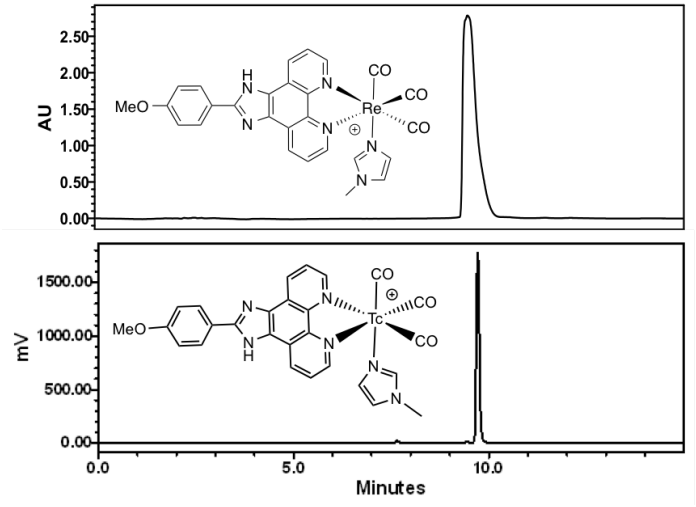

Figure S2.92 UV-HPLC trace of **5c** (top) and γ-HPLC trace of **7c** (bottom) (Method B).

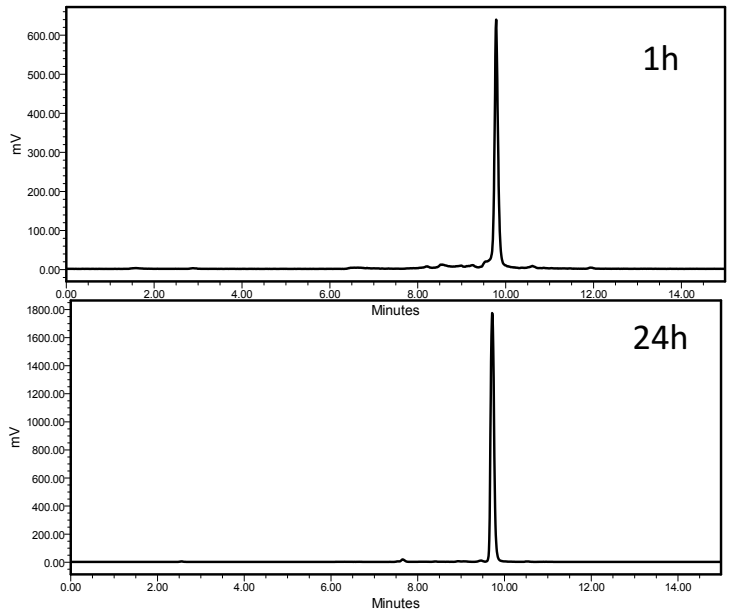

Figure S2.93 γ-HPLC trace of **7c** after 1 and 24 h in saline (Method B).

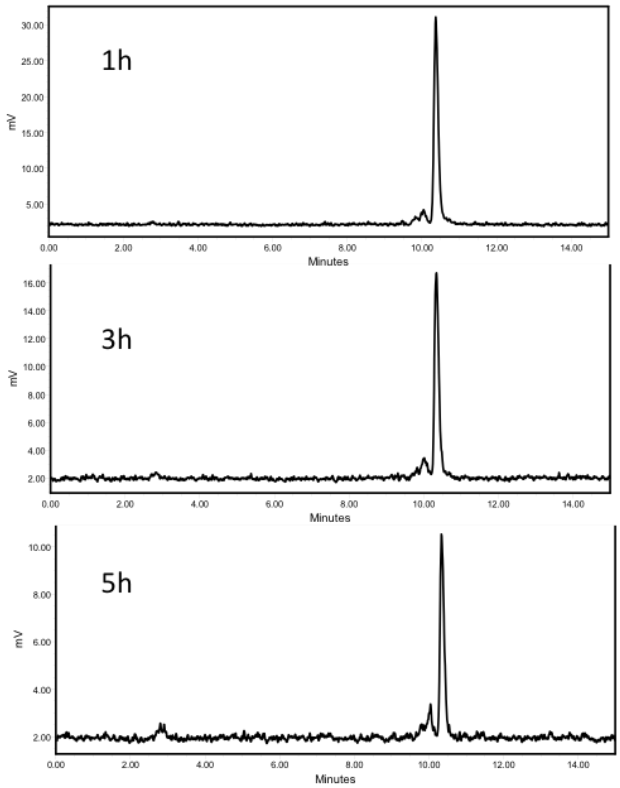

Figure S2.94 γ-HPLC trace of **7c** after 1, 3 and 5 h in histidine (Method B).

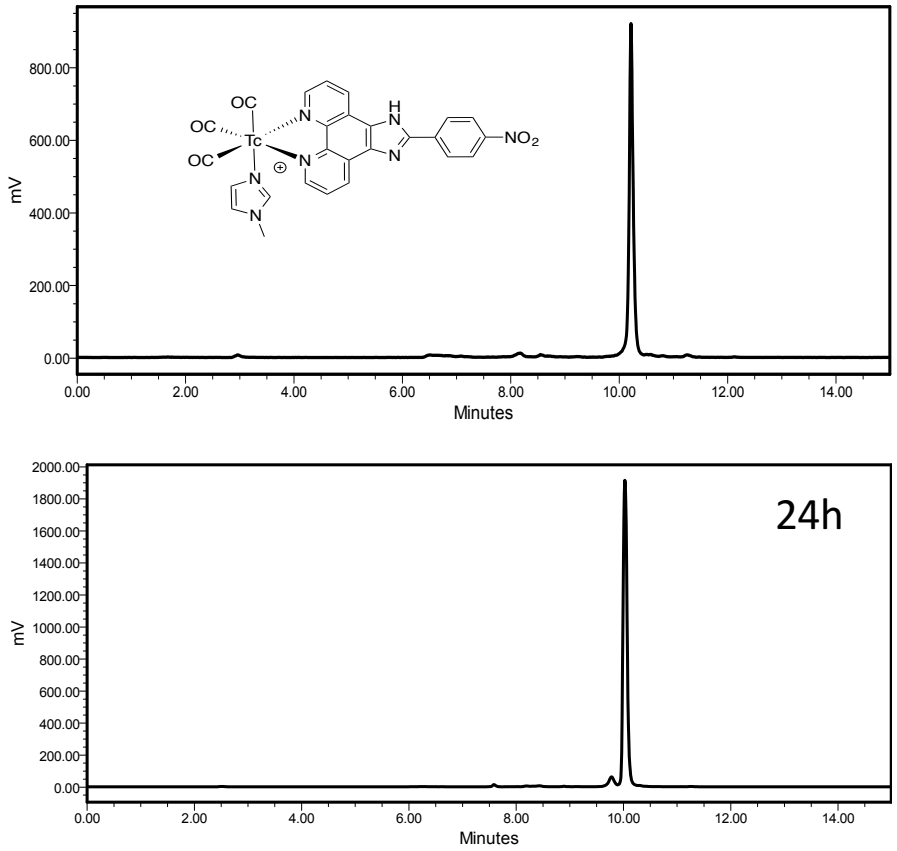

Figure S2.95 γ-HPLC trace of **7d** before (top) and after 24 h (bottom) in saline (Method B).

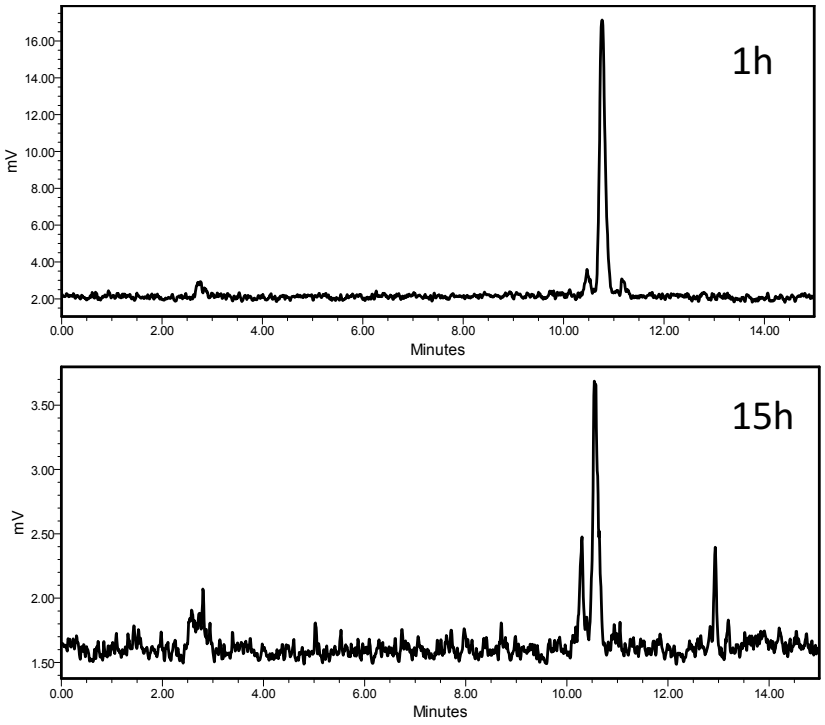

Figure S2.96 γ-HPLC trace of **7d** after 1 and 15 h in histidine (Method B).

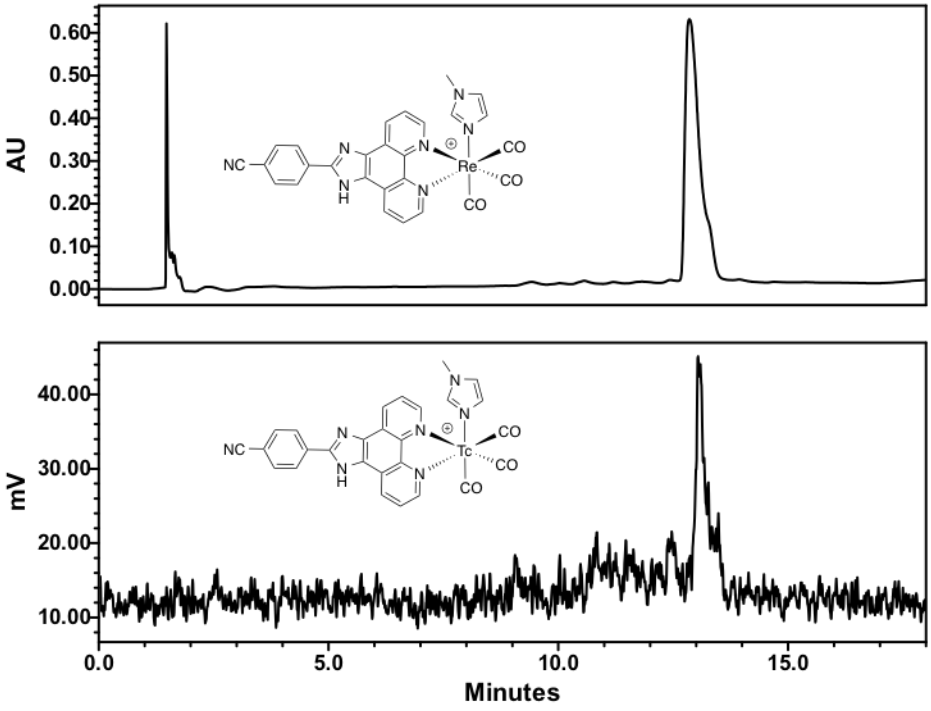

Figure S2.97 UV-HPLC trace of **5e** (top) and γ-HPLC trace of **7e** (bottom) (Method D).

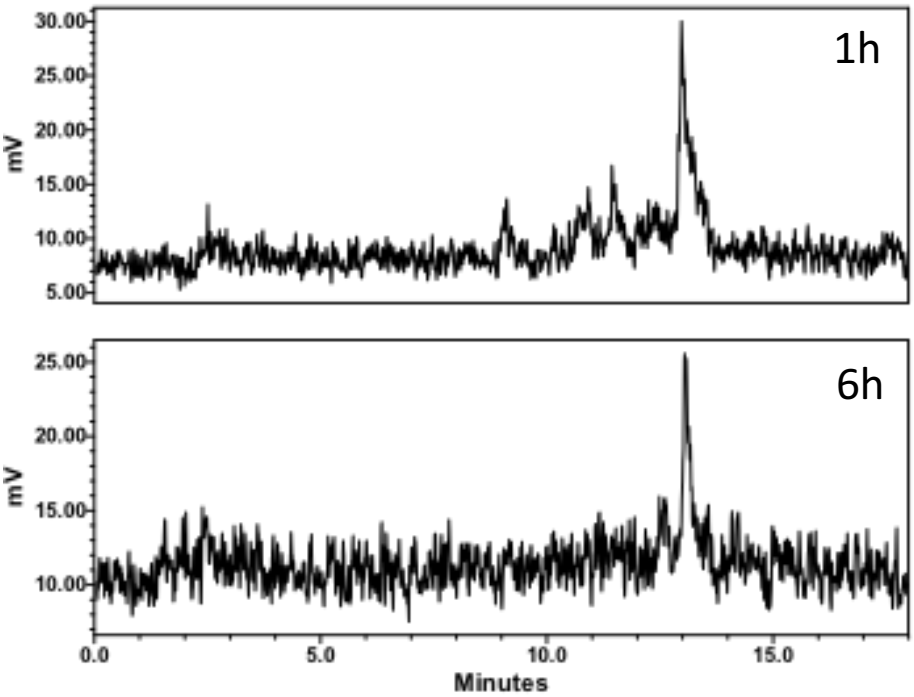

Figure S2.98 γ-HPLC trace of **7e** after 1 and 6 h in saline (Method D).

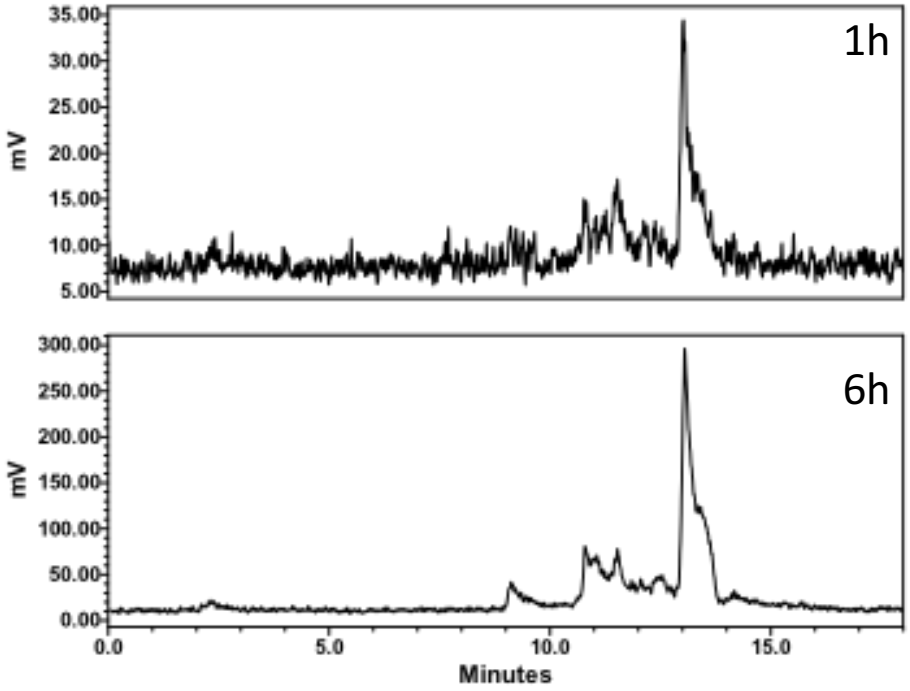

Figure S2.99 γ-HPLC trace of **7e** after 1 and 6 h in cysteine (Method D).

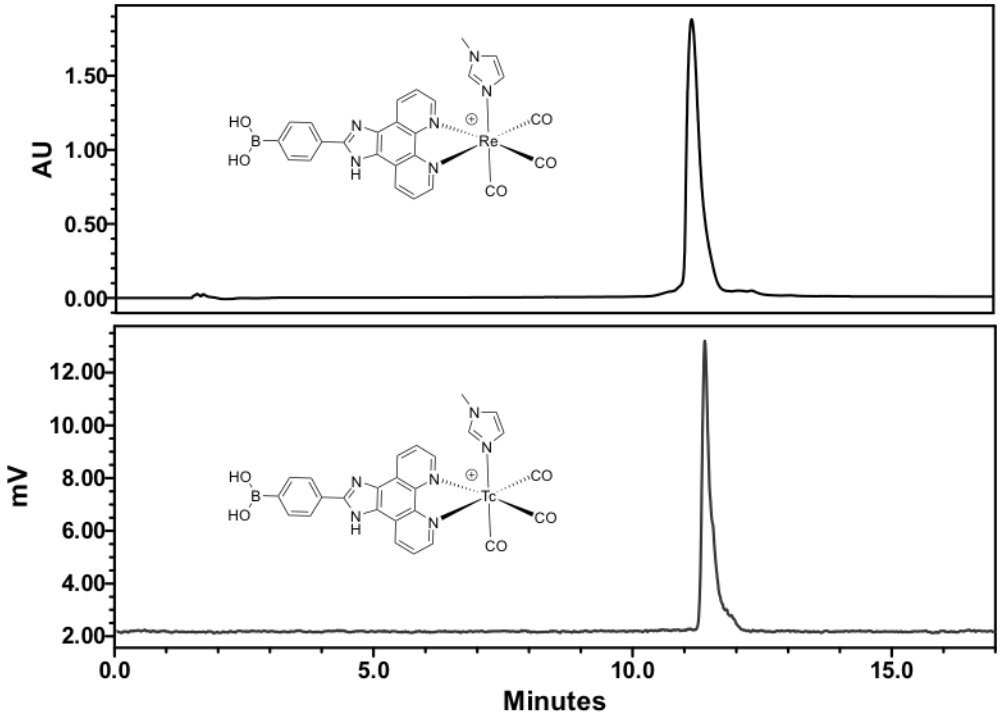

Figure S2.100 UV-HPLC trace of **5f** (top) and γ-HPLC trace of **7f** (bottom) (Method D).

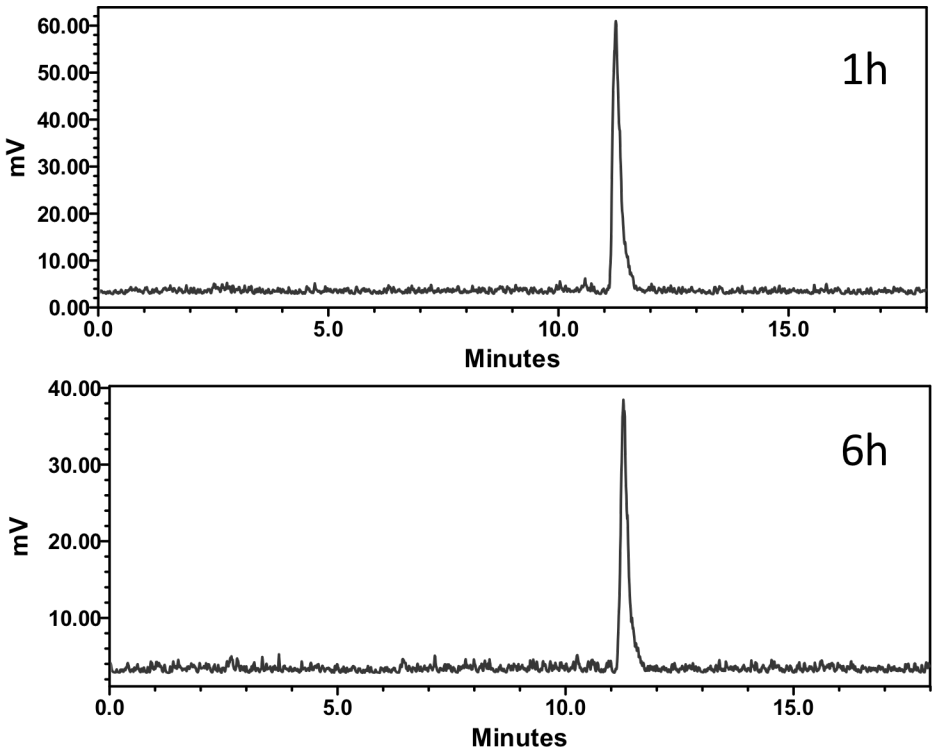

Figure S2.101. γ-HPLC trace of **7f** after 1 and 6 h in saline (Method D).

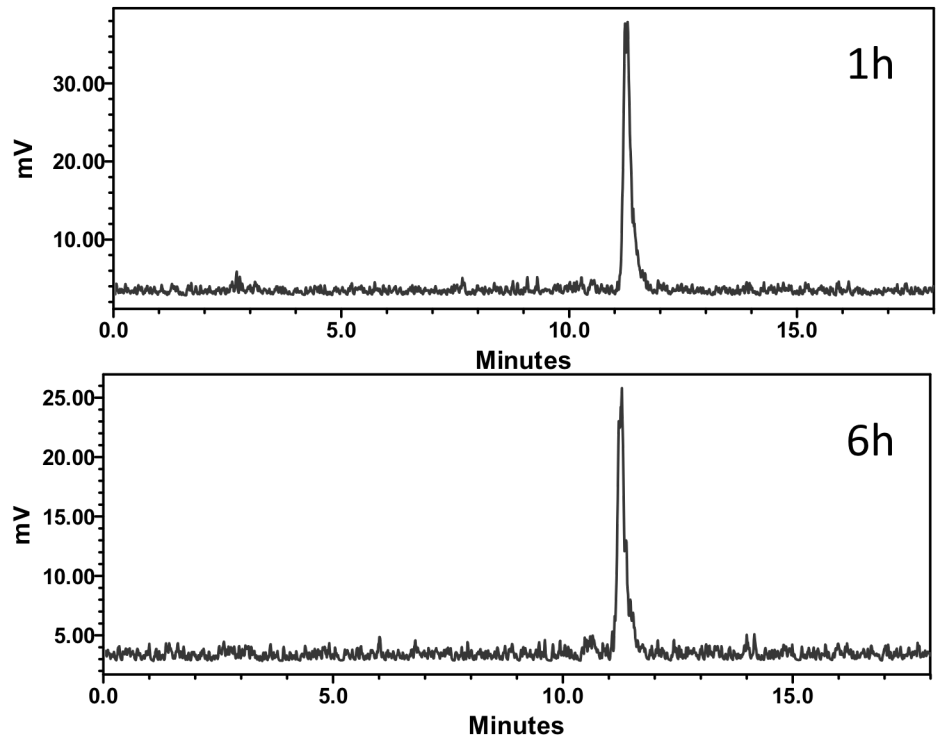

Figure S2.102 γ-HPLC trace of **7f** after 1 and 6 h in cysteine (Method D).

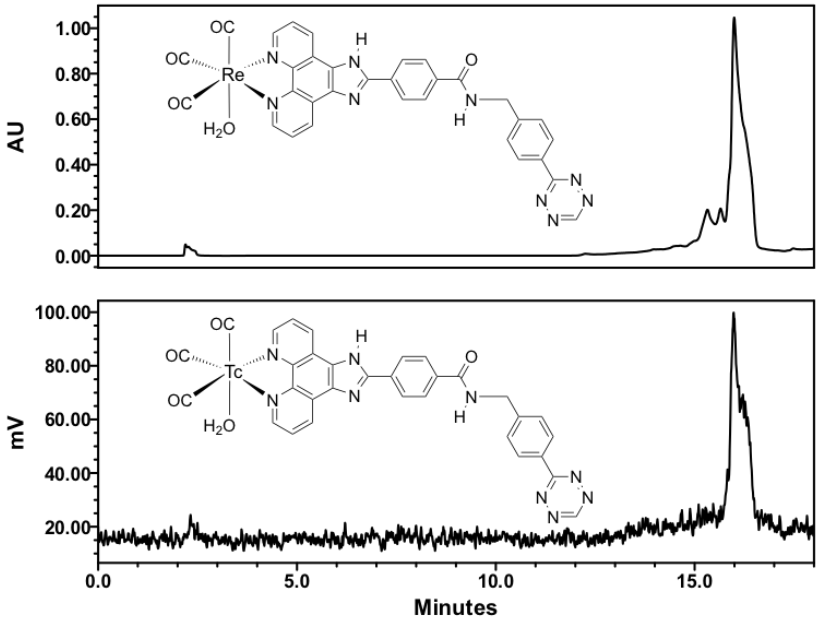

Figure S2.103 UV-HPLC trace of **10** (top) and γ-HPLC trace of **12** (bottom) (Method C).

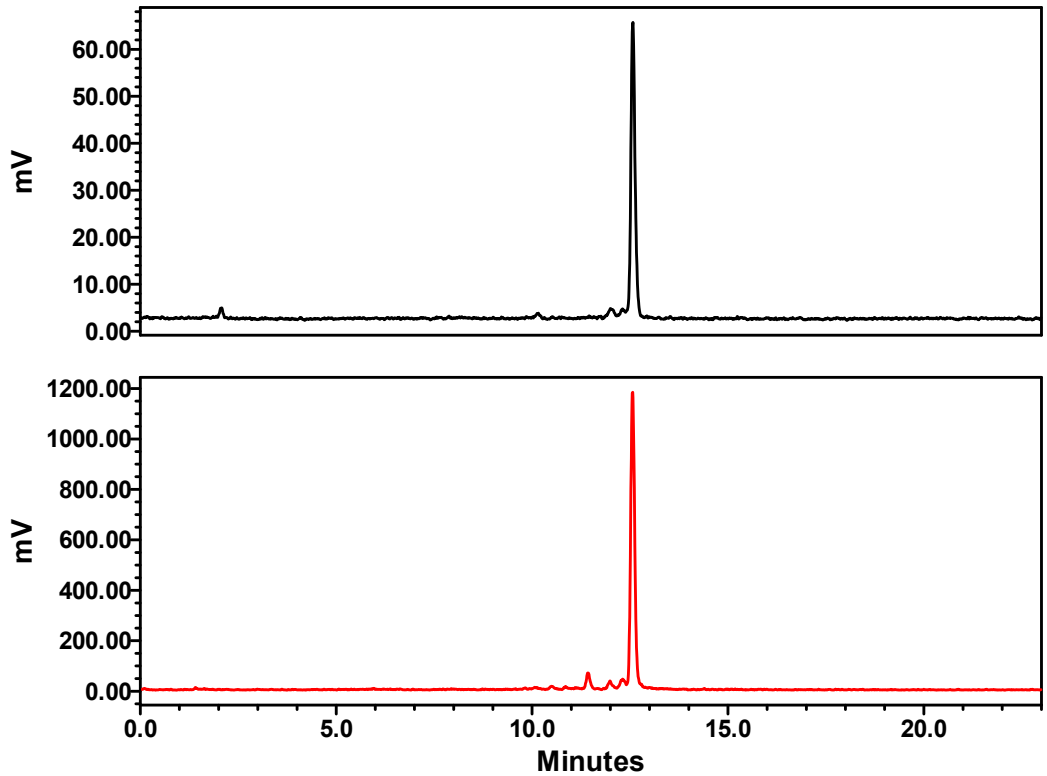

Figure S2.104 γ-HPLC trace of **12** after 0 and 6 h in saline (Method C).

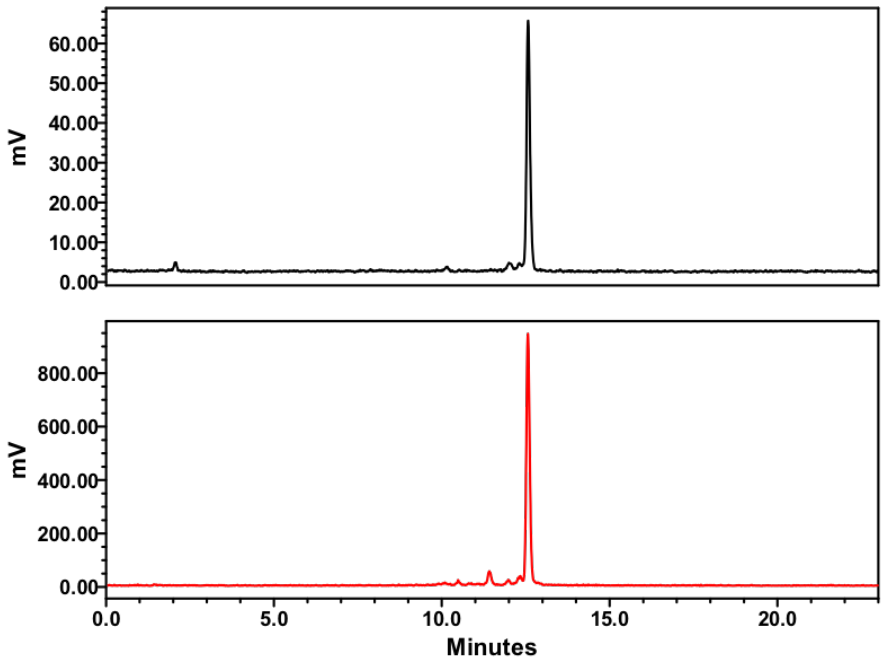

Figure S2.105 γ-HPLC trace of **12** after 0 and 6 h in cysteine (Method C).

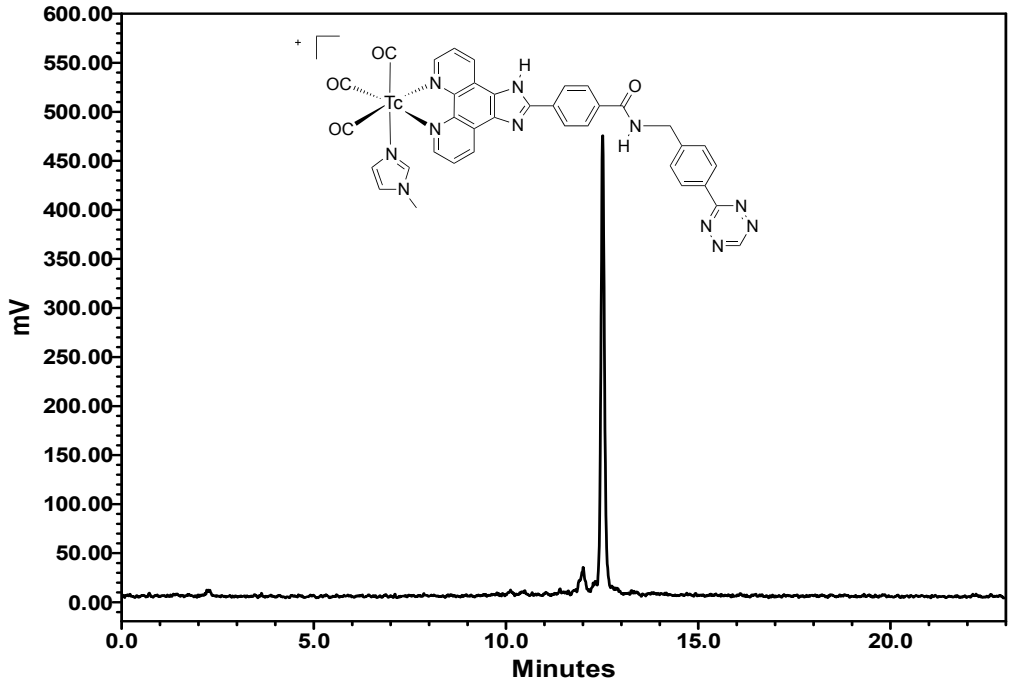

Figure S2.106 γ-HPLC trace of **13** (Method E).

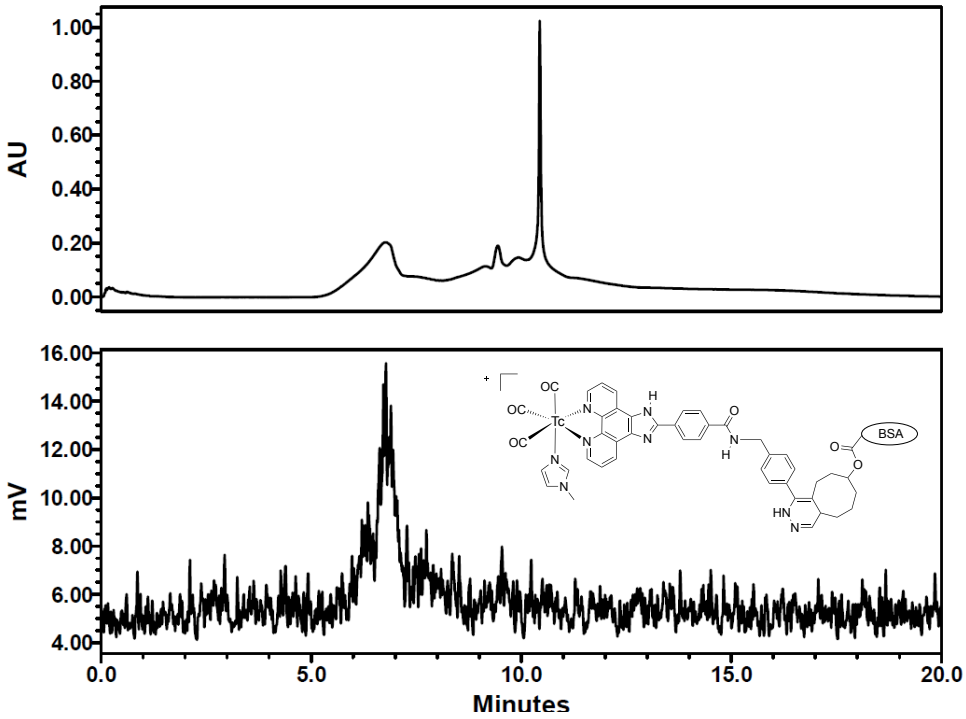

Figure S2.107 UV-HPLC trace of **15** (top) and γ-HPLC trace of **15** (bottom) (Method F).

Appendix II: Synthesis, Characterization and Preliminary Testing of a Near Infrared PIP Derivative

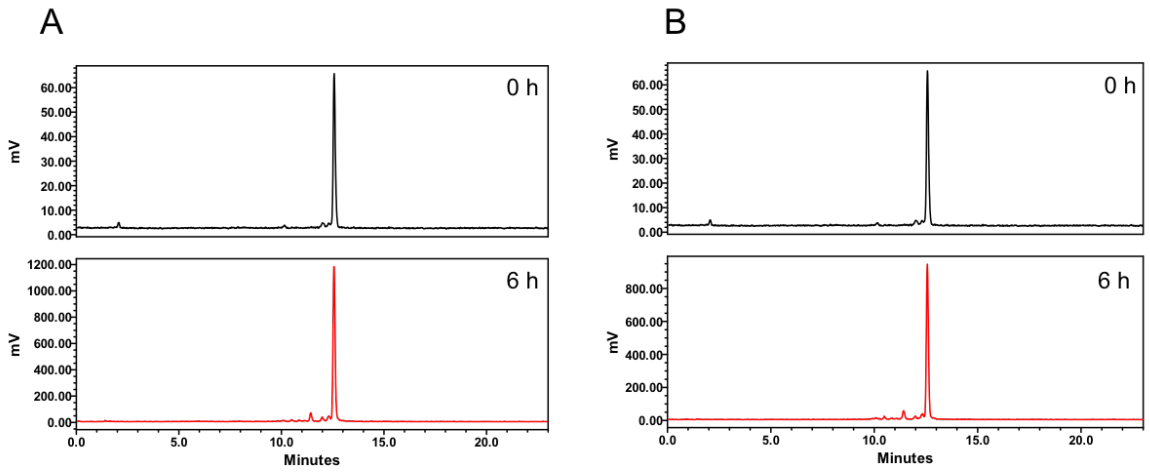

Figure S3.1. Gamma HPLC trace of **13**. A: Stability of **13** in saline. B: Stability of **13** in excess cysteine.

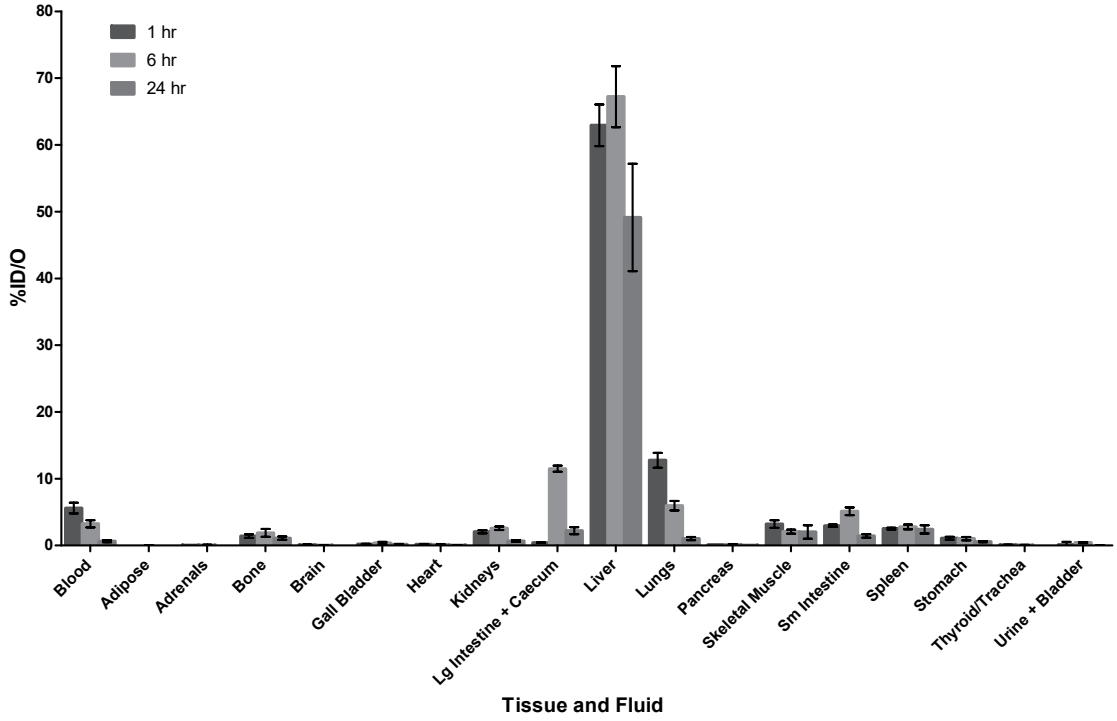

Figure S3.2. Biodistribution data for selected fluids and tissues for **13**. Experiments were performed using Balb/c mice (n=3 per time point) and tissues and fluids were collected at 1, 6, and 24 h post administration. Data is expressed as the mean percent injected dose per organ (%ID/O) ± SEM.

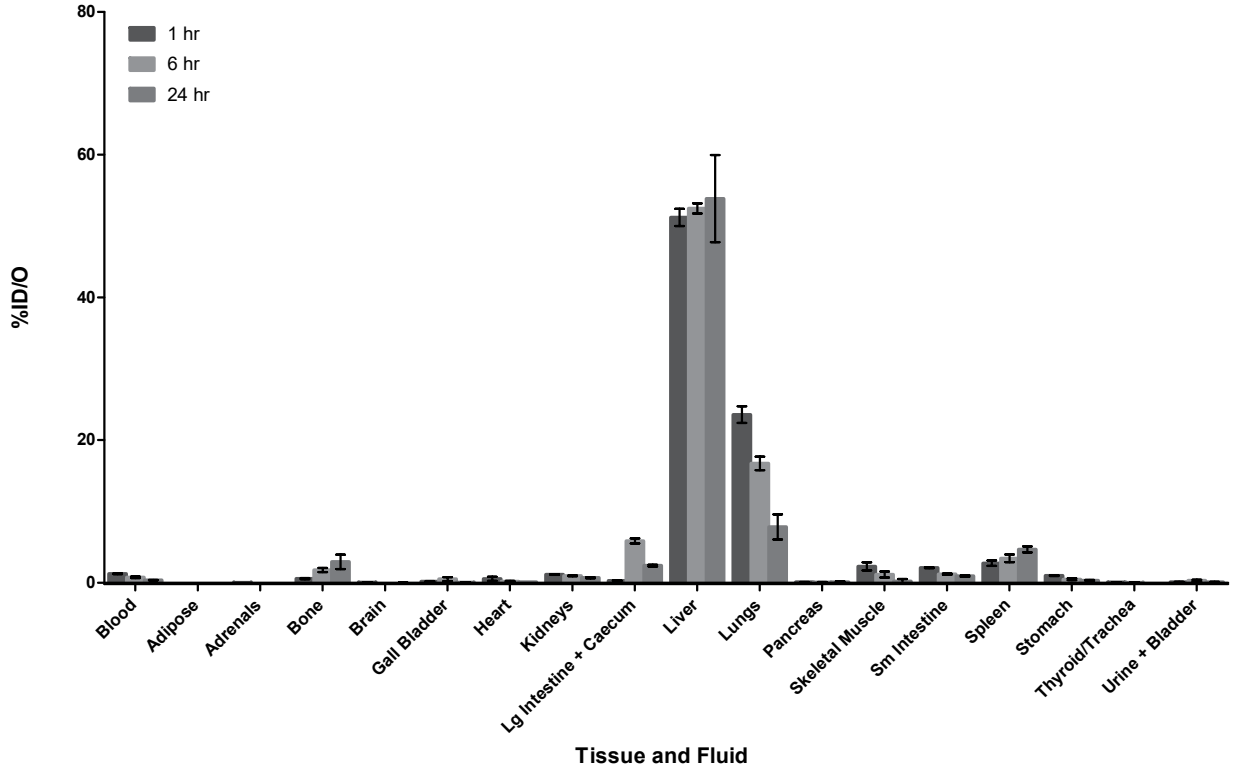

Figure S3.3. Biodistribution data for selected fluids and tissues for **13** with excess NMI. Experiments were performed using Balb/c mice (n=3 per time point) and tissues and fluids were collected at 1, 6, and 24 h post administration. Data is expressed as the mean percent injected dose per organ (%ID/O) ± SEM.

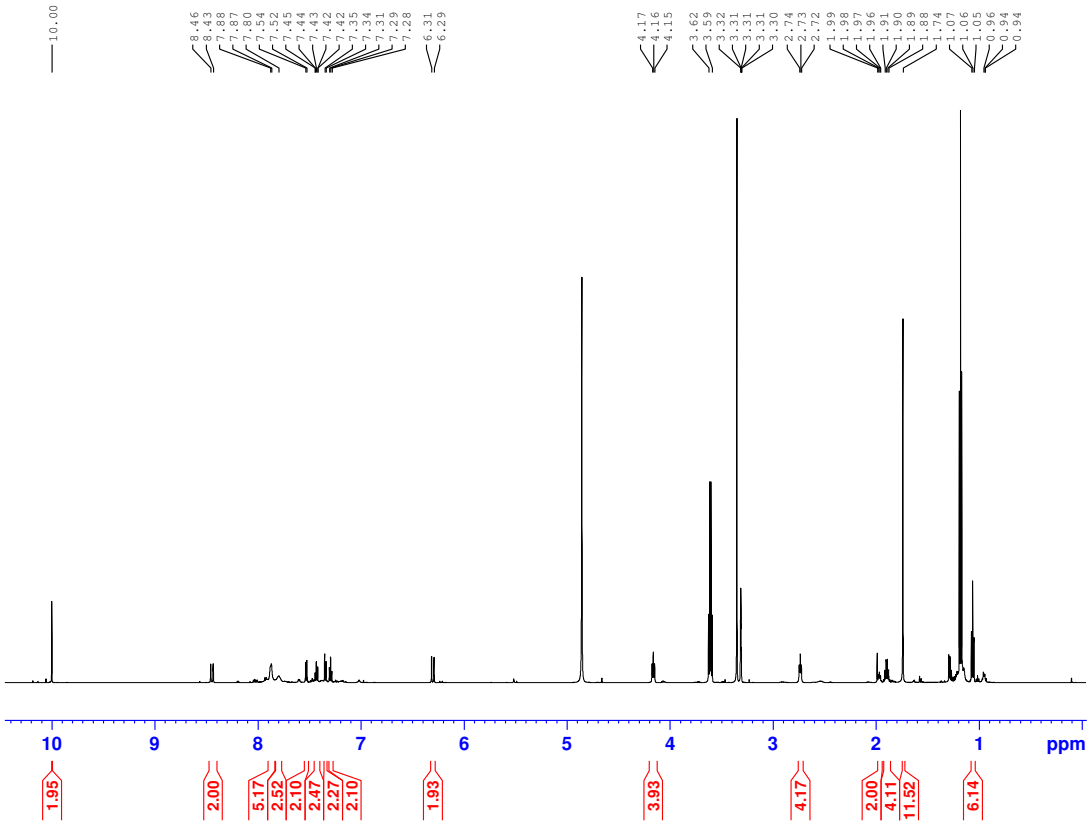

Figure S3.4. Crude ^{1}H NMR of **19**.

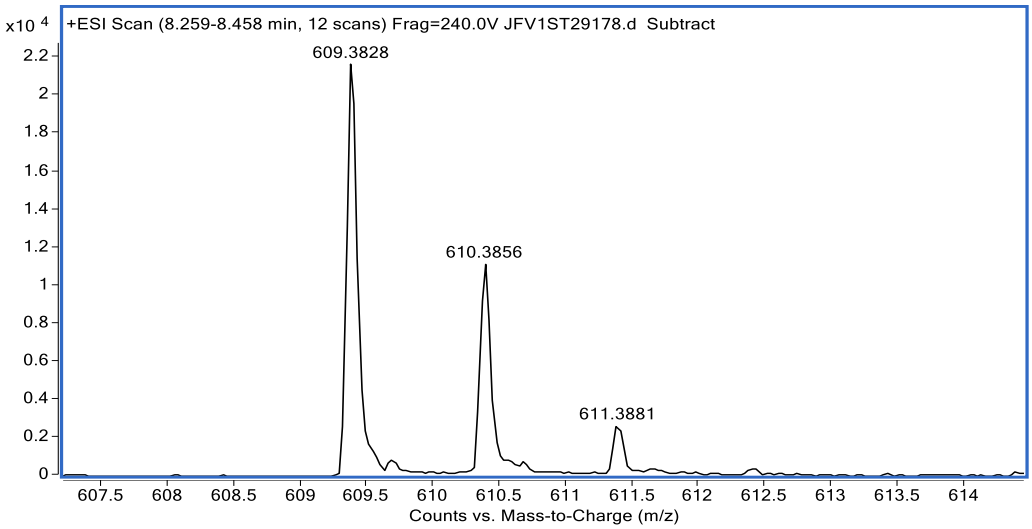

Figure S3.5. HRMS of **19**.

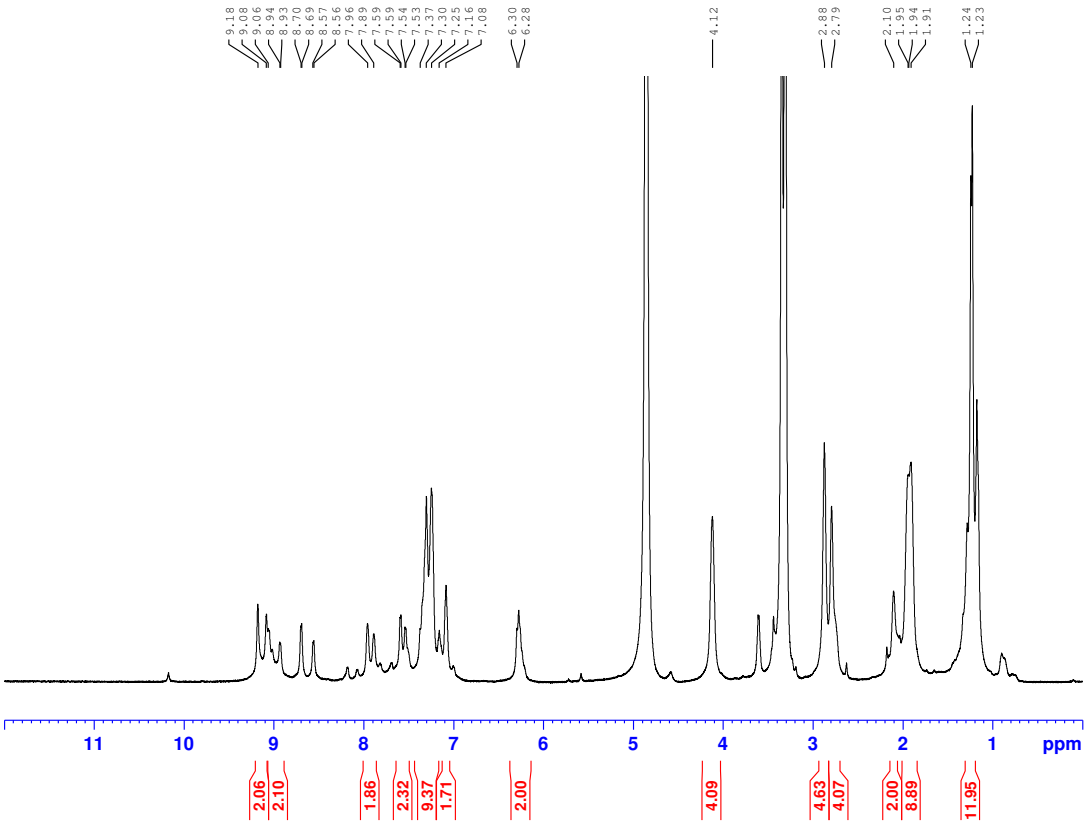

Figure S3.6. Crude ^{1}H NMR of **22**.

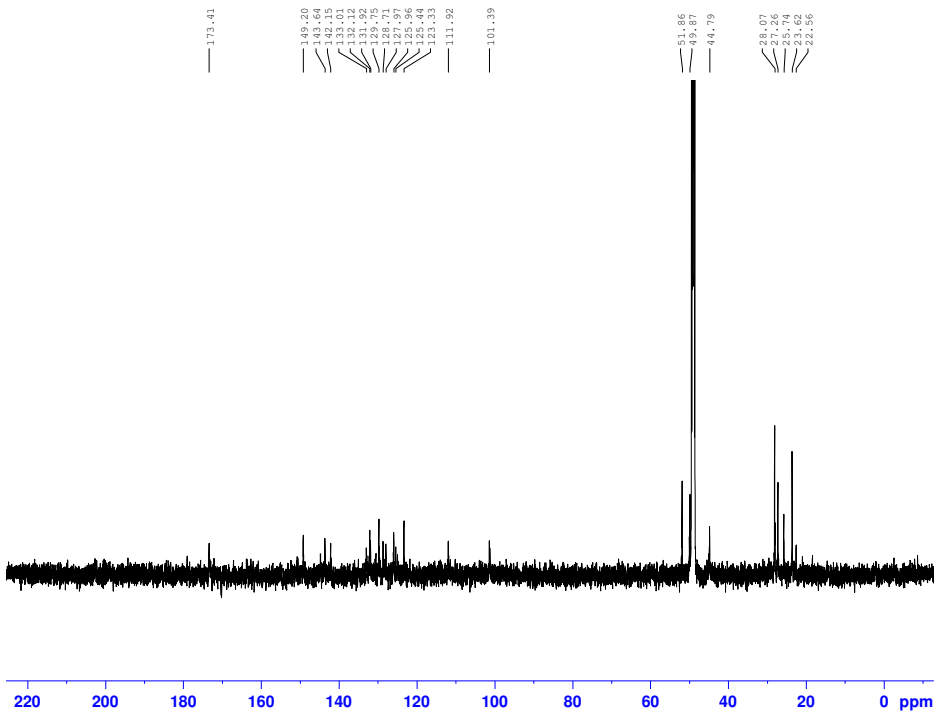

Figure S3.7 Crude ^{13}C NMR of **22**.

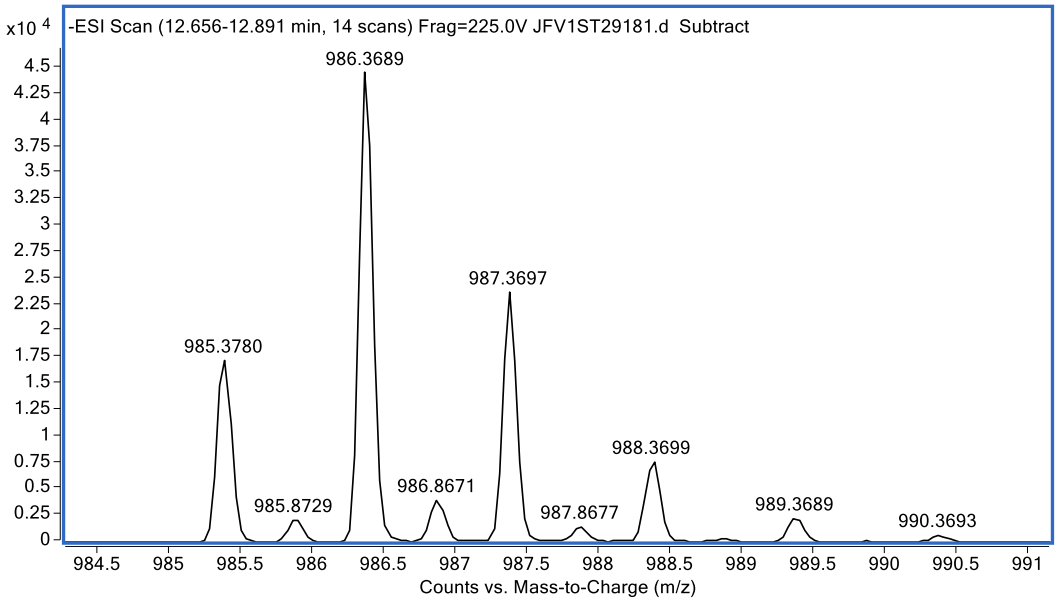

Figure S3.8. HRMS of **22.**

Appendix III: An Albumin-Binding Tetrazine-Derived Near-Infrared Dye as a Facile Reagent for Developing Targeted Photoacoustic Imaging Agents

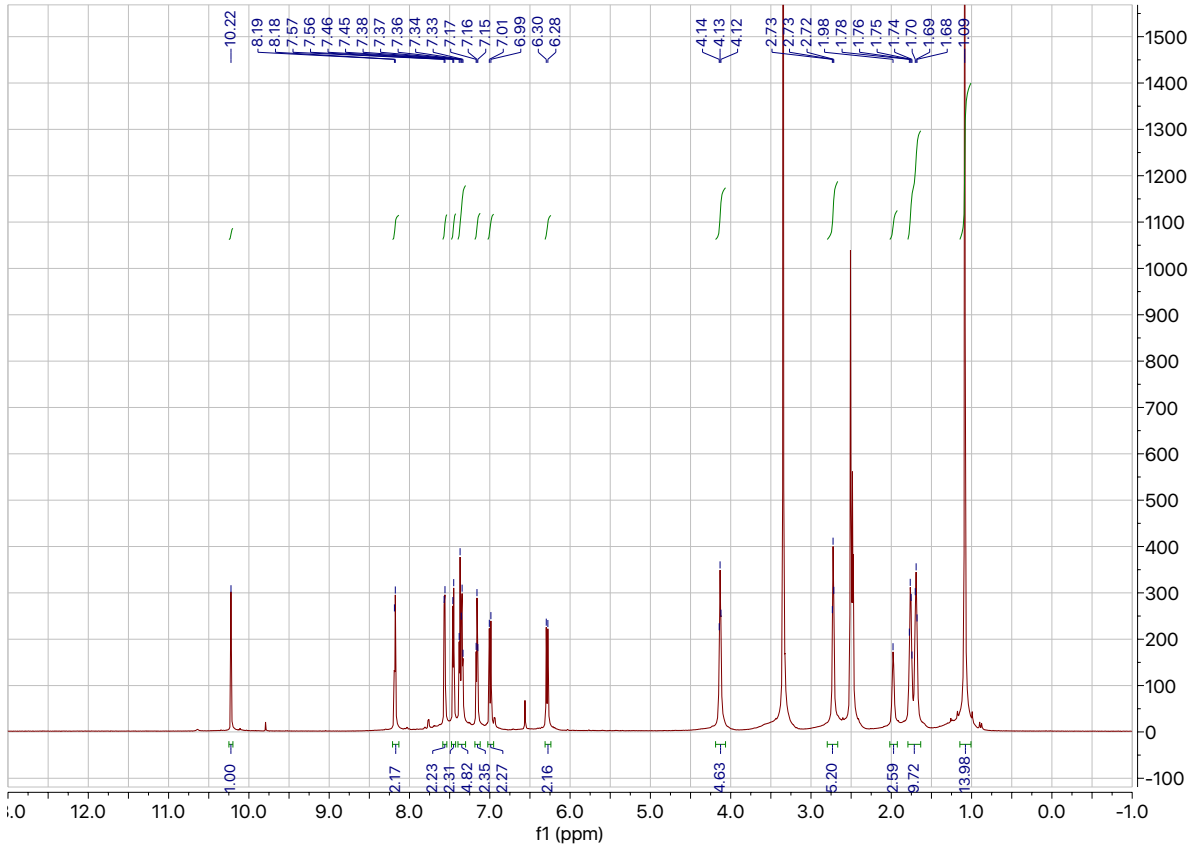

Figure S4.20 ^{1}H NMR $(CD_3)_2SO$, 700 MHz of **20**.

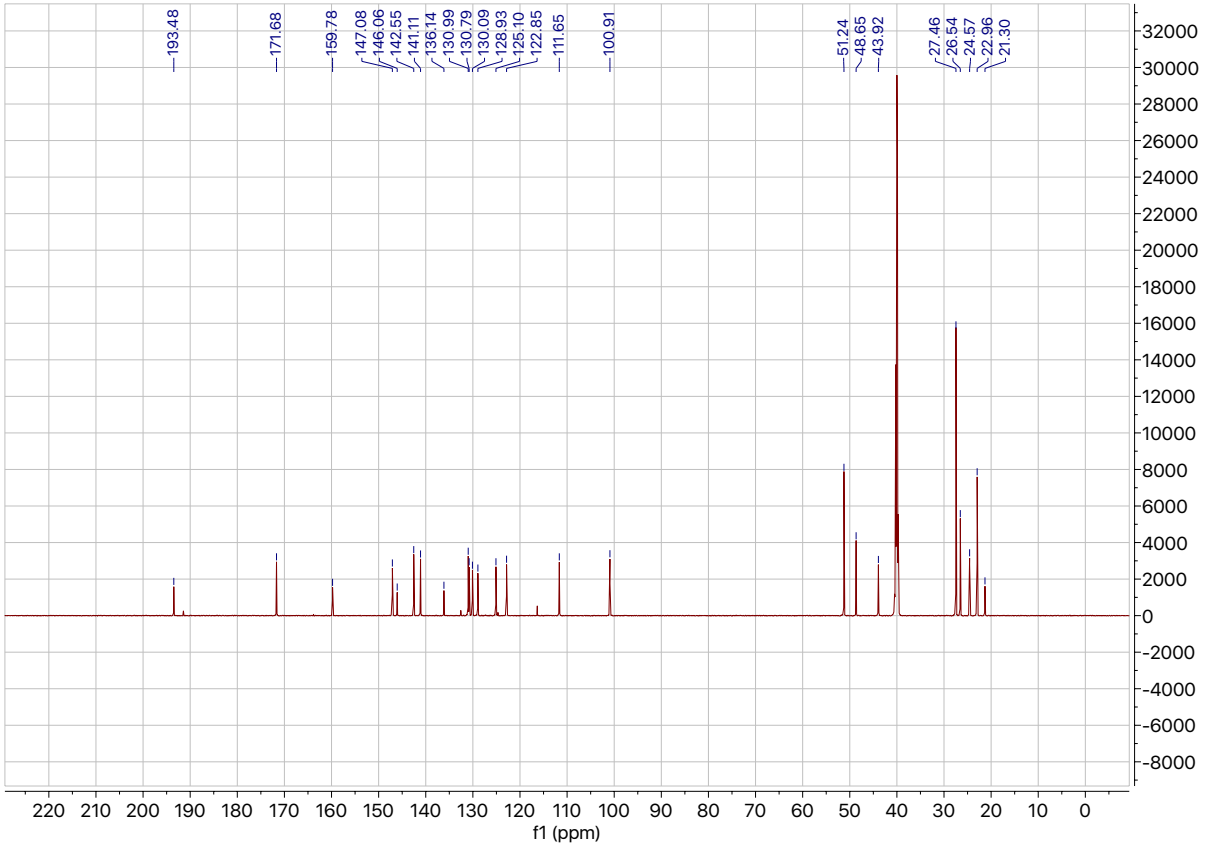

Figure S4.21 ^{13}C NMR $(CD_3)_2SO$, 150 MHz of **20**.

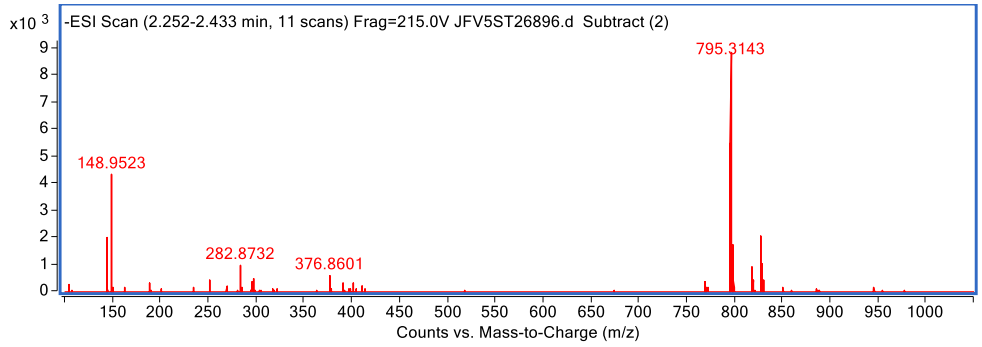

Figure S4.22 HRMS of **20**.

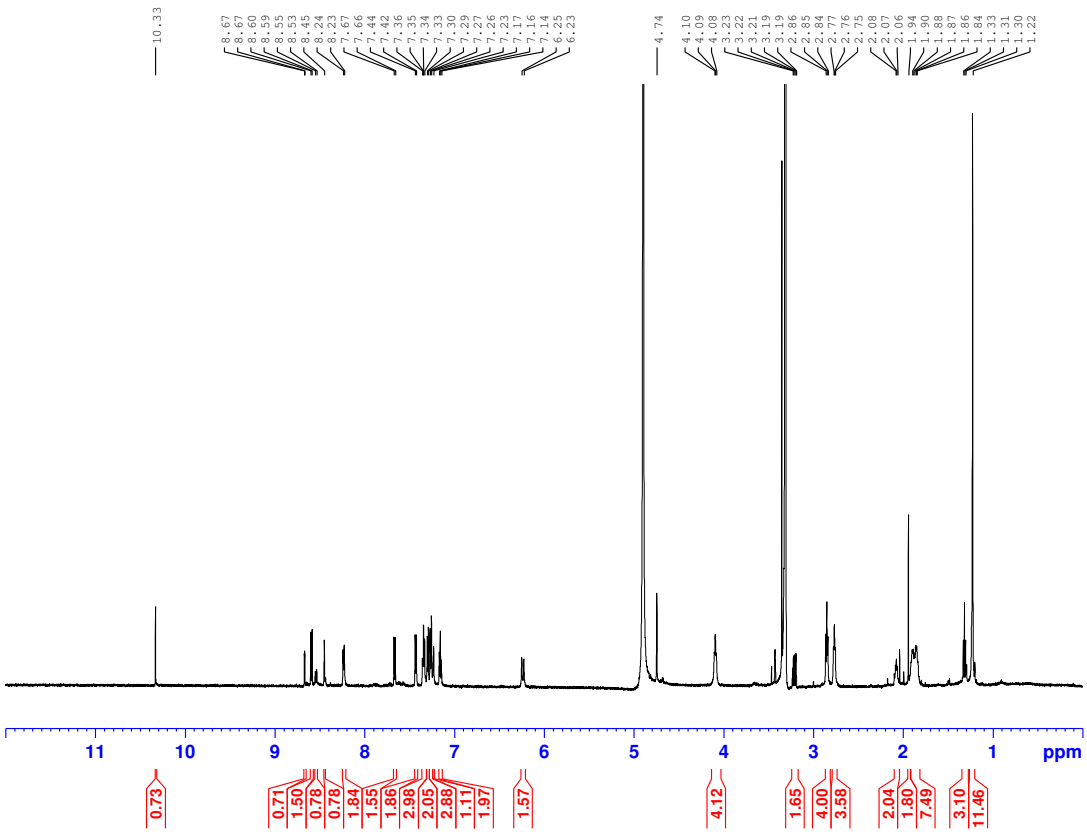

Figure S4.4 ^{1}H NMR CD_3OD, 600 MHz of **28**.

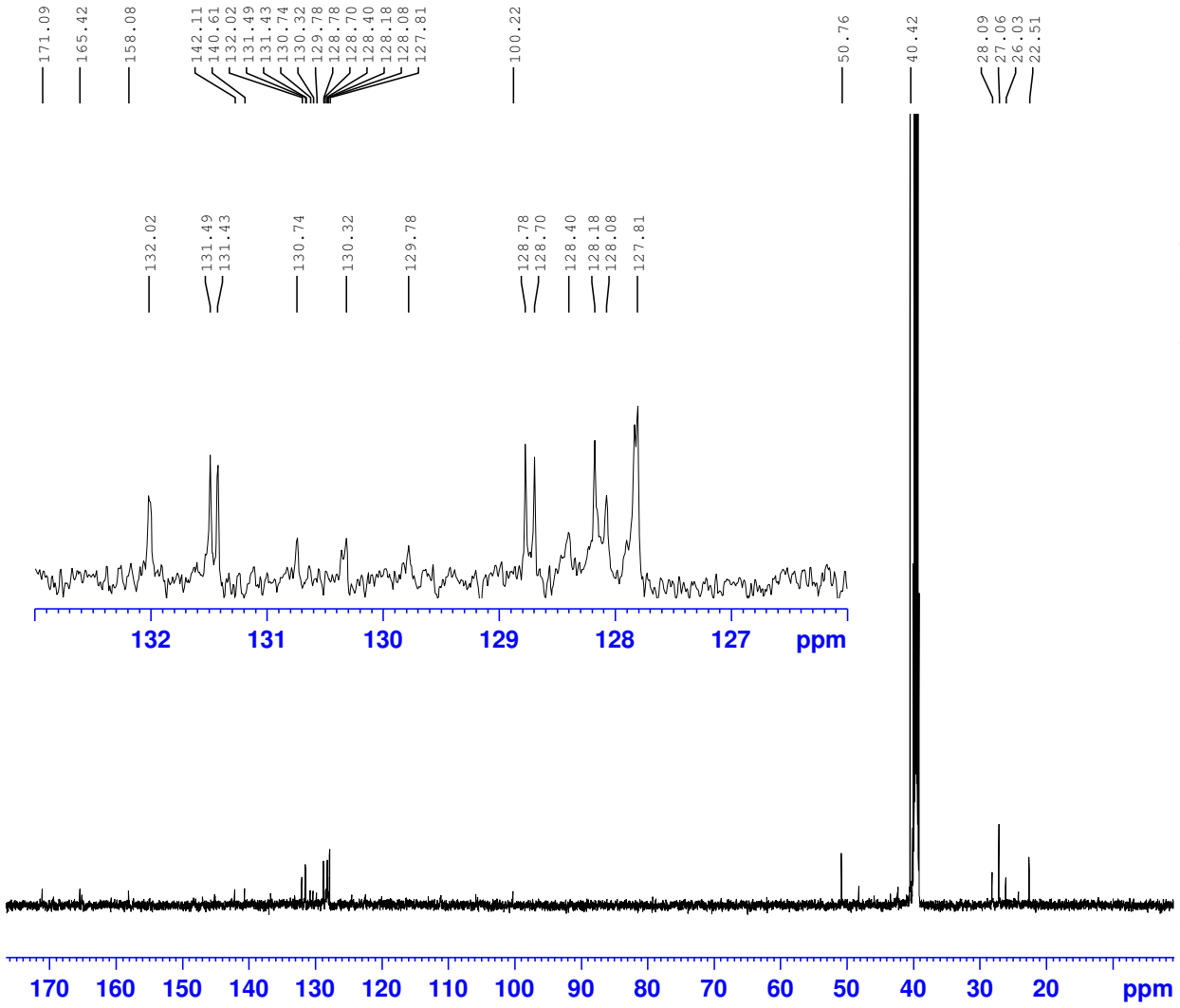

Figure S4.5 ^{13}C NMR $(CD_3)_2SO$, 150 MHz of **28**.

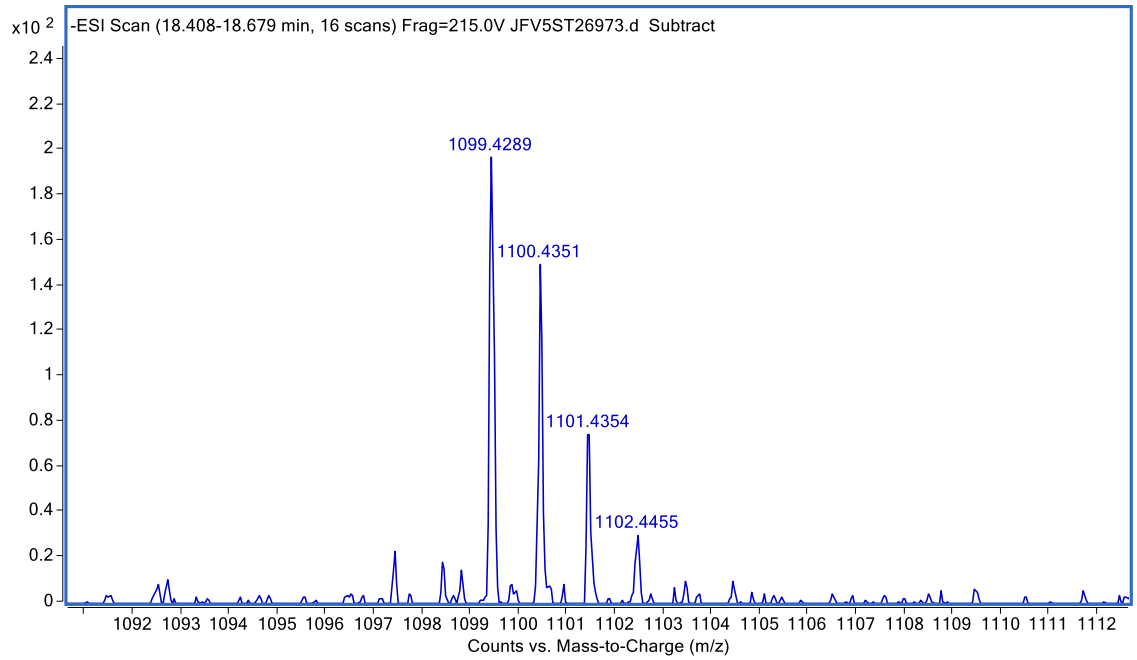

Figure S4.6 HRMS of **28**.

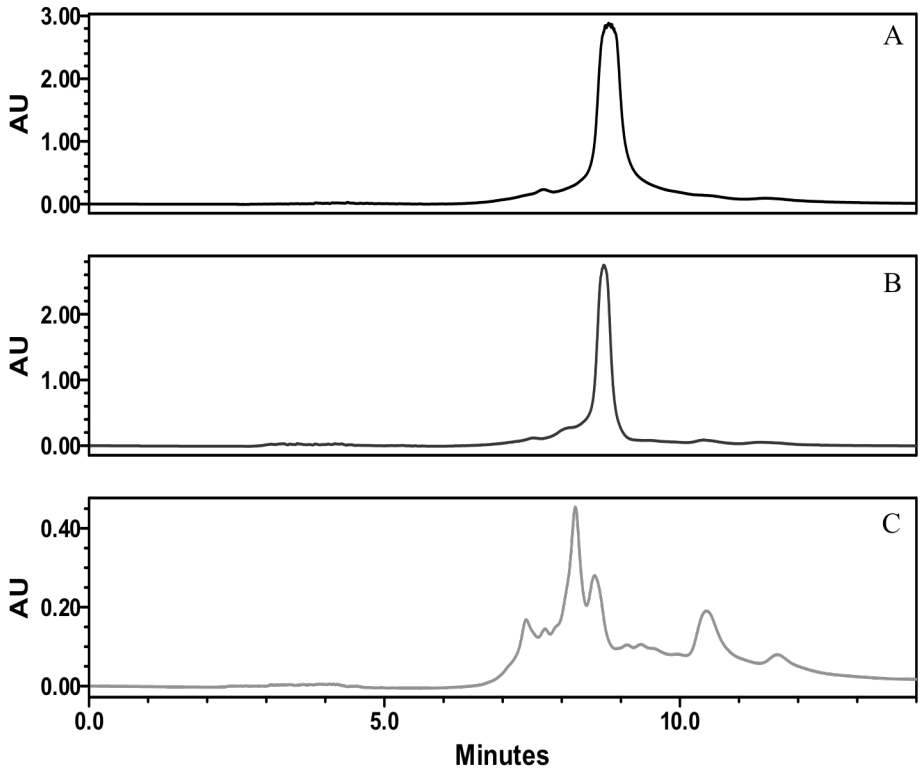

Figure S4.7 Plasma Stability of **28** A) Before addition to plasma, B) 24 h after incubating at 37 °C in plasma, C) Reacting with TCO-BP after 24 h in plasma.

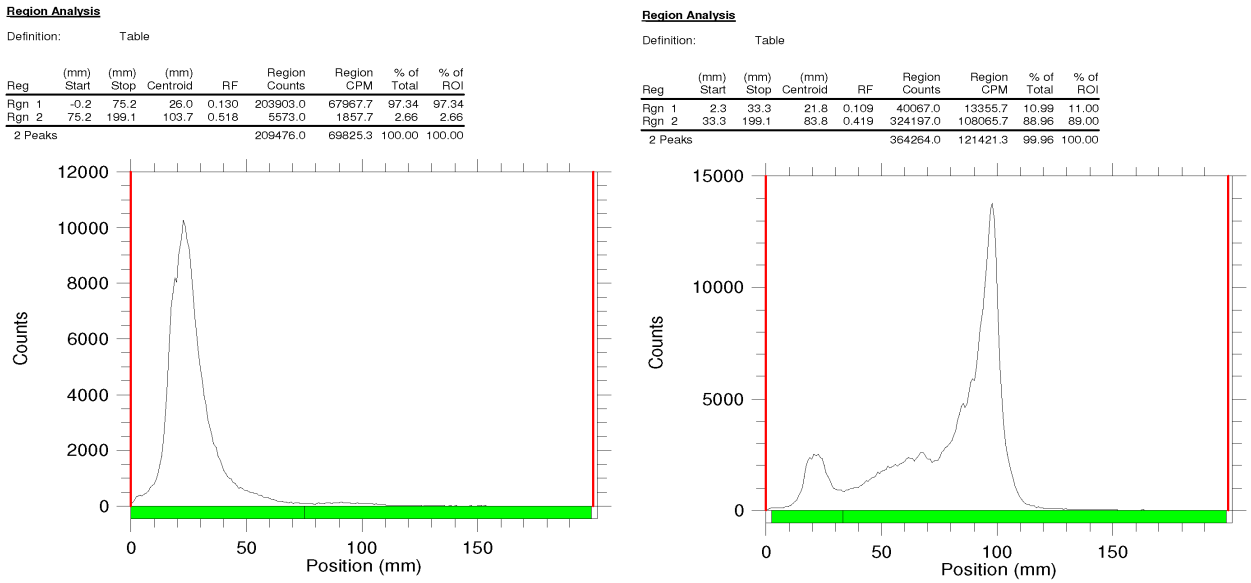

Region Analysis

Definition: Table

Reg	(mm) Start	(mm) Stop	(mm) Centroid	RF	Region Counts	Region CPM	% of Total	% of ROI
Rgn 1	-0.2	75.2	26.0	0.130	203903.0	67967.7	97.34	97.34
Rgn 2	75.2	199.1	103.7	0.518	5573.0	1857.7	2.66	2.66
2 Peaks					209476.0	69825.3	100.00	100.00

Region Analysis

Definition: Table

Reg	(mm) Start	(mm) Stop	(mm) Centroid	RF	Region Counts	Region CPM	% of Total	% of ROI
Rgn 1	2.3	33.3	21.8	0.109	40067.0	13355.7	10.99	11.00
Rgn 2	33.3	199.1	83.8	0.419	324197.0	108065.7	88.96	89.00
2 Peaks					364264.0	121421.3	99.96	100.00

Figure S4.8 RadioTLC traces of **31**. Left: Acetonitrile radioTLC showing 2.66% free pertechnetate. Right: Water radioTLC showing 11% colloidal ^{99m}Tc.

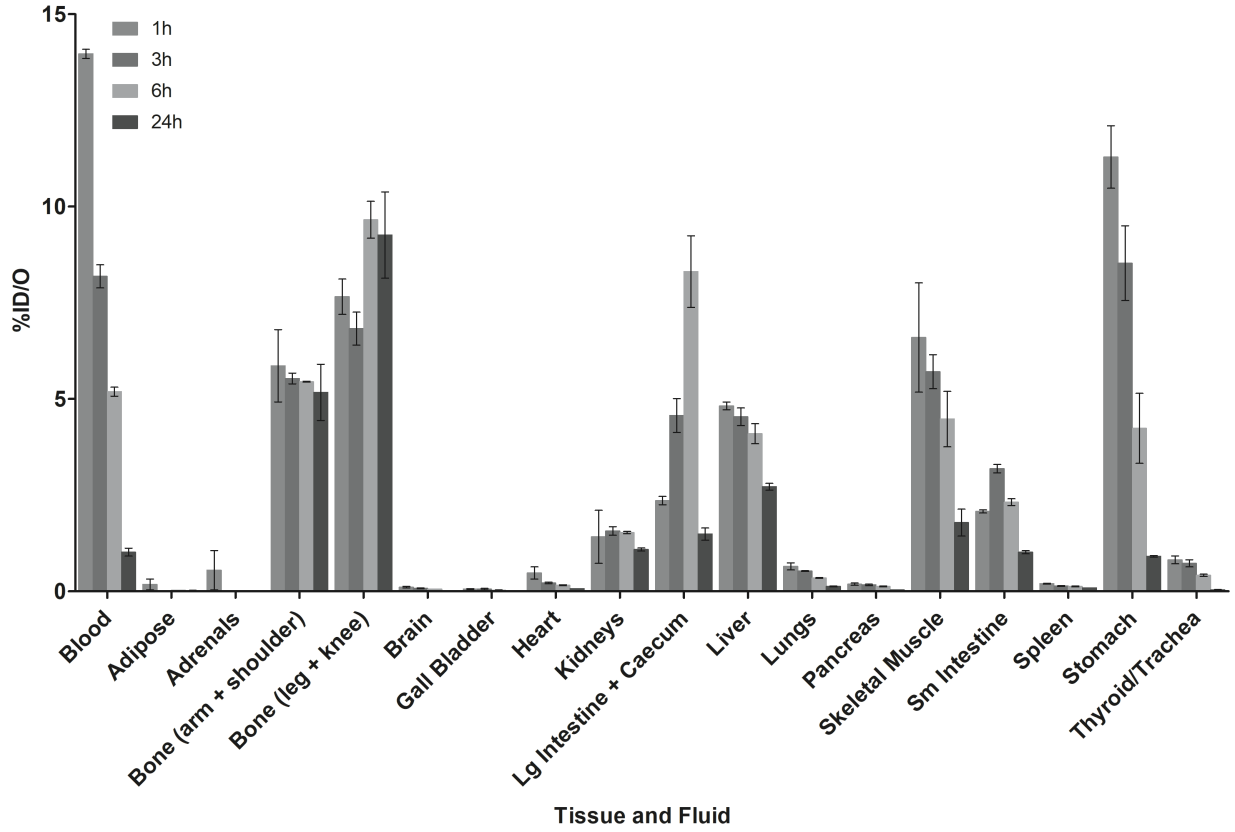

Figure S4.9 Biodistribution data for selected fluids and tissues for active targeting of **32.** Experiments were performed using Balb/c mice (n=3 per time point) and tissues collected at 1, 3, 6, 24 h post administration. Data are expressed as the mean percent injected dose per organ (%ID/O) ± SEM.

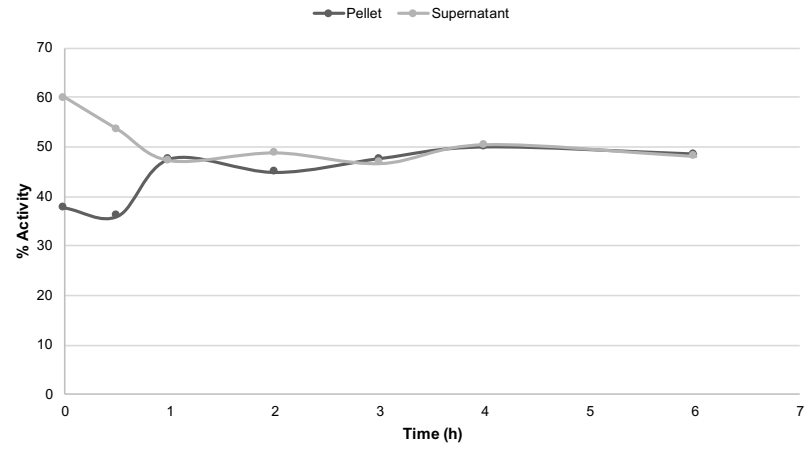

Time (h)	Pellet	Supernatant
0	32.79	52.00
0.5	36.10	53.44
1	47.53	47.27
2	45.29	49.35
3	47.72	46.82
4	46.88	47.42
6	47.83	47.46

Figure S4.10 Plasma binding study of **32**.

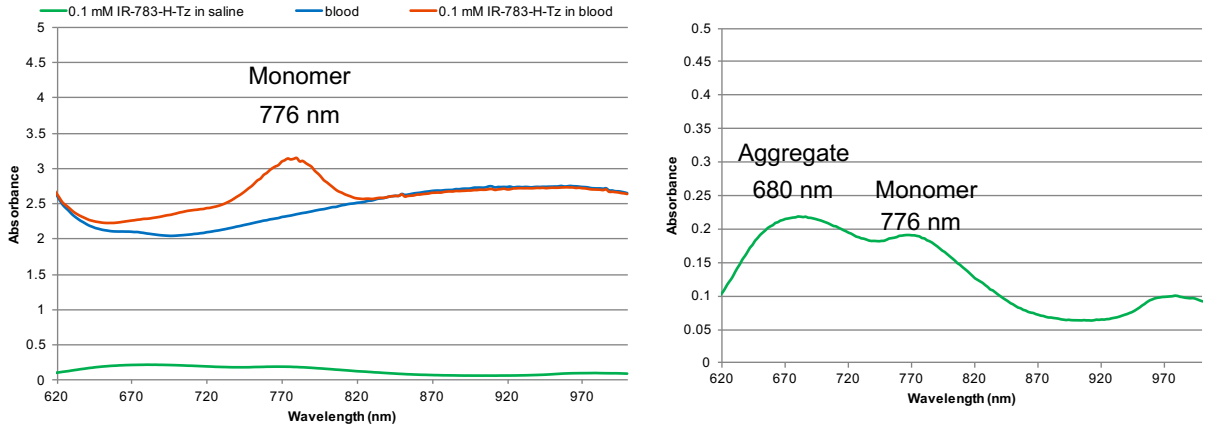

Figure S4.11 Absorbance of 0.1 mM **28** in saline (green), 0.1 mM **28** in whole blood (red), and whole blood alone (blue).

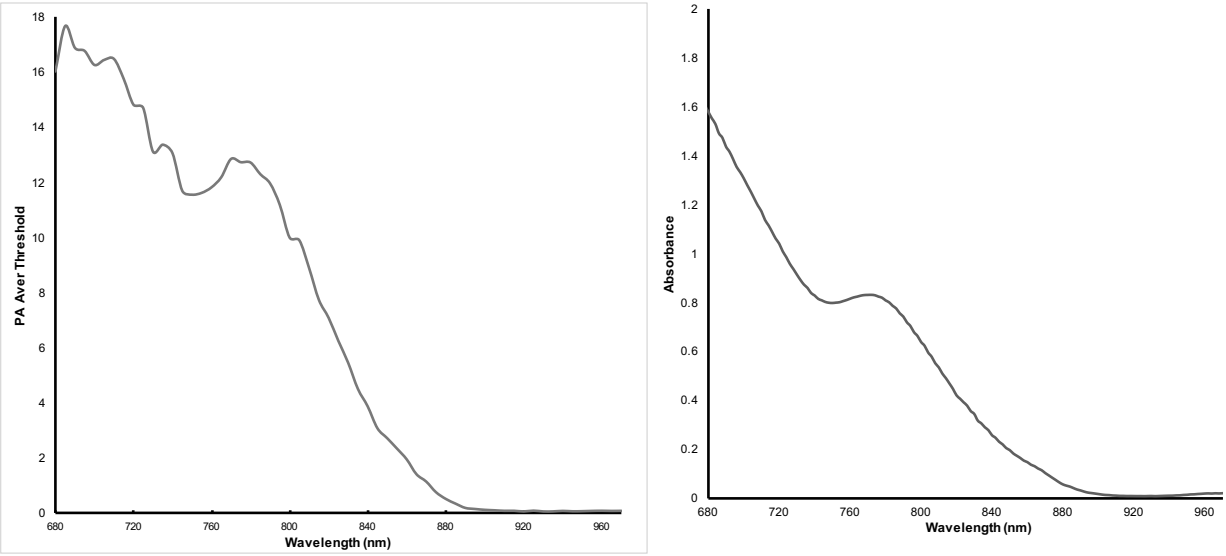

Figure S4.12 Left: PA average threshold spectra of **28**. Right: Absorbance spectra of **28**.

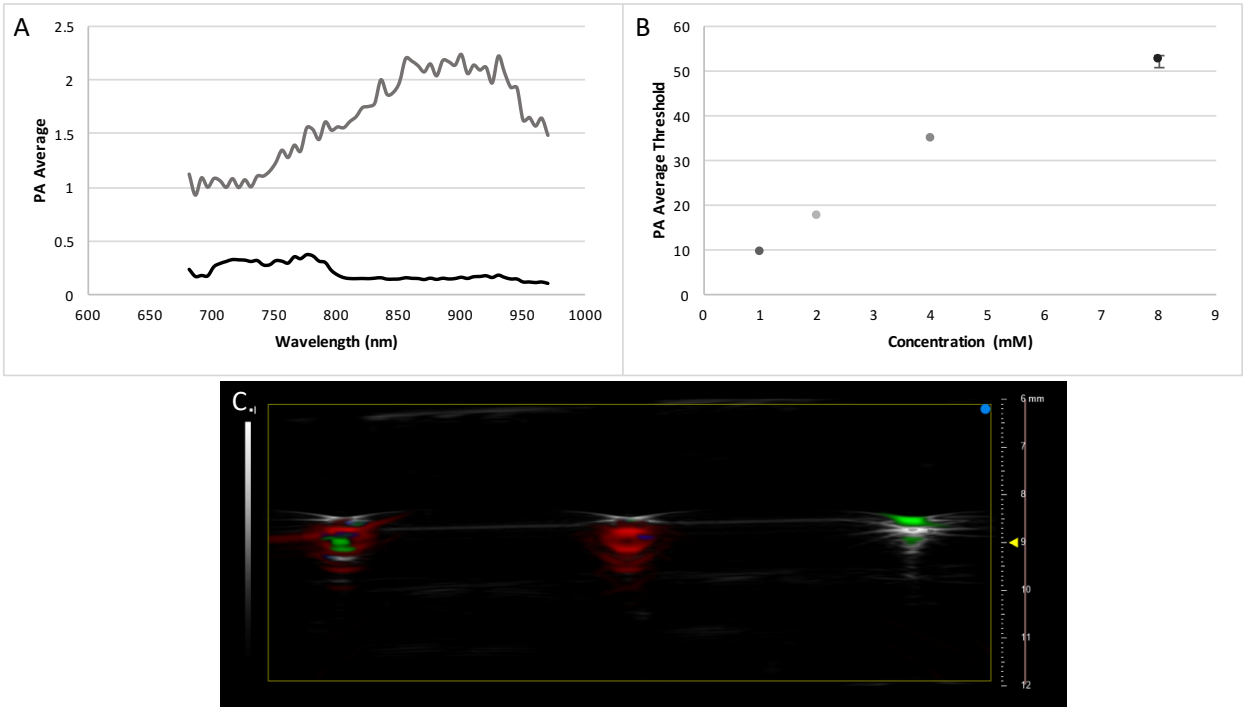

Figure S4.13 A) Normalized PA Spectra of 0.1 mM **28** in saline (black) and blood (grey). B) PA average threshold vs. concentration of **28** at maxima in phantom (775 nm). C) Overlay B-Mode and photoacoustic image in phantom with spectral unmixing of 0.1 mM **28** in blood, and 0.1 mM **28** in saline.

Appendix IV: *In Vivo* Photoacoustic Imaging of Glioblastoma Multiforme

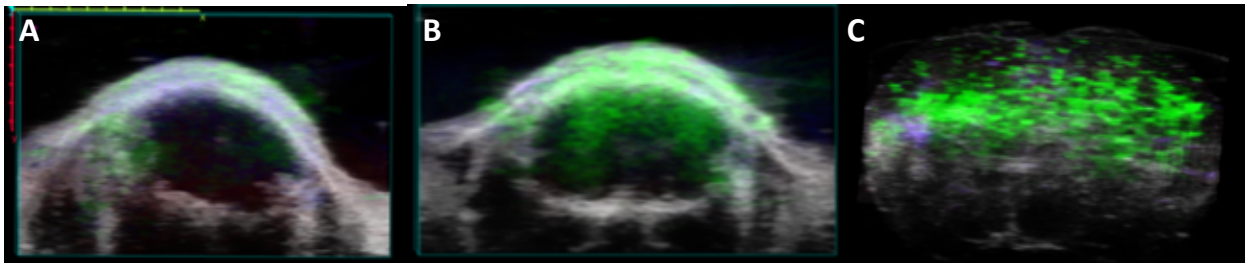

Figure S6.23 PA images of the brain and skull of mouse 1-1 in a glioblastoma model. A: Prior to administration, B: PA image of the same mouse 1 hour after injection, C: ex vivo 1 hour after injection. Red = oxyhemoglobin, Blue = deoxyhemoglobin, Green= **28**.

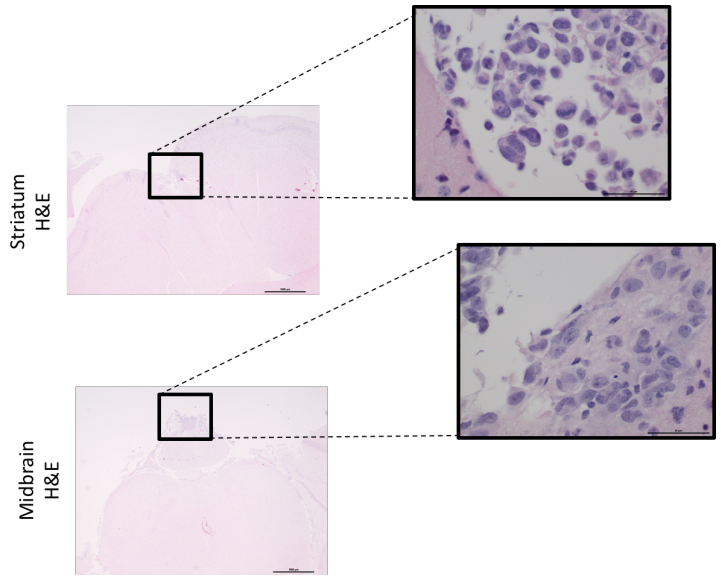

Figure S6.2 Histologic analysis of the infiltration of GBM cells in the striatum and midbrain of mouse 1-1. Representative sections stained with H&E showing the tumour cells in the striatum and midbrain. (Left: scale bar = 1000 μm; Right: scale bar = 50 μm).

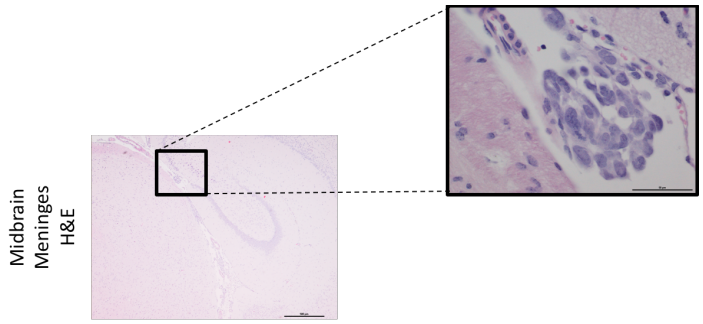

Figure S6.3 Histologic analysis of the infiltration of GBM cells in the midbrain and striatum meninges of mouse 1-1. Representative sections stained with H&E showing the tumour cells in the striatum. (Left: scale bar = 500 μm; Right: scale bar = 50 μm).

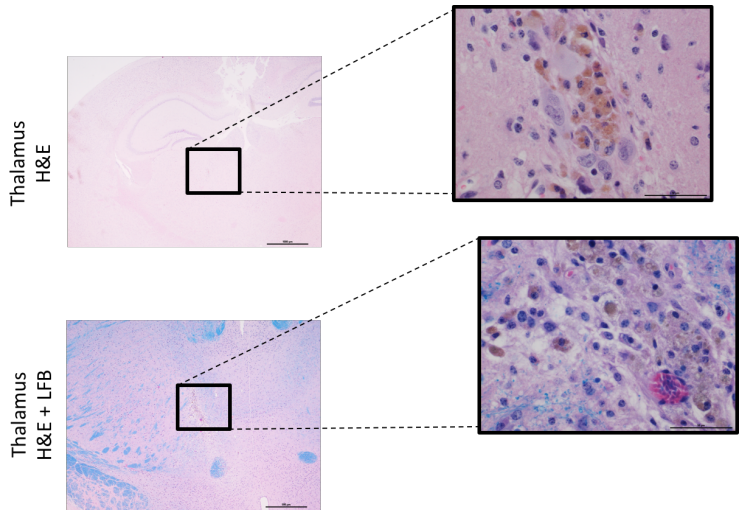

Figure S6.4 Histologic analysis of the infiltration of GBM cells in the thalamus of mouse 1-1. Representative sections stained with H&E or H&E and LFB showing the tumour cells in the thalamus. (Top left: scale bar = 1000 μm; Top right: scale bar = 50 μm; Bottom left: scale bar = 500 μm; Bottom right: scale bar = 50 μm).

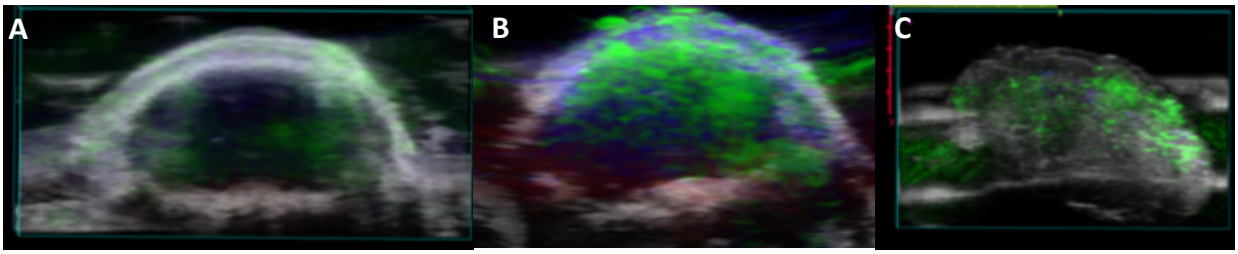

Figure S6.5 PA images of the brain and skull of mouse 1-3 in a glioblastoma model. A: Prior to administration, B: PA image of the same mouse 1 hour after injection, C: ex vivo 1 hour after injection. Red = oxyhemoglobin, Blue = deoxyhemoglobin, Green= **28**.

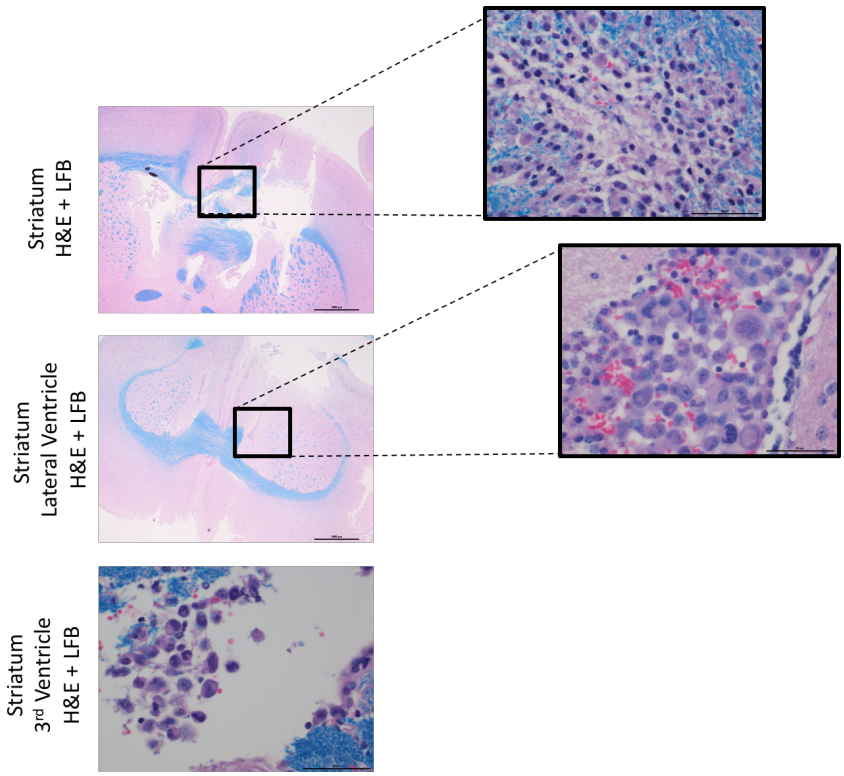

Figure S6.6 Histologic analysis of the infiltration of GBM cells in the striatum and ventricles of mouse 1-3. Representative sections stained with H&E and LFB showing the tumour cells in the striatum and ventricles. (Top left: scale bar = 1000 μm; Top right: scale bar = 50 μm; Middle left: scale bar = 1000 μm; Middle right: scale bar = 50 μm; Bottom left: scale bar = 50 μm).

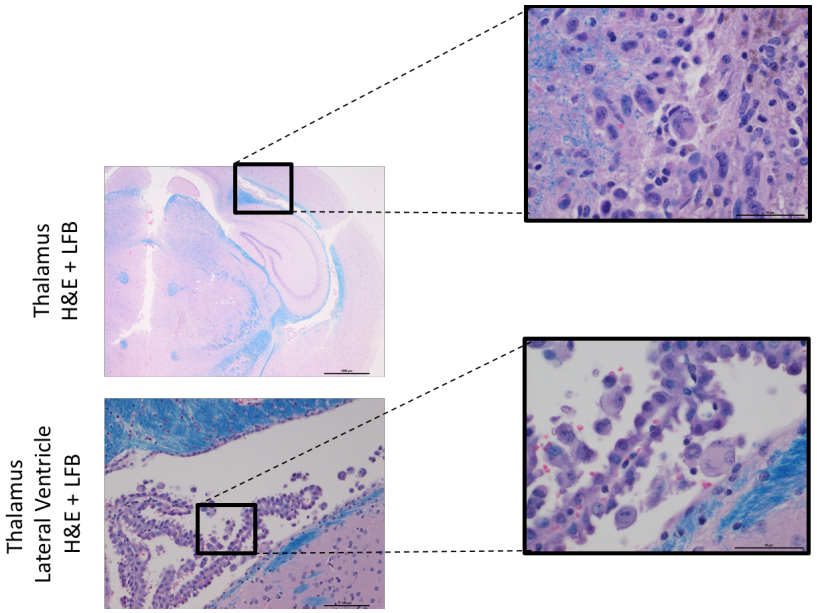

Figure S6.24 Histologic analysis of the infiltration of GBM cells in the thalamus of mouse 1-3. Representative sections stained with H&E and LFB showing the tumour cells in the thalamus. (Top left: scale bar = 1000 μm; Top right: scale bar = 50 μm; Bottom left: scale bar = 100 μm; Bottom right: scale bar = 50 μm).

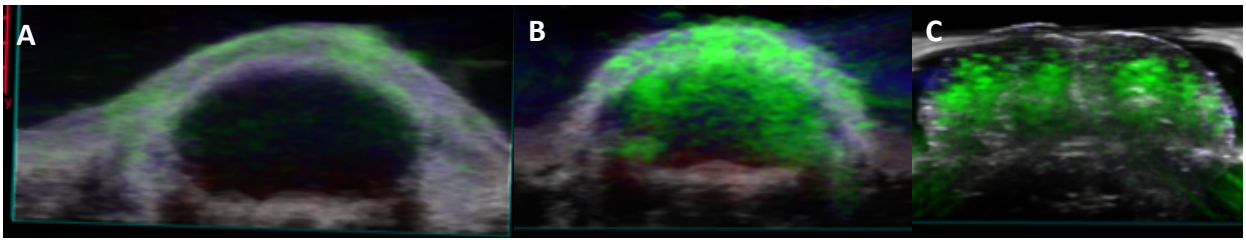

Figure S6.8 PA images of the brain and skull of mouse 1-4 in a glioblastoma model. A: Prior to administration, B: PA image of the same mouse 1 hour after injection, C: ex vivo 1 hour after injection. Red = oxyhemoglobin, Blue = deoxyhemoglobin, Green= **28**.

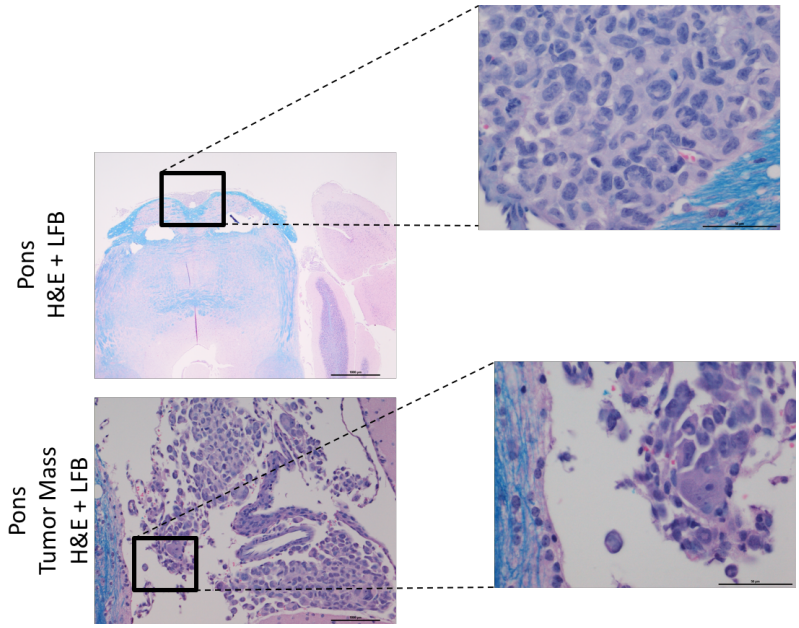

Figure S6.9 Histologic analysis of the infiltration of GBM cells in the pons of mouse 1-4. Representative sections stained with H&E and LFB showing the tumour cells in the pons. (Top left: scale bar = 1000 μm; Top right: scale bar = 50 μm; Bottom left: scale bar = 1000 μm; Bottom right: scale bar = 50 μm).

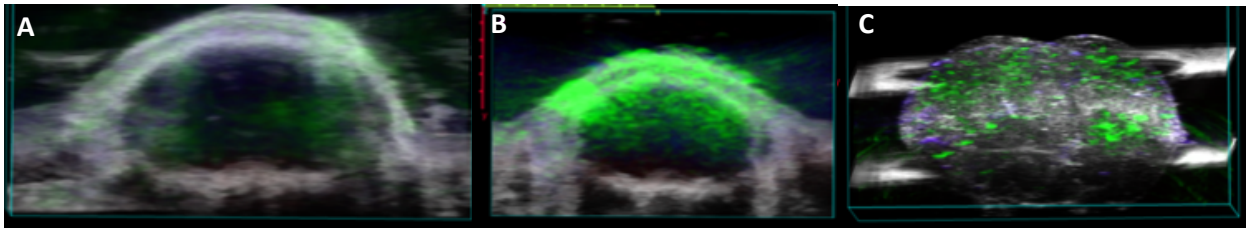

Figure S6.10 PA images of the brain and skull of mouse 1-5 in a glioblastoma model. A: Prior to administration, B: PA image of the same mouse 1 hour after injection, C: ex vivo 1 hour after injection. Red = oxyhemoglobin, Blue = deoxyhemoglobin, Green= **28**.

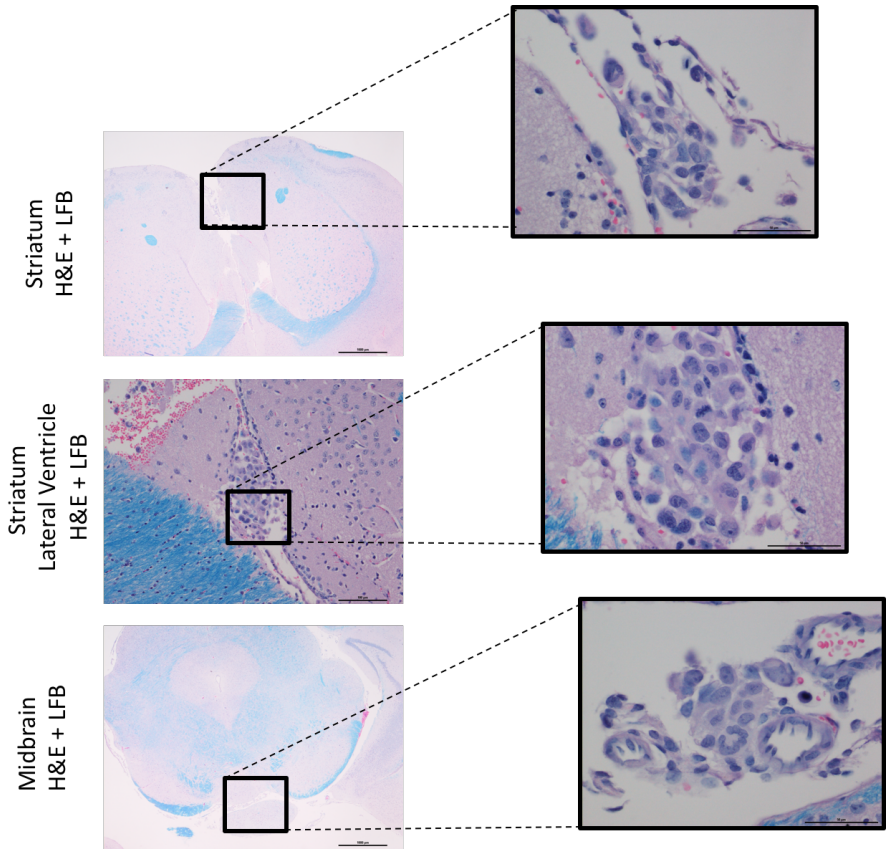

Figure S6.11 Histologic analysis of the infiltration of GBM cells in the striatum and midbrain of mouse 1-5. Representative sections stained with H&E and LFB showing the tumour cells in the striatum and midbrain. (Top left: scale bar = 1000 μm; Top right: scale bar = 50 μm; Middle left: scale bar = 100 μm; Middle right: scale bar = 50 μm; Bottom left: scale bar = 1000 μm; Bottom right: scale bar = 50 μm).